Nanoconfinement of Complex Hydrides in Porous Hosts for Hydrogen Storage Applications

Marc Segalés

A thesis submitted to the University of Glasgow for the degree of Doctor of Philosophy

Supervisor: Prof. Duncan H. Gregory

School of Chemistry

College Science and Engineering

University of Glasgow, December 2015

Abstract

The transition from a fossil fuel-dependent society to a cleaner, more sustainable society will not be possible without renewable energy sources. Hydrogen holds great potential as an energy carrier as an alternative to fossil fuels in such society. However, the compact and safe storage of hydrogen are still major challenges. Solid state hydrogen storage offers the possibility to store hydrogen in solids offering high volumetric and high gravimetric energy densities, while reducing the risks associated when handling hydrogen gas. However, no single system has fully achieved the required properties for on-board mobile applications.

Various approaches can be adopted with the aims of improving the kinetics and thermodynamics of hydrogen sorption. The nanostructuring of materials is one of the more promising strategies to achieve these aims. Reduction of the particle size of hydrides by nanoconfinement in forms of porous matrix leads to an increased surface area of the active material, and shorter diffusion distances for hydrogen atoms or ions to travel in the solid state. Kinetic barriers can be overcome and thermodynamics manipulated. An enhanced dehydrogenation rate and a reduced dehydrogenation temperature can be achieved by impregnating metal hydrides into porous scaffolds.

Two complex hydrides are selected for study in this work; $LiAlH_4$ and $LiNH_2$. $LiAlH_4$, is the lightest of the alanates, with a theoretical hydrogen storage capacity of 10.5 wt.%, and 7.9 wt.% H_2 evolved below 220 °C. $LiNH_2$ mixed with LiH, as part of the Li-N-H system, can reversibly desorb/uptake 6.5 wt.% H_2 at 300 °C. When $LiNH_2$ is heated alone, it releases ammonia (which is decomposed to N_2 and H_2 at higher temperatures > 400 °C).

In this work, $LiAlH_4$ has been impregnated in different types of commercial and synthesised porous carbon scaffolds for the first time. Nanoconfinement of the active material was achieved using solution impregnation with diethyl ether as a solvent. Analogously, the confinement of $LiNH_2$ in porous carbon was achieved "*in-situ*" using lithium-ammonia solutions. Both confined composites showed lower dehydrogenation temperatures in comparison with the respective bulk materials.

The influence of the design of the carbon scaffold (as manifested for example, by the surface area and the pore volume and pore size distribution) on the dehydrogenation behaviour of the impregnated complex hydrides is demonstrated. By judicious selection of an appropriate porous host, we show how it is possible to induce faster H_2 desorption and substantially reduce the desorption temperature.

The onset of hydrogen release for confined $LiAlH_4$ decreased significantly in temperature, being reduced by 51 °C (in both porous hosts used, AX-21 and FDU-15) in comparison with pristine $LiAlH_4$. The temperature at which the hydrogen release was maximised was also lowered (by 16 °C in FDU-15 and by 26 °C in AX-21) in comparison with as-received $LiAlH_4$.

The confined $LiNH_2$ showed a much earlier release of hydrogen compared with as-received $LiNH_2$. Normally $LiNH_2$ would thermally decompose to Li_2NH with ammonia evolution, but ammonia release was eliminated for the confined sample. Reaction with carbon led to irreversible Li_2CN_2 formation and hydrogen evolution. A set of experiments to establish the formation of Li_2CN_2 with physically mixed samples were performed. The physically mixed samples showed hydrogen release between 400 - 450 °C, producing a mixture of Li_2NH and Li_2CN_2, suggesting two decomposition pathways were followed. In contrast, confined $LiNH_2$ released hydrogen *ca.* 220 °C lower than the physically mixed sample, with no detectable trace of ammonia release

Table of Contents

Abbreviations and Definitions

Abbreviations	Definitions
PEMFC	Proton Exchange Membrane fuel cell
PEM	Proton Exchange Membrane
MOF	Metal Organic Framework
U.S D.o.E	United States Department of Energy
AC	Activated Carbon
HSAG	High Surface Area Graphite
OMC	Ordered Mesoporous Carbon
CA	Carbon Aerogel
BET	Brunnauer – Emmet – Teller (can be referred to the theory, the instrument or the data obtained for gas adsorption, depending of the context)
SPS	Solvent Purifier Station
IR	Infra-red
UV	Ultra-violet
ATR	Attenuated Total Reflection
CCD	Charged-coupled device
PXD or PXRD	Powder X-Ray Diffraction
XRD	X-Ray Diffraction
ICSD	Inorganic Crystal Structure Database
IUPAC	International Union of Pure and Applied Chemistry
SEM	Scanning Electron Microscope (or Microscopy) *Also: Secondary Electron Multiplier, depending of the context
TEM	Transmission Electron Microscope (or Microscopy)
EDX	Energy Dispersive X-Ray
SE	Secondary Electrons
BSE	BackScattered Electrons
ESEM	Environmental Scanning Electron Microscope
SAED	Selected Area Electron Diffraction
EELS	Electron Energy Loss Spectroscopy

DTA	Differential Thermal Analysis
DSC	Differential Scanning Calorimetry
TGA	Thermal Gravimetric Analysis
DMA	Dynamic Mechanical Analysis
DEA	Dielectric Thermal Analysis
EGA	Evolved Gas Analysis
TOA	Thermo-Optical Analysis
STA	Simultaneous Thermal Analysis
MS	Mass Spectrometer (or Spectrometry)
CI	Chemical Ionisation
EI	Electron Impact
ESI	Electro-Spray Ionisation
FAB	Fast Atom Bombardment
FD	Field Desorption
FI	Field Ionisation
MALDI	Matrix Assisted Laser Desorption Ionisation
TOF	Time-of-Flight
EO	Ethylene Oxide
PO	Propylene Oxide
EISA	Evaporation Induced Self-Assembly
GPC	Gel Permeation Chromatography
AMU	Atomic Mass Unit
SAXS	Small-Angle X-Ray Scattering
BJH	Barret-Joyner-Halenda (calculation model)
THF	Tetrahydrofuran
MTBE	Methyl tert-butil ether
ICP-OES	inductively coupled plasma optical emission spectrometry
CNT	Carbon nanotubes
TMS	Transition metallic state

List of Tables

List of Figures

Acknowledgements

I would firstly like to thank my supervisor Prof. Duncan H. Gregory for giving me the chance to undertake this experience that was this PhD. I would also like to thank to Prof. Eric Majzoub from University of Missouri – Saint Louis (UMSL) for hosting me in a 3 month internship at his laboratory facilities. Thanks to Stuart Mackay to make lesser all the IT problems. And to Jim Gallagher for all the technical support at the lab. A special thanks too to the people who helped me get started in the academic-research world: Dr. Nuria Tapia- Ruiz, Dr. Tuan Hong and Dr. Natalie Sorbie. Thanks to Jen, Giulia, Hazel and Alan, the guys I started this adventure with, for all the time shared in the lab, in the office, for sharing our down moments as well as the good ones. Thanks to Sina for corrections on chapters. A special thanks to Irene, for always being there and for making the "medical center" a peace/laughter/ranting sanctuary over so many lunch meals. And to the "new ones" for being quite awesome too, like Mimmo for example.

Because life is not only work. Because we work to live, not live to work. For those people who had facilitated me with positive distractions, and helped me getting away from work, like my flatmates Rurru, Dave and Irene M., Amaia, Luis, Francesca, Ruben, Paul and David. For the members of SambaCaramba, thank you for putting some magic on Saturdays mornings. A special thanks goes to Tony Morrison.

Para mí familia. Por haber estado siempre ahí. Por ese amor incondicional. Por esos últimos empujones cuando más negro lo veía todo. Gracias. Y para algunos de ellos: jodeos, que os habéis quedado sin Bernabeu.

Als amics de Mollet. Als de sempre. Aquesta gent amb la qual no importa quant de temps portes fora o quant de temps hagi passat des de l'última visita, gràcies per fer-me sentir sempre com si mai no hagués marxat.

Als de la Uni. Per totes les escapadetes i retrobades durant aquests anys. Perquè sempre han estat a prop fins i tot havent estat voltant per tota Europa.

Als meus pares. No seria qui sóc, no seria on sóc, si no hagués estat per vosaltres. No ha estat fàcil, però no hauria sigut possible sense vosaltres. Gràcies per encoratjar-me sempre a mirar cap endavant, a aspirar a més i a produir a produir. Gracies també a la Tieta, per estar sempre allà. I, com no podia ser d'altra manera, a la persona que m'ha visitat més vegades al llarg d'aquesta aventura. Al Pau. Per no deixar de posar il·lusió i màgia a la meva vida.

And finally thanks to a very special little person. To Loretta. The person who has suffered the most of the collateral damage of this work, and my "thesis moods". Thank you. Thank you for always being there encouraging me and making this much easier.

Chapter 1

1. INTRODUCTION

1.1. Energy demand and dependency on fossil fuels

Energy is the life force of today's society and economy. Our leisure and work as well as our economic, social and physical welfare depend on the uninterrupted and sufficient supply of energy. With the world population being expected to rise (7 bn today, 11 bn by 2050)[1], and the unabated development of new technologies, society will be faced with an increase in energy consumption. A rise of 37 % is expected in primary energy consumption between 2013 and 2035.[2] The question of how this energetic demand will be met has raised a lot of concern. As can be seen in Figure 1-1, we live in a society strongly dependent on fossil fuels (85.8 % of world's primary energy consumption). The materials corresponding to fossil fuels are coal (30 %), natural gas (23.5 %) and oil (32.3 %).

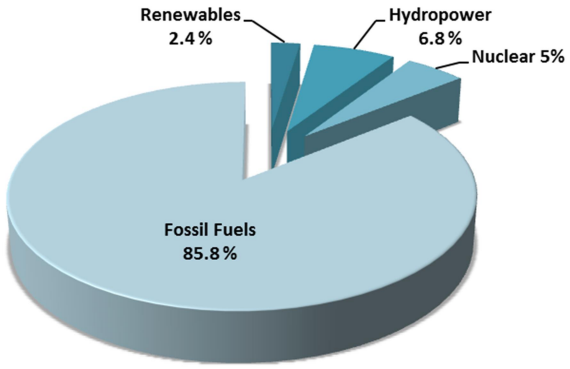

Figure 1-1. Primary energy world consumption in 2014.[3]

The reason why we have such a high dependency on fossil fuels is because they are available and easy to use. Fossil fuels are formed by natural processes such as anaerobic decomposition of buried dead organisms by exposure to heat and pressure in the Earth's crust over periods of millions of years.[4] They range from volatile materials with low carbon:hydrogen ratios like methane (natural gas), to liquid petroleum (oil) to non-volatile materials composed of almost pure carbon (coal). They are considered non-renewable resources; although fossil fuels are continually being formed via natural processes, they have an extremely long formation time. On top of this, the viable reserves are being depleted much faster than new ones are being made.[5] Another issue related to the use of fossil fuels is the formation of carbon dioxide released to the

atmosphere when burning them, which contributes to the greenhouse effect, provoking global warming and climate change.[6]

In order to avoid these drawbacks related to the usage of fossil fuels, an alternative source of energy that can replace fossil fuels should be found. Many alternatives are available, but they have to meet certain requirements to be able to replace fossil fuels, such as practicality, financial cost and environmentally-friendliness.

Renewable energies could be the ideal replacement from an environmental perspective. They are energy sources that are continuously replenished by nature and derived directly from the sun (such as solar, photo-chemical and photo-electric), indirectly from the sun (such as wind, hydropower and photosynthetic energy stored in biomass), and from other natural mechanisms of the environment (such as geothermal and tidal energy). Renewable energy sources have the potential to provide 3078 times the current global energy needs.[7] The only problem is that we do not yet have efficient technology to take advantage of all this energy. Although renewable sources have the potential to be the alternative to fossil fuels, they lack versatility. The success of renewables implementation strongly depends on the availability and abundance of the intended source to be harvested which is dependent on the geographical location (for instance, absence of Sun in Scotland or absence of rivers in dry regions). Renewable sources also have a problem of reliability; they cannot offer a continuous energy supply (for instance windmills do not rotate if the wind does not blow, and solar panels cannot harvest solar energy at night). These drawbacks are among the reasons why only 9.4% of the world's primary energy consumption is currently met by renewable sources (Figure 1-1). This evidence indicates that currently there is no comparable energy alternative to fossil fuels in terms of abundance, affordability, reliability, efficiency, portability and versatility.

These renewable sources produce electricity, which cannot be used for off-grid applications without using energy storage methods. If the electrical energy produced by renewable sources could be converted into a fuel, this energy would be available for off-grid applications, anytime, anywhere.

A proposed energy delivery system using hydrogen as an energy carrier has been proposed to avoid some of the problems that the burning of fossil fuels would cause for future generations.[8]

1.2. The Hydrogen Economy

"Yes, my friends, I believe that water will one day be employed as fuel, that hydrogen and oxygen which constitute it, used singly or together, will furnish an inexhaustible source of heat and light, of an intensity of which coal is not capable….water will be the coal of the future".

Jules Verne
Mysterious Island (1874)

The concept of the Hydrogen Economy proposes using the most abundant element in the universe, hydrogen, as an energy carrier. It is a non-toxic gas that can be produced renewably and used without greenhouse gas emissions.[9] For the implementation of a hydrogen economy several key issues, considered to be the pillars of such a concept, have to be resolved and optimised for making it suitable for large scale applications: hydrogen production, hydrogen storage and hydrogen utilisation. Figure 1-2 shows the schematic hydrogen life cycle in the hydrogen economy.

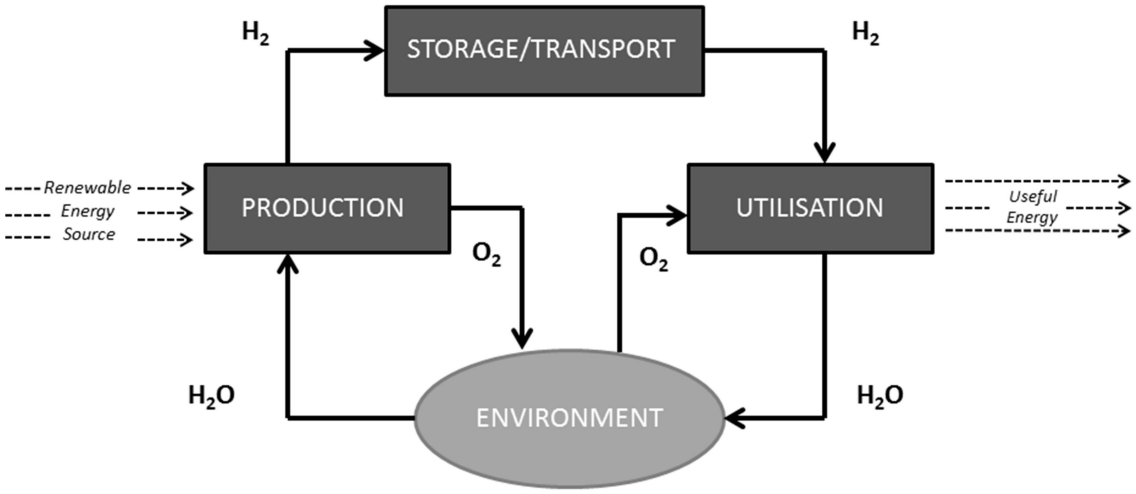

Figure 1-2. Schematic representation of H_2 life cycle for Hydrogen Economy, modified from reference [9].

1.2.1. Hydrogen production

Hydrogen is the most abundant element in the universe. However, on Earth it almost always exists as a compound. This represents a problem, due to the fact that energy has to be invested to produce hydrogen as a diatomic gas.[10] Commonly hydrogen is produced from the steam reforming of natural gas or other fossil fuel-based methods, which accounts for 92% of total production.[11] But hydrogen can also be formed by electrolysis,[12] splitting water into its elements, hydrogen and oxygen (Eq. 1-3). This method requires electricity, that if provided by renewable sources make it a completely sustainable process for the environment. Figure 1-3 shows a schematic representation of an electrolysis cell. Formation of hydrogen happens at the cathode (Eq. 1-1), whereas oxidation of water and formation of oxygen happens at the anode (Eq. 1-2).

At the cathode: $$2H^+ + 2e^- \longrightarrow H_{2(g)} \quad (1\text{-}1)$$

At the anode: $$\boldsymbol{H_2O_{(l)} \longrightarrow \frac{1}{2}O_{2(g)} + 2H^+ + 2e^-} \quad (1\text{-}2)$$

Global reaction: $$H_2O_{(l)} \xrightarrow{Electricity} H_{2(g)} + \frac{1}{2}O_{2(g)} \quad (1\text{-}3)$$

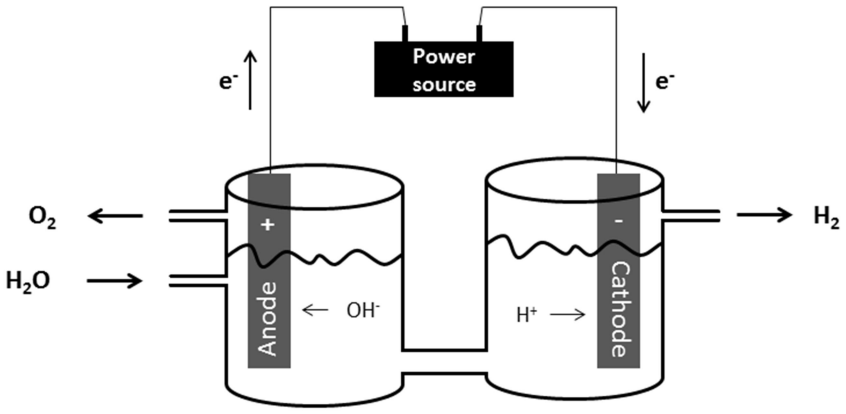

Figure 1-3. Schematic representation of an electrolysis cell, modified from reference [12]

Currently, hydrogen production by electrolysis is more expensive than larger scale-up processes of hydrogen production.[13] However, if non-renewable energy is used for hydrogen production by electrolysis, it actually results in higher emissions compared to gas reforming.[14] Up to date, commercial low temperature electrolysers have system efficiencies of 56 – 73 % (53.4 - 70.1

kWh/kg H_2 at 1 atm and 25 °C)[15], although research for optimization of such systems is continuously ongoing.

1.2.2. Hydrogen storage

Ostensibly, the easiest way to store hydrogen at ambient temperatures is as a gas. The main problem with that is that hydrogen gas has a very low density (0.092 $kg \cdot m^{-3}$).[16] Therefore container vessels with a large volume would be required, which may not be a big issue for stationary applications, but would be impractical for mobile applications.[17] A way to reduce some of the volume would be to compress the hydrogen gas, using high-pressure cylinders that can achieve storage at up to 800 bar of hydrogen.[18] By doing this, the hazard of dealing with hydrogen is magnified: hydrogen is a highly flammable and explosive gas by nature.[19] A database-driven website that collects relevant information (such as incidents) gained from user experience has been established to raise self-awareness about the hazard of hydrogen.[20] Hydrogen can also be stored in the liquid form (b.p H_2: 20 K)[21]. However, the need for low temperature contributes to a greater usage of energy and risks of cryogenic burns. Even though the volumetric density of liquid hydrogen is better than that of hydrogen gas, it still remains too low to be suitable for mobile applications. Also, the thermal insulation of the cryogenic storage vessel and pipes in order to reduce the boil-off of hydrogen has also become a challenge.

An alternative way to store hydrogen is to use solid absorbents that can contain hydrogen as H_2 or H; solid state Hydrogen Storage.[22] This is the focus of the research described in this thesis. A more detailed section on solid state Hydrogen Storage, highlighting the parameters that a hydrogen storage system has to meet will be discussed in (Section 1.3).

1.2.3. Hydrogen Utilisation

The energy carried by hydrogen can be converted into electricity by using a fuel cell. Fuel cells (galvanic cells) use the reverse electrochemical reaction to that of the electrolysis of the water (Eq. 1-6). Hydrogen can be recombined with oxygen to produce electricity. This is a sustainable and clean process compared to the release of noxious gases that result from the combustion of fossil fuels (such as CO_2, CO among others). One of the fuel cells that could be used to harvest the energy from hydrogen could be the proton exchange membrane fuel cell[23] (PEMFC) as shown in Figure 1-4. The hydrogen is delivered to the anode, where it is oxidised into protons and electrons (Eq. 1-4). The electrons circulate from anode to cathode, generating electricity, while

the protons pass through the electrolyte membrane to the cathode. At the cathode, oxygen recombines with the electrons and protons to produce water (Eq. 1-5).[24]

At the anode: $$H_2 \rightarrow 2H^+ + 2e^-$$ (1-4)

At the anode: $$\frac{1}{2}O_2 + 2H^+ + 2e^- \rightarrow H_2O$$ (1-5)

Overall reaction: $$H_2 + \frac{1}{2}O_2 \rightarrow H_2O + electricity + heat$$ (1-6)

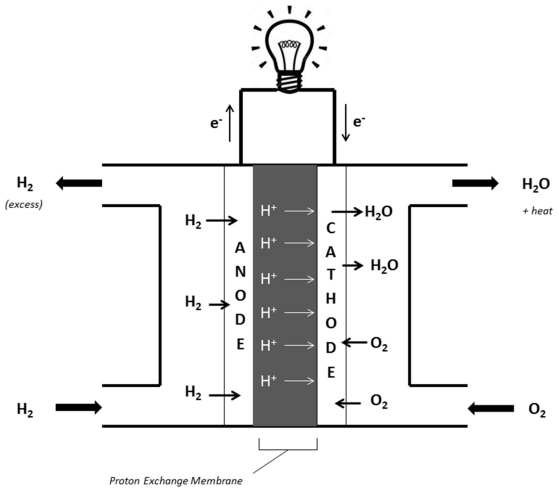

Figure 1-4. Schematic proton exchange membrane fuel cell, modified from reference [25]

The end of the hydrogen energy cycle starts and ends with water, which is environmentally friendly as a residue and can be considered as an infinite resource. These are the two main advantages of using hydrogen as a fuel over fossil fuels. Although the hydrogen economy still has some limitations that need to be addressed in order to be implemented in the near future, it offers a sustainable alternative and is more respectful to the environment than an economy based on fossil fuels. These limitations include hydrogen storage, where there is a need for a system to store large amounts of hydrogen safely and also a way of producing hydrogen sustainably and efficiently that does not require the burning of fossil fuels.

1.3. Solid State Hydrogen Storage

According to Züttel[16] there are 6 possible ways of storing hydrogen:

1) High pressure gas cylinders.
2) Liquid hydrogen in cryogenic tanks.
3) Adsorbed hydrogen on materials with a large specific area.
4) Absorbed hydrogen in interstitial sites in a host metal.
5) Chemically bonded hydrogen in covalent and/or ionic complex compounds.
6) Through oxidation of reactive metals (such as Li, Na, Mg, Al, Zn) with water.

After reviewing the physical storage methods of hydrogen (gas and liquid – 1 and 2) and the problems associated in the sections above, we will discuss solid state hydrogen storage in more detail (3 to 6).

Solid state hydrogen storage offers a safer and a more compact way to storing hydrogen than the physical storage methods. It consists of storing hydrogen in solid adsorbents or absorbents. Hydrogen can be bound to solid materials in several ways. The first one is by physical bonding of H_2 molecules, also referred to as physisorption, where hydrogen is bound to the surface of a host material, usually with a large specific surface area (3). Weak van der Waals interactions (1 – 5 $kJ \cdot mol^{-1}$)[26] exist between the host material and H_2 molecules. Metal organic frameworks(MOFs),[27] carbon nanotubes[28], and clathrate hydrates[29] represent some examples of this kind of storage material.

The second type of hydrogen storage in solid materials is via chemical bonding (4 to 6). This involves splitting the hydrogen molecule into ions or atoms, which form new chemical bonds with the host material, which could be metallic, ionic or covalent[30].

Metal hydrides are formed when hydrogen reacts with certain metals and alloys. H_2 molecules are firstly physisorbed onto the surface of the material, where it dissociates, allowing atomic hydrogen to diffuse into local interstitial sites, forming a solid-solution (4). Examples of metallic hydrides are PdH (from Pd)[31], LiH (from Li)[32], MgH_2 (from Mg) [32], $LaNi_5H_6$ (from $LaNi_5$)[33], and FeTiH or $FeTiH_2$ (from FeTi)[34] among others.

Complex hydrides, have attracted a lot of attention in recent years for hydrogen storage applications because of the possibilities they offer for high volumetric and gravimetric hydrogen densities (e.g. $LiBH_4$ has the highest H_2 capacity of 18.5 wt.% H_2).[35] These will be discussed in more detail later. They belong to group (5) of Züttel's classification of hydrogen storage methods.

The last way of storing hydrogen (6) is via the chemical reaction with water. The classic example is the reaction between sodium metal and water which produces hydrogen gas and sodium hydroxide (Eq. 1-7).[36] The reaction is not directly reversible but metallic sodium can be obtained again by reduction of sodium hydroxide in a furnace *via* thermal treatment. The combustion of the hydrogen produced will form another water molecule which can be recycled to generate more hydrogen.

$$2Na + 2H_2O \rightarrow 2NaOH + H_2 \quad (1\text{-}7)$$

1.3.1. The ideal solid state hydrogen storage material/system

Solid state hydrogen storage offers a safer alternative to physical storage of hydrogen. However, there are many different systems and materials with potential hydrogen storage characteristics/properties. The desired properties for an ideal hydrogen storage system would consider weight, volume, safety, cost, reversibility and the rate of hydrogen uptake and release by the system.

The United States Department of Energy (U.S D.o.E) has set targets for on-board hydrogen storage systems for light-duty vehicles (Table 1-2). For these targets, there are two hydrogen energy density properties that are vital for superior performance; volumetric density ($kWh \cdot L^{-1}$ or $kg \cdot m^{-3}$) and gravimetric density ($kWh \cdot kg^{-1}$). These refer to the system (including storage vessels, connections and pipelines) not materials values, as far as U.S. D.o.E is concerned. For the gravimetric density of a material, the weight percent capacity (w.t%) of hydrogen is the most frequently used. The weight percentage of an adsorbed gas is the total weight of the system including the weight of the gas adsorbed.

Obviously, the requirements of the hydrogen storage material would vary depending on the application to be used. For instance, for mobile applications the volumetric and gravimetric densities are crucial characteristics, whereas for stationary applications these are perhaps not as important.

Table 1-1. U.S. Department of Energy hydrogen storage systems targets for on-board mobile applications. Modified from reference [37].

	Units	2010	2015	Ultimate
Volumetric density	w.t.%	4.5	5.5	7.5
	$kWh \cdot kg^{-1}$	1.5	1.8	2.5
Gravimetric density	$kg \cdot m^{-3}$	28	40	70
	$kWh \cdot L^{-1}$	0.9	1.3	2.3
System filling time	min (5 kg)	4.2	3.3	2.5
	kg $H_2 \cdot min^{-1}$	1.2	1.5	2
Storage system cost	$\$ \cdot kWh^{-1}$	4	2	TBD
Fuel cost*	$\$ \cdot gge^{-1}$	3-7	2-4	2-3

includes off-board costs such as liquefaction, compression, fuel regeneration, etc.* ***gge* *corresponds to gasoline gallon equivalent untaxed, independent of production pathway*

Hydrogen storage materials are plotted according to their volumetric and gravimetric densities in Figure 1-5. These densities are of significant importance for a high performance solid state storage material. One of the families of materials that have attracted increasing attention for their H_2 capacities are light metal hydrides. The theoretical hydrogen storage capacities of these materials are promising, with a decrease in gravimetric capacities upon descending any given group in the periodic table (Group I: 12.68 w.t % H_2 and 0.75 w.t. % H_2, for LiH and CsH respectively and Group II: 18.28 w.t % H_2 and 1.44 w.t % H_2 for BeH_2 and BaH_2 respectively).[38]

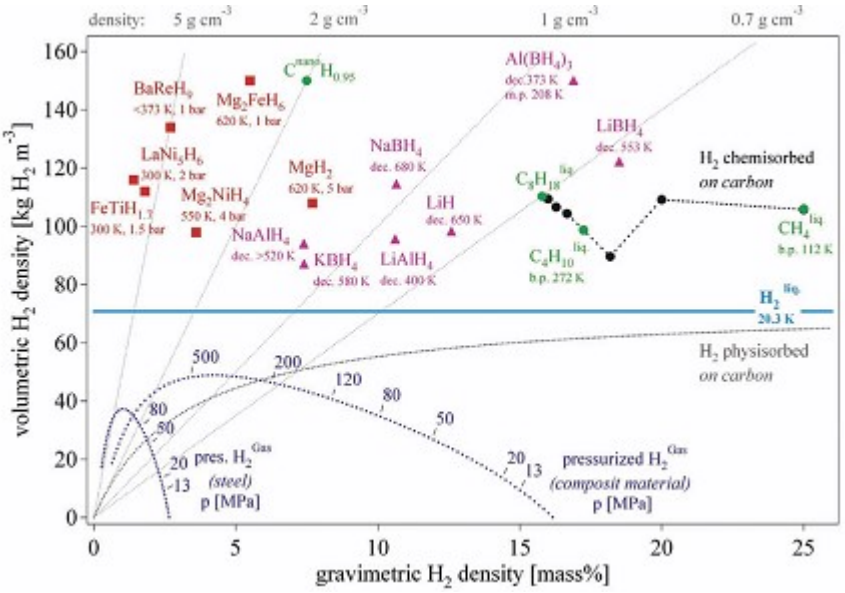

Figure 1-5. Volumetric and gravimetric H_2 density of some selected hydrogen storage materials. Reprinted with the permission of [36]. Copyright 2015 Elsevier.

Some of these light metal hydrides can be combined with other transition metals or Group XIII elements, to form complex hydrides that have higher theoretical capacities than the component light metals (e.g. $LiBH_4$,[35] Mg_2FeH_6,[39]…).

1.3.2. Complex hydrides

These hydrides have been extensively studied because of the possibilities for high volumetric and gravimetric hydrogen densities. Complex hydrides form ionic or covalent compounds upon hydrogenation. They are inorganic salts in which hydrogen is bonded to central atoms in "complex" anions such as; alanates ($[AlH_4]^-$), amides ($[NH_2]^-$) and borohydrides ($[BH_4]^-$). The number of elements that can form complex hydrides with a decent w.t.% H is limited, involving light-weight elements from groups 1, 2 and 3 of the periodic table. Alanates and amides will be discussed in more detail, since they are the types of material which the work in this thesis has been focused on.

1.3.2.1. Alanates

Alkali metal alanates undergo dehydrogenation at temperatures below 300 °C (where M= Li: 175 °C, Na: 265 °C, K: 290 °C) following the general dehydrogenation reaction:

$$MAlH_4 \rightarrow MH + Al + \frac{3}{2}H_2 \qquad (1\text{-}8)$$

The corresponding metal hydride product of the above dehydrogenation can undergo further hydrogen release at temperatures higher than 400 °C. However, it has been evidenced for $LiAlH_4$, $NaAlH_4$ and $KAlH_4$, that the dehydrogenation pathway in fact occurs via an intermediate formation, and further decomposition (Eq. 1-9 and Eq. 1-10).

$$3MAlH_4 \rightarrow M_3AlH_6 + 2Al + 3H_2 \qquad (1\text{-}9)$$

$$M_3AlH_6 \rightarrow 3MH + Al + \frac{3}{2}H_2 \qquad (1\text{-}10)$$

$LiAlH_4$ undergoes a phase transition at 160 - 177 °C before undergoing the first dehydrogenation step, which leads to Li_3AlH_6 (Eq. 1-9) at 187 – 218 °C (ΔH = -10 kJ·mol^{-1} H_2). A second

dehydrogenation is observed at 228 – 282 °C (ΔH = 25 kJ·mol^{-1} H_2), corresponding to the decomposition of Li_3AlH_6 leading to LiH formation. Finally the dehydrogenation of LiH was observed at 370 – 483 °C (ΔH = 140 kJ·mol^{-1} H_2) leading to LiAl formation. [40, 41]

The first dehydrogenation of $NaAlH_4$ to give Na_3AlH_6 is observed at 210 – 220 °C (ΔH = 40.9 kJ·mol^{-1}), which is followed by the second dehydrogenation at ca. 250 °C (overall ΔH = 54.5 kJ·mol^{-1} H_2).[42,43]

Finally, $KAlH_4$ dehydrogenates to K_3AlH_6 at much higher temperatures (300 °C) than the analogous process for $LiAlH_4$ and $NaAlH_4$. The second and third dehydrogenations occur at 340 and 430 °C, respectively.[44]

Alkali metal alanates are not the only one reported in the literature. Two alkaline earth metal alanates, $Mg(AlH_4)_2$, $Ca(AlH_4)_2$ have also been reported as a possible hydrogen storage materials. In contrast with alkali metal alanates, dehydrogenation of $Mg(AlH_4)_2$ does not form any intermediate. At 163 °C, the dehydrogenation of the hydride proceeds according to Eq. 1-11. Magnesium hydride formed will undergo dehydrogenation at 287 °C to produce Mg metal that will react with aluminium at 400 °C to form Al_3Mg.[45]

$$Mg(AlH_4)_2 \rightarrow MgH_2 + Al + 3H_2 \qquad (1\text{-}11)$$

Calcium aluminium hydride undergoes dehydrogenation at 138 °C, via the intermediate $CaAlH_5$, which decomposes forming calcium hydride with hydrogen evolution at 249 °C (Eq. 1-12 and Eq. 1-13).[46]

$$Ca(AlH_4)_2 \rightarrow CaAlH_5 + Al + \frac{3}{2}H_2 \qquad (1\text{-}12)$$

$$CaAlH_5 \rightarrow CaH_2 + 2Al + 3H_2 \qquad (1\text{-}13)$$

A summary of the respective thermodynamic and other relevant data for selected alanates is shown in Table 1-2.

Table 1-2. Desorption temperature, storage capacity (w.t. % H_2) and enthalpy of desorption of selected alanates.

Alanate	w.t.% H_2	T des. / °C	Δh des. / kJ·mol^{-1}	Ref.
$LiAlH_4$	5.3	160- 177	-10	[40],[41]
Li_3AlH_6	2.6	228 -282	25	
$NaAlH_4$	3.7	210-220	40.9	[42],[43]
Na_3AlH_6	1.9	250	54.5	
$KAlH_4$	5.7	300	-	[44]
$Mg(AlH_4)_2$	9.36	163	1.7	[45]
$Ca(AlH_4)_2$	7.8	138	-7	[46]
$CaAlH_5$	4.2	249	31	

An alternative to lower the hydrogen release temperatures of lithium aluminium hydride will be explored in Chapter 4.

1.3.2.2. Amides and the Li-N-H system

Amide decomposition usually results in ammonia release rather than that of H_2. They started to be considered as potential hydrogen storage elements when Chen et.al discovered the reversible hydrogen store lithium nitride Li_3N in 2002, forming the Li – N – H system,[47] in which lithium amide ($LiNH_2$) and lithium imide (Li_2NH) are the hydrogenated forms of lithium nitride. Therefore, $LiNH_2$ releases hydrogen when mixed with lithium hydride according to the reverse reaction in Eq. 1-14:

$$Li_3N + H_2 \leftrightarrow Li_2NH + LiH + H_2 \leftrightarrow LiNH_2 + 2LiH \qquad (1\text{-}14)$$

The theoretical gravimetric capacity of the system is 11.5 % although experimentally it effectively stores 9.3 -10 % w.t.

For hydrogen storage applications only the second reversible part of the reaction (Eq. 1-14) is considered ($Li_2NH/LiNH_2$) due to the more favourable thermodynamics (ΔH = -44.5 kJ·mol^{-1} H_2, which is ΔH = -148 kJ·mol^{-1} H_2 for Li_3N/Li_2NH).[48] However, the temperatures for hydrogen cycling remain unsuitable for mobile hydrogen storage applications. One of the alternatives that has been suggested to lower the desorption temperature of the system was to substitute Li atoms from

$LiNH_2$ with more electronegative atoms than Li to weaken the bonding between the metal cation and $[NH_2]^-$ unit. As a result, desorption temperatures were decreased *ca*. 150 °C, in the substituted amide $(Li,Mg)NH_2$.[49]

Catalysts have also been used to improve desorption temperatures in the Li –N – H system. Ichikawa et. al added 1 % of $TiCl_3$ as a catalyst, resulting in 5.5 w.t % hydrogen release between 150 – 250 °C, without ammonia formation.[50] The decomposition pathway and the exact influence of the catalyst are not yet known.

A more detailed discussion about the Li –N –H system, and another alternative to enhance the decomposition temperatures of lithium amide will be explored in Chapter 5.

1.4. Nanosizing

Solid state hydrogen storage seems to be the alternative that offers the most promising results for storing hydrogen in a safe and compact way. The ideal solid state hydrogen storage material should have a high gravimetric and volumetric capacity and store hydrogen reversibly with fast hydrogen release and uptake kinetics at moderate temperature and pressure. In addition, the reaction should proceed with suitable thermodynamics (low heat exchange) and the material should be prepared from abundant and cheap elements.[51] Using light metal hydrides has the potential of meeting almost all of the above-mentioned requirements. The only drawback is that the utilisation of these materials for hydrogen storage applications is often not feasible because of unfavourable kinetics and/or thermodynamics.

One approach to enhance the hydrogen (de)sorption kinetics is nanostructuring. Nanoparticles have significantly different properties compared to bulk materials[52]. These differences in respect to the bulk materials stem from: a) increased surface area, b) reduced diffusion distances, c) increased number of atoms at the grain boundaries and d) intimate contact between different reacting solids. These nanoscale properties enhance the uptake and release of hydrogen thus enhancing the reaction kinetics. For instance, a schematic representation between bulk and nanoscale uptake/release of hydrogen is shown in Figure 1-6. The bulk material will have a longer diffusion distance for a hydrogen molecule to be absorbed within it (by forming H atoms and subsequent M-H bonds) when compared to the nanomaterial case where the surface area is much higher and the diffusion lengths lower. This should result in a faster hydrogen exchange rate in a nanomaterial than in the equivalent bulk material.[53]

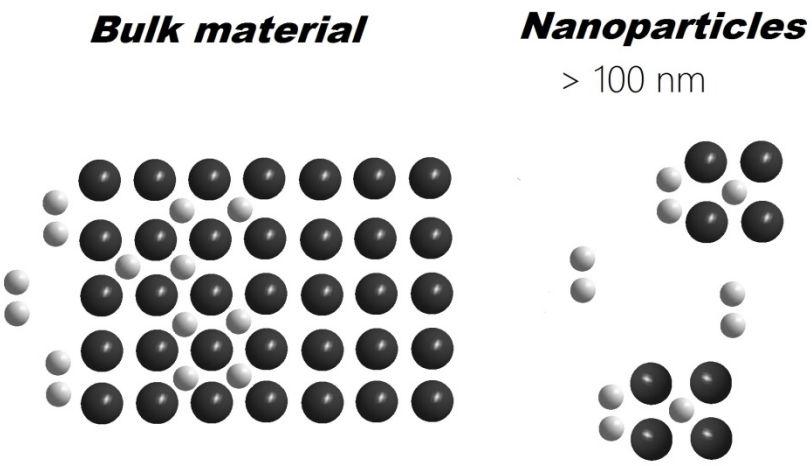

Figure 1-6. Schematic representation of molecular hydrogen exchange (white atoms) in a bulk material and in nanoparticles of a certain metal (dark-grey atoms). Modified from reference [53]

1.4.1. Ball milling

The common method to produce metal hydride nanoparticles is by high-energy ball milling. The size of the bulk material can be easily reduced mechanically to less than 100 nm. For instance, the solubility of hydrogen in nanocrystalline Pd (8-12 nm) can be increased by a factor of 10-30 in comparison with polycrystalline samples (10-20 μm).[54] MgH_2 nanoparticles also show improved hydrogen sorption kinetics in comparison with the equivalent bulk material.[55] Theoretical studies suggest that the increased surface area of MgH_2 nanoparticles by ball-milling destabilizes the hydride and reduces the reaction enthalpy.[56] Results from several experiments and computational studies have demonstrated that the thermodynamics and kinetics of hydrogen sorption/desorption in metal hydrides can be improved by nanosizing.[57,58, 59, 60]

However, nanostructuring using ball milling technique cannot easily obtain crystallite sizes less than 10 nm. Furthermore, the samples can be easily contaminated with traces of metals from the balls and nanoparticles have the tendency to grow into larger particles by sintering upon hydrogen release and uptake cycles.[61,62] The main drawback of ball-milling is that it can lead to uneven size distributions and agglomeration (which can increase the size of particles) in the sample.[63, 64, 65]

A new approach to overcome the aforementioned limitations is nanoconfinement, which is the main topic of this thesis.

1.4.2. Nanoconfinement

Nanoconfinement is a recently developed synthesis technique that consists of confining the potential hydrogen storage material into a nanoporous scaffold material. The high surface area porous solid acts as a support and template for the active phase, which is recrystallized from the liquid solution to adopt the size of the host pores. There are several synthetic methods to deposit the active material in a porous matrix; the most typical ones being solution impregnation and melt infiltration (Figure 1-7) which will be reviewed and explained below.

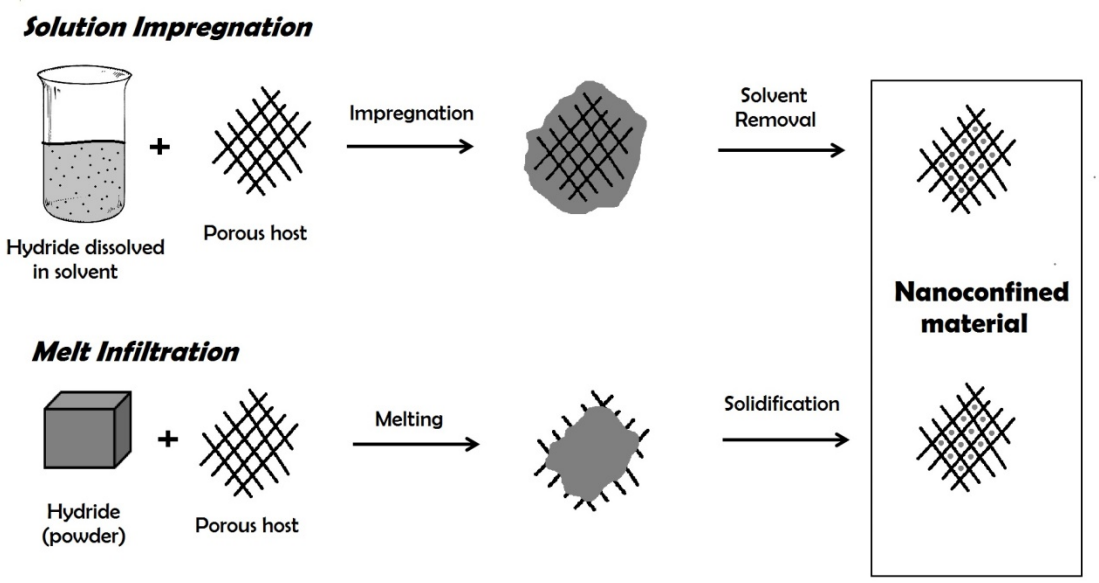

Figure 1-7. Schematic representation of the main confinement methods with porous hosts. Modified from reference[66]

1.4.2.1. Porous materials for nanoconfinement of hydrides

The choice of the porous material is crucial when it comes to nanoconfinement synthesis. There are many different materials that can act as porous hosts for confinement of hydrides (Table 1-3), as long as they meet certain requirements:

1. Inert: if they react with the material to be confined, or form a byproduct in a side reaction, the active material would most probably lose its hydrogenation/dehydrogenation properties and become inactive.
2. Light: using a heavy host will compromise the gravimetric capacity of a hydrogen storage material because of the introduction of "dead weight". "Dead weight" refers to the

inactive scaffold that does not contribute to the release of hydrogen. For instance, in a hydride:carbon system, the amount of hydrogen that can be absorbed by the carbon is considered negligible under working conditions.

3. Allowing high loadings: for the amount of host to be minimized and therefore the "dead weight" effect. Materials that allow high loadings are those which have high surface area and high pore volumes.
4. Cheap and abundant: to facilitate a potential future scale-up process.

Table 1-3. Summary of the different porous hosts that can be used for confinement of hydrides. Modified from reference [67]

Host type	Examples of porous hosts	Abbreviation	Surface area / $m^2 \cdot g^{-1}$	Mean pore size / nm	References
Carbon materials	Activated Carbon	AC	> 1500	<4	[68]
	High surface area graphite	HSAG	580	<4	[69]
	Ordered mesoporous carbon	OMC	500 – 1000	2 - 6	[70], [71]
	Carbon Aerogels	CA	600 – 1000	7 - 25	[72], [73]
Metal organic frameworks	MOF HKUST	MOFH	> 2000	0.9 - 1.6	[74], [75]
Silica Materials	SBA-15	SBA-15	> 700	1.5-10	[76], [77]
	MCM-41	MCM-41	> 1000	5 - 30	[78], [79]

1.4.2.2. Solution impregnation

Also known as solvent mediated infiltration (or wet impregnation), the method consists of dissolving the active hydrogen storage material in a specific solvent to form a homogenous solution. Then the porous host is added to the homogenous solution, allowing impregnation of the solution within the structure of the porous host. Upon solvent removal, the active material precipitates in the porous host, adopting the size of the pores characteristic of the host.[80]

The main advantage of solution impregnation as compared to melt infiltration (see below) is that the former can be performed under milder conditions of pressure and temperature.

The choice of solvent is a key factor for this method since it has to meet several requirements, which are explained below. First of all, the solvent needs to be inert towards the active material and the porous hosts to avoid decomposition of the hydride and/or the host material. In addition, the amount of active material to be loaded into the porous host is limited by its solubility in the chosen solvent. This is due to the fact that in cases of low solubility, several impregnation steps have to be performed in order to achieve a considerable material loading. Lastly, the solvent should be easy to remove by being weakly coordinated to both active material and porous host. THF and ethers are the solvents most commonly used in metal hydride confinement. [81, 82, 83]

There are several hydrides that cannot be prepared by this method because of a lack of a suitable solvent. This is the case for the Li-N-H system, where to date, no suitable solvent has been found to dissolve Li_3N to perform solution impregnation.[84] In this thesis, an alternative route for the synthesis of Li-N-H materials to be used in confinement has been achieved by using the hydrogenated product of the $Li_3N - H_2$ reaction ($LiNH_2$). Results of this route are reported and discussed in chapter 5.

A variation of the solution impregnation method is the direct synthesis of nanoconfined metal hydrides. This involves the confinement of a metal hydride precursor (e.g. $MgBu_2$ in heptane (1M))[85, 86] directly in the porous host followed by hydrogenation of the confined material (in this case at 170 °C and 50 bar H_2 for 24 h, to give confined MgH_2).

1.4.2.3. Melt infiltration

This method consists of melting the material to be confined in the presence of the selected porous host for direct infiltration. The melt solidifies inside the porous host and thus, the particles adopt the size of the pores of the host.[80]

It can be used as an infiltration method only when the melting point of the hydride is lower than the decomposition temperature of the inert porous material. A common complication when using melt infiltration is that the hydride releases hydrogen before or during melting. Even though this can be solved by applying hydrogen pressure during melting,[87, 88, 89] it restricts its use to laboratories which have appropriate equipment to apply the necessary hydrogen pressure and limits its widespread use.

The main advantage of melt infiltration over solution impregnation methods is that the synthetic route is more direct because no solvent is needed. In principle, full loading of the porous host can be readily achieved since the method is not restricted by the solubility of the hydride in the solvent.

Table 1-4. Summary of work published in the literature on nanoconfinement of hydrides within porous hosts. Modified from reference [67] (host abbreviations can be found in Table 1-3)

Hydride@Host	Surface area / $m^2 \cdot g^{-1}$	Pore size / nm	Total volume / $cm^3 \cdot g^{-1}$	Infiltration method	Solvent or atmosphere	Reference
$Mg(BH_4)_2$@AC	860	<2	0.61	Solvent	Et_2O (0.3M)	[90]
MgH_2@CA	720	13	0.8	Melt	Ar	[91]
MgH_2@AC	1820	0.5 - 3	0.79	$MgBu_2$	Ar	[92]
MgH_2@HSAG	550	2 - 3	0.65	Melt	Ar	[93]
$LiBH_4$@OMC	1060	4	1.1	Solvent	MTBE (0.1 M)	[81]
$LiBH_4$@SBA-15	1012	4.7 - 6.5	0.35 to 0.83	Melt	H_2 (100 bar)	[89]
$NaAlH_4$@CA	770	13	0.8	Melt	H_2 (183 bar)	[94]
$NaAlH_4$@SBA-15	450	10	-	Solvent	THF (0.2 M)	[82]
NH_3BH_3@SBA-15	900	7.5	1.2	Solvent	MeOH (5.4 M)	[95]
NH_3BH_3@CA	500	5	0.7	Solvent	THF (3.2 M)	[83]
$LiAlH_4$@AC	2160	<4 - 10	1.18	Solvent	Et_2O	This work
$LiAlH_4$@OMC	500	4	0.32	Solvent	Et_2O	This work
$LiNH_2$@OMC	500	4	0.32	*"In-situ"*	Li-NH_3 solution	This work

1.5. Aims and scope of this thesis

This chapter introduces briefly the reader to matters of both the current state of energy supply and demand and the society dependency on fossil fuels. A detailed discussion of the Hydrogen economy, as an alternative to fossil fuels, including its benefits and limitations is presented. Hydrogen storage, in particular, has been discussed since this is the main issue that the work in this thesis addresses. After this short introduction, state-of-the-art techniques to improve some of the properties of the potential materials to be used for hydrogen storage have been reviewed. In particular, the concept of nanoconfinement, which is the main synthetic approach used in this work is introduced.

The main aims of this thesis are:

1. To investigate the hydrogen release properties of $LiAlH_4$ and $LiNH_2$ and enhance them by optimization of the nanoconfinement approach by solution impregnation within different types of carbon porous hosts.

2. To develop alternative novel routes of nanoconfinement by solution impregnation for a hydrogen storage material that cannot be dissolved in any suitable solvent ($LiNH_2$).

In general this work aims to expand the current knowledge in nanoconfinement techniques in the context of hydrogen storage (which can be used in other fields, such as batteries[96,97], and catalysis[98,99]). More specifically attempts were made to improve the properties of two potential high performing hydrogen storage materials, by taking advantage of the particle size tailoring effect that the nanoconfinement approach offers, which might lead to hydrogen release of the complex hydrides at lower temperatures. Hopefully the humble contribution of this work will get us closer to a safer, unpolluted and environmentally-friendly society.

1.6. REFERENCES

1. P. Gerland, A. E. Raftery, H. Ševčíková, N. Li, D. Gu, T. Spoorenberg, L. Alkema, B. K. Fosdick, J. Chunn, N. Lalic, G. Bay, T. Buettner, G. K. Heilig and J. Wilmoth, *Science (New York, N.Y.)*, 2014, **346**, 234-237.
2. BP, Energy Outlook 2035, February 2015, http://www.bp.com/content/dam/bp/pdf/Energy-economics/energy-outlook-2015/Energy_Outlook_2035_booklet.pdf, (accessed 02/10/2015).
3. BP, Statistical Review of World Energy, June 2015, http://www.bp.com/content/dam/bp/pdf/Energy-economics/statistical-review-2015/bp-statistical-review-of-world-energy-2015-full-report.pdf, (accessed 02/10/15).
4. I. Graham, *Fossil Fuels: A Resource Our World Depends on*, Heinemann Library, 2005.
5. I. S. a. A. U.S Energy Information Administration, U.S. Crude Oil and Natural Gas Proved Reserves, http://www.eia.gov/naturalgas/crudeoilreserves/, (accessed 05/10/2015).
6. N. Oreskes, *Science (New York, N.Y.)*, 2004, **306**, 1686.
7. O. Ellabban, H. Abu-Rub and F. Blaabjerg, *Renewable and Sustainable Energy Reviews*, 2014, **39**, 748-764.
8. B. E. E. Systems, C. A. S. F. H. P. Use, D. E. P. Sciences, N. R. Council and N. A. Engineering, *The Hydrogen Economy:: Opportunities, Costs, Barriers, and R&D Needs*, National Academies Press, 2004.
9. G. W. Crabtree, M. S. Dresselhaus and M. V. Buchanan, *Print edition*, 2004, **57**, 39-44.
10. A. Züttel, A. Remhof, A. Borgschulte and O. Friedrichs, *Philosophical Transactions of the Royal Society of London A: Mathematical, Physical and Engineering Sciences*, 2010, **368**, 3329-3342.
11. I. S. a. A. U.S Energy Information Administration, The Impact of Increased Use of Hydrogen on Petroleum Consumption and Carbon Dioxide Emissions, http://www.eia.gov/oiaf/servicerpt/hydro/appendixc.html).
12. P. Atkins and J. de Paula, *Atkins' Physical Chemistry*, OUP Oxford, 2014.
13. J. D. Holladay, J. Hu, D. L. King and Y. Wang, *Catalysis Today*, 2009, **139**, 244-260.
14. C. Koroneos, A. Dompros, G. Roumbas and N. Moussiopoulos, *International Journal of Hydrogen Energy*, 2004, **29**, 1443-1450.
15. J. Turner, G. Sverdrup, M. K. Mann, P.-C. Maness, B. Kroposki, M. Ghirardi, R. J. Evans and D. Blake, *International Journal of Energy Research*, 2008, **32**, 379-407.
16. A. Züttel, *Naturwissenschaften*, 2004, **91**, 157-172.
17. L. Schlapbach and A. Zuttel, *Nature*, 2001, **414**, 353-358.

18. R. H. Crabtree, *Energy Production and Storage: Inorganic Chemical Strategies for a Warming World*, Wiley, 2013.
19. U.S Department of Energy: Hydrogen Safety Bibliographic Database, http://www.hydrogen.energy.gov/biblio_database.html, (accessed 07/10/2015).
20. H2 Incidents http://www.h2incidents.org/, (accessed 23/09/15).
21. E. Wiberg and N. Wiberg, *Inorganic Chemistry*, Academic Press, 2001.
22. T. K. Mandal and D. H. Gregory, *Annual Reports Section "A" (Inorganic Chemistry)*, 2009, **105**, 21-54.
23. D. Bessarabov, H. Wang, H. Li and N. Zhao, *PEM Electrolysis for Hydrogen Production: Principles and Applications*, CRC Press, 2015.
24. F. Barbir, in *PEM Fuel Cells*, ed. F. Barbir, Academic Press, Burlington, 2005, DOI: http://dx.doi.org/10.1016/B978-012078142-3/50003-3, pp. 17-32.
25. F. Barbir, in *PEM Fuel Cells*, ed. F. Barbir, Academic Press, Burlington, 2005, DOI: http://dx.doi.org/10.1016/B978-012078142-3/50005-7, pp. 73-113.
26. M. Bastos-Neto, C. Patzschke, M. Lange, J. Mollmer, A. Moller, S. Fichtner, C. Schrage, D. Lassig, J. Lincke, R. Staudt, H. Krautscheid and R. Glaser, *Energy & Environmental Science*, 2012, **5**, 8294-8303.
27. J. Kim, S. Yeo, J.-D. Jeon and S.-Y. Kwak, *Microporous and Mesoporous Materials*, 2015, **202**, 8-15.
28. F. Costanzo, P. L. Silvestrelli and F. Ancilotto, *Journal of Chemical Theory and Computation*, 2012, **8**, 1288-1294.
29. H. Lee, J.-w. Lee, D. Y. Kim, J. Park, Y.-T. Seo, H. Zeng, I. L. Moudrakovski, C. I. Ratcliffe and J. A. Ripmeester, *Nature*, 2005, **434**, 743-746.
30. J. Yang, A. Sudik, C. Wolverton and D. J. Siegel, *Chemical Society Reviews*, 2010, **39**, 656-675.
31. B. D. Adams and A. Chen, *Materials Today*, 2011, **14**, 282-289.
32. B. Sakintuna, F. Lamari-Darkrim and M. Hirscher, *International Journal of Hydrogen Energy*, 2007, **32**, 1121-1140.
33. G. Liang, J. Huot and R. Schulz, *Journal of Alloys and Compounds*, 2001, **320**, 133-139.
34. J. J. Reilly and R. H. Wiswall, *Inorganic Chemistry*, 1974, **13**, 218-222.
35. U. Eberle, M. Felderhoff and F. Schüth, *Angewandte Chemie International Edition*, 2009, **48**, 6608-6630.
36. A. Züttel, *Materials Today*, 2003, **6**, 24-33.

37. U.S Department of Energy - Onboard Hydrogen Storage for Light-Duty Fuel Cell Vehicles, http://energy.gov/sites/prod/files/2015/05/f22/fcto_targets_onboard_hydro_storage_explanation.pdf, (accessed 19/10/2015).
38. H. Reardon, University of Glasgow, 2014.
39. M. Polanski, T. K. Nielsen, Y. Cerenius, J. Bystrzycki and T. R. Jensen, *International Journal of Hydrogen Energy*, 2010, **35**, 3578-3582.
40. J. Block and A. P. Gray, *Inorganic Chemistry*, 1965, **4**, 304-305.
41. J. R. Ares, K. F. Aguey-Zinsou, M. Porcu, J. M. Sykes, M. Dornheim, T. Klassen and R. Bormann, *Materials Research Bulletin*, 2008, **43**, 1263-1275.
42. E. C. Ashby and P. Kobetz, *Inorganic Chemistry*, 1966, **5**, 1615-1617.
43. X. Ke and I. Tanaka, *Physical Review B*, 2005, **71**, 024117.
44. H. Morioka, K. Kakizaki, S.-C. Chung and A. Yamada, *Journal of Alloys and Compounds*, 2003, **353**, 310-314.
45. M. Fichtner, O. Fuhr and O. Kircher, *Journal of Alloys and Compounds*, 2003, **356–357**, 418-422.
46. S. Y. Zaginaichenko, D. V. Schur, Z. A. Matysina, A. Veziroglu, D. A. Zaritskii, T. I. Shaposhnikova and M. T. Gabdullin, *International Journal of Hydrogen Energy*, 2015, **40**, 7617-7627.
47. P. Chen, Z. Xiong, J. Luo, J. Lin and K. L. Tan, *Nature*, 2002, **420**, 302-304.
48. T. Ichikawa, N. Hanada, S. Isobe, H. Leng and H. Fujii, *The Journal of Physical Chemistry B*, 2004, **108**, 7887-7892.
49. S. Orimo, Y. Nakamori, G. Kitahara, K. Miwa, N. Ohba, T. Noritake and S. Towata, *Appl. Phys. A*, 2004, **79**, 1765-1767.
50. T. Ichikawa, S. Isobe, N. Hanada and H. Fujii, *Journal of Alloys and Compounds*, 2004, **365**, 271-276.
51. M. Felderhoff, C. Weidenthaler, R. von Helmolt and U. Eberle, *Physical Chemistry Chemical Physics*, 2007, **9**, 2643-2653.
52. E. Roduner, *Chemical Society Reviews*, 2006, **35**, 583-592.
53. X. Chen, C. Li, M. Gratzel, R. Kostecki and S. S. Mao, *Chemical Society Reviews*, 2012, **41**, 7909-7937.
54. R. Kirchheim, T. Mütschele, W. Kieninger, H. Gleiter, R. Birringer and T. D. Koblé, *Materials Science and Engineering*, 1988, **99**, 457-462.
55. L. Zaluski, A. Zaluska and J. O. Ström-Olsen, *Journal of Alloys and Compounds*, 1997, **253–254**, 70-79.
56. J. J. Liang, *Appl. Phys. A*, 2005, **80**, 173-178.

57. R. W. P. Wagemans, J. H. van Lenthe, P. E. de Jongh, A. J. van Dillen and K. P. de Jong, *Journal of the American Chemical Society*, 2005, **127**, 16675-16680.
58. C. N. R. Rao, S. R. C. Vivekchand, K. Biswas and A. Govindaraj, *Dalton Transactions*, 2007, DOI: 10.1039/B708342D, 3728-3749.
59. C. N. R. Rao, A. Müller and A. K. Cheetham, *The Chemistry of Nanomaterials: Synthesis, Properties and Applications*, Wiley, 2006.
60. F. Maximilian, *Nanotechnology*, 2009, **20**, 204009.
61. B. Vigeholm, J. Kjøller, B. Larsen and A. Schrøder Pedersen, *International Journal of Hydrogen Energy*, 1983, **8**, 809-817.
62. C. Zlotea, C. Chevalier-Cesar, E. Leonel, E. Leroy, F. Cuevas, P. Dibandjo, C. Vix-Guterl, T. Martens and M. Latroche, *Faraday Discussions*, 2011, **151**, 117-131.
63. P. L. Guzzo, A. A. A. Tino and J. B. Santos, *Powder Technology*, 2015, **284**, 122-129.
64. S. A. Hewitt, T. Laoui and K. K. Kibble, *International Journal of Refractory Metals and Hard Materials*, 2009, **27**, 66-73.
65. C. d. S. Torres and L. Schaeffer, *Materials Research*, 2010, **13**, 293-298.
66. P. E. de Jongh and P. Adelhelm, *ChemSusChem*, 2010, **3**, 1332-1348.
67. T. K. Nielsen, F. Besenbacher and T. R. Jensen, *Nanoscale*, 2011, **3**, 2086-2098.
68. N. R. Khalili, J. D. Vyas, W. Weangkaew, S. J. Westfall, S. J. Parulekar and R. Sherwood, *Separation and Purification Technology*, 2002, **26**, 295-304.
69. H.-Q. Li, Y.-G. Wang, C.-X. Wang and Y.-Y. Xia, *Journal of Power Sources*, 2008, **185**, 1557-1562.
70. T.-Y. Ma, L. Liu and Z.-Y. Yuan, *Chemical Society Reviews*, 2013, **42**, 3977-4003.
71. Y. Meng, D. Gu, F. Zhang, Y. Shi, L. Cheng, D. Feng, Z. Wu, Z. Chen, Y. Wan, A. Stein and D. Zhao, *Chemistry of Materials*, 2006, **18**, 4447-4464.
72. E. J. Zanto, S. A. Al-Muhtaseb and J. A. Ritter, *Industrial & Engineering Chemistry Research*, 2002, **41**, 3151-3162.
73. D. Wu and R. Fu, *Microporous and Mesoporous Materials*, 2006, **96**, 115-120.
74. H. K. Chae, D. Y. Siberio-Perez, J. Kim, Y. Go, M. Eddaoudi, A. J. Matzger, M. O'Keeffe and O. M. Yaghi, *Nature*, 2004, **427**, 523-527.
75. J.-L. Zhuang, D. Ceglarek, S. Pethuraj and A. Terfort, *Advanced Functional Materials*, 2011, **21**, 1442-1447.
76. A. Katiyar, S. Yadav, P. G. Smirniotis and N. G. Pinto, *Journal of Chromatography A*, 2006, **1122**, 13-20.
77. L. Cao, T. Man and M. Kruk, *Chemistry of Materials*, 2009, **21**, 1144-1153.
78. X. Zhao, G. Lu, G. Millar and X. Li, *Catal Lett*, 1996, **38**, 33-37.

79. W. Sangchoom and R. Mokaya, *Journal of Materials Chemistry*, 2012, **22**, 18872-18878.
80. M. Fichtner, *Physical Chemistry Chemical Physics*, 2011, **13**, 21186-21195.
81. S. Cahen, J. B. Eymery, R. Janot and J. M. Tarascon, *Journal of Power Sources*, 2009, **189**, 902-908.
82. S. Zheng, F. Fang, G. Zhou, G. Chen, L. Ouyang, M. Zhu and D. Sun, *Chemistry of Materials*, 2008, **20**, 3954-3958.
83. S. Sepehri, A. Feaver, W. J. Shaw, C. J. Howard, Q. Zhang, T. Autrey and Cao, *The Journal of Physical Chemistry B*, 2007, **111**, 14285-14289.
84. R. Demir-Cakan, W. S. Tang, A. Darwiche and R. Janot, *Energy & Environmental Science*, 2011, **4**, 3625-3631.
85. T. K. Nielsen, K. Manickam, M. Hirscher, F. Besenbacher and T. R. Jensen, *ACS Nano*, 2009, **3**, 3521-3528.
86. Z. Shu, F. G. Adam, L. V. A. Sky, L. Maribel, L. Ping, C. A. Channing, J. V. John and M. J. Craig, *Nanotechnology*, 2009, **20**, 204027.
87. X. Liu, D. Peaslee, C. Z. Jost and E. H. Majzoub, *The Journal of Physical Chemistry C*, 2010, **114**, 14036-14041.
88. X. Liu, D. Peaslee and E. H. Majzoub, *Journal of Materials Chemistry A*, 2013, **1**, 3926-3931.
89. P. Ngene, P. Adelhelm, A. M. Beale, K. P. de Jong and P. E. de Jongh, *The Journal of Physical Chemistry C*, 2010, **114**, 6163-6168.
90. S. Sabrina, D. K. Kenneth, Z.-K. Zhirong, B. Eisa Gil, F. Maximilian and C. H. Bjørn, *Nanotechnology*, 2009, **20**, 505702.
91. F. G. Adam, C. A. Channing, L. V. A. Sky, L. Ping and J. V. John, *Nanotechnology*, 2009, **20**, 204005.
92. Z. Zhao-Karger, J. Hu, A. Roth, D. Wang, C. Kubel, W. Lohstroh and M. Fichtner, *Chemical Communications*, 2010, **46**, 8353-8355.
93. P. E. d. Jongh, R. W. P. Wagemans, T. M. Eggenhuisen, B. S. Dauvillier, P. B. Radstake, J. D. Meeldijk, J. W. Geus and K. P. d. Jong, *Chemistry of Materials*, 2007, **19**, 6052-6057.
94. R. D. Stephens, A. F. Gross, S. L. V. Atta, J. J. Vajo and F. E. Pinkerton, *Nanotechnology*, 2009, **20**, 204018.
95. A. Gutowska, L. Li, Y. Shin, C. M. Wang, X. S. Li, J. C. Linehan, R. S. Smith, B. D. Kay, B. Schmid, W. Shaw, M. Gutowski and T. Autrey, *Angewandte Chemie International Edition*, 2005, **44**, 3578-3582.
96. W.-J. Kwak, Z. Chen, C. S. Yoon, J.-K. Lee, K. Amine and Y.-K. Sun, *Nano Energy*, 2015, **12**, 123-130.

97. D. Blanchard, A. Nale, D. Sveinbjörnsson, T. M. Eggenhuisen, M. H. W. Verkuijlen, Suwarno, T. Vegge, A. P. M. Kentgens and P. E. de Jongh, *Advanced Functional Materials*, 2015, **25**, 169-169.

98. Y. Zhao, L. Jiao, Y. Liu, L. Guo, L. Li, H. Liu, Y. Wang and H. Yuan, *International Journal of Hydrogen Energy*, 2014, **39**, 917-926.

99. R. Dehghan-Niri, J. C. Walmsley, A. Holmen, P. A. Midgley, E. Rytter, A. H. Dam, A. B. Hungria, J. C. Hernandez-Garrido and D. Chen, *Catalysis Science & Technology*, 2012, **2**, 2476-2484.

Chapter 2

2. EXPERIMENTAL

Several different analytical techniques were used in order to fully investigate the properties and characteristics of the materials studied in this work. The aim of this chapter is to describe the characterisation techniques and methods used, with specific theoretical and technical information.

2.1. Inert-atmosphere handling techniques

Most of the compounds used in this work are air-sensitive, which usually means they are oxygen- and/or moisture-sensitive. This is why these types of materials have to be deal with under inert atmosphere to exclude air and moisture, in order to preserve their intrinsic properties. There are mainly two general techniques for handling these compounds, both used in this work[1]:

- Schlenk line: involves bench-top operations with special glassware (described in Section 2.1.1)
- Gloveboxes: conventional manipulations are performed in an inert-atmosphere box. (described in Section 2.1.2)

2.1.1. Schlenk line

The Schlenk line, developed by the German chemist Wilhelm Schlenk, is an apparatus used in synthetic inorganic and organic chemistry, particularly for handling air and moisture sensitive compounds. It allows work to be carried out under an inert atmosphere (usually nitrogen or argon) and/or under vacuum, without the need for changing the Schlenk Flask to another line[1]. The following list describes some of the most common operations that can be easily performed using a Schlenk line:

- Any operation involving oxygen and moisture sensitive materials (no matter if it is the starting materials or the final products), due to the inert gas atmosphere supplied.
- To remove the last traces of solvent or water from a sample, using the vacuum system and the liquid nitrogen cold trap.
- Setting up the atmosphere inside the Schlenk flask to either vacuum or inert gas atmosphere for further manipulations (for example, introduction of the Schlenk flask in a glovebox)
- Any combinations of the above.

The Schlenk line used in this work (Figure 2-1) consists of two manifolds with a number of ports using inert (usually argon or nitrogen) gas or vacuum for multiple reactions or manipulations. One manifold is connected to a source of purified inert gas (pureshield Argon gas cylinder, from BOC) and the other one is connected to the vacuum pump. The inert gas line is vented trough an oil bubbler, providing an oxygen- and moisture-free atmosphere to the system. The oil bubbler allows the user to monitor the flow of inert gas (by visual inspection of the speed of the bubbles formed), and also to detect any gas flow problems in the line such as an overpressure building up in the system or leaks. The solvent vapours or gaseous reaction products are outgassed through the vacuum line. In order, to avoid damaging the vacuum pump, a liquid nitrogen cold trap (77 °K or -196 °C)[2] is used to condense any products evolved from the Schlenk Flask.[3]

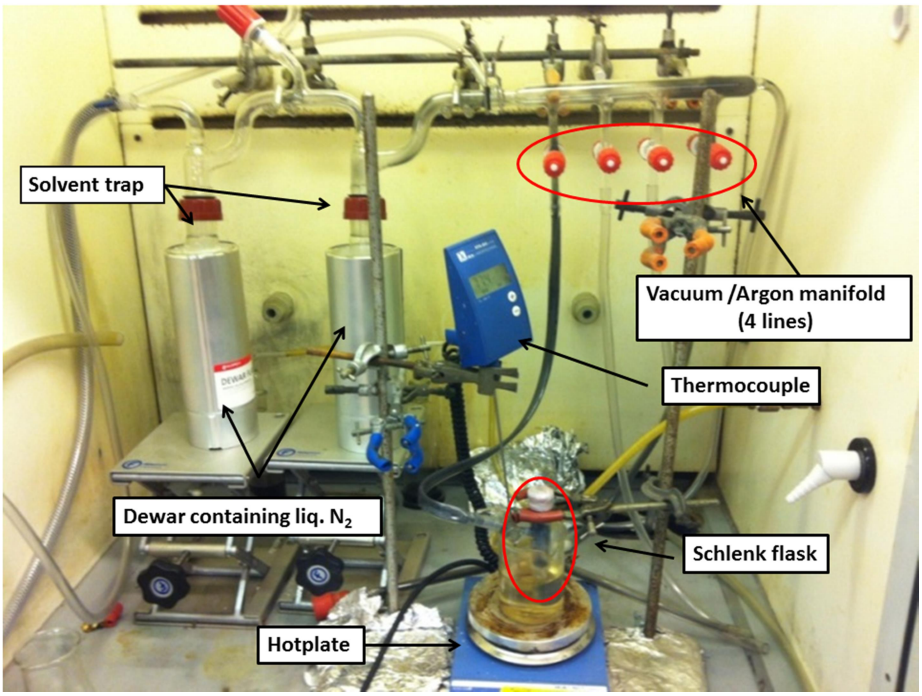

Figure 2-1. Schlenk line set-up, with all the important parts labelled.

Schlenk flasks or tubes are made of borosilicate glass such as Pyrex, and have a PTFE or ground glass stopcock (which has to be greased before every use) fitted at the side arm, where they are connected to a rubber hose from the Schlenk line. This arrangement allows the vessel to be evacuated or filled with inert gas easily. The Schlenk flask or tube (Figure 2-2) can be immersed in an oil bath or placed on a hot plate/magnetic stirrer if the operation requires it.

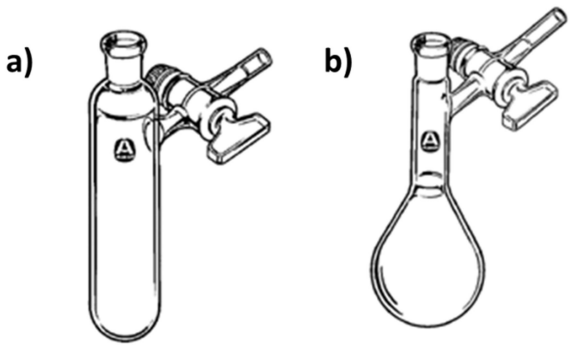

Figure 2-2. Images of the glassware used in the Schlenk line: a) Schlenk tube and b) Schlenk flask. (images from Sigma Aldrich)[4]

Although the Schlenk line is a really useful apparatus for handling air- and moisture-sensitive materials, there are some safety issues to be aware of. There are 4 main hazards associated with the use of the Schlenk line:

1 – Cryogenic Hazards associated with the use of liquid nitrogen. Inappropriate use of liquid nitrogen can cause cold burns. All the safety regulations (*e.g* wearing cryogenic gloves and face shield) must be followed when dealing with liquid nitrogen.

2 – Explosions due to overpressure of inert gas. A gas-accessible way out of the Schlenk line has to be present and maintained in good conditions when flushing inert gas through the system.

3 – Explosions due to oxygen condensation in the cold trap. Oxygen has a slightly higher boiling point (-183 °C) than nitrogen (-196 °C),[5] therefore the former will condense from the atmosphere and could be collected in the trap if the Dewar flask containing liquid nitrogen is attached to the trap when the system is not under vacuum but open to the atmosphere. Liquid oxygen has a deep blue colour and in the presence of organic solvents could generate peroxides which could lead to an explosion. To avoid this, the system should be evacuated completely before attaching the liquid nitrogen trap.

4 – Implosions due to the use of high vacuum. Any piece of glassware which is found to be cracked or scratched should not be used.

2.1.2. Glove box

A glove box is a sealed receptacle filled with inert gas, allowing the handling of air-sensitive materials without exposing them to the atmosphere.[6] The box is made of stainless steel with a glass window and rubber gloves to facilitate the introduction of the user's hands to perform the manipulations inside.

Figure 2-3. MBraun LABStar Glove Box, filled with Argon atmosphere.

The atmosphere inside the box is kept free from moisture and oxygen by cycling inert gas through molecular sieves and a catalyst, respectively. The molecular sieves capture any moisture present in the atmosphere of the box whereas the catalyst will trap any presence of oxygen. Oxygen and moisture levels inside the box are normally below 0.5 ppm (tracked by oxygen and moisture analysers). The samples or any laboratory equipment is introduced or emptied from the box using the evacuable ports attached to the box. These ports act as an antechamber to avoid exposing the box to the atmosphere. The ports are evacuated and filled with inert gas three times before opening the inner door of the port to the box, to ensure no oxygen or moisture from the outside atmosphere remains in the port.

To maintain low enough levels of both moisture and oxygen inside the box, the catalyst and molecular sieves have to be regenerated frequently. The regeneration process consists of flowing an appropriate regeneration gas (Argon gas with 5% H_2 for an Argon-filled box and Nitrogen gas with 5% H_2 for a Nitrogen-filled box) during 12-16 hours.[7]

The manipulations usually performed inside the glove boxes include preparing reactions (weighing, mixing and grinding samples), preparing samples for characterization (*e.g.* Raman, X-ray, BET) and storing samples and starting materials.

The glove boxes used in this project were an MBraun Labstar (Figure 2-3), alpha (argon filled) and omega (nitrogen filled) models from Saffron Scientific and an MBraun UniLab (argon filled) as a permanent environment for the STA apparatus. Oxygen and moisture levels inside the boxes are normally below 0.5 ppm (tracked by oxygen and moisture analysers).

2.1.3. Solvent purifier system

For the solution impregnation process used in the confinement of some of the materials described in this work (Section 1.4.2.2), organic solvents were needed. The need for anhydrous solvents is imperative when working with moisture-sensitive products.[8] The general procedure to obtain anhydrous solvents is distilling them in the presence of a hygroscopic substances: like molecular sieves, alkali metals (such as sodium) or alkali bases (such as potassium hydroxide, barium oxide or aluminium oxide, amongst others).[9]

Figure 2-4. Solvent Purifier system at University of Glasgow (3rd floor).

The solvents used in this work were obtained from the PureSolv MD 5[10] Solvent Purifier System (SPS, 3rd floor) from the School of Chemistry at the University of Glasgow (Figure 2-4). The solvents available on this Solvent Purifier System were THF, Ether, Toluene, Acetonitrile and DCM. The columns of this purifier system are filled with aluminium oxide molecular sieves (apart from the toluene column). A periodic analysis of the water content is performed in order to check the level of purity of the solvents dispensed from the Solvent Purifier System (Figure 2-5). Diethyl ether was used for this work and the water content of this solvent collected from the SPS was lower than 7 ppm.

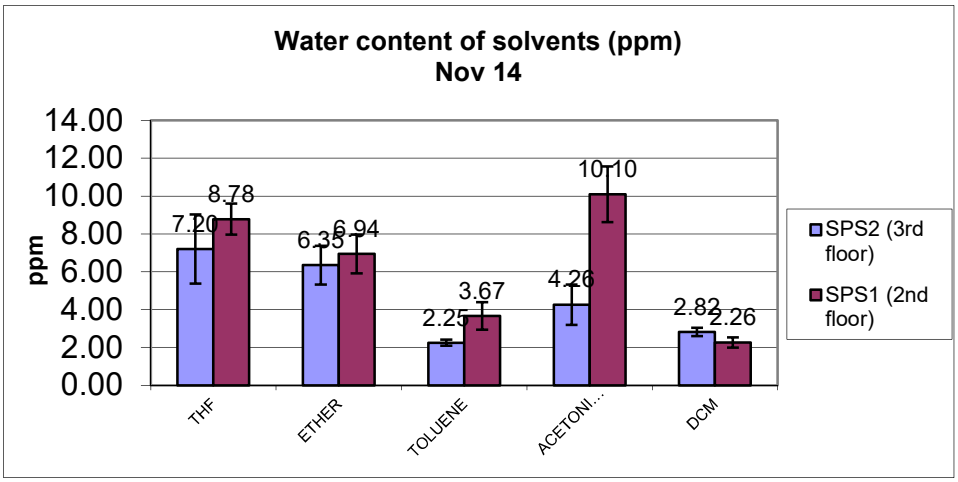

Figure 2-5. Water content in ppm on the solvents dispensed from the Solvent Purifier Systems available at the School of Chemisty at the University of Glasgow. The solvents used in this work were usually dispensed form the Solvent Purifier System located in the 3rd floor.

2.2. Characterisation techniques

Most of the techniques used for characterization in this work are based on interactions of electromagnetic radiation with matter.[11] Electromagnetic radiation is composed of electromagnetic waves produced when charged particles are accelerated and they consist of oscillations in electric and magnetic fields, perpendicular to each other, that can travel through space, as shown in Figure 2-6.

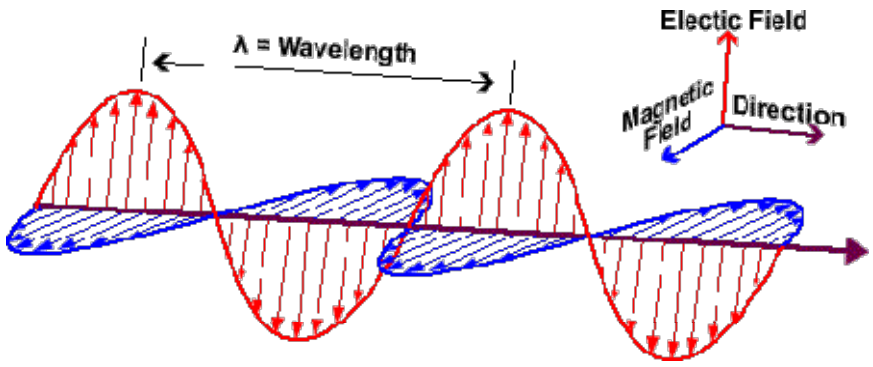

Figure 2-6. Electromagnetic wave, showing the perpendicular electric field and the magnetic field components, adapted from reference [12].

The waves carry energy, momentum and angular momentum away from their source and can transfer those quantities to the matter with which they interact.[13] Electromagnetic radiation can be ordered in the electromagnetic spectrum as a function of frequency or wavelength (high frequency will mean higher energy electromagnetic waves) as seen in Figure 2-7.

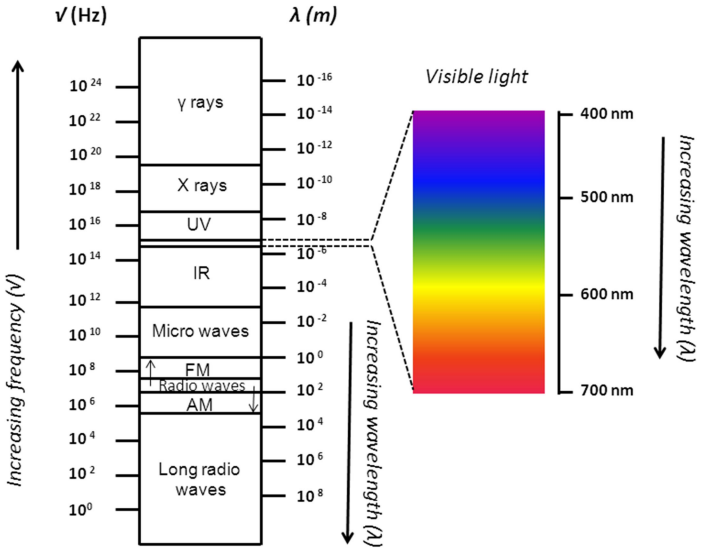

Figure 2-7. Electromagnetic spectrum showing radiation from high frequencies (γ-rays) to low frequencies (radio waves). Modified from reference [13].

Electromagnetic waves are characterized by wavelength (λ) and frequency (ν).[11,14] The wavelength is defined as the distance between any two adjacent identical points of a wave, whereas frequency is defined as the number of wavelengths of that wave that pass a fixed point in one unit of time (usually one second).

$$\nu = \frac{c}{\lambda} \qquad (2\text{-}1)$$

where ν is usually represented with Hz (= s^{-1}), c is defined as the speed of light (c = $3 \cdot 10^8$ $m \cdot s^{-1}$), which is at the speed that an electromagnetic wave will travel under vacuum.

In vibrational spectroscopy, the term wavenumber (usually m^{-1}) is also commonly used and is defined by:

$$\bar{\nu} = \frac{\nu}{c} \qquad (2\text{-}2)$$

By combining the last 2 equations:

$$\bar{\nu} = \frac{\nu}{c} = \frac{1}{\lambda} \quad (m^{-1}) \qquad (2\text{-}3)$$

If a molecule interacts with an electromagnetic field, a transfer of energy from the field to the molecule can occur only when Bohr's frequency condition is satisfied:

$$\Delta E = h\nu = h\frac{c}{\lambda} = hc\bar{\nu} \qquad (2\text{-}4)$$

Where h is the Planck's constant ($6.626 \cdot 10^{-34}$ J·s) and ΔE is the difference in energy between two quantized states. Therefore, ν and $\bar{\nu}$ are proportional to the energy of transition.

If the following is supposed:

$$\Delta E = E_2 - E_1 \qquad (2\text{-}5)$$

where E_2 and E_1 are the energies of the excited and ground states, respectively. The molecule will absorb energy when it undergoes a transition from a state of low energy (E_1) to a state of high energy (E_2), and therefore lose energy when the transition is from E_2 to E_1.

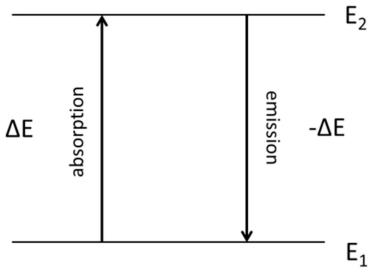

Figure 2-8. Electronic absorption and emission between 2 energy levels. Modified from reference [13].

Absorption and emission spectroscopy give the same information about energy level separations, but practical considerations generally determine which technique is used.

Transitions between electronic energy levels, also known as electronic excitation, are stimulated by, or are able to emit ultraviolet, visible or near infrared radiation. Core-electron excitation and nuclear excitation are stimulated by, or emit X-ray and γ-ray respectively. Lower frequency waves, such as microwaves and far infrared radiation, are either emitted or stimulate molecular rotation and molecular vibration transitions respectively.

The following brief introduction provides the basic concepts for a better understanding of Raman and IR spectroscopy.

2.2.1. Raman Spectroscopy

Raman spectroscopy is an analytical technique, discovered by the Indian physicist, Sir C.V. Raman, used for the study of molecular vibrations.[19] Raman spectroscopy is based on the inelastic scattering of monochromatic light by certain molecules.

Raman spectra are formed as a result of light photons being absorbed temporarily by molecules and gaining or decreasing small increments of energy through changes in the molecular rotational and vibrational energies before being reemitted as scattered light.[20] This re-emitted frequency provides information about vibrational and rotational transitions in molecules. These vibrational transitions occur between 10^{-6} – 10^{-4} m in wavelength in the electromagnetic spectrum, corresponding to near infrared light. These numbers will be the difference between incident and re-emitted radiation. For Raman Spectroscopy the source of electromagnetic radiation (laser) is usually in the range of visible, near infrared or near ultraviolet light. Either a UV (wavelength: 325 nm) or green (wavelength: 532 nm) laser was used in this spectrometer.

A Raman spectrum is obtained when the sample is irradiated by a laser beam in the UV-visible region ($\boldsymbol{\nu}$), and the scattered light produced is observed by the detector. The scattering process happens in two steps where a photon collides with the electrons of a molecule promoting them from a ground electronic state to a virtual excited electronic state, and then a second photon leaves the molecule when the electrons come back from the excited state to the ground state. Raman spectroscopy measures the difference between these two steps. There are two types of possible light scattering[21] (Figure 2-9):

- Elastic Scattering: the scattered light has the same frequency as the incident beam ($\boldsymbol{\nu}$). It is also called *Rayleigh scattering.* Electrons in a ground state are promoted to a virtual excited state and back to the ground state.
- Inelastic (Raman) Scattering: the scattered light has a different frequency ($\boldsymbol{\nu} \pm \boldsymbol{\nu}$i) from the incident beam. $\boldsymbol{\nu}$i corresponds to the vibrational frequency of a molecule. Depending on the frequency of the scattered light, inelastic scattering is divided into 2 types:

    - Stokes radiation: when the reemitted frequency is ($\boldsymbol{\nu} - \boldsymbol{\nu}$i), as a result of the incident beam losing energy to the sample. Electrons in a ground state are promoted to a virtual excited state and back to a less energetic electronic level than that of the ground state.
    - Anti-Stokes radiation: when the reemitted frequency is ($\boldsymbol{\nu} + \boldsymbol{\nu}$i), as a result of the incident beam gaining from the sample. Electrons in a ground state are promoted to a virtual excited state and back to a more energetic electronic level than that of the ground state.

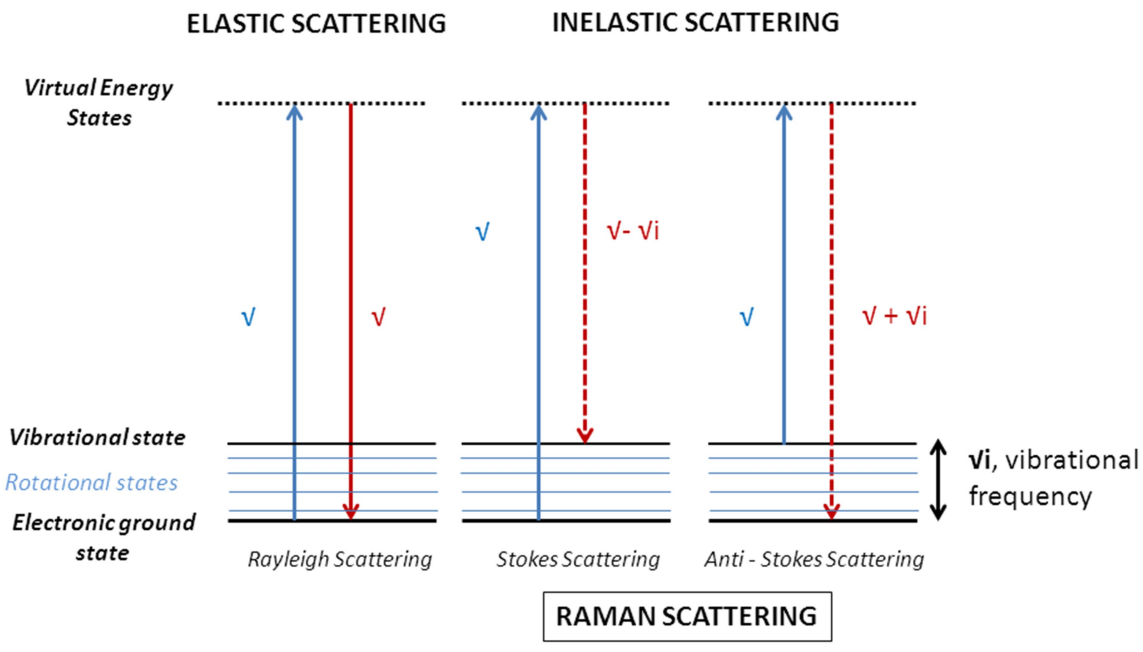

Figure 2-9. Origins of Rayleigh and Raman Scattering. Modified from reference [15].

The majority of the incident radiation will scatter elastically. Only 10^{-7} % will inelastically scatter. Before reaching the detector, the photons which are elastically scattered will be captured in a lens which only will let through the photons inelastically scattered.[21] Raman spectra would then be obtained, consisting of numerous peaks with varying intensity each of them corresponding to a molecular bond vibration. Spectra obtained are unique for a particular material and can therefore be used as a fingerprint to characterize the molecule, consulting Raman libraries and Group Theory to assign bonding modes from the Raman Spectra.[18, 22]

Not all the molecules are Raman active: for Raman scattering to occur, the interaction of the molecule with light must cause a change in the polarizability of the molecule. That means that a change in the molecular electric dipole of the molecule is required for a molecule to exhibit Raman scattering. The intensity of the peaks will be proportional to the change of the polarizability of the molecule. For instance, a highly symmetric molecule (eg. CH_4) will be Raman inactive because its polarizability is identical at any orientation, so only Rayleigh scattering will be observed.[23]

The Raman spectrometer used for this work was a Horiba LabRAM HR confocal microscope system with a 532 nm green laser (Figure 2-10). A hole aperture of 50 µm, 600 grating/mm, 50x objective lens and a Synapse CCD detector were used at room temperature.

Powdered air sensitive samples were placed in a glass capillary and sealed before running the analysis. Spectra were usually collected over a period of several minutes from an average of multiple scans, normally at a range of 10 cm^{-1} to 3500 cm^{-1}.

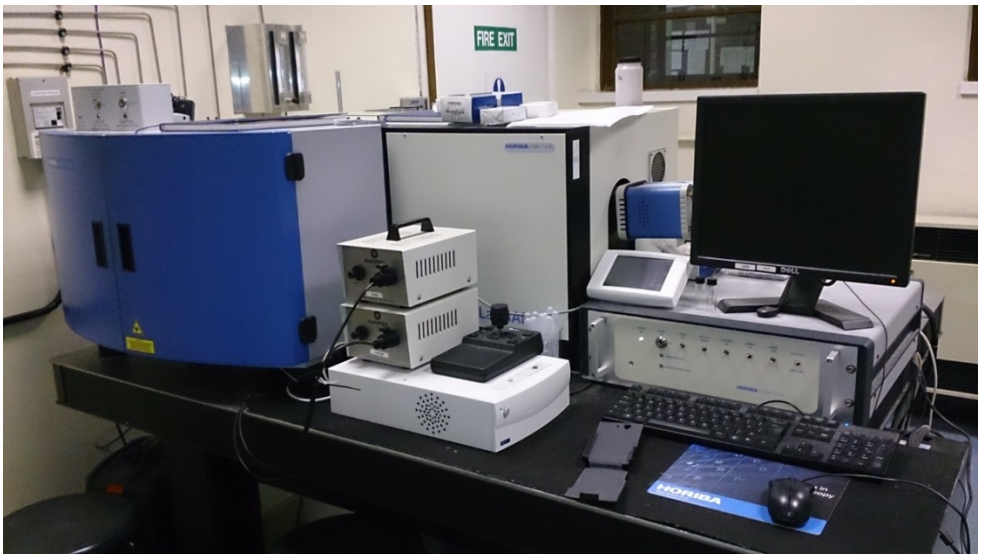

Figure 2-10. Raman spectrometer used in this work: Horiba LabRAM HR.

2.2.2. Powder X-Ray Diffraction

Powder X-ray Diffraction (PXD) is an analytical technique used to identify and characterize unknown microcrystalline or powder materials. Structural analysis of samples was performed on synthesised materials and for ex-situ samples following thermal analysis. X-ray diffraction offers a convenient and quick characterisation technique, providing structural analysis by probing samples with X-rays.[24]

2.2.2.1. Crystallography and diffraction

In order to understand how an X-ray beam interacts with a crystalline sample, some basic concepts need to be described. Crystallography is the science that determines the arrangement of atoms in a crystalline solid.[25] Crystalline solids have a lattice structure, with the atoms undertaking a regularly repeating pattern, which constitutes a unique, highly ordered arrangement of atoms, ions or molecules. This can be simplified to a singular repeating component known as the unit cell (Figure 2-11). The unit cell, which is the basic building block, repeats in a regular manner in all directions, in a perfect regular way. The length of the unit cell (a, b, c) and the angles (α, β, γ) are known as the lattice parameters.

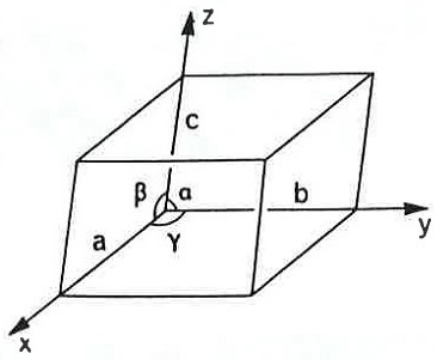

Figure 2-11. A unit cell showing the axial lengths and interaxial angles. Modified from reference [26].

The unit cell shapes are determined by minimum symmetry requirements of particular crystalline structure. Seven possible crystal systems exist, which denote all the possible shapes a unit cell can adopt: cubic, tetragonal, trigonal, orthorhombic, hexagonal, monoclinic and triclinic (Figure 2-12a). At the same time, the unit cell has up to four lattice types depending on the position of the lattice points[26] (Figure 2-12b).

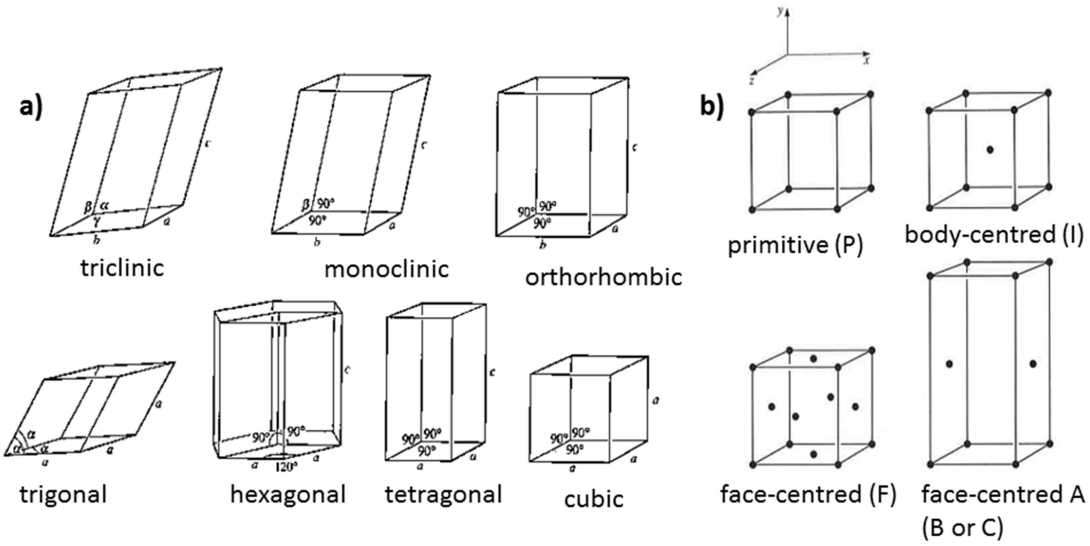

Figure 2-12. a) The unit cells of the seven crystal systems. b) The 4 different types of three-dimensional unit cells: Primitive (P), body-centred (I), face-centred (F), and face- centred A, B or C (A shown) unit cells. Modified from reference [27].

The diffraction of X-rays by crystals provides structural information about the arrangement of the ions, atoms or molecules in the crystals. X-ray diffraction results from constructive and destructive interference caused by scattering of X-rays from atoms in a regular way, with diffraction lines appearing at angles that satisfy Bragg's law, deduced by the English physicist Sir W. H. Bragg:[28]

$$n\lambda = 2dsin\theta \qquad (2\text{-}6)$$

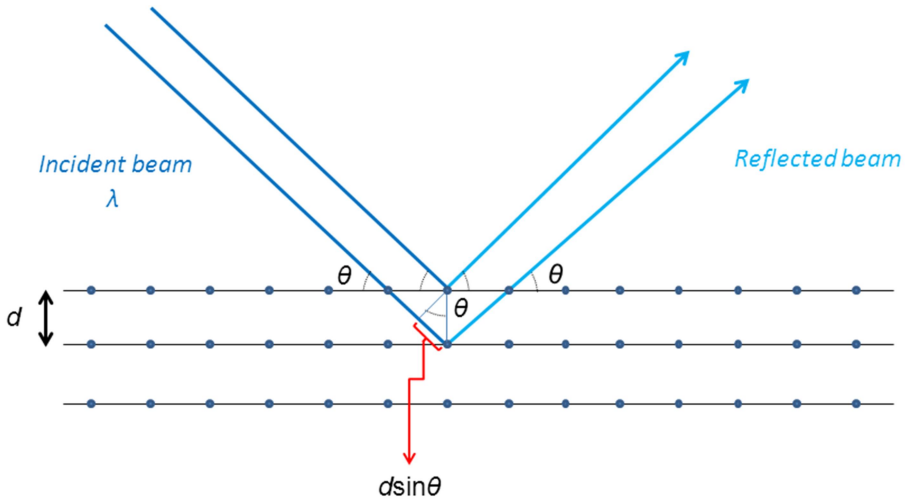

Figure 2-13.Schematic representation of the diffraction process, illustrating Bragg's Law.

Where n is an integer number, λ describes the wavelength of the incident X-rays, d is the perpendicular distance between the adjacent planes and ϑ is the angle of incidence.

Crystal structure information is deduced by collecting the reflected beam which is represented as a function of the diffraction angle. The crystal system of a crystalline solid is derived from the interplanar spacing information collected in the diffraction experiment and the Miller indices (h, k and l)[24], which are used to describe the parallel planes of atoms that intersect with the axes of the unit cell (a, b and c). Bravais lattice notation also provides further information about crystal configuration (14 possible). Combining these definitions with the possible types of the 3D lattice (Figure 2-12) and point group symmetries, result in 230 space groups. Assignment of these groups is essential to indicate the crystallographic nature of sample and predict or define some of its properties. The International Tables for X-Ray Crystallography gather all the information about each of the space groups.[29]

2.2.2.2. X-ray instrumentation

Usually X-ray diffractometers consist of three basic elements: an X-ray tube, a sample holder, and an X-ray detector.

X-rays are generated by heating a filament to produce electrons, accelerating the electrons toward a target by applying a voltage, and bombarding the target material usually (Cu, Fe, Mo, Cr)

with electrons. When electrons have sufficient energy to remove inner shell electrons of the target material, characteristic X-ray spectra are produced.[30] These spectra consist of several components, the most common being K_α and K_β. K_α consists, in part, of $K_{\alpha1}$ and $K_{\alpha2}$. The specific wavelengths are characteristic of the target material. Emission of the electromagnetic radiation is then filtered by foils, to produce monochromatic X-rays needed for diffraction. Copper is the target material used in this work, with K_α radiation of 1.5418 Å (Figure 2-14).

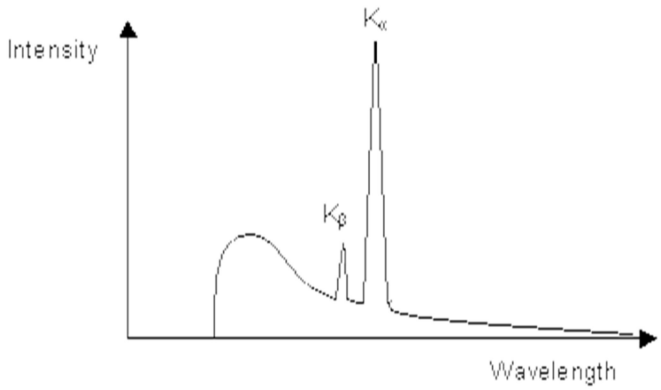

Figure 2-14. Spectrum of the X-ray emission of a copper source. Modified from reference [31].

These X-rays are directed to the sample. As the sample and detector are rotated, the intensity of the reflected X-rays is recorded. When the geometry of the incident X-rays impinging the sample satisfies the Bragg Equation, constructive interference occurs and a peak in intensity occurs. A detector records and processes this X-ray signal and converts the signal to a count rate which is then obtained as a diffraction pattern in the computer.

Diffraction patterns shown in this work were collected using a Bruker D8 Advance diffractometer (Figure 2-15), with Cu $K_{\alpha1}$ radiation, and collected over a 2ϑ range of 5-85° for phase analysis. The step size and scan speed use was 0.0167° at 1.57°·min^{-1}. To prepare a sample for PXD, it was ground using a mortar and pestle in order to obtain a fine product and to ensure a homogenous powder. Powders were placed in glass capillaries of 0.5 mm diameter, inside the glove box. Each capillary was aligned on the capillary holder using a simple optical microscope. After this, the capillary holder is mounted in the instrument, where it would be radiated by the X-ray beam. Once the diffraction pattern was obtained, PowderCell[32] software was used to plot the data obtained and the ICSD database[33] (Inorganic Crystal Structure Database) was consulted for peak fitting and overall crystal structure identification.

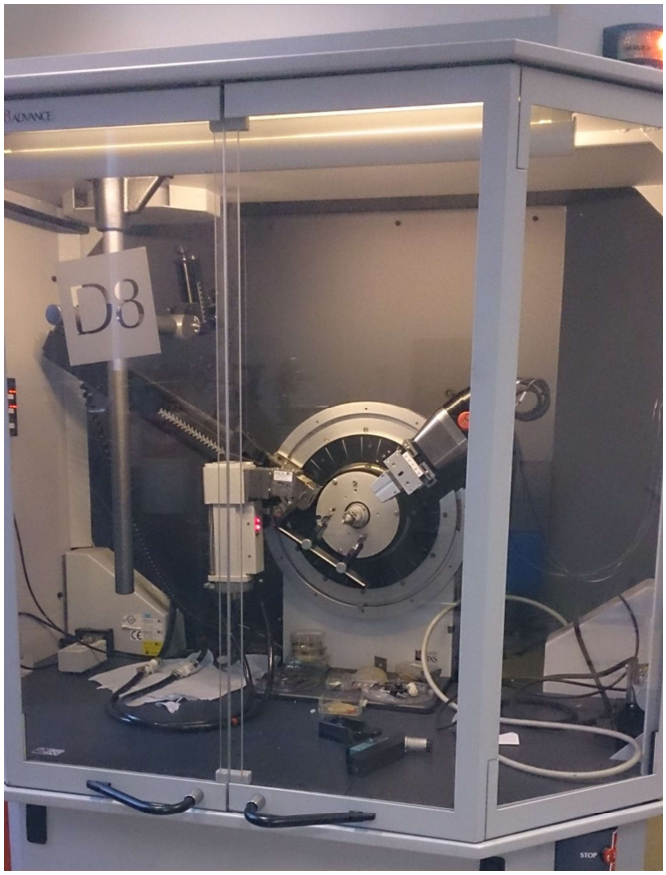

Figure 2-15. Powder X-Ray diffractometer, Bruker D8, used for structural characterization in this work.

2.2.3. Gas adsorption (BET)

Surface area and pore volume determines many physical and chemical properties of materials. The determination of the surface area and the pore volume has been crucial in this project, since porous hosts have been used for the confinement of guest materials. Knowing the surface area and pore volume of the carbon hosts prior to confinement was necessary in order to determine the maximum amount of guest sample that could be confined. The decrease of both surface area and the pore volume for the confined samples would raise some evidence that the pores of the carbon host were occupied by the impregnated material.

The specific surface area of a solid material is usually measured by physical adsorption of a gas (usually N_2) on the surface of the solid material and by calculating the amount of adsorbate gas corresponding to a monomolecular layer on the surface (monolayer formation

shown in Figure 2-16). The physical gas adsorption results from relatively weak forces (Van der Waals forces) between the adsorbate gas molecules and the adsorbent surface of the solid material. In contrast to chemical adsorption, also called chemisorption, during physical adsorption, the sorbed molecules are not restrained to specific sites on the surface of the tested solid and are free to cover the whole surface. For this reason, determination of surface areas is possible.[34] The measurement is usually carried out at the temperature of liquid nitrogen (77 °K).[2]

In 1916 Irving Langmuir developed the theory of monolayer adsorption by describing the dependence of the surface coverage of an adsorbed gas on the pressure of the gas above the surface.[35] This was carried out at a fixed temperature. Several years later, in 1938 S. Brunauer, P. H. Emmett and E. Teller presented the BET theory for the first time[36] (BET is an abbreviation of the first initials of their family names: Brunauer – Emmet –Teller). The BET theory expands Langmuir's treatment to account for multilayer adsorption. Nowadays it is still considered the best known method for the measurement of the surface areas of a porous material. The BET theory is a rule for physical adsorption of gas molecules on a solid surface and it is the main base for the analysis techniques that are used for the measurement of specific surface areas of the material.

For this extension to the Langmuir theory to be successfully applied to multilayer adsorption, several assumptions must be made, including;[37]

- The number of gas molecule layers adsorbed on the surface of the solid increases infinitely at saturation pressure
- The first and second layers have different energies of adsorption, and thereafter all layers have the same adsorption energy as the second
- Each layer can be characterised through application of the Langmuir theory

Considering these assumptions leads to the resulting BET equation, expressed by:

$$\frac{p}{v_o[p_o - p]} = \frac{1}{v_m c} + \frac{c-1}{v_m c}\left(\frac{p}{p_o}\right) \qquad (2\text{-}7)$$

where p and p_o are the saturation and equilibrium pressure, respectively, of adsorbate gas at the experimental adsorption temperature, v_o is the volume of adsorbed gas, v_m is the volume of gas adsorbed in the monolayer, and c is the BET constant. This constant is related to heats of adsorption and liquefaction of the gaseous layers, which is expressed by:

$$c = exp\left(\frac{E_1 - E_L}{RT}\right) \quad (2\text{-}8)$$

where E_1 is the heat of adsorption corresponding to the first layer, E_L is the heat of adsorption of the second and subsequent layers, and is equal to the heat of liquefaction, R is the molar gas constant ($J \cdot mol^{-1} \cdot K^{-1}$) and T is the absolute temperature (K).

A plot of the amount of gas adsorbed at a certain temperature against the relative pressure is called a sorption isotherm (Figure 2-16). It is usually presented as the volume of adsorbed gas versus the relative pressure, (P/Po).

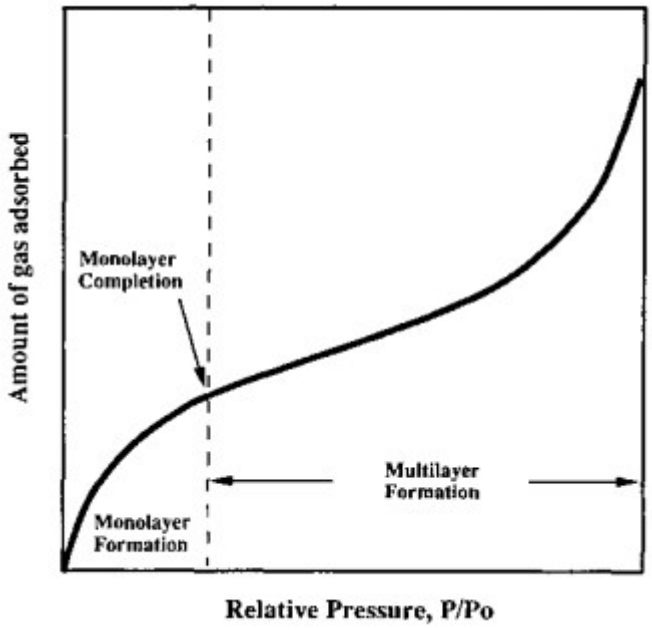

Figure 2-16. Sorption Isotherm showing monolayer and multilayer formation. Relative pressure (P/Po) is plotted against amount of gas adsorbed. Modified from reference [37].

To determine the specific surface area (S) and total surface area (S_{total}) of material, the following equations are used:

$$S_{total} = \frac{(v_m N s)}{V} \quad (2\text{-}9)$$

$$S = \frac{S_{total}}{m} \quad (2\text{-}10)$$

Where S_{total} is the total surface area (m^2), S is the specific surface area ($m^2 \cdot g^{-1}$), v_m is the volume of gas adsorbed in the monolayer, m is the sample weight, V is the adsorbent gas molar volume, N is Avogadro's number and s is the adsorption cross section (which is defined as the area occupied by a single adsorbed gas molecule)

Surface area analysis, mainly total surface area and average pore diameter, were determined using a Micromeretics Gemini III 2375 surface area analyser (Figure 2-17), with liquid Nitrogen and Nitrogen gas as the adsorbate. Air- and moisture –sensitive samples were prepared and weighed inside a glove box. The instrument did not have a special set up for loading air- and moisture –sensitive samples, therefore such samples were loaded to the instrument as quickly as possible. Degassing the samples at over 100 °C prior to analysis is a common procedure for gas sorption techniques, in order to remove moisture from the sample and make sure that the pores are fully available for absorption. This procedure was only carried out for samples prior to confinement (as-received carbon hosts). No degassing step was done on the confined samples before surface area analysis because the synthesis of confined samples includes a drying step to remove the solvent used, which will also remove anything blocking the pores. After confinement all the samples were treated as air- and moisture –sensitive, hence the possibility of moisture presence was negligible.

Figure 2-17. Micromeretics Gemini III 2375 surface area analyser.

2.2.3.1. Classification of adsorption isotherms and pores sizes

The majority of physisorption isotherms can be grouped into six types[38] shown in Figure 2-18.

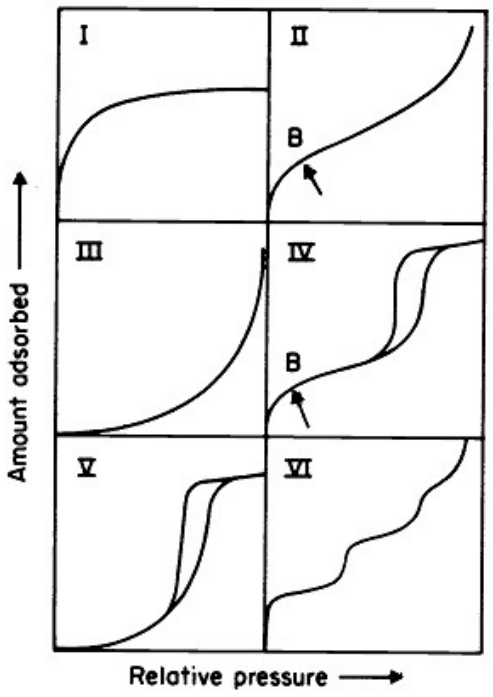

Figure 2-18. Different types of isotherms. X axis shows relative pressure, also expressed as p/po and Y axis shows the amount of gas adsorbed (N_2 gas). Modified from reference [38].

- *Type I* isotherm: This isotherm is concave to the p/p_O axis. The absorbed amount of adsorbate approaches a limiting value as $p/p_O \rightarrow 1$. This type of isotherm is representative of microporous solids having relatively small external surfaces (e.g. activated carbons, molecular sieve zeolites and certain porous oxides).
- *Type II* isotherm: This isotherm is the normal form of isotherm obtained with a non-porous or macroporous adsorbent. It represents unrestricted monolayer-multilayer adsorption. Point B, which represents the beginning of the almost linear middle section of the isotherm, is taken to indicate the stage at which monolayer coverage is complete and multilayer adsorption about to begin.
- *Type III* isotherm: This isotherm shows amount of gas adsorbed increases without limit as $p/p_O \rightarrow 1$ (and therefore it does not exhibit a Point B, which means monolayer formation is missing). These types of isotherms are not common.

- *Type IV* isotherm: The most characteristic features of this type of isotherm is the hysteresis loop, which represents capillary condensation taking place in mesopores, and the limiting uptake over a range of high p/p_O. The initial part of this isotherm is attributed to monolayer-multilayer adsorption since it follows the same path as the corresponding part of Type II isotherm obtained with the given adsorptive on the same surface area of the adsorbent in a non-porous form. Type IV isotherms are given by mesoporous adsorbents.
- *Type V* isotherm: This type of isotherm it is related to Type III isotherm (it is also uncommon), where the adsorbent – adsorbate interaction is weak, but is obtained with certain porous adsorbents.
- Type VI isotherm: This isotherm represent stepwise multilayer adsorption on a uniform non-porous surface. The step-height now represents the monolayer capacity for each adsorbed layer and, in the simplest case, remains nearly constant for two or three adsorbed layers.

As reported by the International Union of Pure and Applied Chemistry (IUPAC), in the context of physisorption the pores of any porous substance can also be classified according to their sizes:[38]

- Macropores: pores with widths exceeding 50 nm
- Mesopores: pores of widths between 2 nm and 50 nm
- Micropores: pores with widths not exceeding about 2 nm.

The pores of the porous carbons materials used in this work fall within the mesoporous and microporous classification.

For a typical analysis in the BET apparatus, the sample vial was weighed before introducing the sample. If the sample for analysis was air-sensitive, the vial was loaded with the sample inside the glove box under inert atmosphere, and the vial was weighed again. By weight difference, the total mass of the sample was calculated. Usually about 30-40 mg of sample was loaded into the BET vial. If the sample was not outgassed already, the vial was left overnight at 100 °C under a helium gas flow. The surface area, pore volume and pore diameter were obtained from the data report automatically created from the BET analysis software.

2.2.4. Electron microscopy

Electron microscopes use electrons to create an image of a sample. They have much better resolution than optical microscopes and they can reach the nanometre scale, which is the reason why these kinds of electron microscopes are widely used in the nanotechnology field. The 2 main different types of electron microscopes are the scanning electron microscope (SEM) and the transmission electron microscope (TEM), both of them were used in this work and are detailed below.

2.2.4.1. Scanning Electron Microscopy (SEM)

SEM was used to obtain information regarding the size, morphology and topography of the materials in this work. This is a type of electron microscope that uses a high-energy electron beam to generate a variety of signals at the surface of solid specimens. The signals that derive from the interaction between the electron beams and the sample are used to create an image of the sample and reveals information about the topography and morphology of the mentioned sample.[39]

The SEM consists of an electron gun which produces a beam of electrons thermionically (Figure 2-19). These electrons are produced when a high voltage is applied to a filament of either tungsten (W) or lanthanum hexaboride (LaB_6). The beam of electrons is focused by a condenser lens and projections apertures and is directed to the sample. Scanning coils ensure the entire sample surface is scanned and the detector will receive the signals of the scattered electron beam after interaction with the sample, and converted into electric signals to image the sample. Scanning electron microscopes have at least one detector (usually a secondary electron detector), and most have additional detectors (backscattered detectors or X-ray detectors, the latter permits energy dispersive X-ray spectroscopy (EDX)).

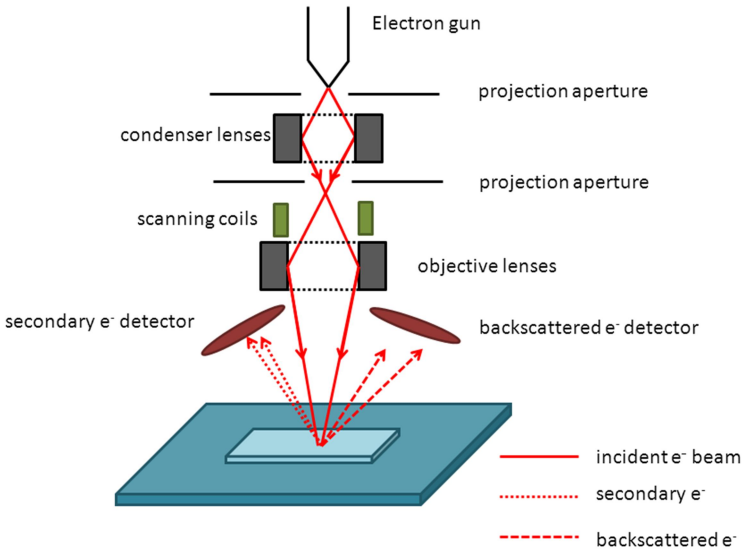

Figure 2-19. The basic components of a conventional SEM. Modified from reference [40].

When the electron beam reaches the sample, the electrons interact with the atoms of the sample producing several signals. This interaction either results in elastic or inelastic scattering of the incident electrons. The several signals produced (Figure 2-20) consist of secondary electrons (SE) and backscattered electrons (BSE), which are the ones used to form an image of the sample but production of Auger electrons, X-rays and light emission (cathodoluminiscence) also occurs:[41]

- Secondary electrons: these electrons are low energy electrons formed from the inelastic scattering of the incident electron beam with the outer shell electrons of the atoms in the sample, which receive enough energy from the incident electron beam to be ejected from the atom. These electrons produced provide image contrast and also give topographical information about the sample.

- Backscattered electrons: these are high energy electrons produced from the elastic collision of the incident beam with an atom nucleus of the sample. Because of this interaction with the nucleus, backscattered electron intensity increases with higher atomic numbers. These electrons produced give topographical information about the sample but different from that of the secondary electrons as backscattered electrons penetrate deeper in the sample.

- Auger electrons: these electrons are produced due to inelastic scattering of the incident electron beam. The incident beam of electrons can create some vacancies in inner atomic

shells. In order to fill these vacancies, another electron from a higher energy level falls down in the vacancy, producing a release of energy. This energy can be transferred to a neighbouring electron which would be ejected and named an Auger electron.

- X-rays: the emission of X-rays is produced by a similar process to the formation of Auger electrons. X-rays will be emitted when a higher energy electron fills the vacancy created of a lower energy level. This characteristic X-ray emission can be used for Energy dispersive X-ray spectroscopy (EDX), which provides information about the composition of the sample and element abundance.

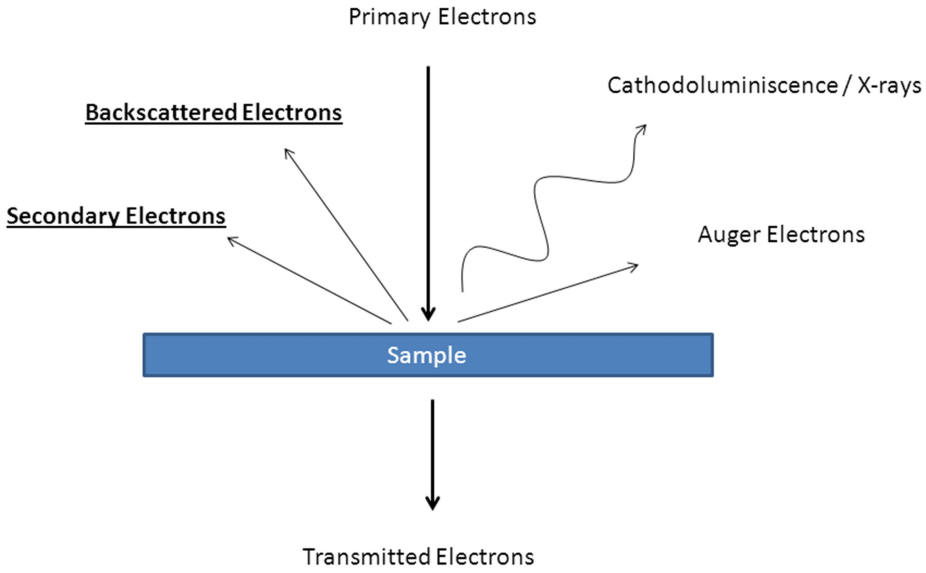

Figure 2-20. Schematic drawing of signals for a sample generated by the electron incident beam. Modified from reference [41].

SEM characterisation was used in this work to acquire information about the morphology and the topology of the samples. Measuring the particles of the SEM pictures by a specific imaging software (ImageJ) also provided information about the particle size of the samples.

The scanning electron microscope used for this work was a Philips XL30 ESEM (Figure 2-21). This microscope uses a tungsten filament as a source of electron beam, at an acceleration voltage of 20-25 kV and a working distance of 12.5 mm. The whole SEM chamber operates under high vacuum in order to prevent scattering due to air or dust particles and to avoid oxidation of the high temperature tungsten filament.[42] To prepare the samples the product was sprinkled, inside the glove box, on a carbon tab fixed to a metal stub. Some of the samples had to be coated in

order to provide electron conductivity at the surface. This will prevent the sample from charging, avoiding brightness issues, and facilitating the acquisition of quality images. A gold sputter coater was used and the samples were coated with a fine layer of gold-palladium. The SEM used in this work did not have any air-sensitive setup for the loading of samples. Samples were introduced in the microscope as quickly as possible to minimise air exposure.

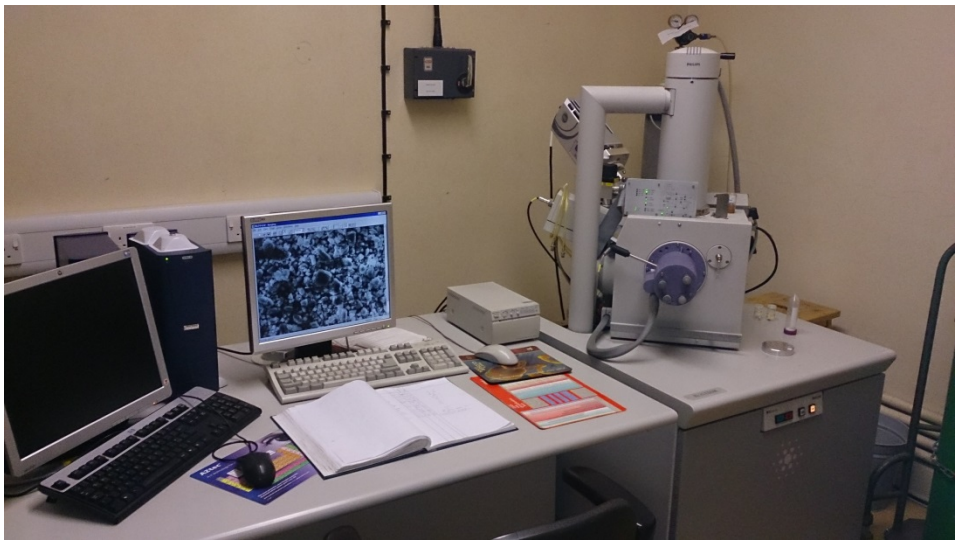

Figure 2-21. Philips XL30 SEM used in this work and located at the School of Chemistry, University of Glasgow.

2.2.4.1.1. Energy dispersive X-ray Spectroscopy (EDX)

As described above, the interaction between the incident electron beam and the sample leads to X-ray generation. These characteristic X-rays emitted from the sample carry specific information about local element composition, which can be used as a powerful microanalytical tool combining SEM and EDX spectrometers. Therefore, X-Ray microanalysis enables qualitative and quantitative element analysis from either a point or area of interest of the sample as well as the mapping of the distribution of various elements, simultaneously with SE and BSE imaging.[41]

EDX analysis, however, has some limitations. Light elements ($Z < 11$) cannot be routinely analysed by EDX: For instance, Hydrogen and Helium ($Z = 1, 2$ respectively) do not have characteristic X-rays. Lithium ($Z = 3$) to Neon ($Z = 10$) have characteristic X-rays but they are too low in energy to

be detected by an EDX detector. Nevertheless, EDX analysis is a very useful and reliable analytical technique for heavier elements.[43]

EDX analysis was conducted using an Inca Energy 250 System within the SEM chamber in order to determine elemental analysis. (This elemental analysis could not be performed for light elements such as H or Li, but it was used in this work for Al determination, for example).

2.2.4.2. Transmission Electron Microscopy (TEM)

A transmission electron microscope, similar to the scanning electron microscope uses a high-energy electron beam to create a high magnification image of the sample.[44] The basic instrumentation of the TEM is very similar to SEM instrumentation: an electron gun, series of lenses and the detector. The main difference between SEM and TEM is that in TEM the beam of electrons uses transmitted electrons instead of scattered electrons (SEM), to form an image.

There are different modes of contrast formation including, bright field imaging and electron diffraction.[45] Bright field images, which are the standard type for TEM imaging, are obtained when the objective aperture is centred on the transmitted (non-diffracted) electron beam. The contrast obtained in these images is generated from the electron beam - sample interaction. The brighter the area in the image the less interaction the electron beam had with the sample. Therefore, preparation of thin samples is crucial in TEM imaging, in order to have a homogeneous sample thickness, and also to allow sufficient transmission of electrons through the sample.

TEM characterisation was used in this work to acquire higher resolution images than the ones obtained from SEM. TEM images were used to obtain further information about the topography and morphology of the sample.

The transmission electron microscope used in this work was a FEI Techni T20 TEM (Figure 2-22), using an electron gun with a LaB6 filament at 200 kV. The images were recorded with using a SIS Megaview III CCD camera. EELS mapping was acquired by a Gatan Image Filter EELS spectrometer. Operation of the TEM was conducted by Mr. Colin How, from the Physics Department.

Figure 2-22. Transmission electron microscope column.

2.2.4.2.1. EELS spectroscopy

Electron energy loss spectroscopy (EELS) is a complimentary technique to transmission electron microscopy. EELS consists of analyzing the energy distribution of the electron beam generated in the transmission electron microscope after interaction with the sample.[46] As described in the SEM section, when the electron beam interacts with the sample, different radiation is produced from that interaction. EELS spectrometers attached in the TEM column, detect the difference in energy (energy loss) in the electrons scattered inelastically after interaction with the sample. This energy loss can be assigned to characteristic element atoms; hence assignment of the atoms present in the sample can be performed. Like EDX spectroscopy, EELS spectroscopy enables qualitatively and quantitatively elemental analysis from a point or area of interest of the sample as well as mapping of distribution of various elements (EELS mapping).[47]

2.2.5. Thermal Analysis

Thermal analytical techniques measure the change of a specific property of a material as a function of temperature. This allows access to important information (including thermodynamics and kinetics) about the decomposition or dehydrogenation pathway of the selected materials to study.[48]

There are numerous techniques available: the primary differences in the techniques are the properties of the material being studied. Three thermal analysis techniques have been used for the characterization of the samples in this work: thermogravimetric analysis (TGA), differential thermal analysis (DTA) and evolved gas analysis (EGA), the latter using a Mass Spectrometer (MS) (in *italics* in Table 2-1)

Table 2-1. Common Thermal Analysis Methods and the properties measured. Modified from reference [49].

Method	Abbreviation	Property Measured
Differential Thermal Analysis	DTA	Temperature difference
Differential Scanning Calorimetry	DSC	Enthalpy
Thermogravimetric Analysis	TGA	Mass difference
Dynamic Mechanical Analysis	DMA	Deformation
Dielectric Thermal Analysis	DEA	Deformation
Evolved gas analysis	EGA	Gaseous decomposition
Thermo-optical analysis	TOA	Optical properties

2.2.5.1. Simultaneous Thermal Analysis (STA)

Simultaneous Thermal Analysis (STA) generally refers to the simultaneous application of thermogravimetry analysis (TGA) and differential thermal analysis (DTA) to the same sample in a single instrument. The experiment conditions are exactly identical for the TGA and DTA signals (same atmosphere, gas flow rate, vapour pressure of the sample, heating rate, thermal contact to the sample crucible and sensor, radiation effect, etc.). The information gathered was enhanced by coupling the STA instrument to an Evolved Gas Analyzer (EGA), specifically a mass spectrometer (MS). TGA is an experimental method where changes in mass are used to detect and measure the

chemical or physical processes that occur upon heating a sample.[50] DTA measures the difference in temperature between the sample and a reference as the furnace heats (or cools). The temperatures of both the sample and reference material increase, or decrease, uniformly until the sample reaches a point that it undergoes a phase change or chemical reaction, which is either endothermic or exothermic and the difference in temperature is recorded.[15] These combined techniques allow determination of chemical reactions or phase changes and identification of evolved products throughout the heating programme. This allows one to establish the decomposition and reaction mechanisms of the systems studied.

STA is performed by heating two crucibles under the same conditions, sitting on high sensitive thermocouples, which will keep track of temperature differences and weight differences. One of the crucibles is the reference crucible (empty crucible) and the other the sample crucible (Figure 2-23).

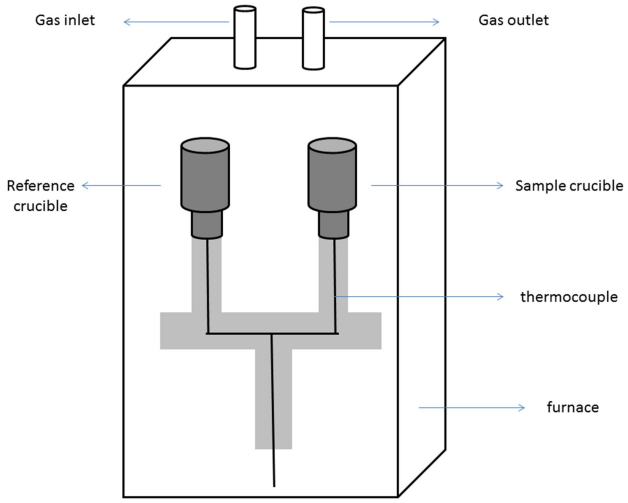

Figure 2-23. Schematic representation of the crucible system used in the furnace of the STA. Modified from reference [50].

The crucibles used for STA analysis were alumina pans (Al_2O_3) resistant to high temperatures and chemical erosion. The crucibles were cleaned and reused for future analysis. After every run the crucibles were properly cleaned with water, and then placed in an *aqua regia* (mixture of HNO_3 : HCl – 1 : 3 in volume)[51] bath overnight. After this the pans were calcined at 1200 °C for over 6 hours.

2.2.5.2. Mass Spectrometry

Mass spectrometry is a widely applicable analytical complementary tool to STA. Neither TGA nor DTA can identify the gaseous species that might evolve from thermal treatment of samples. However, a mass spectrometer directly attached to STA will be able to characterise the gaseous species released during thermal treatment, in order to understand fully any process that might have occurred.

All mass spectrometers consist of these basic components,[52] as can also be seen in Figure 2-24:

- Sample inlet: to introduce the compound that is to be analysed into the mass spectrometer.
- Ion source: Produces the ions from the sample to be analysed, as described in Figure 2-25.
- Mass analyser: Separates the various ions formed according to their m/z ratio, through the use of an electric field and/or magnetic field.
- Ion detector: "Counts" the ions emerging from the analyser and measures their abundance and converts those ions into electrical signals that can be processed.
- Signal Processor: Process the signals from the detector that are transmitted to the computer, where a mass spectrum will be plotted.

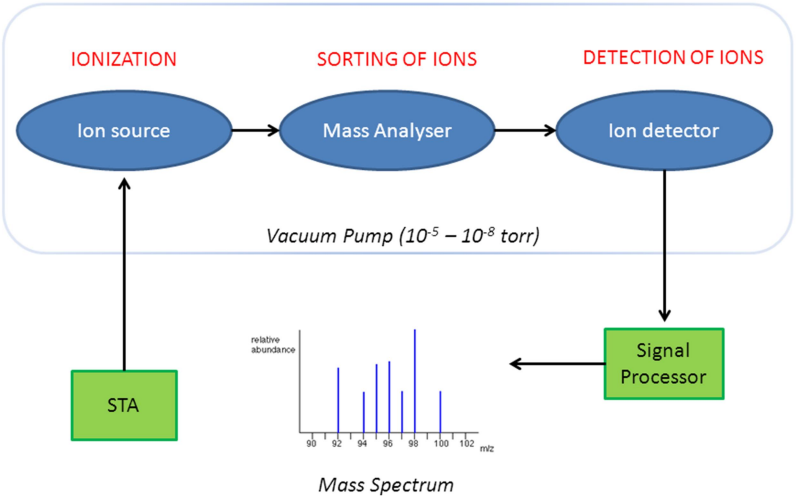

Figure 2-24. Schematic representation of the components of a Mass Spectrometer. Modified from reference [52].

To prevent the collision of ions with residual gas molecules during their way from the ion source to the detector, mass spectrometers are operated under high vacuum. These collisions are

possible because the ions are formed with excess energy. To avoid this, the vacuum in the ion source should be employed to minimize the levels of contaminants and atmospheric gases such as oxygen.

Table 2-2 summarises the most common ionization sources, analysers and detectors used in mass spectrometry. The ones in italics are the ones used in this work and will be described below.

Table 2-2. Summary of the most common techniques and parts used as ionization sources, analyzers and detectors in mass spectrometry.

Ionization sources	Analysers	Detectors
Chemical Ionisation (CI)	*Quadrupole*	*Electron Multiplier*
Electron Impact (EI)	Time-of-Flight (TOF)	*Faraday Cup*
Electrospray Ionization (ESI)	Magnetic Sectors	
Fast Atom Bombardment (FAB)		
Field Desorption/Ionisation (FD/FI)		
Matrix Assisted Laser Desorption Ionisation (MALDI)		

2.2.5.2.1. Ion source

The first step in the mass spectrometric analysis of compounds is the production of gas-phase ions of the compound, which can be performed via different ionization methods (Table 2-2).

The molecule to analyse is ionised by losing an electron, forming a molecular positive ion which normally undergoes fragmentations. Since it is a radical ion with an odd number of electrons, fragmentation can occur to give either a radical and an ion with an even number of electrons, or a molecule and a new radical ion (Figure 2-25b).

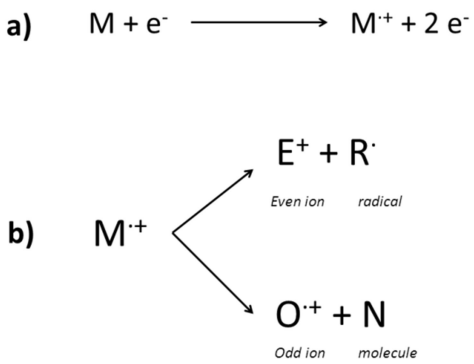

Figure 2-25. a) Mechanism of ion pair formation by electron ionization b) Fragmentation path of ion pair molecule, leading to formation of even ion or odd ion molecule.[15]

2.2.5.2.2. Quadrupole mass Analyser

These ions are then separated in the mass analyser, which in this work is a quadrupole mass analyser (Figure 2-26). The quadrupole analyser is a device which uses the stability of the trajectories in oscillating electric fields to separate ions according to their *m/z* ratios.

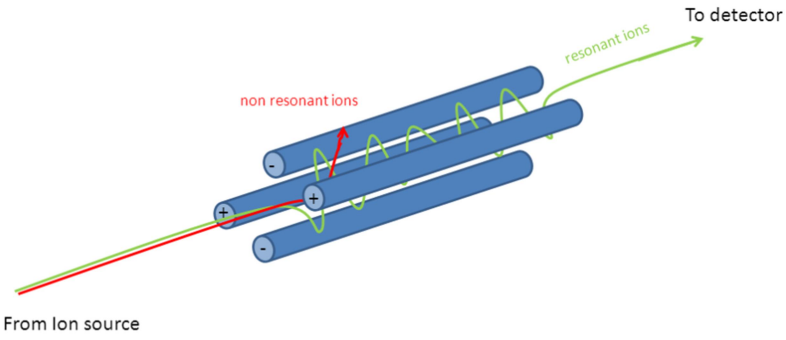

Figure 2-26. Schematic representation of a quadrupole mass analyser illustrating that only the resonant ions will travel to the detector. Non resonant ions will collide with the analyser rods and discharge. Modified from reference [53].

Ions coming from the ion source and traveling between the rods of the quadrupole are subjected to the influence of an electric field. A positive ion entering the space between the rods will be electrostatically attracted towards the negative rod. If the potential changes before it discharges itself on this rod, the ion will change direction. Only ions of a certain *m/z* ratio will reach the

detector (resonant ions) for a given ratio of voltages: other ions have unstable trajectories and will collide with the rods, discharging themselves (non resonant ions). This allows selection of an ion with a particular *m/z* or allows the operator to scan for a range of *m/z* values by continuously varying the applied voltage.

2.2.5.2.3. Detectors

The ions that pass through the mass analyser are then detected and transformed into a usable signal by a detector. Detectors are able to generate an electric current from the incident ions that is proportional to their abundance. Because the number of ions leaving the mass analyser is generally quite small, amplification is obtain necessary to obtain usable signal.

In the mass spectrometer used for this work, two types of detectors can be selected: Faraday cup and secondary electron multiplier (SEM – not to be confused with *scanning electron microscope*). A faraday cup is made of metal cup or a cylinder with a small orifice (Figure 2-27). Ions reach the inside of the cup and are neutralized by accepting electrons as they hit the walls. This leads to a current through the resistor. The discharge current is then amplified and detected.

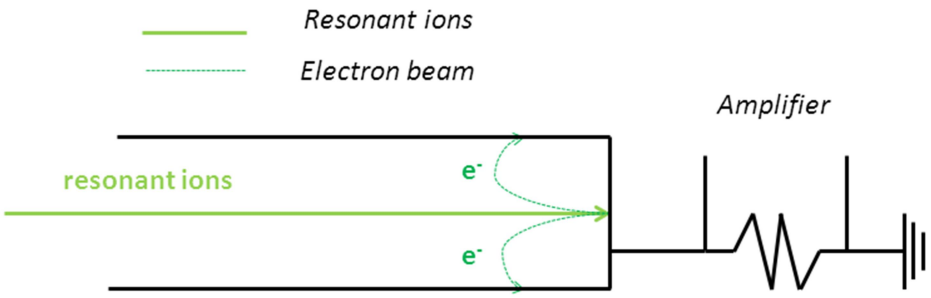

Figure 2-27. Schematic representation of a faraday cup detector. Modified from reference [52].

This detector has a cup-like shape to recapture secondary electrons that are created upon ion impact of the positive ions. The charge associated with an electron leaving the wall of the detector is identical to the arrival of a positive ion. These secondary electrons that are emitted when an ion strikes the wall are an important source of errors, and should be minimised to improve accuracy of this detector. The shape of the cup and a carbon coat in the walls of the detector are features that minimise this effect.

The other detector used in this instrument is the secondary electron multiplier (Figure 2-28), the most common detector used in Mass Spectrometry. This detector consists of several dynodes, which are electrodes that serve as an electron multiplier through secondary emission. The first dynode is a conversion dynode, at high potential, whose polarity is opposed to the charge of the resonant ions coming from the mass analyser.

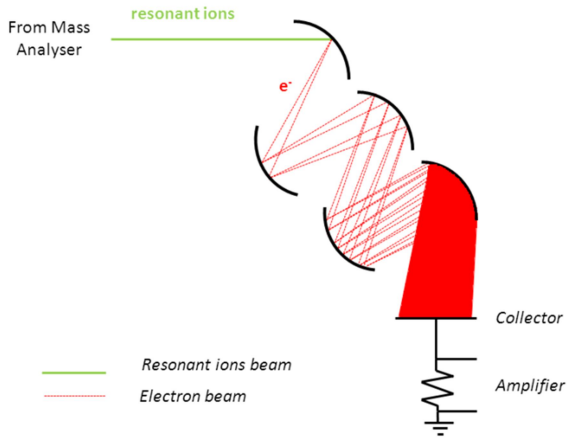

Figure 2-28. Schematic representation of a secondary electron multiplier detector. Modified from reference [52].

When the ions strike on this conversion dynode, several secondary electrons are emitted. These electrons are then accelerated to the next dynode because it is held at a lower potential. This process continues as the secondary electrons travel towards the ground potential. Therefore a cascade of electrons is created and the final flow of electrons provides an electric current at the end of the electron multiplier that is then increased by an amplifier.

In general, a secondary electron multiplier detector has higher sensitivity and higher signal-to-noise ratio (which means that the detection limit can be lowered by several orders of magnitude) than a Faraday cup detector. In the mass spectrometer used in this work there are two modes of detecting the evolved gasses:

- Full mass scan: a range *m/z* ratio is selected, and the instrument will track any gas molecule that belongs within these range (*e.g m/z* = 0 - 200 amu). The secondary electron multiplier detector is used for this full scan mode, since higher sensitivity is required. This mode is very useful in the case there is uncertainty about which gaseous products will be evolved.

- Individual mass scan: specific *m/z* ratios corresponding to the interest gaseous products evolved are selected to be tracked (*e.g* to track water and argon: *m/z* = 18 and 40 amu).

2.2.5.2.4. Instrumentation

STA analyses were performed in a Netzsch STA 409 analyser, located permanently in a glove box filled with argon atmosphere (Figure 2-29). The information gathered was enhanced by coupling the STA instrument to a Hiden Analytical HPR20 mass spectrometer.

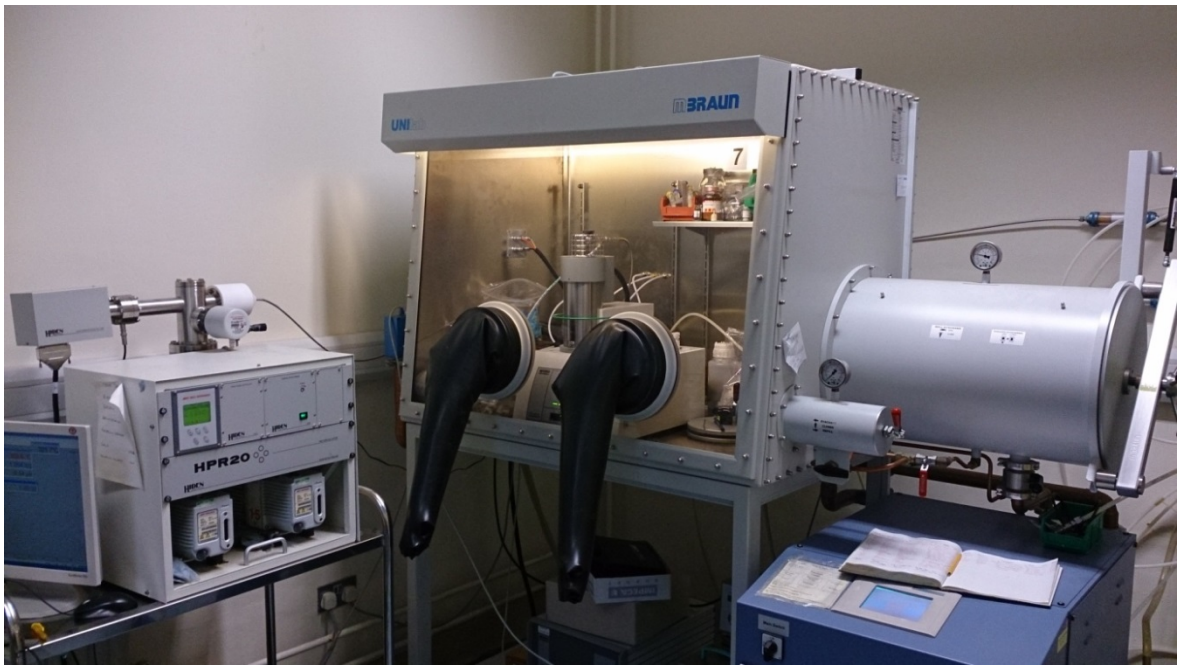

Figure 2-29. STA analyser, placed in a argon-filled glove box, coupled to a MS analyser.

Before running any sample on the STA system, a trial experiment was performed using the same conditions in a furnace in the laboratory (sample amount, atmosphere, heating ramp and target temperature). The purpose of this trial experiment is to ensure that the decomposition, dehydrogenation or any other thermal event that might occur could be safely handled inside the STA chamber (for example, in order to avoid any overpressure of the gases evolved or explosive decomposition that might damage the STA apparatus). The mass of sample used for the STA was usually between 20-30 mg, depending on the amount of sample available for the analysis. The

appropriate data obtained from the thermal analysis run was treated with the Netsch Proteus Software.

Calibration of the STA apparatus is needed prior to sample analysis. (Calibration of the STA was done in the Gregory Lab every 2 months). The calibration was performed using calibration standards (Barium carbonate, potassium chromate, zinc metal, indium metal, bismuth metal and potassium perchlorate) which covered the total temperature range over which the materials in this work were analysed. 30 mg of each standard was heated thrice to above its melting point. The characteristic peak temperature and onset temperatures for the calibration standards was determined and temperature and sensitivity calibration files were compiled. A calcium oxalate standard was used to verify the calibration files, where the melting point, onset temperatures and mass losses associated with the three thermal events associated with its decomposition were verified with literature values. After verification, the calibration files were used in each measurement.

Once the sensitivity calibration files are compiled and before a sample can be analysed in a STA experiment, a correction file is needed. This involves heating an empty sample pan using the conditions required for the sample being studied. The correction file contains the information about the heating conditions for the sample and also the thermal profile of the sample pan.

2.3. REFERENCES

1. Shriver, D. F.; Drezdzon, A., *The Manipulation of Air-Sensitive Compounds*. Wiley: 1986.
2. Nitrogen - Element information, properties and uses | Periodic Table. http://www.rsc.org/periodic-table/element/7/nitrogen (accessed 04/12/14).
3. Errington, R. J., *Advanced Practical Inorganic and Metalorganic Chemistry*. Taylor & Francis: 1997.
4. Schlenk Flasks - Sigma-Aldrich Glassware Catalog. http://www.sigmaaldrich.com/labware/glassware-catalog/flasks-schlenk.html (accessed 05/12/14).
5. Zhang, T.; Isobe, S.; Wang, Y.; Oka, H.; Hashimoto, N.; Ohnuki, S., A metal-oxide catalyst enhanced the desorption properties in complex metal hydrides. *Journal of Materials Chemistry A* **2014,** *2* (12), 4361-4365.
6. Ashby, E. C.; Schwartz, R. D., A glove box system for the manipulation of air sensitive compounds. *Journal of Chemical Education* **1974,** *51* (1), 65.
7. Zintl, E.; Harder, A.; Dauth, B., Gitterstruktur der Oxide, Sulfide, Selenide und Telluride des Lithiums, Natriums und Kaliums. *Zeitschrift fuer Elektrochemie* **1934,** *40*, 588-593.
8. Armarego, W. L. F.; Chai, C. L. L., *Purification of Laboratory Chemicals*. Butterworth-Heinemann: 2003.
9. Williams, D. B. G.; Lawton, M., Drying of Organic Solvents: Quantitative Evaluation of the Efficiency of Several Desiccants. *The Journal of Organic Chemistry* **2010,** *75* (24), 8351-8354.
10. Balema, V. P.; Pecharsky, V. K.; Dennis, K. W., Solid state phase transformations in LiAlH4 during high-energy ball-milling. *Journal of Alloys and Compounds* **2000,** *313* (1–2), 69-74.
11. Ebbing, D.; Gammon, S. D., *General Chemistry*. Cengage Learning: 2012.
12. Wahab, M. A.; Beltramini, J. N., Catalytic nanoconfinement effect of in-situ synthesized Ni-containing mesoporous carbon scaffold (Ni-MCS) on the hydrogen storage properties of LiAlH4. *International Journal of Hydrogen Energy* **2014,** *39* (32), 18280-18290.
13. Atkins, P.; de Paula, J., *Atkins' Physical Chemistry*. OUP Oxford: 2010.
14. Tipler, P. A.; Mosca, G., *Physics for Scientists and Engineers*. W. H. Freeman: 2004.
15. Skoog, D. A.; Holler, F. J.; Nieman, T. A., *Principles of Instrumental Analysis*. Saunders College Pub.: 1998.
16. Ghosh, S. N., 5 - IR Spectroscopy. In *Handbook of Analytical Techniques in Concrete Science and Technology*, Ramachandran, V. S.; Beaudoin, J. J., Eds. William Andrew Publishing: Norwich, NY, 2001; pp 174-204.

17. Fahrenfort, J., Attenuated total reflection: A new principle for the production of useful infra-red reflection spectra of organic compounds. *Spectrochimica Acta* **1961,** *17* (7), 698-709.
18. Socrates, G., *Infrared and Raman Characteristic Group Frequencies: Tables and Charts*. Wiley: 2004.
19. Raman, C. V., *Indian Journal of Physics* **1928,** *2*, 387-398.
20. Ferraro, J. R.; Nakamoto, K., *Introductory Raman Spectroscopy*. Academic Press: 1994.
21. Nakamoto, K., *Infrared and Raman Spectra of Inorganic and Coordination Compounds, Theory and Applications in Inorganic Chemistry*. Wiley: 2008.
22. Vincent, A., *Molecular Symmetry and Group Theory: A Programmed Introduction to Chemical Applications*. Wiley: 2013.
23. Hollas, J. M.; Chemistry, R. S. o., *Basic Atomic and Molecular Spectroscopy*. Royal Society of Chemistry: 2002.
24. Michael M. Woolfson, M. S. W., *An Introduction to X-ray Crystallography*. Cambridge University Press: 1978.
25. Clegg, W., *Crystal structure analysis : principles and practice*. International Union of Crystallography ; Oxford University Press: [Chester]; Oxford; New York, 2001.
26. Glusker, J. P., *Crystal structure analysis for chemists and biologists*. VCH: New York, 1994.
27. Smart, L.; Moore, E., *Solid state chemistry : an introduction*. CRC Press: Boca Raton, 2005.
28. Bragg, W. H., *Proc. Camb. Phil. Soc* **1913,** *17*, 43.
29. Nielsen, T. K.; Polanski, M.; Zasada, D.; Javadian, P.; Besenbacher, F.; Bystrzycki, J.; Skibsted, J.; Jensen, T. R., Improved Hydrogen Storage Kinetics of Nanoconfined NaAlH4 Catalyzed with TiCl3 Nanoparticles. *ACS Nano* **2011,** *5* (5), 4056-4064.
30. Chatterjee, A. K., 8 - X-Ray Diffraction. In *Handbook of Analytical Techniques in Concrete Science and Technology*, Ramachandran, V. S.; Beaudoin, J. J., Eds. William Andrew Publishing: Norwich, NY, 2001; pp 275-332.
31. Klose, M.; Lindemann, I.; Minella, C. B.; Pinkert, K.; Zier, M.; Giebeler, L.; Nolis, P.; Baró, M. D.; Oswald, S.; Gutfleisch, O.; Ehrenberg, H.; Eckert, J., Unusual oxidation behavior of light metal hydride by tetrahydrofuran solvent molecules confined in ordered mesoporous carbon. *Journal of Materials Research* **2014,** *29*, 55-63.
32. Andreasen, A.; Vegge, T.; Pedersen, A. S., Dehydrogenation kinetics of as-received and ball-milled. *Journal of Solid State Chemistry* **2005,** *178* (12), 3672-3678.
33. Kostka, J.; Lohstroh, W.; Fichtner, M.; Hahn, H., Diborane Release from LiBH4/Silica-Gel Mixtures and the Effect of Additives. *The Journal of Physical Chemistry C* **2007,** *111* (37), 14026-14029.

34. Flick, E. W., *Handbook of Adhesives Raw Materials*. Noyes Publications: 1989.
35. Langmuir, I., The Adsoprtion of gases on plane surfaces of glass, mica and platinum. *Journal of the American Chemical Society* **1918,** *40* (9), 1361-1403.
36. Brunauer, S.; Emmett, P. H.; Teller, E., Adsorption of Gases in Multimolecular Layers. *Journal of the American Chemical Society* **1938,** *60* (2), 309-319.
37. Skalny, J.; Hearn, N., 13 - Surface Area Measurements. In *Handbook of Analytical Techniques in Concrete Science and Technology*, Ramachandran, V. S.; Beaudoin, J. J., Eds. William Andrew Publishing: Norwich, NY, 2001; pp 505-527.
38. Sing, K. S. W.; Everett, D. H.; Haul, R. A. W.; Moscou, L.; Pierotti, R. A.; Rouquerol, J.; Siemieniewska, T., Reporting Physisorption Data for Gas/Solid Systems. In *Handbook of Heterogeneous Catalysis*, Wiley-VCH Verlag GmbH & Co. KGaA: 2008.
39. Sarkar, S. L.; Aimin, X.; Jana, D., 7 - Scanning Electron Microscopy, X-Ray Microanalysis of Concretes. In *Handbook of Analytical Techniques in Concrete Science and Technology*, Ramachandran, V. S.; Beaudoin, J. J., Eds. William Andrew Publishing: Norwich, NY, 2001; pp 231-274.
40. Schatten, H., *Scanning Electron Microscopy for the Life Sciences*. Cambridge University Press: 2012.
41. Reichelt, R., Scanning Electron Microscopy. In *Science of Microscopy*, Hawkes, P.; Spence, J. H., Eds. Springer New York: 2007; pp 133-272.
42. Echlin, P., *Handbook of Sample Preparation for Scanning Electron Microscopy and X-Ray Microanalysis*. Springer: 2011.
43. Plerdsranoy, P.; Utke, R., Confined LiBH4–LiAlH4 in nanopores of activated carbon nanofibers. *International Journal of Hydrogen Energy* **2015,** *40* (22), 7083-7092.
44. Nellist, P., Scanning Transmission Electron Microscopy. In *Science of Microscopy*, Hawkes, P.; Spence, J. H., Eds. Springer New York: 2007; pp 65-132.
45. Williams, D. B.; Carter, C. B., *Transmission Electron Microscopy: A Textbook for Materials Science*. Springer: 2009.
46. Egerton, R., *Electron Energy-Loss Spectroscopy in the Electron Microscope*. Springer US: 2011.
47. Allen, L. J.; D'Alfonso, A. J.; Findlay, S. D.; LeBeau, J. M.; Lugg, N. R.; Stemmer, S., Elemental mapping in scanning transmission electron microscopy. *Journal of Physics: Conference Series* **2010,** *241* (1), 012061.
48. Cheng, S. Z. D.; Li, C. Y.; Calhoun, B. H.; Zhu, L.; Zhou, W. W., Thermal analysis: the next two decades. *Thermochimica Acta* **2000,** *355* (1–2), 59-68.

49. Lever, T.; Haines, P.; Rouquerol, J.; Charsley Edward, L.; Van Eckeren, P.; Burlett Donald, J., ICTAC nomenclature of thermal analysis (IUPAC Recommendations 2014). In *Pure and Applied Chemistry*, 2014; Vol. 86, p 545.

50. Ramachandran, V. S., 4 - Thermal Analysis. In *Handbook of Analytical Techniques in Concrete Science and Technology*, Ramachandran, V. S.; Beaudoin, J. J., Eds. William Andrew Publishing: Norwich, NY, 2001; pp 127-173.

51. Zlotea, C.; Chevalier-Cesar, C.; Leonel, E.; Leroy, E.; Cuevas, F.; Dibandjo, P.; Vix-Guterl, C.; Martens, T.; Latroche, M., Synthesis of small metallic Mg-based nanoparticles confined in porous carbon materials for hydrogen sorption. *Faraday Discussions* **2011,** *151* (0), 117-131.

52. de Hoffmann, E.; Stroobant, V., *Mass Spectrometry: Principles and Applications*. Wiley: 2013; Vol. 7Chapter 2.

53. Benedikt, J.; Hecimovic, A.; Ellerweg, D.; Keudell, A. v., Quadrupole mass spectrometry of reactive plasmas. *Journal of Physics D: Applied Physics* **2012,** *45* (40), 403001.

Chapter 3

3. PREPARATION AND CHARACTERIZATION OF POROUS CARBONS

3.1. INTRODUCTION

Porous, or activated, carbons are a form of carbon with small, low-volume pores that provide the carbon with high surface area available for chemical reactions or adsorption. Porous materials (mainly carbon - and silica-derived materials) have given great contributions to many fields, like adsorption, bioreactors, gas and water purification[1,2,3,4,5,6] among others, owing to their large surface areas. Porous materials have also been widely used in energy conversion and storage applications, shown to contribute improvements in the fields of photosynthesis[7], photocatalytic H_2 production,[8,9] photocatalysis,[10] batteries,[11,12] fuel cells,[13,14] dye sensitized solar cells[15] and, more relevant to the outline of this work: direct H_2 storage on porous materials[16,17] or for use as porous hosts for active H_2 storage materials, e.g. hydrides[18] as alanates.[19]

Due to the exponential growing interest on this type of porous materials and the many fields that can benefit from their properties, a lot of effort has been focused on synthesis of methods which allow the tailoring and tuning of the porous materials characteristics as needed. For instance, intrinsic porous materials properties such as pore-size distribution, structure/ordering of the pores and surface area can be tailored as shown in published literature.[20, 21, 22, 23]

For the purpose of this work, two very different types of porous carbons have been used: first an amorphous high surface area activated carbon with a broad pore-size distribution, named AX-21 (purchased commercially) and second a lower surface area hexagonal structured carbon, labelled FDU-15 (from the original's author name) with a distinctive sharp pore-size distribution. The latter was synthesised by the organic-organic assembly of copolymers formed by blocks of ethylene oxide (EO) and propylene oxide (PO), as EO_x-PO_y-EO_z (where x, y and z are repetitions of the block units), mixed with a resol solution via evaporation induced self-assembly (EISA) synthesis.[23]

In the original paper,[23] four possible family structures were obtained by simply adjusting the molar ratio of phenol : template or the EO : PO blocks in the polymer templates. The family members include two-dimensional hexagonal selected for this work (space group, *p*6*m*), three-dimensional bicontinuous (*Ia*$\bar{3}$*d*), body-centred cubic (*Im*$\bar{3}$*m*), and lamellar mesostructures.

AX-21 was initially selected for this work due its high surface area and high pore volume available for hosting hydrogen storage materials. However, AX-21 has a broad pore-size distribution, offering many different sizes of pores. Due to this, FDU-15 seemed like a good carbon choice to

offer sharp contrast to the structure of AX-21. FDU-15 is an ordered hexagonal carbon with a sharp pore-size distribution and close to homogenous pore size. Therefore, a comparative study would potentially allow an evaluation of which pore size contributes the most to any effects observed. The ordered nature of FDU-15 would also facilitate clarity in characterization techniques such, as electron microscopy.

In order to achieve a broad knowledge of the characteristics of both carbons prior to confinement experiments, it was important to assess the advantages and disadvantages of each host. This chapter details the synthesis of FDU-15 and the characterization of both FDU-15 and AX-21.

In the context of physisorption the pores of any porous substance can also be classified according to their sizes (according to the International Union of Pure and Applied Chemistry, IUPAC[24]):

- Macropores: pores with widths exceeding 50 nm.
- Mesopores: pores of widths between 2 nm and 50 nm.
- Micropores: pores with widths not exceeding about 2 nm.

The pores of the carbon materials used in this work should fall within the mesoporous and microporous classifications.

3.2. EXPERIMENTAL

3.2.1. FDU -15 preparation

Porous carbon was prepared in this work by synthesis of phenolic resins as precursors. Mixing these phenolic resins with triblock copolymers, which act as soft templates, leads to porous carbon of tuneable structures, surface areas, pore volumes and pore sizes.[23]

3.2.1.1. Synthesis of phenolic resins

The synthesis of low molecular phenolic resins were prepared by mixing phenol (purified by redistillation, ≥ 99 %, Sigma Aldrich) and formaldehyde solution (37 wt.% in H_2O containing 10 - 15 % methanol as stabilizer, Sigma Aldrich) in a base-catalysed process (NaOH 20 wt.% aqueous solution). The overall reaction can be seen in Figure 3-1. In a typical procedure, 6.1 g of phenol were melted at 40 °C in a flask and mixed with 1.3 g of NaOH (20 wt.% aqueous solution) while stirring. After 10 minutes, 10.5 g of formaldehyde was added dropwise. Then the mixture was brought up to 70 °C and stirred for 1 hour. After this, the pH was adjusted at room temperature with a 0.6 M solution of HCl, until a value of 7 – 7.5 was achieved. All the water present in the mixture, mainly due to the neutralization of the initial NaOH, was removed in the Schlenk line under vacuum below 50 °C. A thick oily product was formed as water was depleted from the mixture, and 40 ml of dry ethanol were added to the final product. The flask was shaken until the resin was totally dissolved in ethanol, and the mixture was left overnight to allow the salt, NaCl, from HCl/NaOH neutralization to sink. The resin was decanted in order to separate the salt from the next step. The molar ratio of starting materials used for the preparation of this phenolic resin was 1 : 2 : 0.1 of phenol : formaldehyde : NaOH. According to the literature, the phenolic resins prepared following this procedure had a weight-average molecule weight smaller than 500 amu, determined by gel permeation chromatography (GPC).[23]

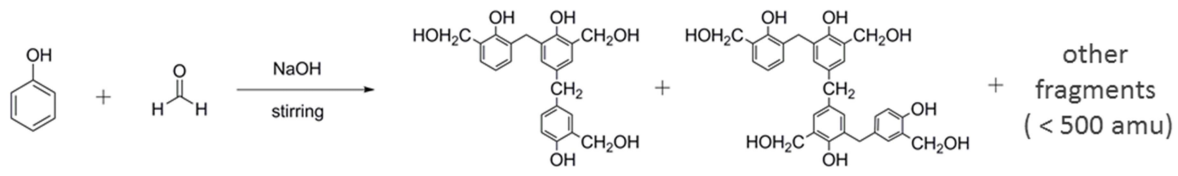

Figure 3-1. Base-catalysed reaction of phenolic resins.

3.2.1.2. Synthesis of FDU-15 mesoporous polymers with a hexagonal structure

Triblock copolymer Pluronic F127 (Mw = 12.600, EO_{106}-PO_{70}-EO_{106}, Sigma Aldrich) was dissolved in 250 ml of ethanol at 40 °C. The phenolic resin was added and properly mixed with the triblock copolymer and placed in a wide tray to allow the ethanol to evaporate for 2 days (Figure 3-2a). It is in this step, while the ethanol is evaporating, that the structure of the material is formed by the EIS method (evaporation-induced self-assembly). The molar ratio to obtain polymers with a hexagonal structure was 1 : 2 : 0.1 : 0.012 of phenol : formaldehyde : NaOH : F127. Varying the molar ratio of phenol precursor : template or the EO : PO segment in the triblock copolymer will vary the level of curvature introduced in the final material, leading to a different type of structure, from the 4 different families reported in the original paper.

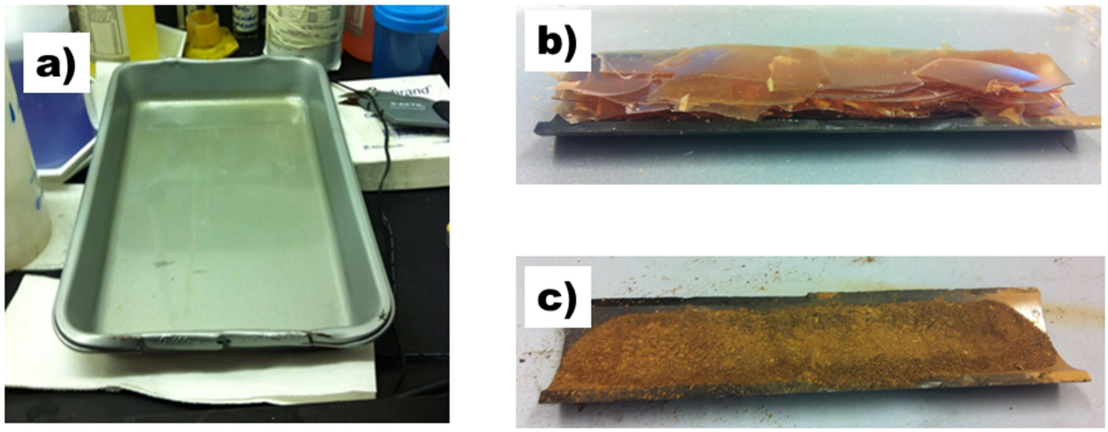

Figure 3-2. Images taken in some of the middle steps of the porous carbon FDU-15 synthesis: a) evaporation of ethanol solution in the tray, where EISA takes place, b) Polymer film obtained after polymerization, and c) Fine powder after mechanical grinding, prior to calcination and carbonization.

3.2.1.3. Synthesis of FDU-15 carbons with hexagonal structure

After 2 days of evaporating the mixture of phenolic resin and copolymer, a thin, transparent, elastic film formed in the tray (Figure 3-2a). The tray was placed into an oven for thermopolymerization at 100 °C for 24 hours. This allows the materials to crosslink to form a more rigid structure. The film obtained after this process is now more rigid and darker in colour than in the previous step (Figure 3-2b). The film was scraped from the tray and crushed into a fine powder using an electrical grinder for 2 minutes (Figure 3-2c). The resulting powder was

calcinated in a tubular furnace with Argon gas (pureshield, BOC) with a flow rate of 105 $cm^3 \cdot min^{-1}$. The temperature programme applied was from room temperature to 350 °C at the rate of 1 °C min^{-1}. The temperature was held at 350 °C for 2 hours to ensure the removal of the triblock copolymer template was complete. The template removal step is followed by a calcination step: the furnace was heated at a rate of 1 °C min^{-1} to 600 °C before increasing the heating rate was increased to 5 °C min^{-1}. The temperature was increased to 800 °C and held for 2 hours.

Figure 3-3 shows a summary of the preparation and the state of the carbon in each step of the preparation.

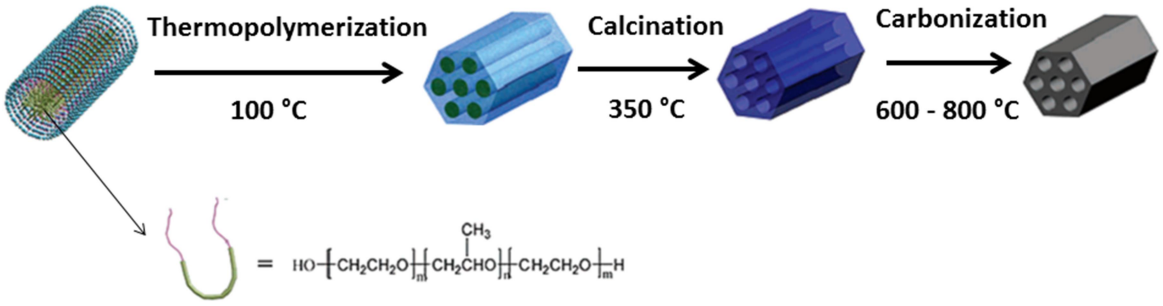

Figure 3-3. Graphic representation of the carbon preparation, showing every step involved in the synthesis.

3.2.2. Activated carbon, AX-21

The superactivated carbon AX-21 was obtained from Anderson Development Company. The high surface area activated carbon AX-21 was manufactured by an alkali activation process, patented by Standard Oil Company.[25] This process consists in activating the petroleum coke with molten KOH, and a washing step to remove any KOH still present.

3.2.3. Instrumentation

Before using either of the porous carbons, each was dried thoroughly *in vacuo* at 500 °C for at least 6 hours, to ensure that the internal volume was fully available and no impurities or previous adsorbed gases were present (such as CO_2, moisture). After the drying step, the carbons were handled as air-sensitive materials, due to their hygroscopic nature.

For TEM and SEM analysis a small amount of the carbons was sprinkled over the TEM/SEM sample holder. Standard TEM sample preparation, consisting of dispersing the material to be examined with a highly volatile solvent (such as ethanol) in order to achieve a good dispersion, was not followed in this work due to the reactivity of some of the materials to be confined in such solvents. In order to obtain carbon TEM images comparable with the material@carbon TEM images, the same sample preparation was therefore followed for all samples. For SEM images analysis, the software ImageJ[26] was used to measure the particle size and plot a particle size distribution after measuring few hundreds of particles. Powder Xray diffraction (XRD) was performed on a Bruker D8 Advance diffractometer X-ray diffraction (XRD) system with Cu Kα radiation source (λ = 1.54Å) and collected over a 2ϑ range of 5-85 ° for phase analysis. The step size and scan speed use was 0.0167 ° at 1.57 ° min^{-1}. Nitrogen adsorption isotherms were measured at 77 K, for surface area, pore size distribution, and pore volume analysis. The Brunauer-Emmett-Teller (BET) method was used to calculate the specific surface areas. The total pore volume was estimated from the adsorbed amount at a relative pressure P/P_0 of 0.98 based on the Barrett-Joyner-Halenda (BJH) calculation model.[27]

3.3. RESULTS AND DISCUSSION

3.3.1. FDU-15

The transmission electron microscopy (TEM) images of FDU-15 (Figure 3-4a) show an overlapping layer of columns, which evidences the highly ordered structure. This result is consistent with an hexagonal arranged structure, from previous SAXS characterization.[23] In this published work resolved peaks could be assigned to planes of a highly ordered 2-D hexagonal structure (*p6m*).[28]

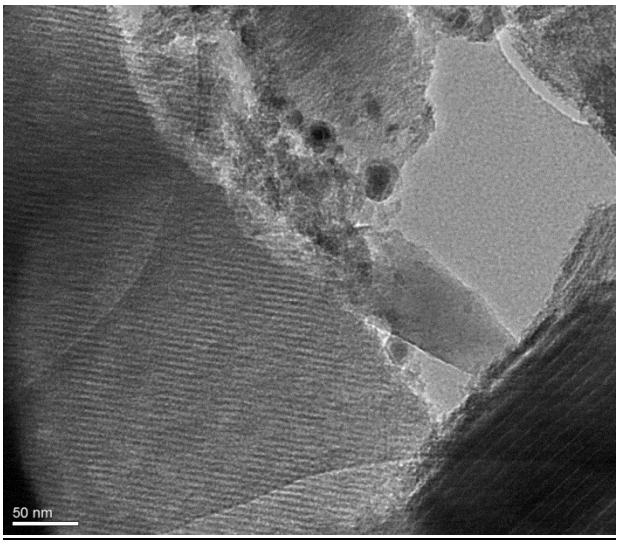

Figure 3-4. TEM image at 240.000x magnification showing a regular array of columns.

Figure 3-5a depicts the N_2 sorption isotherms for FDU-15, showing a classic example of isotherm type-IV, with the presence of a hysteresis loop associated with capillary condensation taking place in mesopores.[24] The hysteresis loop has the shape of a type-H2, typical of materials, such as inorganic oxide gels and porous glasses with a distribution of pore size and pore shape that are not well-defined. However, the pore-size distribution plot presented in Figure 3-5b, shows a narrow pore-size distribution, with a peak maximum at 3.69 nm and no important contribution from pores greater in diameter than 4 nm. This distribution is not consistent with a type-H2 hysteresis loop, and would be more representative of materials which present adsorption with a hysteresis loop type-H1. Type-H1 hysteresis loops are typical from porous materials forming agglomerates or compacts of certain blocks arranged in a regular array and do present a narrow distribution of pore size. Therefore, it can be concluded that the hysteresis loop observed in Figure 3-5a, has a typical type H2 shape but the long range order structure in the porous material gives the material a narrow pore-size distribution, common from hysteresis loops type H1.

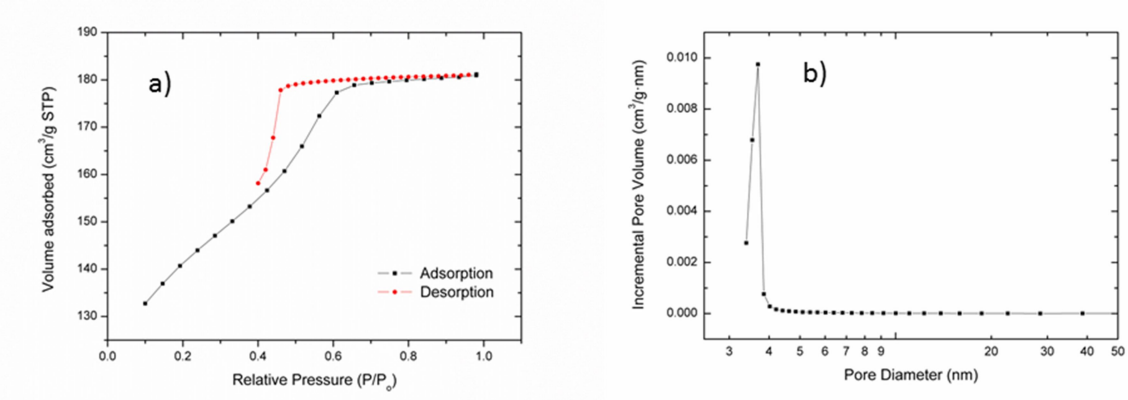

Figure 3-5. Output gas adsorption data for FDU-15: a) Nitrogen adsorption-desorption showing the volume adsorbed with the relative pressure and b) Pore-size distribution showing incremental volume in relation with pore diameter.

SEM images in Figure 3-6a shows the particle morphology and particle size of the porous carbon FDU-15. No evidence of long range ordered features could be observed in the particles, due to instrument limitations (in contrast with the TEM images). However, the particle size distribution (Figure 3-6b) shows that the size of the carbon particles is quite disperse, ranging from 10 to 115 µm across. By plotting the cumulative frequency, it has been found that 80 % of the particle sizes can be found between 10 and 55 µm across, with the maximum relative frequencies between 30 - 35 µm across. The heterogeneity of the particles size could be modified by the grinding time and grinding method to which the precursors were exposed, prior to the thermal treatment. This parameter has been optimized by the authors, to ensure obtaining a reasonable yield of the final product after carbonization and calcination steps.

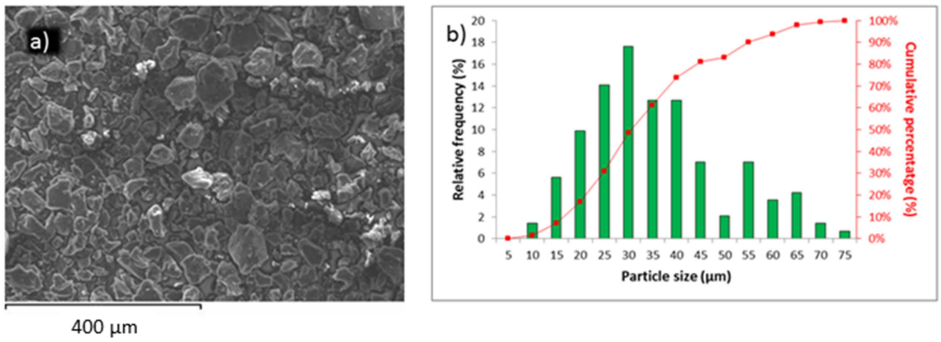

Figure 3-6. a) SEM image of the porous carbon FDU-15 and b) Histogram of particle size distribution (µm) with relative frequency (%) and accumulative percentage. Further supplementary data available.[29] (Values and further SEM images in Appendix Section 7.1)

Figure 3-7 shows an XRD pattern of the FDU-15 sample, which is consistent with that of the Supporting Information from the author's original paper.[23] The diffraction pattern exhibits broad peaks and an absence of any Bragg reflections. This reveals the amorphous nature of material. However, there is obviously some short range ordering in the carbon, as seen in the TEM image.

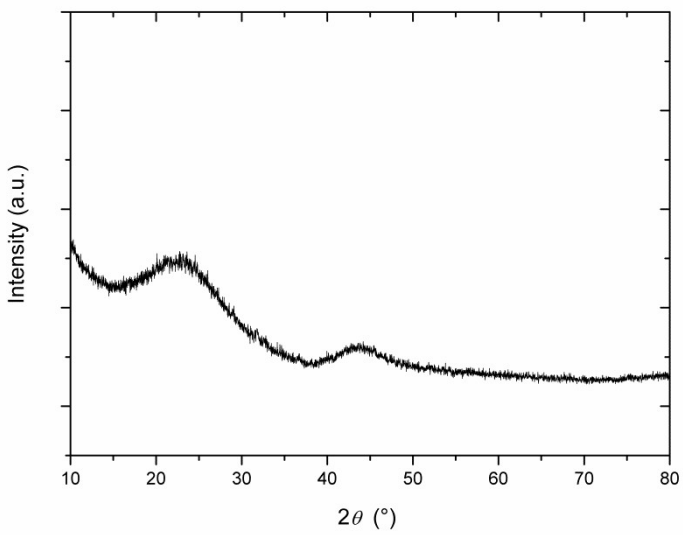

Figure 3-7. Diffraction data obtained from FDU-15 porous carbon.

The broad peaks located at approximately 23° and 44° indicate the existence of carbon planes, similar to those of graphite (reflections of graphite: (002) = 23° and (100) = 45 °).[30]

3.3.2. AX-21

TEM images of AX-21 (Figure 3-8) show the morphology of the AX-21 particles and describes disordered and aggregated particles of carbon. No evidence of long range order could be observed, showing the amorphous character of this carbon, which contrasts with the hexagonal ordered structure from FDU-15 (Figure 3-4a).

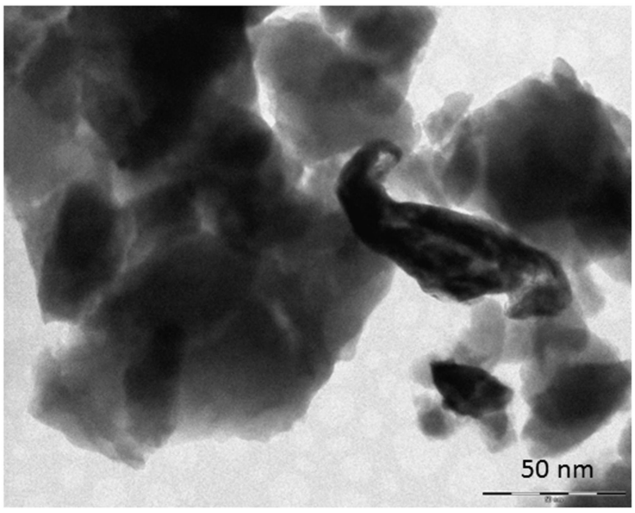

Figure 3-8. TEM image at 240.000x magnification of AX-21 porous carbon.

The N_2 isotherm adsorption-desorption isotherm at 77 K for AX-21 is shown in Figure 3-9a, which has a mixed type in the IUPAC classification:[24] 1) the shape of a typical type –I isotherm, with high uptake at lower pressures, typical for solids that demonstrate microporous adsorption and 2) the typical shape of a type –IV isotherm, showing an open knee, no clear plateau and a clearly defined slope at intermediate and high relative pressures.

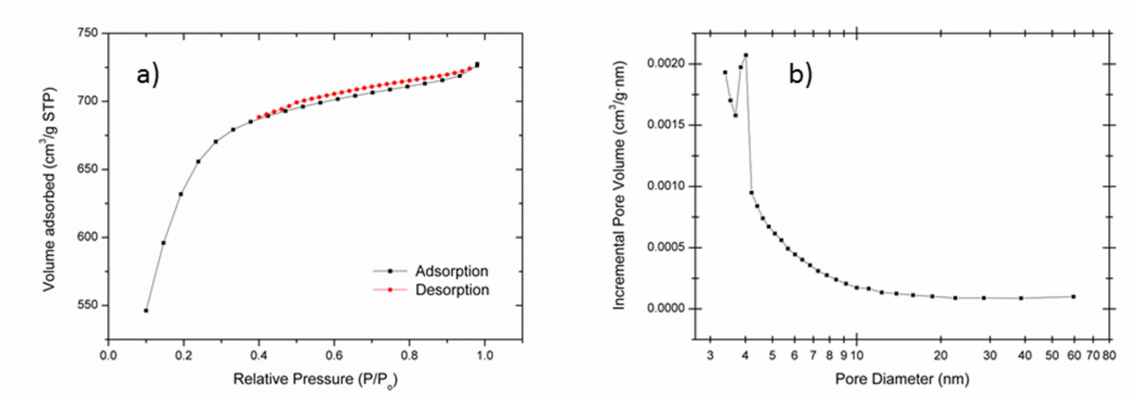

Figure 3-9. a) Nitrogen adsorption-desorption showing the volume adsorbed with the relative pressure and b) Pore-size distribution showing incremental pore volume against pore diameter.

Additionally, a desorption hysteresis loop due to adsorbate condensation in the mesopores is apparent. All these facts reflect the transition from microporosity to mesoporosity, giving evidence that several types of pores are present in AX-21, which is in good agreement with the broad pore size distribution (Figure 3-9b). A pore diameter peak maximum can be observed at 4.03 nm, although the contribution of smaller and bigger diameter pores should not be neglected in this case. The data obtained from the instrument used in this work, did not allow detection of pores having smaller sizes than 3.38 nm. However, other research groups have characterized this activated carbon with instruments able to detect lower pore sizes,[31] and it has been reported that a large numbers of pores are present in the range of 1 – 2 nm which would be consistent with the N_2 isotherm adsorption-desorption obtained in this work. All these facts evidence the presence of different types of pores; micropores, mesopores and macropores, the latter being the least significant.

SEM images show (Figure 3-10a) the particle morphology and particle size of the porous carbon AX-21. The particle size distribution (Figure 3-10b) shows that the size of the carbon particles is disperse, but not as much as it was in FDU-15 (Figure 3-6b). Particles range from 2 - 36 µm across. By plotting the cumulative frequency, it has been found that 80 % of the particle sizes can be found between 2 - 16 µm across with maximum relative frequencies between 5 - 6 µm across.

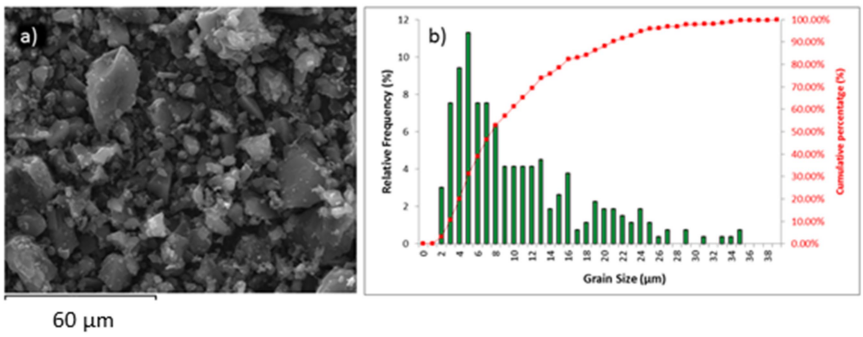

Figure 3-10. a) SEM image of the porous carbon AX-21 and b) Histogram of particle size distribution (µm) with relative frequency (%) and cumulative percentage. Further supplementary data available.[29] (Values and further SEM images in Appendix Section 7.1)

X-ray diffraction profiles shown in Figure 3-11, exhibit a broad reflection (centred at 27°), corresponding to the carbon (002) reflection that is typical of graphitic carbon materials with a low degree of graphilization.[32] This, combined with the absence of any clear Bragg reflections,

reveals a predominantly amorphous structure and supports evidence that AX-21 has a more amorphous character than the other porous carbon used in this work, FDU-15.

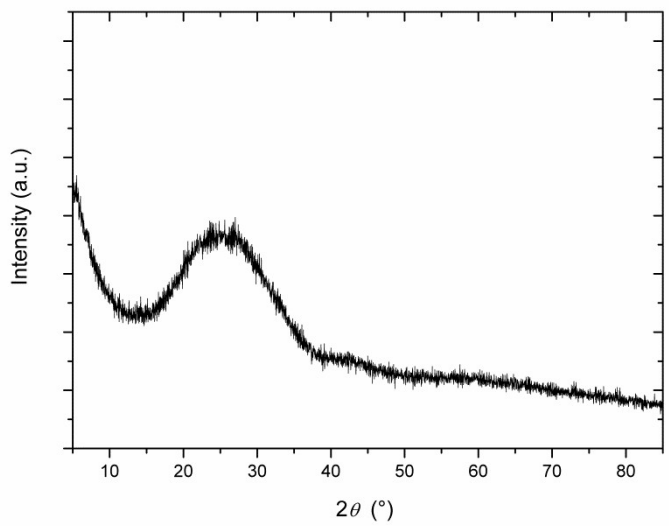

Figure 3-11. Diffraction data obtained from AX-21 porous carbon.

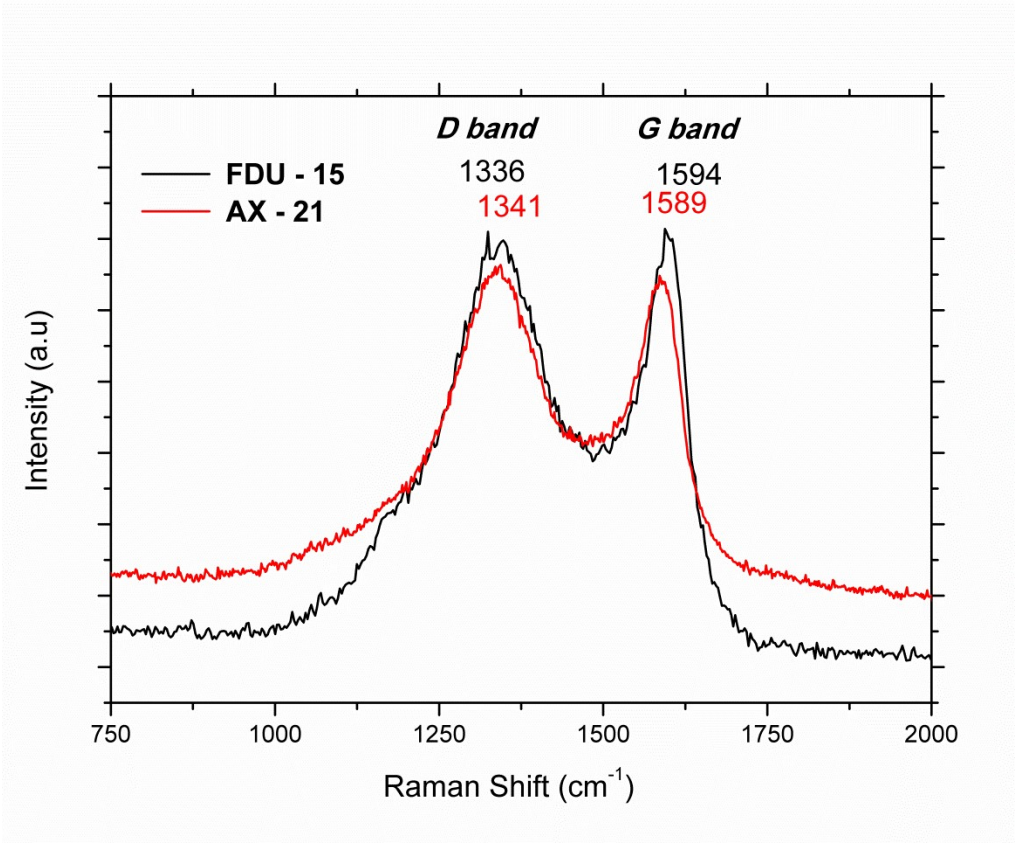

Figure 3-12. Raman spectra of the porous carbons presented in this chapter, showing the presence of D and G bands.

Raman spectra of the both AX-21 and FDU-15 porous carbons are shown in Figure 3-12, presenting D bands centred at 1336 and 1341 cm^{-1} and G bands centred at 1591 and 1589 cm^{-1}, for FDU-15 and AX-21 respectively. The G band is a characteristic feature of graphitic layers, while the D band corresponds to disordered carbon or defective graphitic structures. Raman spectroscopy is sensitive to structural variations in carbon materials. Relative ratios of the G band to the D band (I_G/I_D) illustrate the degree of graphitization.[11] For instance, a low I_G/I_D band intensity ratio indicates the generation of large amounts of defects.[33] For both carbons the values I_G/I_D were almost constant ($I_G/I_D \sim 1$) suggesting that both local carbon structures contained both graphitic and disordered carbon atoms.[34,35]

Table 3-1 show the most relevant properties characterized in this chapter of both carbons for summary and comparison purposes.

Table 3-1. Summary of the results from FDU-15 and AX-21.

	BET surface area / $m^2 \cdot g^{-1}$	**Total pore Volume / $cm^3 \cdot g^{-1}$**	**Particle size distribution / µm**	**Pore size distribution / nm**
FDU - 15	500.7	0.32	*80 % population:* 10 - 55 *Max frequency:* 30 - 35	Max. peak at 3.69 Negligible contribution above 4 nm pores
AX - 21	2162.7	1.18	*80 % population:* 2 – 16 *Max frequency:* 5 - 6	Max. peak at 4.03 Contribution of micro- and mesopores

3.4. CONCLUSIONS

In this chapter the two porous carbons used for subsequent confinement within this thesis have been fully characterized. An ordered porous carbon has been successfully prepared (FDU-15) following the preparation methods reported in the literature, via evaporation induced self-assembly (EISA) mechanism. All the characterisation carried out in this work is in good agreement with the results published by the original authors.[23] TEM analysis along with BET adsorption isotherms confirm the structure as nanoporous (sharp pore-size distribution, containing micro- and mesopores) and well ordered. The particle size distribution of FDU-15, calculated by SEM images, is quite heterogeneous, which is probably caused by the grinding conditions that the precursors were exposed to. XRD data and Raman spectra show that even though the materials have some amorphous character, there is some underlying structure, both in the bulk powder and in individual particles. The highly ordered 2-D hexagonal structure with space group *p6m,* is not evident, but there is an apparent layering in the material, as observed by the bright and dark columns in the TEM images.

Activated porous carbon, commercially purchased as AX-21, is the other type of carbon used in this work. The properties of this carbon differ substantially with FDU-15. TEM analysis, along with BET/BJH adsorption isotherms confirm the structure as nanoporous (broad pore-size distribution) and amorphous. In contrast to FDU-15, AX-21 possesses different-sized porous, ranging from micropores to macropores, including mesopores, being the macropores the least signinficant. A schematic representation of the distribution of these pores can be seen in Figure 3-13.

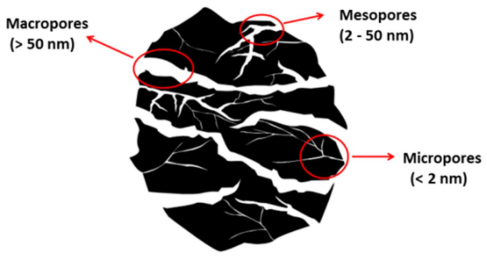

Figure 3-13. Schematic representation of the different size of pores of the activated carbon AX-21. Modified from reference [36].

The particle size of AX-21, calculated by SEM images, seems to be more homogenous than FDU-15. This is probably caused by the grinding method used for the commercially preparation of this carbon.

3.5. REFERENCES

1. S. Baskaran, J. Liu, K. Domansky, N. Kohler, X. Li, C. Coyle, G. E. Fryxell, S. Thevuthasan and R. E. Williford, *Advanced Materials*, 2000, **12**, 291-294.
2. X. He and D. Antonelli, *Angewandte Chemie International Edition*, 2002, **41**, 214-229.
3. J. Zhao, F. Gao, Y. Fu, W. Jin, P. Yang and D. Zhao, *Chemical Communications*, 2002, DOI: 10.1039/B110637F, 752-753.
4. S. Gaspard, N. Passe-Coutrin, A. Durimel, T. Cesaire and V. Jeanne-Rose, in *Biomass for Sustainable Applications: Pollution Remediation and Energy*, The Royal Society of Chemistry, 2014, DOI: 10.1039/9781849737142-00046, pp. 46-105.
5. A. S. Mestre, C. Freire, J. Pires, A. P. Carvalho and M. L. Pinto, *Journal of Materials Chemistry A*, 2014, **2**, 15337-15344.
6. J. Y. Ying, C. P. Mehnert and M. S. Wong, *Angewandte Chemie International Edition*, 1999, **38**, 56-77.
7. K. Hajdu, C. Gergely, M. Martin, L. Zimányi, V. Agarwal, G. Palestino, K. Hernádi, Z. Németh and L. Nagy, *Nanoscale Res Lett*, 2012, **7**, 1-6.
8. J. Zhang, Y. Wang, J. Jin, J. Zhang, Z. Lin, F. Huang and J. Yu, *ACS Applied Materials & Interfaces*, 2013, **5**, 10317-10324.
9. Y. Zhang, J. Liu, G. Wu and W. Chen, *Nanoscale*, 2012, **4**, 5300-5303.
10. F. Dong, M. Ou, Y. Jiang, S. Guo and Z. Wu, *Industrial & Engineering Chemistry Research*, 2014, **53**, 2318-2330.
11. F. Zheng, Y. Yang and Q. Chen, *Nat Commun*, 2014, **5**.
12. L. Fu, K. Tang, K. Song, P. A. van Aken, Y. Yu and J. Maier, *Nanoscale*, 2014, **6**, 1384-1389.
13. M. W. Reed and R. J. Brodd, *Carbon*, 1965, **3**, 241-246.
14. J. H. Bang, K. Han, S. E. Skrabalak, H. Kim and K. S. Suslick, *The Journal of Physical Chemistry C*, 2007, **111**, 10959-10964.
15. Y. Li, Z.-Y. Fu and B.-L. Su, *Advanced Functional Materials*, 2012, **22**, 4634-4667.
16. H. Wang, Q. Gao and J. Hu, *Journal of the American Chemical Society*, 2009, **131**, 7016-7022.
17. M. Sevilla, A. B. Fuertes and R. Mokaya, *International Journal of Hydrogen Energy*, 2011, **36**, 15658-15663.
18. M. Konarova, A. Tanksale, J. Norberto Beltramini and G. Qing Lu, *Nano Energy*, 2013, **2**, 98-104.
19. X. Fan, X. Xiao, J. Shao, L. Zhang, S. Li, H. Ge, Q. Wang and L. Chen, *Nano Energy*, 2013, **2**, 995-1003.

20. F. Alves and I. Nischang, *Chemistry – A European Journal*, 2013, **19**, 17310-17313.
21. L. Borchardt, M. Oschatz and S. Kaskel, *Materials Horizons*, 2014, **1**, 157-168.
22. L.-C. Lin, M. Thirumavalavan, Y.-T. Wang and J.-F. Lee, *Colloids and Surfaces A: Physicochemical and Engineering Aspects*, 2010, **369**, 223-231.
23. Y. Meng, D. Gu, F. Zhang, Y. Shi, L. Cheng, D. Feng, Z. Wu, Z. Chen, Y. Wan, A. Stein and D. Zhao, *Chemistry of Materials*, 2006, **18**, 4447-4464.
24. K. S. W. Sing, D. H. Everett, R. A. W. Haul, L. Moscou, R. A. Pierotti, J. Rouquerol and T. Siemieniewska, in *Handbook of Heterogeneous Catalysis*, Wiley-VCH Verlag GmbH & Co. KGaA, 2008, DOI: 10.1002/9783527610044.hetcat0065.
25. 4082694, 1978.
26. C. A. Schneider, W. S. Rasband and K. W. Eliceiri, *Nat Meth*, 2012, **9**, 671-675.
27. E. P. Barrett, L. G. Joyner and P. P. Halenda, *Journal of the American Chemical Society*, 1951, **73**, 373-380.
28. D. Zhao, J. Feng, Q. Huo, N. Melosh, G. H. Fredrickson, B. F. Chmelka and G. D. Stucky, *Science (New York, N.Y.)*, 1998, **279**, 548-552.
29. M. Segales, Supplementary Deposited Data, 2015 http://dx.doi.org/10.5525/GLA.RESEARCHDATA.240
30. C. Pechyen, D. Atong, D. Aht-Ong and V. Sricharoenchaikul, *Journal of Solid Mechanics and Materials Engineering*, 2007, **1**, 498-507.
31. T. Otowa, R. Tanibata and M. Itoh, *Gas Separation & Purification*, 1993, **7**, 241-245.
32. Z. Wang, X. Xiong, L. Qie and Y. Huang, *Electrochimica Acta*, 2013, **106**, 320-326.
33. A. C. Ferrari and D. M. Basko, *Nat Nano*, 2013, **8**, 235-246.
34. W. Chaikittisilp, M. Hu, H. Wang, H.-S. Huang, T. Fujita, K. C. W. Wu, L.-C. Chen, Y. Yamauchi and K. Ariga, *Chemical Communications*, 2012, **48**, 7259-7261.
35. P. Zhang, F. Sun, Z. Xiang, Z. Shen, J. Yun and D. Cao, *Energy & Environmental Science*, 2014, **7**, 442-450.
36. SUJATA CARBONS PVT. LTD., http://sujatacarbons.com/activated-carbon.html, (accessed 20/03/2015).

Chapter 4

4. NANOCONFINEMENT OF LITHIUM ALUMINIUM HYDRIDE IN POROUS HOSTS

4.1. INTRODUCTION

Complex hydrides containing aluminium (alanates, containing the AlH_4^- anion) have several advantages over other metal hydride systems. Alanates are interesting because of the large amount of hydrogen that can be stored per unit weight of storage material. These potential benefits of alanates are eclipsed by the fact that they cannot be used to store hydrogen at moderate pressure and temperature reversibly.

This present work focuses on the lightest alanate $LiAlH_4$. Lithium aluminium hydride, or lithium alanate was first synthesized in 1947[1] and since then several groups have studied this system, mainly because of the potential application of this material as an on-board hydrogen storage material. The overall theoretical hydrogen content of lithium aluminium hydride is relatively high; 10.6 wt. % hydrogen. It was established that hydrogen was released at 150 °C, but 220 °C was needed to complete the decomposition to LiH and Al. In 1966, Li_3AlH_6 was synthesised for the first time,[2] and this phase was established to be the intermediate phase during the decomposition of $LiAlH_4$. Therefore, including LiH decomposition[3], $LiAlH_4$ decomposition undergoes a three step reaction upon heating. The first two steps lead to Al, LiH and hydrogen at T < 250 °C through the intermediate Li_3AlH_6, according to Eq. 4-1 and Eq. 4-2.[4,5] Decomposition of $LiAlH_4$ is found to be exothermic (ΔH = -10 kJ·mol^{-1} H_2[6]) and the decomposition of Li_3AlH_6 endothermic (ΔH = 25 kJ·mol^{-1} H_2[6]). The third reaction (Eq. 4-3) also releases hydrogen, when LiH and Al react with each other,[7] although the high temperatures and the high enthalpy of dehydrogenation (ΔH = 140 kJ·mol^{-1} H_2[6]) needed for this last reaction are too high to be considered as a hydrogen storage reaction for mobile applications. Only Eq. 4-1 and Eq. 4-2 would be considered.

$$3LiAlH_4 \xrightarrow{150\text{–}175\ ^\circ C} Li_3AlH_6 + 2Al + 3H_2 \qquad 5.3\ \text{wt \% } H_2 \qquad (4\text{-}1)$$

$$Li_3AlH_6 \xrightarrow{180-220\ ^\circ C} 3LiH + Al + \frac{3}{2}H_2 \qquad 2.6\ \text{wt \% } H_2 \qquad (4\text{-}2)$$

$$3LiH + 3Al \xrightarrow{>400\ ^\circ C} 3LiAl + \frac{3}{2}H_2 \qquad 2.6\ \text{wt \% } H_2 \qquad (4\text{-}3)$$

Reactions 1 and 2, are heat-rate dependent and thus the decomposition temperatures can be reduced to 112 and 127 °C respectively using very slow heating rates (0.015 °C/min).[8]

The crystal structure of $LiAlH_4$ was first studied by Sklar, et al. by single crystal X-ray diffraction.[9] Further neutron diffraction studies were also performed on $LiAlH_4$ by Hauback et. al.,[10] showing that $LiAlH_4$ crystallises in a monoclinic cell with space group $P2_1/c$ (a = 4.8254(1), b = 7.8040(1), c = 7.8968(1) Å and β = 112.268(1)° and Z = 4).

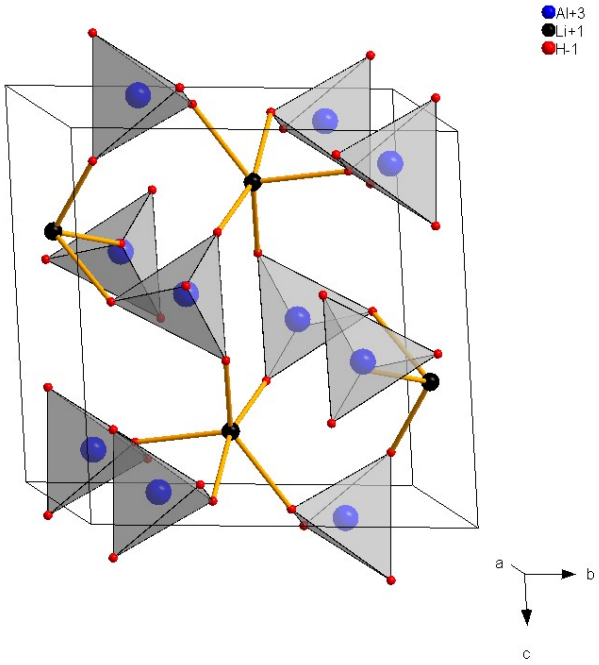

Figure 4-1. Crystal structure of $LiAlH_4$: AlH_4 are linked via Li atoms

The structure consists of isolated AlH_4 tetrahedra connected via Li atoms. The Li atoms are bonded to one hydrogen from each of the five surrounding AlH_4 tetrahedra and adopt trigonal bipyramidal coordination.

Although $LiAlH_4$ seems to be a viable candidate for hydrogen storage applications, poor kinetics and lack of reversibility with respect to hydrogen absorption/desorption represent a noticeable drawback to overcome. Several approaches have been tried in order to reduce the dehydrogenation temperatures of $LiAlH_4$. Adding $TiAl_3$ decreased the temperatures for reactions 1 and 2 by 50 °C and 20 °C respectively,[11] whereas $TiCl_3 \cdot 1/3AlCl_3$ reduced the temperatures by 60 and 25 °C respectively.[12] Jensen et al. reported a facile cycling process of Ti-Doped $LiAlH_4$ in 2009, involving rehydrogenation of the resulting products of reaction 2 (LiH and Al) in an autoclave at room temperature with dimethyl ether and excess hydrogen (100 bar).[13] Dehydrogenation of the $LiAlH_4$ formed (recharged) gave 7 wt. % H_2, almost the same as the as-received $LiAlH_4$.

$TiCl_3$ has not only been used to rehydrogenate $LiAlH_4$, but also to modify the hydrogen desorption properties acting as a catalyst in the work reported by Langmi, et. al.[14] Doping $LiAlH_4$ with low levels of $TiCl_3$ (0.05 – 0.5 mol %) advances its thermal decomposition by 60 – 75 °C, so that dehydrogenation occurs below the melting point of $LiAlH_4$.

Nanoconfinement has also become a strong tool to change physicochemical properties of metal hydrides. By nanosizing and scaffolding materials in porous hosts, control over the kinetics, reversibility and equilibrium pressure of hydrogen storage systems can be gained.[15] Faster kinetics for hydrogen release and hydrogen uptake are achieved by reducing the size of metal hydrides to the nanometer range. Some examples of improvements of the properties of different hydrides by using these approaches are now discussed.

Sodium alanate ($NaAlH_4$) is one of the most studied complex metal hydrides. Similarly to $LiAlH_4$, it decomposes in several hydrogen release steps, via a Na_3AlH_6 intermediate, to NaH, giving 7.4 wt.% hydrogen for full decomposition. Bulk $NaAlH_4$, without a catalyst, starts releasing hydrogen around 180 °C, whereas when this is supported on a surface-oxidized carbon nanofiber support by impregnation techniques, it starts to release hydrogen at 40 °C.[16] Confinement of $NaAlH_4$ in nanoporous carbon (in 2 - 3 mm and 10 - 15 nm diameter pores) by wet impregnation, facilitates hydrogen release at lower temperatures than for the bulk material (considerable hydrogen release at 100 - 120 °C) and rehydrogenation at mild conditions (24 bar H_2 at 160 °C).[17] The $NaAlH_4$ confined in the smallest pores showed the lowest hydrogen release temperatures. Confined material showed a strong difference in thermodynamics, with presence of $NaAlH_4$ instead of Na_3AlH_6 under the rehydrogenation conditions at which Na_3AlH_6 should be formed.

Nielsen et. al, combined two different approaches to lower the hydrogen desorption temperature of $NaAlH_4$, using a catalytic scaffold, which consisted of carbon aerogel doped with $TiCl_3$ nanoparticles,[18] lowering the hydrogen desorption temperature below that of the bulk and catalyst-free confined materials, starting hydrogen release at 33 °C (Figure 4-2).

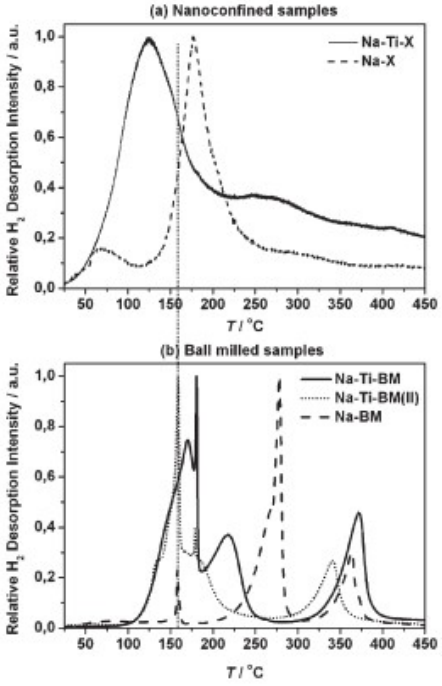

Figure 4-2. Hydrogen TPD-MS profiles measured with a heating rate of 5 C min-1 of a) Nanoconfined samples (Na-X = $NaAlH_4$@C, Na-Ti-X = $NaAlH_4$@C(Ti)) and b) Ball milled samples. Reprinted with the permission of [18]. Copyright 2015 American Chemical Society.

Another interesting group of complex metal hydrides is the alkali metal borohydride, such as $LiBH_4$ which contains 18.5 wt.% hydrogen. However, the high desorption temperature (~500°C), the evolution of toxic diborane (B_2H_6) on decomposition,[19] and inaccessible rehydrogenation conditions of 350 bar of hydrogen and 600 °C limit its practical application as a hydrogen storage material. $LiBH_4$ full pore filling in a porous host can be achieved by melt infiltration, leading to faster kinetics, and lowering the hydrogen desorption temperature by 75 °C.[20] Increased cycling capacity over multiple sorption cycles can also be achieved. $LiBH_4$ can also be deposited using the solution impregnation approach, where the borohydride can be dissolved in ether solutions to be confined, for instance in mesoporous carbon of 4 nm pore diameter. The confined material shows improved desorption kinetics with a hydrogen release of 3.4 wt. % in 90 min at 300 °C.[21] THF was initially tried as solvent but ability of THF to solvate some metal hydrides, forming very stable etherates (present in the XRD pattern - Figure 4-3), made the solvent removal process difficult, since the temperature needed was close to the dehydrogenation temperature. Heavy ethers, such as methyl tert-butil ether (MTBE), were easier to remove from $LiBH_4$ by simply drying at room temperature under vacuum.

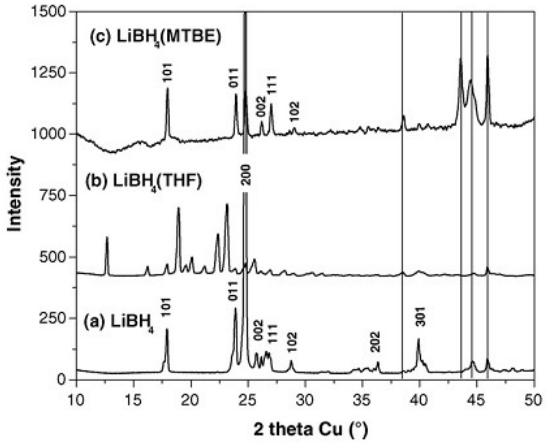

Figure 4-3. Powder X-ray diffraction patterns of a) commercial $LiBH_4$, b) $LiBH_4$ previously dissolved in THF and c) $LiBH_4$ previously dissolved in MTBE. The reflections due to the sample holder (Be) are shown as lines. Reprinted with the permission of [21]. Copyright 2015 Elsevier.

It is difficult to talk about hydrogen storage without mentioning magnesium hydride (MgH_2), the ionic hydride most studied for hydrogen storage applications. Its considerable hydrogen content (7.65 wt. %) makes it a good candidate, but has slow sorption kinetics and high thermodynamics (hydrogen release starting at 650 °C). The lack of solubility of MgH_2 and Mg in regular solvents makes it impossible to apply solution impregnation methods, leaving only in-situ confinement from a precursor (dibutyl magnesium, $MgBu_2$) or melt infiltration, as possible approaches to confine MgH_2 on porous hosts. Confinement of MgH_2 by organometallic precursors in carbon aerogels led to over 5 times faster dehydrogenation kinetics than bulk MgH_2.[22] The complete desorption of MgH_2 was achieved before the onset temperature of bulk MgH_2, when this was confined in mesoporous carbon (Figure 4-4).[23]

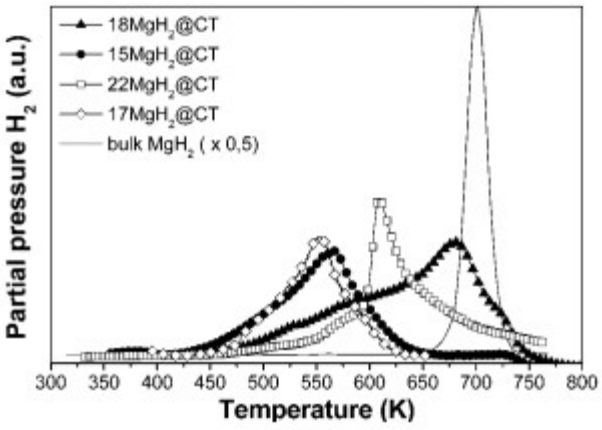

Figure 4-4. Hydrogen TDS spectra of the $xMgH_2$@C (where x stands for the Mg content determined by ICP-OES in metal weight percent) recorded with a temperature ramp of 10 °C min^{-1}. Reprinted with the permission of [23]. Copyright 2015 Royal Society of Chemistry.

Confinement of light metal hydrides, such as MgH_2, $NaAlH_4$, $NaBH_4$, $LiBH_4$ has been deeply studied and well reported, using all different porous hosts and confinement approaches. However a lack of published work for the confinement of $LiAlH_4$ was detected. The reason being is the difference in the melting point and the first dehydrogenation temperature, which allows confinement of these materials either by solution impregnation or melt infiltration (where a higher loading of the material in the carbon can be achieved). $LiAlH_4$ has a 1st dehydrogenation step immediately after melting, leaving a very narrow temperature window in which to perform melt infiltration. Therefore, solution impregnation seems like the most convenient technique to use for the confinement of $LiAlH_4$.

Aguey-Zinsou et. al reported (once this project had started) the first confinement of $LiAlH_4$ nanoparticles (and other hydrides) within carbon nanotubes (CNT's) of 2 nm pore diameter by a wet chemical approach,[24] using THF as a solvent. The 3 encapsulated hydrides showed improved hydrogen desorption temperatures. For $LiAlH_4$ confined within CNT's, the hydrogen desorption maximum was observed at 120 °C, far below the decomposition temperature of bulk $LiAlH_4$ (Figure 4-5). However, little information was given on the characterization of these materials.

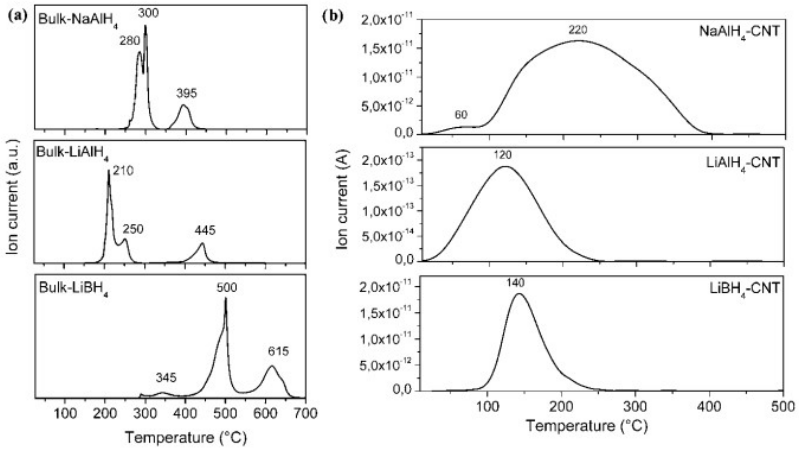

Figure 4-5. TPD plots of: a) bulk hydrides $NaAlH_4$, $LiAlH_4$ and $LiBH_4$ as received and b) after their respective incorporation in CNT's. Reprinted with the permission of [24]. Copyright 2015 Royal Society of Chemistry.

Recent work by Eckert et al. studied the effect that THF had on confined $LiAlH_4$ in mesoporous carbon CMK-3 by solution impregnation using THF as a solvent.[25] Upon heating, $LiAlH_4$ is unusually oxidized by coordinated tetrahydrofuran solvent molecules. The onset for hydrogen release was found at 127 °C, with several fragments of THF detected in the mass spectra (Figure 4-6).

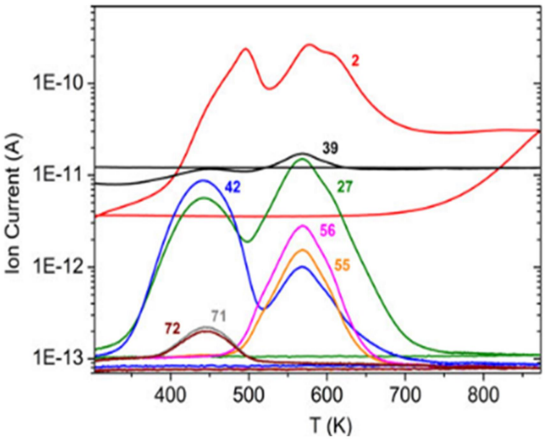

Mass number	Fragment
2	H_2
27	$C_2H_3^+$
39	$C_3H_3^+$
42	$C_3H_6^+$
55	$C_4H_7^+$
56	$C_4H_8^+$
71	$C_4H_7O^+$
72	$C_4H_8O^+$

Figure 4-6. MS profiles including the numbers of the respective fragments evolving during the heat treatment of $LiAlH_4$@CMK-3. The assignment of the fragments is given in the table. Reprinted with the permission of [25]. Copyright 2015 Cambridge University Press.

In this chapter, confinement of $LiAlH_4$ in different porous hosts (AX-21 and FDU-15 are fully detailed in Chapter 3) has been attempted in order to improve its dehydrogenation properties and make it a more suitable candidate for hydrogen storage applications. The reason for selecting $LiAlH_4$ as the material to confine in a porous host is because of the lack of reported literature on the confinement of this material. This work aims to expand the knowledge about this matter, by performing solution impregnation with diethyl ether, a solvent never reported before for the confinement of $LiAlH_4$.

4.2. EXPERIMENTAL

All the samples prepared in this chapter have been manipulated in an argon filled recirculating glove box or using a Schenk line under an argon gas flow or vacuum. The porous carbon hosts used for this work were either commercial AX-21 or FDU-15 prepared in the lab, as described in Section 3.2. Commercial $LiAlH_4$ (powder, reagent grade, 95%) was purchased from Sigma Aldrich.

Physical mixtures of $LiAlH_4$ and porous carbon host (sample 1: $LiAlH_4$ + AX-21 and sample 3: $LiAlH_4$ + FDU-15) were prepared for comparison purposes and were mixed and ground with a mortar and pestle to achieve a good dispersion of powders.

Two different confined samples were prepared and characterised in this work. $LiAlH_4$ was confined in two different porous carbon hosts, AX-21 (sample 2: $LiAlH_4$@AX-21) and FDU-15 (sample 4 – $LiAlH_4$@FDU-15). The synthesis procedure for incorporating $LiAlH_4$ into the carbon hosts was solution impregnation, as described in Section 1.4.2.2. Dried diethyl ether was used as a solvent of choice. A certain amount of the porous host and $LiAlH_4$, summarized in Table 4-1 (given by the available pore volume of the respective porous carbon hosts, as described in the in the Appendix Section 7.2) was weighed in a glove box and placed in a Schlenk flask with a magnetic stirrer and properly sealed with a rubber septum to avoid air-exposure. The Schlenk flask was attached to the Schlenk line under a continuous flow of argon. The solvent was introduced in the schlenk flask very slowly by perforing the septum with a needle attached to a glass syringe filled with diethyl ether. A typical volume of 10 ml was used to dissolve $LiAlH_4$. The rubber septum was tightly covered with parafilm after solvent insertion to minimise any possible air-exposure. The sample was gently stirred overnight with a magnetic stirrer under an argon flow. After the overnight impregnation procedure, the solvent was slowly removed from the schlenk flask under vacuum at room temperature. Diethyl ether has a very low boiling point, which makes it possible to evaporate it at room temperature under vacuum (10^{-3} atm). Once the sample was solvent free, the sample was left under vacuum for 30 minutes at room temperature and then for 2 h at 50 °C, to make sure the sample was completely dry with no trace of solvent.

Table 4-1. Description of the samples analysed and discussed in the chapter.

Samples	Identity	Carbon	$LiAlH_4$ / g	C / g	% confinement	% w.t. $LiAlH_4$
1	physically mixed ($LiAlH_4$ + C)	AX-21	0.2	0.2	-	50
2	confined sample ($LiAlH_4$@C)	AX-21	0.2	0.2	92.6	50
3	physically mixed ($LiAlH_4$ + C)	FDU-15	0.055	0.2	-	22
4	confined sample($LiAlH_4$@C)	FDU-15	0.055	0.2	95	22

Nitrogen adsorption isotherms were measured at 77 K using a Micromeretics Gemini III 2375 surface area analyser. Before analysis, the samples were degassed under vacuum at different temperatures depending on the nature of the sample. The Brunauer-Emmet-Teller (BET) method was used to calculate the specific surface areas using data adsorption in a relative pressure range from 0.4 to 1 P/Po. The total pore volume was estimated from the adsorbed N_2 amount based on the Barret-Joyner-Hallenda (BJH) calculation model.

The morphology of the samples was investigated using a Philips XL30 scanning electron microscope (SEM) and high-resolution transmission electron microscopy (FEI Techni T20 TEM), as described in Section 2.2.4.1. Particle size distribution histograms were obtained from the SEM images obtained of the products, measured and analysed by the image processing software ImageJ.[26] A population of over 300 particle measurements were taken to create the histograms at different magnifications, depending on the size of the particles studied. SEM enabled energy-dispersive X-ray spectroscopy (EDX) mapping to be performed, yielding elemental analysis of the surface of the materials, whereas TEM allowed electron energy loss spectroscopy (EELS) mapping to be performed. Both techniques were used to study the elemental distribution in the samples studied.

Samples were analysed by powder X-ray diffraction (PXD), as described in Section 2.2.2.2. Sealed capillaries were prepared and analysed on the Bruker D8 diffractometer. Diffraction data were collected from 5 -85 ° of 2ϑ for 1 hour or 14 hours at a step size of 1.3 °/min and 0.09 °/min respectively, depending on the nature of the sample.

Thermal programmed desorption studies of the samples prepared were performed using a Netzsch STA 409 analyser, which was coupled to a Hiden HPR 20 Mass Spectrometer for evolved gas analysis (as described in Section 2.2.5.2.4). Hydrogen gas was the most relevant gas tracked on the Mass Sprectrometer, although other gases were also tracked (such as H_2O or O_2). Measurements were performed in an argon-filled recirculating glove box, with 30 mg of sample typically used.

Raman spectroscopy was performed using a Horiba LabRAM spectrometer HR confocal microscope system with a 532 nm green laser. A hole aperture of 50 μm, 600 grating/mm, 50x objective lens and a Synapse CCD detector were used at room temperature. Powdered air sensitive samples were placed in a glass capillary and sealed before running the analysis. Spectra were usually collected over a period of several minutes from an average of multiple scans, normally at a range of 50 cm^{-1} to 2500 cm^{-1}.

4.3. RESULTS AND DISCUSSION

4.3.1. Commercial $LiAlH_4$ characterisation

4.3.1.1. Structural characterisation

Figure 4-7a shows the X-ray diffraction pattern obtained for as-received $LiAlH_4$. The offset in Figure 4-7a shows the 45 – 53 ° range of 2ϑ). The pattern matches well to the $LiAlH_4$ reflections model from the ICSD database;[27] reflections were calculated by PowderCell. The morphology of the as-received $LiAlH_4$ is shown in the SEM Figure 4-7b, where it can be seen that the bulk material is formed of grains of heterogeneous sizes, over the range 6 – 26 µm wide across.

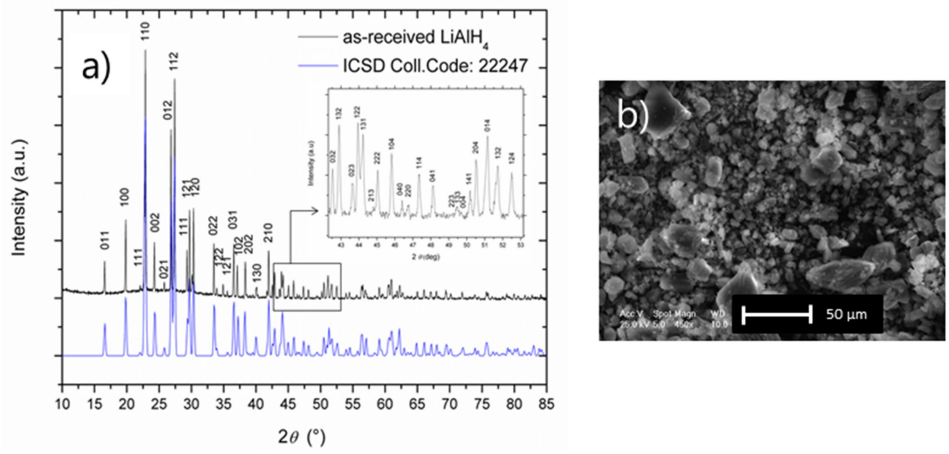

Figure 4-7. a) XRD powder pattern obtained of as-received $LiAlH_4$. Characteristic Bragg reflections are calculated from the ICSD database,[27] b) SEM image of the as-received $LiAlH_4$ (x450 magnification).

Figure 4-8 shows the Raman spectrum of as-received $LiAlH_4$. Other than the vibrational and librational modes at low wavenumber, the characteristic sharp and distinctive bending modes for the H – Al – H bond and the stretching modes for the Al – H bond are prominent in the spectrum.

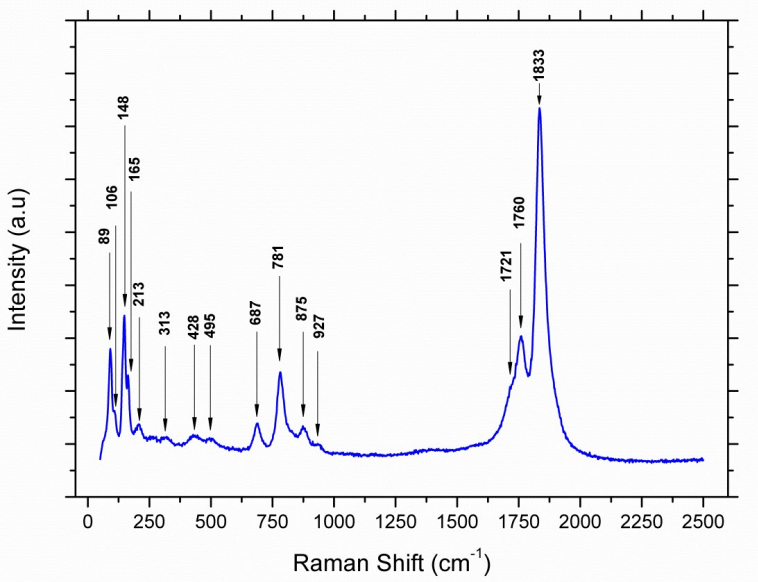

Figure 4-8. Raman frequencies obtained from $LiAlH_4$ as-received.

A summary of all the Raman frequencies and their respective vibrational mode assignments is shown in Table 4-2. The measured frequencies are shown in comparison with the values obtained previously in the literature, which are in good agreement.[28,29]

Table 4-2. Raman frequencies and vibrational mode assignments for $LiAlH_4$ in this work and results obtained in previous work for comparison.

Raman shift (cm^{-1})			Vibrational Mode Assignments	
DAC as-loaded (Chellapa et al.[28])	powder Raman (Bureau et al.[29])	This work (powder Raman)		
88	95	89	Translation	
102	112	106		
141	143	148		
157	151	-		
201	165	165		
225	220	213	Libration	
312	322	313		
434	438	428		
495	510	495		
688	690	687	Bending	$\delta(AlH_2)$
778	780	781		sym - $\delta(AlH_2)$
816	830	-		$\delta(AlH_2)$
878	882	875		$\delta(AlH_2)$
933	950	927		$\delta(AlH_2)$
1720	1722	1721	Stretching	ν (Al-H)
1754	1762	1760		asym -ν (Al-H)
1829	1837	1833		sym - ν (Al-H)

4.3.1.2. Dehydrogenation studies

The decomposition properties of commercial $LiAlH_4$, used in this work are shown in Figure 4-9. The TG profile (Figure 4-9a) shows 3 distinctive mass loss steps, each of them corresponding to the decomposition reactions (Eqs. 4-1 to 4-3) of $LiAlH_4$. The first mass loss step, starting at ca. 160 °C, is 5.20 wt.% and corresponds to the decomposition of $LiAlH_4$ and formation of Li_3AlH_6 (Eq. 4-1). The second mass loss step, starting at around 180 °C, is 2.3 wt.% and corresponds to the decomposition of Li_3AlH_6 and formation of LiH (Eq. 4-2). And the final step has a mass loss starting at around 390 °C of 1.8 wt.% and corresponds to the decomposition of LiH (Eq. 4-3). The overall mass loss is 9.3 wt.% which is close to the maximum theoretical hydrogen total amount for $LiAlH_4$, of 10.5 wt.% (Appendix Section 7.2). H_2 releases matching the correspondent mass losses were observed for each step (Figure 4-10).

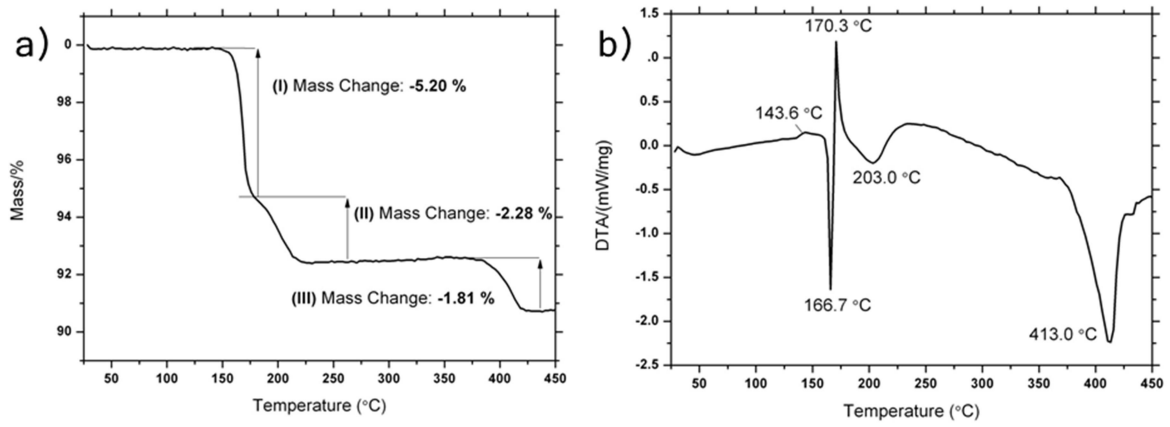

Figure 4-9. a) TG profile of $LiAlH_4$ as-received at a heating rate of 2 °·min^{-1} to 450 °C under Argon atmosphere. b) Simultaneous DTA profile of as-received $LiAlH_4$ (y > 0 = exothermic and y < 0 = endothermic)

The DTA profile (Figure 4-9b), recorded simultaneously with the TG profile, show 5 distinctive events, 3 of them corresponding to mass loss events seen in the TGA profile. The first peak occurs at ca. 143 °C and has a very low intensity. According to Dymova et al.[3] this peak corresponds to the reaction between traces of hydroxide impurities found on the surface of the $LiAlH_4$ particles reacting with the hydride atom from $LiAlH_4$ to form Al-O-Al with a negligible release of hydrogen, (not detected in the mass spectrum in Figure 4-10). The second peak is a sharp endothermic peak, with a maximum at 166 °C, followed by a very sharp exothermic peak, with a maximum at 170 °C. These 2 events correspond to the melting of $LiAlH_4$ immediately followed by the first dehydrogenation step of $LiAlH_4$.[30] A further thermal event, seen as a broad endothermic peak

(which begins immediately after the previous exothermic peak) has a maximum at 203 °C. This corresponds to the dehydrogenation of Li_3AlH_6. Finally, the last peak is endothermic in nature, with a maximum at 413 °C, and originates from LiH dehydrogenation. These results are in good agreement with previous work published in the literature.[3]

The parallel MS recording shows only hydrogen desorption. In Figure 4-10 the plot for m/z = 2 is shown as a function of time and temperature. Three distinctive steps can be observed from the hydrogen desorption, which is consistent with the observed TG and DTA profiles, and can be correlated to the 3 decomposition steps which $LiAlH_4$ undergoes upon thermal treatment. The maxima for each of these steps occurs at 173 °C (starting at 154 °C), 209 °C (starting at 193 °C) and 416 °C (starting at 380 °C). The first step is the most intense one and corresponds to the first dehydrogenation step where the largest amount of hydrogen is evolved (5.2 wt.%, Eq. 4-1). The second step happens immediately after the first one, with a lower intensity than the first step and corresponds to the dehydrogenation of Li_3AlH_6, with correspondingly a lower amount of hydrogen desorbed (2.3 wt.%, Eq. 4-2). And the last step, with a similar low intensity as the second step (1.8 wt.%, Eq. 4-3), occurs at much higher temperature and corresponds to the dehydrogenation of LiH.

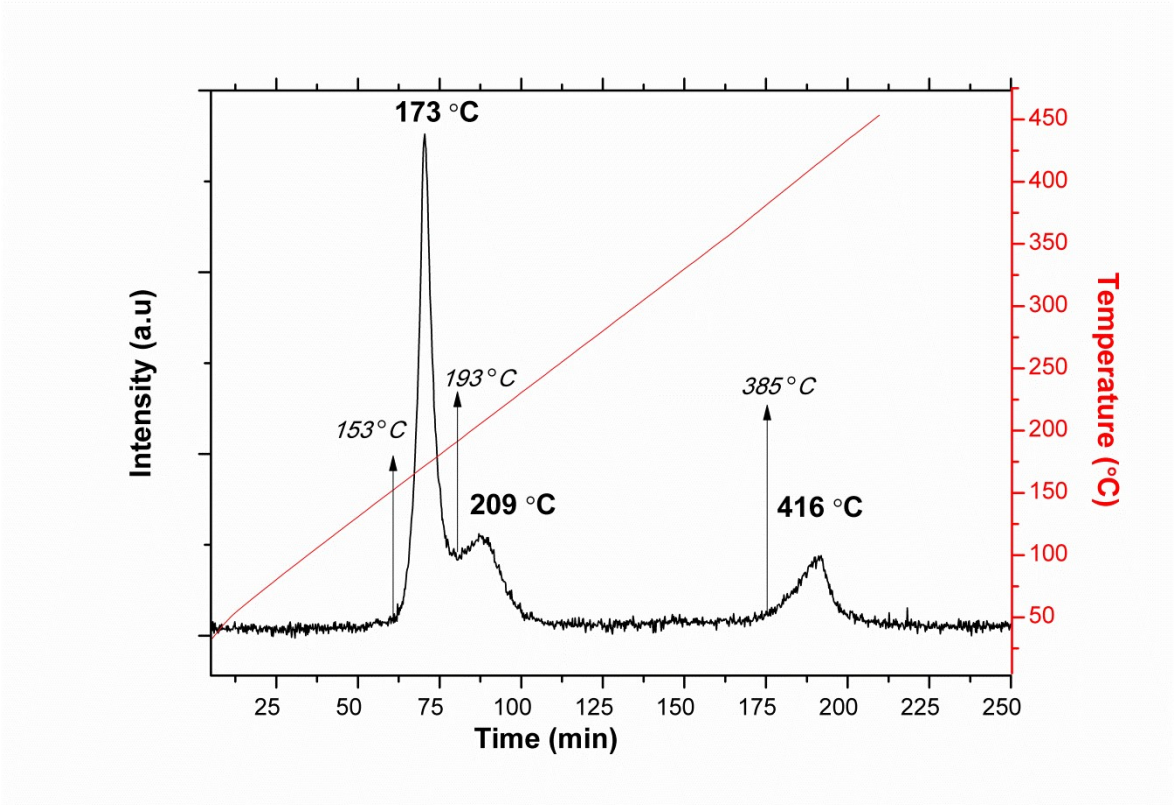

Figure 4-10. MS profile recording hydrogen evolution (m/z = 2) of as-received $LiAlH_4$, coupled to the STA apparatus to evaluate the gasses evolved from the sample during thermal decomposition.

Table 4-3. Summary of results obtained for as-received $LiAlH_4$

	DTA maximum peak	H_2 Mass Loss		MassSpec		Reaction Assignment
Events	T (°C)	expected (%)	obtained (%)	Peak onset T (°C)	Peak Maximum T (°C)	
1	143.6	-	-	-	-	-Al-OH + -Al-H→ -Al-O-Al- + H_2 [3]
2	166.7	-	-	-	-	Melting $LiAlH_4$
3	170.3	5.3	5.2	153	173	Decomposition $LiAlH_4$ (Eq. 4-1)
4	203.0	2.6	2.28	193	209	Decomposition Li_3AlH_6 (Eq. 4-2)
5	413	2.6	1.81	385	410	Decomposition LiH (Eq. 4-3)

The summary Table 2 collects the data obtained from the TG-STA and Mass Spec. All the thermal events observed are in good agreement with published work[3] and could be assigned to a known thermal event or reaction. The first event observed in the DTA graph (Figure 4-9b) can be assigned to the reaction of oxygen impurities in the surface of the starting material, reacting with one of the hydrides of $LiAlH_4$, resulting in negligible hydrogen desorption (not observed in Figure 4-10), as discussed by Dymova et. al.[3]

4.3.1.3. Post thermal treatment structural characterisation

The lithium aluminium hydride was characterized by powder X-ray diffraction (PXD) ex-situ before thermal treatment and after reaction 2 (260 °C) and 3 (450 °C) (Figure 4-11). The powder pattern for the sample treated at 260 °C (Figure 4-11b), shows sharp Bragg's reflections in good agreement with the characteristic reflections from both LiH and Al metal phase. These two products have very similar diffraction patterns due to the fact that they crystallize in the same cubic same space group ($Fm\bar{3}m$, nº 225) with similar lattice parameters (LiH: a = 4.0834(5)[31] and Al: a = 4.05925(5)[32]). But a magnification of higher values of 2ϑ for the sample treated at 260 °C (Figure 4-12), shows that Al phase is predominant in the pattern. This result is in good accordance with previous studies in the literature.[33,34]

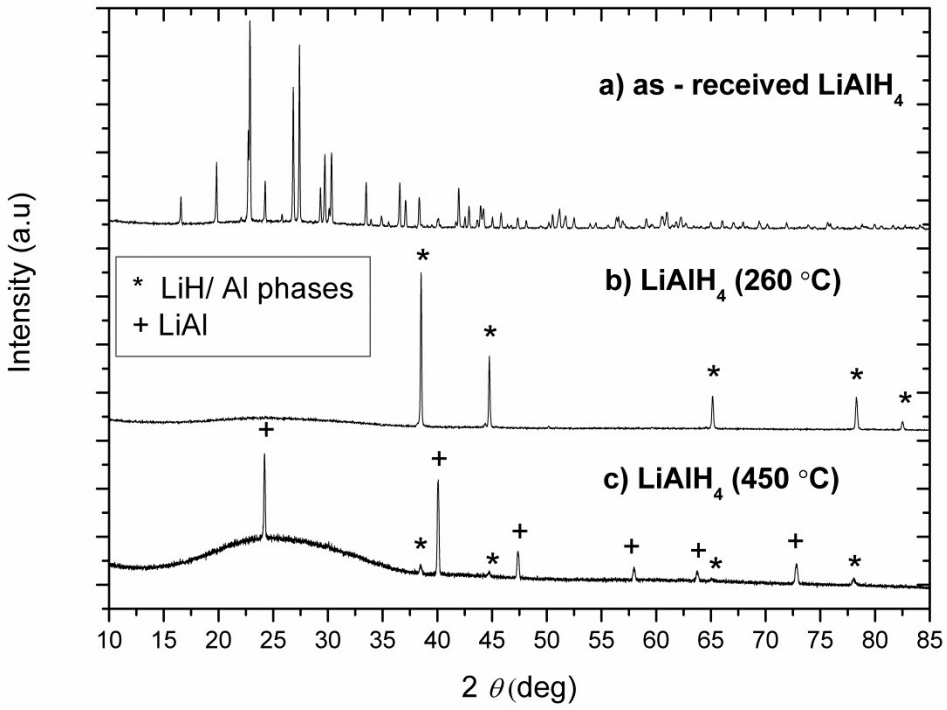

Figure 4-11. PXRD patterns of: a) as-received $LiAlH_4$, b) $LiAlH_4$ thermally treated at 260 °C c) $LiAlH_4$ thermally treated at 450 °C. To assign the Bragg reflections present in the samples, the following phases have been used from the ICSD database *LiH (collection code 28557)*[31], *Al (collection code 43492)*[32], LiAl (collection code 1924).[35]

The powder pattern for the sample treated at 450 °C (Figure 4-11c), shows sharp Bragg reflections at 2ϑ: 24.2, 40, 47.4, 58, 63.8, 72.8° in addition to the reflections already seen from thermally treating $LiAlH_4$ at 260 °C (Figure 4-11b), although in this powder pattern their intensities have decreased substantially. It can also be observed that the amorphous character of the sample has increased after being treated at 450 °C, as can be seen from the amorphous background in the low angle section of the pattern, indicating a certain degree of disorder upon formation of LiAl. The new reflections in this sample belong to the LiAl phase, formed after reaction 3 ($Fd\bar{3}m$, a = 6.37(1)[35]). This new phase is formed after LiH and Al react with each other releasing hydrogen, as shown by the MS in Figure 4-10. This explains the decrease in intensity of the reflections from the LiH and Al phases, which are being consumed to form the LiAl phase. The formation of this new phase could explain the introduction of the amorphous background, by particle agglomeration of this new phase upon heating. From Figure 4-12 it can be seen that after reaction 3, there is still some presence of Al /LiH phase, suggesting that the last reaction might not be completed. It is not possible to see the reflections of LiH at high angles after reaction 2 (Figure 4-12a). These results are in good accordance with other similar work published,[34] where there is the difficulty of to distinguish the LiH and Al phase. It seems that the Al phase is easier to detect at higher angles, but

this does not mean that LiH is not present and possibly shielded by Al reflections at lower angles. If LiH was not present in the sample there could be no hydrogen desorption at over 400 °C (Figure 4-10). Some authors,[5,7] have suggested that this last reaction happens via the intermediate stage of LiH dehydrogenation to form lithium (Eq. 4-4) which then reacts with the Al present (Eq. 4-5).

$$LiH \rightarrow Li + \frac{1}{2} H_2 \qquad (4\text{-}4)$$

$$Li + Al \rightarrow LiAl \qquad (4\text{-}5)$$

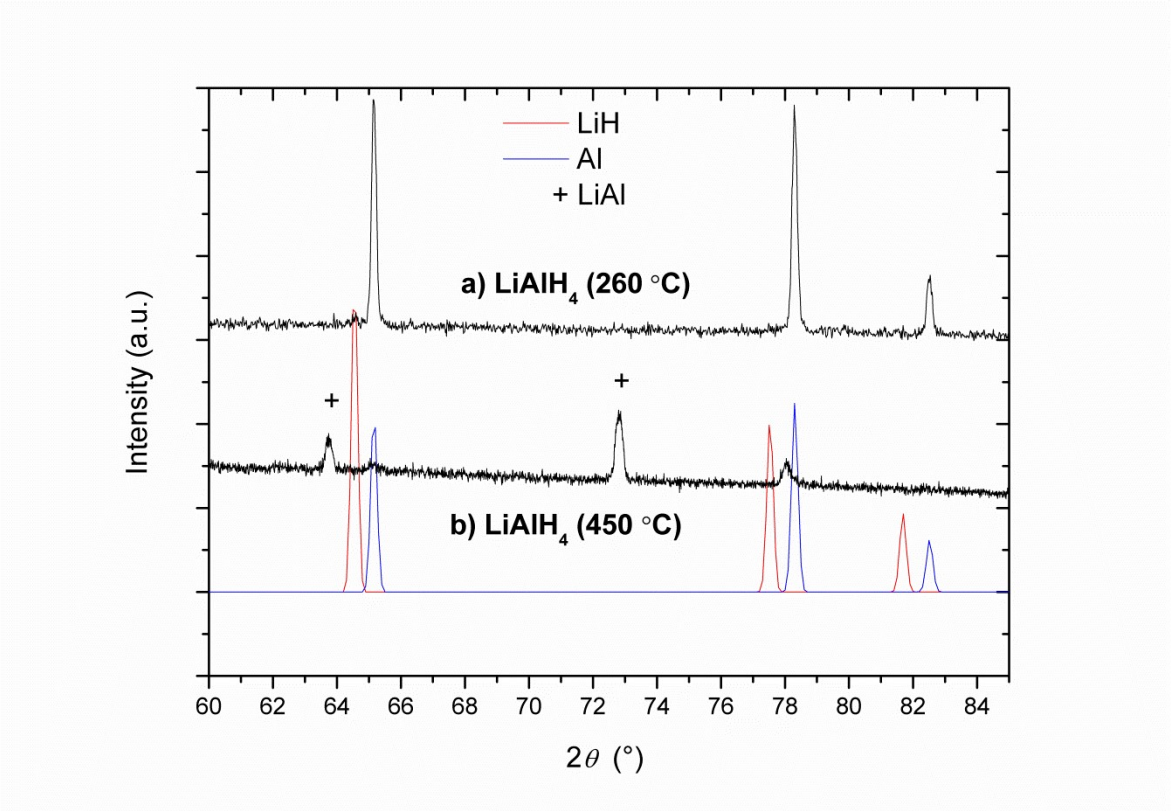

Figure 4-12. Magnification of higher values of 2θ for $LiAlH_4$ treated at 260 °C (a) and 450 °C (b). (ICSD database *LiH (collection code 28557)*[31], *Al (collection code 43492)*[32]).

4.3.2. Choice of solvent

The remaining work carried in this chapter consists of attempting to confine the $LiAlH_4$ into the pores of porous carbon hosts by dissolving the $LiAlH_4$ in a solvent and mixing it with the carbon host, to impregnate the carbon with the solution of $LiAlH_4$. The hydride is "forced" to precipitate inside of the pores of the carbon host upon removal of the solvent.

In order to be able to dissolve $LiAlH_4$ for further confinement, the need of an adequate solvent is required. The solvent to be used should be inert towards $LiAlH_4$ and be able to dissolve the alanate without changing its properties when recrystallized.

Water should not be used, since $LiAlH_4$ reacts violently with water and atmospheric moisture, forming LiOH and $Al(OH)_3$ according to the following reaction:[36]

$$LiAlH_4 + 4\,H_2O \rightarrow LiOH + Al(OH)_3 + 4\,H_2 \qquad (4\text{-}6)$$

There are, though, many solvents that could be used in order to dissolve $LiAlH_4$. $LiAlH_4$ is stable and soluble in many ethereal solvents, the most common being THF (2.96 mol·L^{-1})[1] and diethyl ether (5.92 mol·L^{-1}).[37]

Diethyl ether was selected, due to its higher solubility and for being the solvent most commonly used for standard recrystallization of $LiAlH_4$, in order to separate the impurities that $LiAlH_4$ might present.[38] In fact, in the original synthesis of $LiAlH_4$, reported in 1947, diethyl ether was the solvent used in the reaction between LiH and AlH_3. Lithium alanate was obtained after evaporating the solvent.[1]

Diethyl ether (CH_3CH_2-O-CH_2CH_3), is a non-polar solvent, with a low dielectric constant and a boiling temperature of 34 °C.[39] This means that the solvent can be removed easily at room temperature under vacuum.

As can be seen from Figure 4-13, the pattern can be assigned to $LiAlH_4$ reflections and so recrystallisation in diethyl ether yields pure phase alanate.

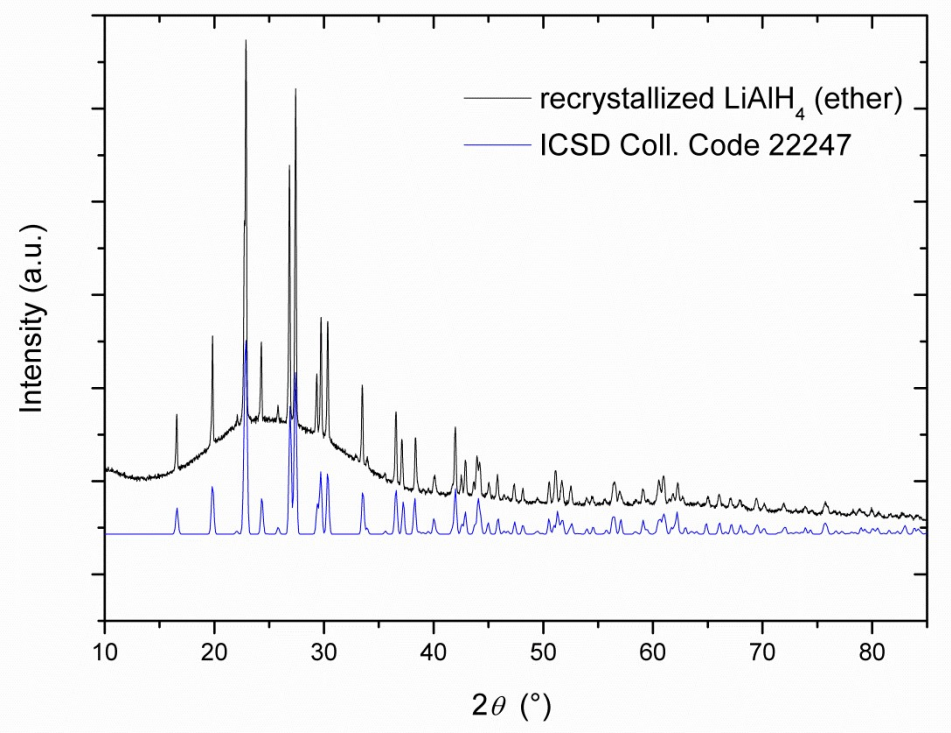

Figure 4-13. XRD powder pattern obtained of the recrystallized $LiAlH_4$ using diethyl ether as a solvent, along with the $LiAlH_4$ Bragg reflection from the ICSD database.[27]

Figure 4-14 shows TGA and DTA results obtained from the recrystallized sample. Both the DTA peaks and the mass losses values are in good agreement with the ones obtained from the as-received $LiAlH_4$. All the values obtained are collected and compared with those obtained from as-received $LiAlH_4$ in Table 4-4**.**

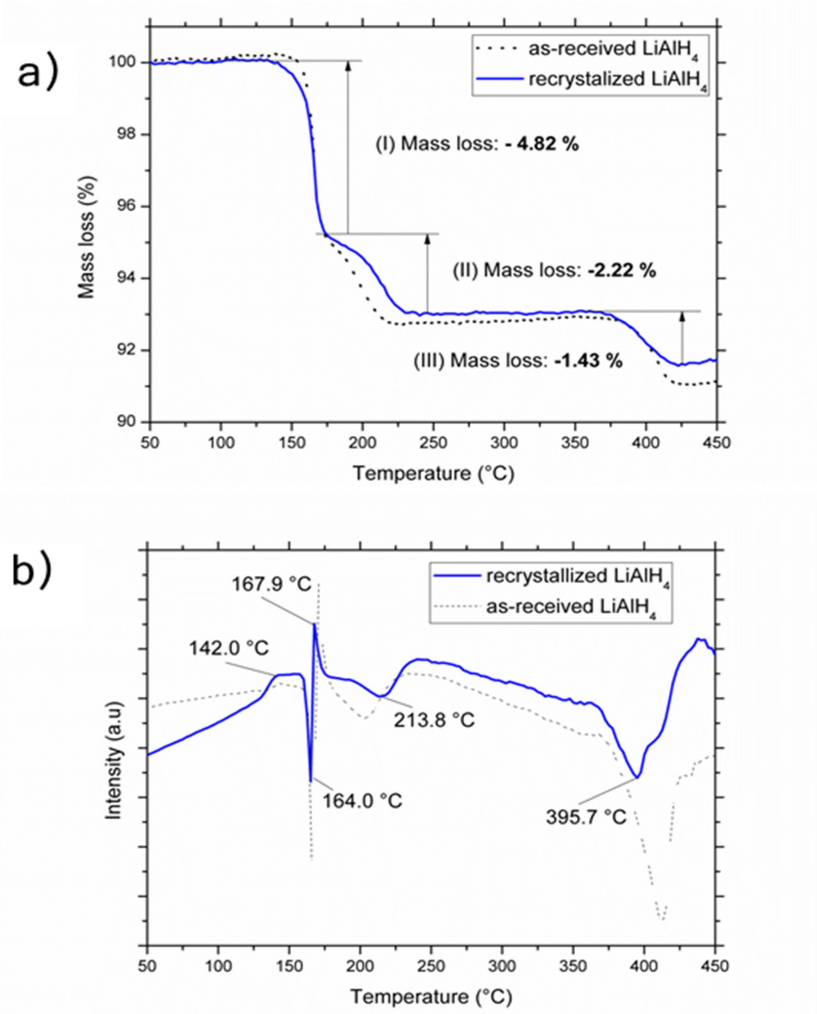

Figure 4-14. a) TG profile of recrystallized $LiAlH_4$ at a heating rate of 2 °·min^{-1} to 450 °C under an argon atmosphere. b) Simultaneous DTA profile of recrystallized $LiAlH_4$. In both graphs the data obtained from as-received $LiAlH_4$ are shown for comparison.

Figure 4-15 shows the hydrogen mass spectra obtained from the recrystallized sample. The three distinctive hydrogen release steps belonging to each dehydrogenation reaction are observed in the same range of temperatures and with the same shape as the as-received $LiAlH_4$.

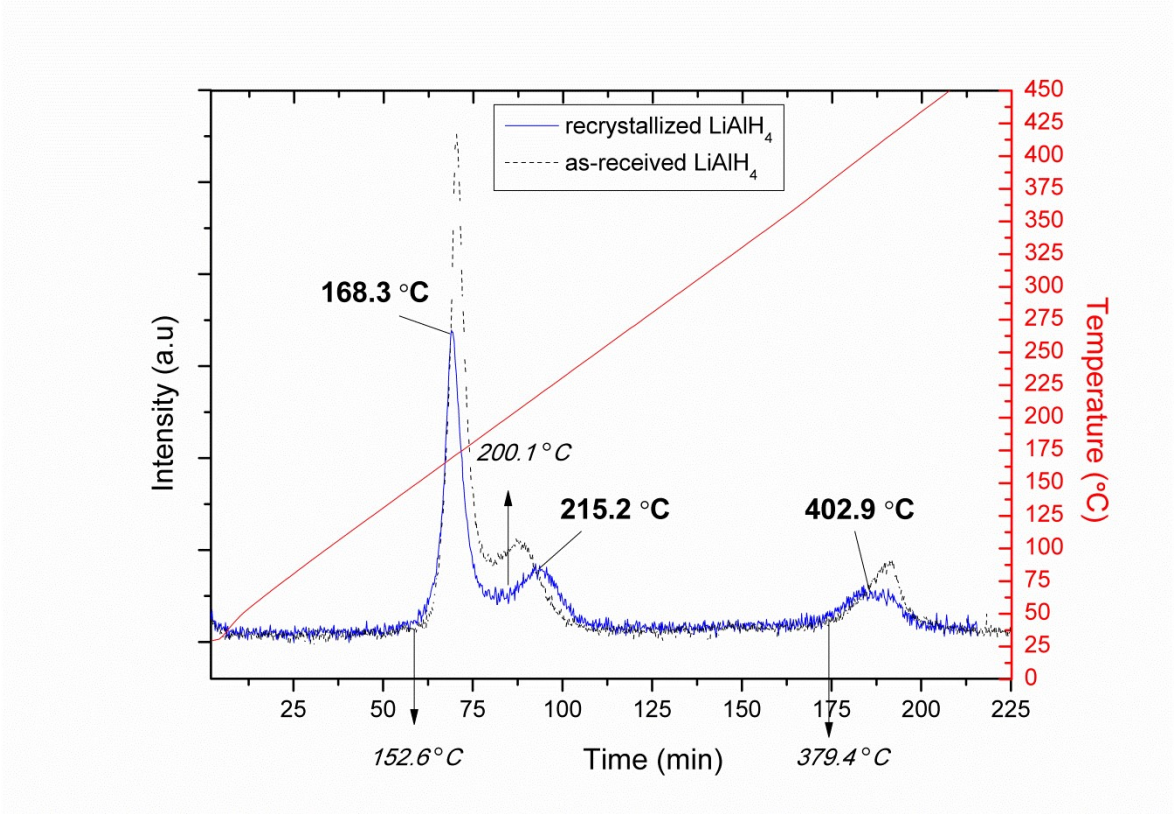

Figure 4-15. MS profile recording hydrogen evolution (m/z = 2) from recrystallized $LiAlH_4$, Data obtained from as-received $LiAlH_4$ is shown for comparison.

Table 4-4 collects all the measurements for the recrystallized sample and as-received samples. The hydrogen desorption temperatures for the recrystallized material are in good agreement with the as-received $LiAlH_4$, with a difference of less than 8 °C for any of the dehydrogenation steps. Mass losses observed for the recrystallized $LiAlH_4$ are a slightly lower than those observed for as-received $LiAlH_4$. Although the results of the measurements obtained for the recrystallized material are slightly different from the as-received material, it seems safe to assume that diethyl ether does not change the structural characteristics and intrinsic properties of $LiAlH_4$, making it a suitable solvent for the purpose of this work.

Table 4-4. Summary of results obtained for recrystallized $LiAlH_4$. Values obtained for as-received $LiAlH_4$ are shown below in brackets for comparison purposes.

Events	DTA peak T (°C)	H_2 Mass Loss		MassSpec		Reaction
		Calculated (%)	Obtained (%)	Starting Peak T (°C)	Max. Peak T (°C)	
1	142 *(143.6)*	-	-	-	-	--Al-OH + --Al-H -> --Al-O-Al-- + H_2
2	164.0 *(166.7)*	-	-	-	-	Melting $LiAlH_4$
3	167.9 *(170.3)*	5.3	4.82 (*5.2*)	152.6 *(153.5)*	168.3 *(173.3)*	Decomposition $LiAlH_4$ (Eq. 4-1)
4	213.8 *(203)*	2.6	2.22 (2.28)	200.1 *(192.7)*	215.2 *(209)*	Decomposition Li_3AlH_6 (Eq. 4-2)
5	395.7 *(413)*	2.6	1.43 (1.81)	379.4 *(378.9)*	402.9 *(416.3)*	Decomposition LiH (Eq. 4-3)

4.3.3. $LiAlH_4$ confinement in AX-21

4.3.3.1. Structural characterization

Figure 4-16 shows a comparison of the N_2 absorption/desorption isotherms at 77 K of as-received dried AX-21 and samples 1 and 2. A summary of the specific surface area and the total pore volume of each sample are shown in Table 4-5. It can be easily observed that the three samples show a different behaviour on the amount of nitrogen adsorbed at 77 K. However, the isotherm of as-received AX-21 and sample 1 have the same isotherm type (type I), whereas sample 2 exhibits a type II isotherm, characteristic from non-porous adsorbents[40] (as confirmed by the values obtained recollected in Table 4-5). $LiAlH_4$ seems to be blocking the pores of the carbon host in sample 2, decreasing notably the amount of nitrogen that the sample can absorb, and thus altering the shape of the isotherm. As-received AX-21 after a drying step, is the sample that adsorbed the largest volume of nitrogen, as expected. The calculated BET surface area and total pore volume of AX-21 are 2162.7 $m^2 \cdot g^{-1}$ and 1.18 $cm^3 \cdot g^{-1}$, respectively. Sample 1 showed much less adsorption than AX-21, but could still be considered as a porous material, with a calculated BET specific surface area and total pore volume of 960.0 $m^2 \cdot g^{-1}$ and 0.56 $cm^3 \cdot g^{-1}$ respectively, whereas sample 2 showed relatively little adsorption with a calculated BET specific surface area and total pore volume are of 6.8 $m^2 \cdot g^{-1}$ and 0.02 $cm^3 \cdot g^{-1}$ respectively.

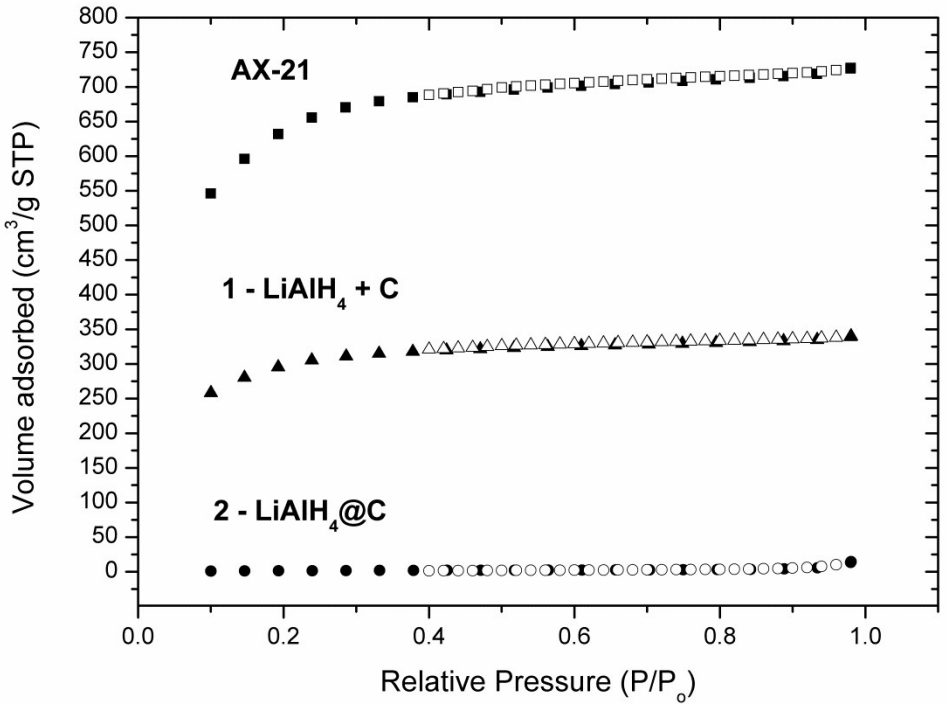

Figure 4-16. Comparison of N_2 absorption/desorption isotherms at 77 K of dried AX-21, sample 1 and sample 2. Further supplementary data available.[41]

Table 4-5. Summary of the BJH model calculations results for specific BET surface area and total pore volume of each sample.

Sample	BET surface area / $m^2 \cdot g^{-1}$	Total pore Volume / $cm^3 \cdot g^{-1}$
AX-21	2162.7	1.18
1	960.0	0.56
2	6.8	0.02

This reduction of the specific surface area and total pore volume of the confined samples indicates a blocking or filling of the pores by $LiAlH_4$, which is much more effective than in the physical mixture of carbon and $LiAlH_4$. It is difficult to be certain whether the $LiAlH_4$ is actually confined in the pores or supported on the carbon surface. Both cases could in principle lead to a highly reduced surface area and total pore volume.

SEM images in Figure 4-17 (a and b) show the particle morphology and particle size of the as-received $LiAlH_4$. It can be observed from the SEM images and the particle size distribution (Figure 4-17c) that the particle size is quite heterogeneous, ranging from 6 to 62 µm across. By plotting the cumulative frequency, it has been found that 80 % of the particle sizes can be found between 6 and 26 µm across, with the maximum relative frequencies between 10 - 12 µm across. The confined sample particle morphology and particle size is somewhat different from that of the as-received $LiAlH_4$, as can be observed in the SEM images (Figure 4-19 a and b) and from the particle size distribution (Figure 4-19c). The particle size range is narrower for the confined sample, from 4 to 40 µm across and 80 % of the particle sizes range between 4 and 16 µm across, with the maximum relative frequencies between 9 - 11 µm across.

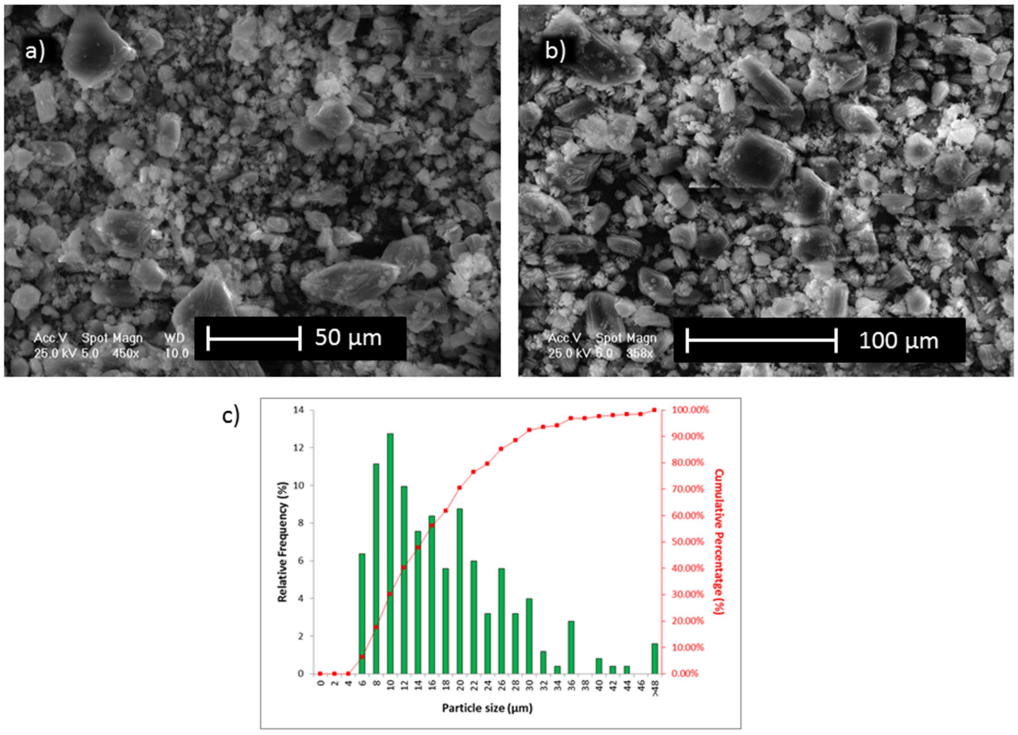

Figure 4-17. a - b) SEM images of the as-received $LiAlH_4$ and c) Histogram of particle size distribution (µm) with relative frequency (%) and accumulative percentage.

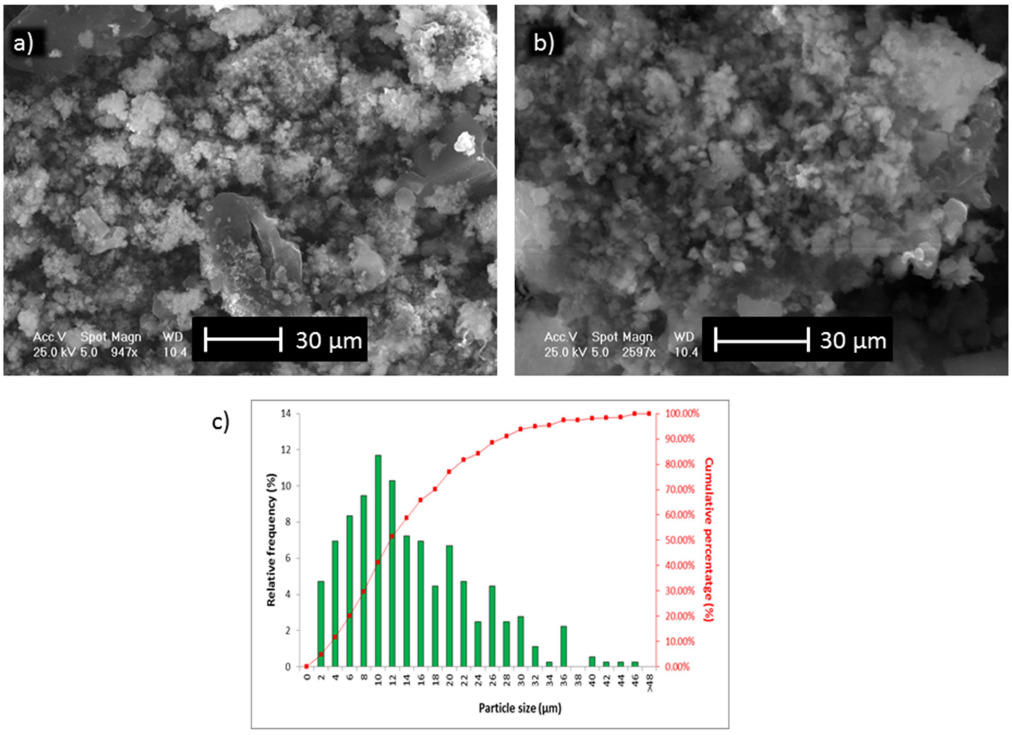

Figure 4-18. a - b) SEM images of sample 1 and c) Histogram of particle size distribution (µm) with relative frequency (%) and accumulative percentage.

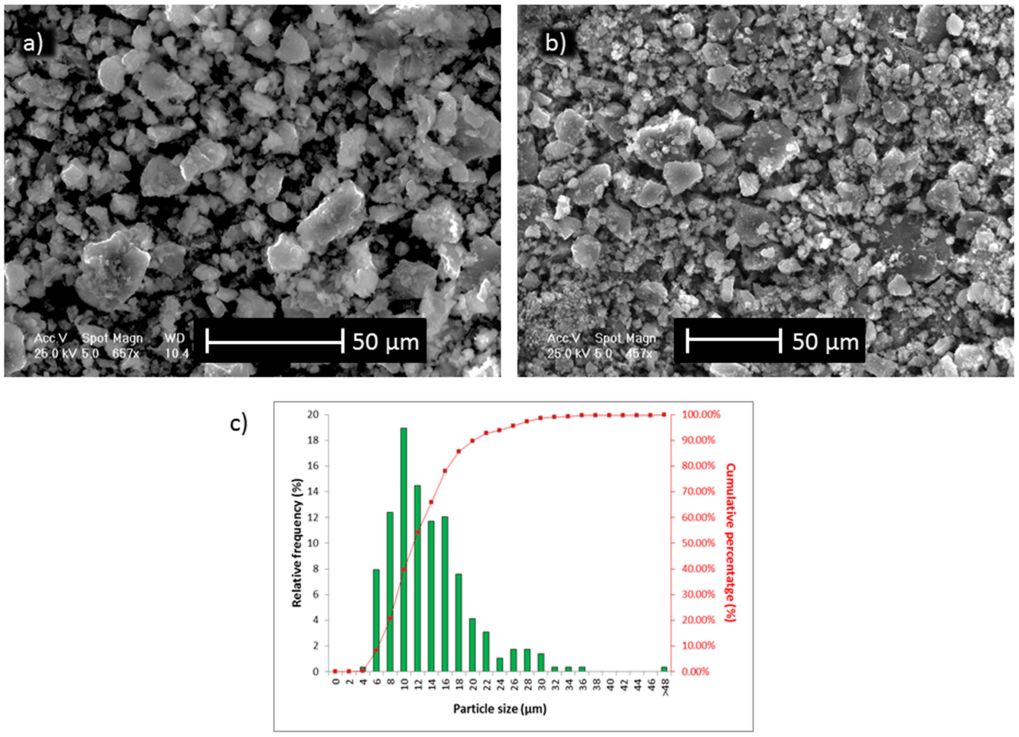

Figure 4-19. a - b) SEM images of sample 2 and c) Histogram of particle size distribution (µm) with relative frequency (%) and accumulative percentage.

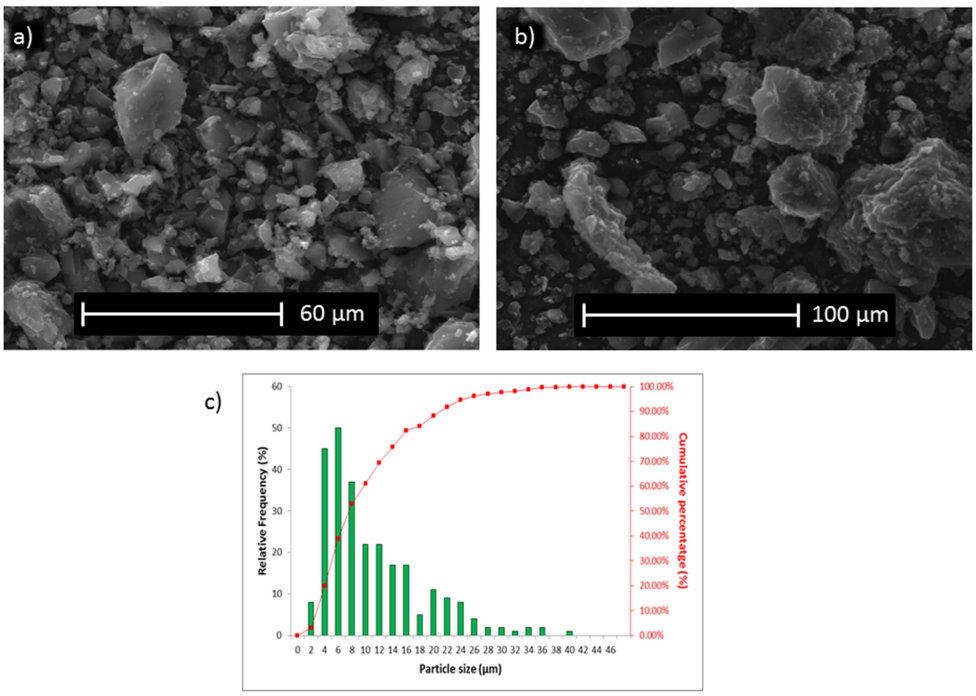

Figure 4-20. a - b) SEM images of AX-21 and c) Histogram of particle size distribution (µm) with relative frequency (%) and accumulative percentage.

Although the maximum relative frequencies from the as-received $LiAlH_4$ and sample 2 particles sizes are very similar (10 – 12 μm and 9 – 11 μm, respectively), it can be observed that there is a decrease of the overall particle size in sample 2 (6 – 62 μm and 4 – 40 μm, respectively; 6 – 26 μm and 4 – 16 μm at the 80% population level). The particle size in sample 1 lies between that of the alanate starting material and sample 2. That the sizes and shapes of the confined sample are more similar to those of AX-21 sample than to those of $LiAlH_4$, reinforces the assumption that AX - 21 acts as a crystallisation template for $LiAlH_4$, restricting the size of the recrystallized $LiAlH_4$ and reducing the composite overall particle size.

Table 4-6. Summary of the results obtained in Figure 4-17 - Figure 4-20c.

	Particle size distribution / μm		
Sample	*100 % population*	*80 % population*	*Max. frequency (%)*
AX - 21	2 – 35	2 - 16	5 – 6
$LiAlH_4$	6 – 62	6 – 26	10 – 12
1	2 - 48	2 - 22	10 -12
2	4 - 40	4 – 16	9 – 11

In addition to the SEM characterization of the sample, EDX elemental analysis and mapping have been performed on the samples. Figure 4-21 shows the SEM image of a selected sample area (a), the EDX mapping of the selected area (b) and the EDX spectrum (c), respectively for different samples. As mentioned in Section 2.2.4.1.1, EDX cannot detect light elements like H and Li, which are two main elements on most of the samples of interest of this work, but is very useful for detecting heavier elements like Al, O and even C.

The SEM instrument used for this work does not have an air-sensitive loading system for the samples. The samples were prepared inside an argon-filled glovebox and transported in sealed vials, without contact with air, until they were loaded on the instrument as quickly as possible, where they were exposed to the atmosphere for only a few seconds. This brief exposure to the atmosphere could influence the oxygen content observed by EDX analysis; porous carbon can uptake moisture and oxygen from the atmosphere, whereas $LiAlH_4$ could form LiOH and $Al(OH)_3$ layers when exposed to the atmosphere (Eq. 4-6). Even if these passivation products are formed,

the content of Al should remain constant in the sample. The $LiAlH_4$ – C distribution in the sample (especially when comparing sample 1 and 2), should also remain unchanged. Negligible chlorine and sulfur presence is detected (less than 1 %) in the EDX spectra. All the results collected from EDX characterization and mapping results are summarized in Table 4-7.

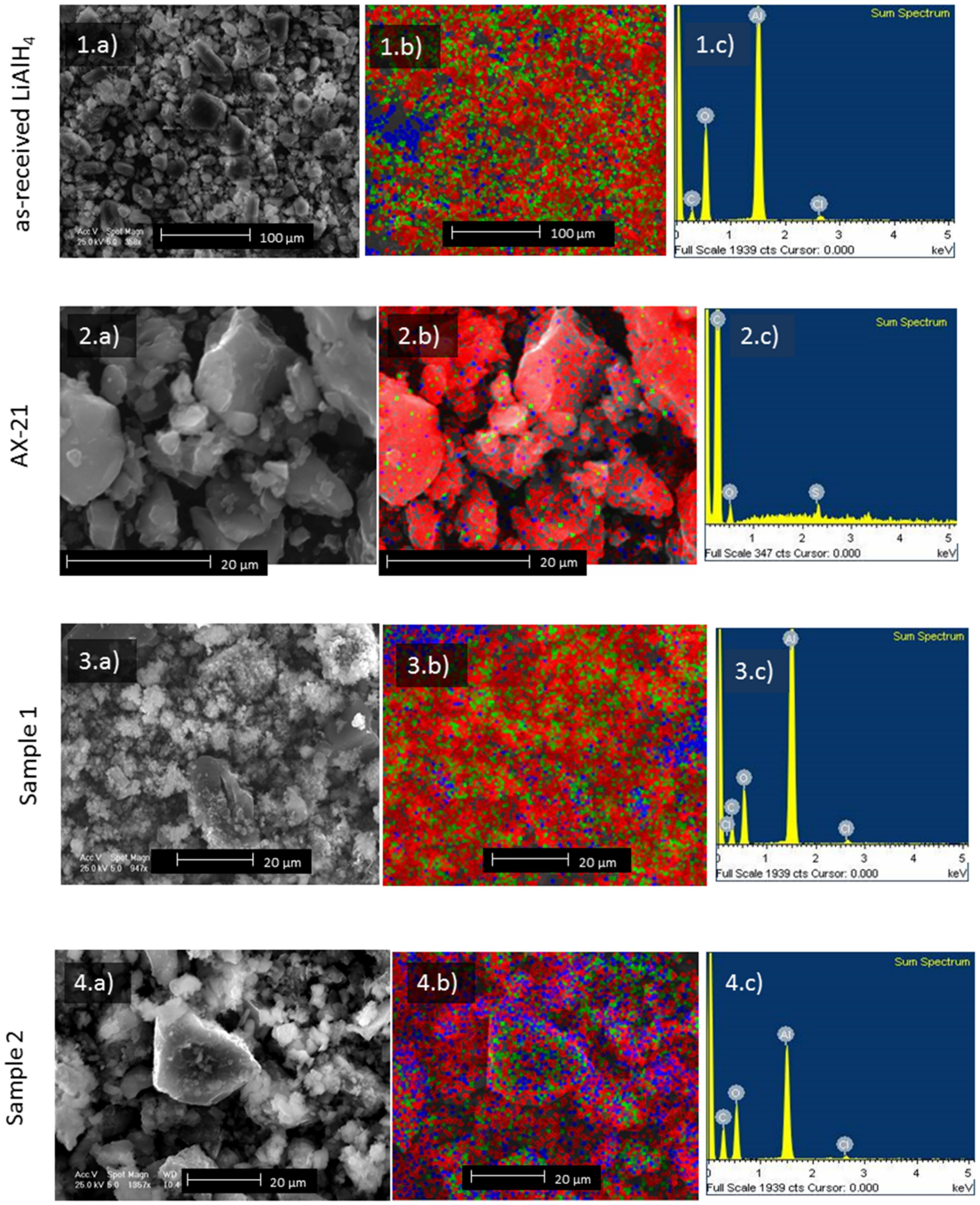

Figure 4-21. a) SEM images of the selected areas used for EDX measurements, b) EDX mapping images and c) EDX spectra of different samples analysed. For image 2b), the colour legend is as follows: C (red), O (blue), Sulphur (green)), whereas for the rest of the samples the colour legend is as follows: Al (red), C (blue), O (green). Further supplementary data available.[41]

Table 4-7. Summary table collecting the percentages in weight of the main elements, collected by EDX characterisation.

	C (% weight)	O (% weight)	Al (% weight)	O : Al ratio
as- received $LiAlH_4$	17.8	55.9	25.8	2.17
AX-21 dried	93.0	6.6	-	
1	32.0	41.0	26.6	1.54
2	39.5	47.4	12.7	3.73

The high content of carbon from as-received $LiAlH_4$ almost certainly originates from the carbon tab, used to fix the sample to the stub sample holder. Comparing EDX mapping images from Figure 4-21b, it can be observed that the elemental profile of sample 1 resembles that of as-received $LiAlH_4$, where the carbon is covered by Aluminium and Oxygen. However, as observed in Figure 4-21.4b, for sample 2 the elemental distribution is totally different, much more homogenous, with some Aluminium (green) on the edges of the carbon particles. Considering the O : Al ratio in Table 4-7, and assuming equal exposure times to the atmosphere, it can be seen that as-received $LiAlH_4$ and sample 1 have similar O : Al ratios. However, sample 2 has more than twice oxygen content per aluminium content than sample 1. This could indicate that the $LiAlH_4$ particles supported in the carbon have reduced their size by the confinement method compared to the as-received $LiAlH_4$, making them more reactive to oxygen. It is well known that reducing the particle size to the nanometer scale can change the physicochemcial properties of the materials, destabilizing them and making them more reactive.[42]

TEM characterisation and EELS mapping were also performed in order to obtain a better understanding of the dispersion of the alanate in the porous host. Figure 4-22 shows the bright field TEM images of dried porous carbon sample 2. For sample 2, in Figure 4-22 (c-d), darker sports can be observed in some bigger particles, which indicates that $LiAlH_4$ was impregnated into the carbon with large voids between the hydride particles. Similar images to those in figure 22c-d have been reported in the literature from the confinement of other alanates and borohydrides ($LiAlH_4$, $NaAlH_4$ and $LiBH_4$)[24] and hydrides (MgH_2).[23]

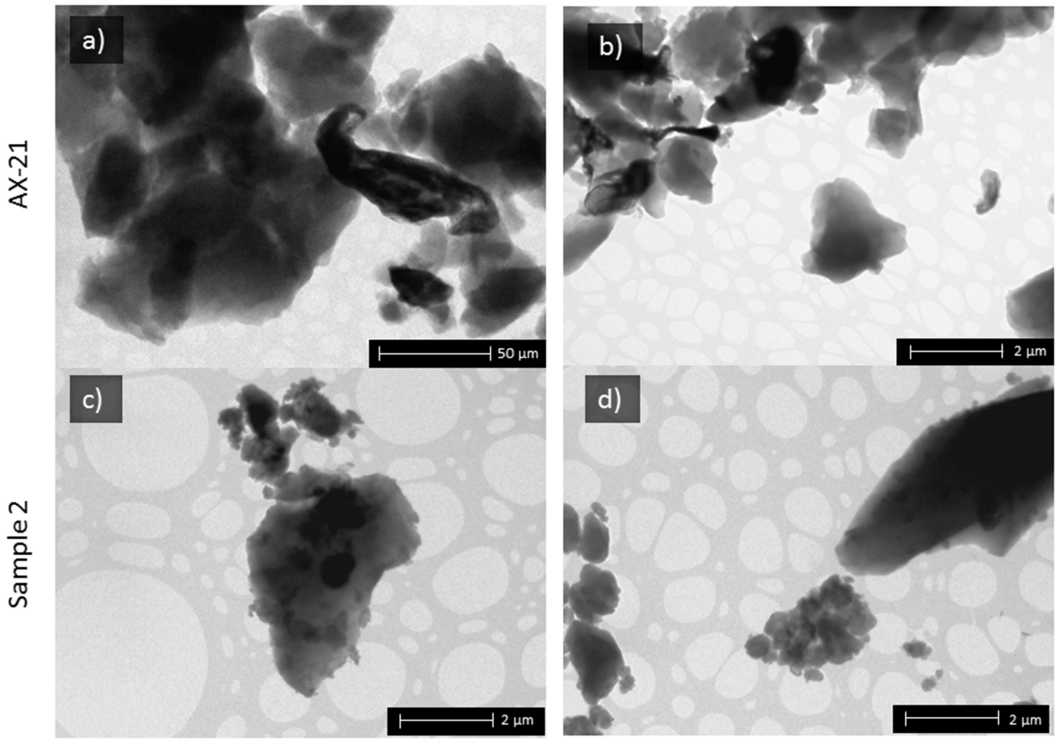

Figure 4-22. Bright field TEM images of: (a, b) AX-21 and (c, d) sample 2.

Figure 4-23 shows different sets of bright field images with their respective EELS mapping. AX-21 showed only carbon and oxygen presence as already confirmed by EDX characterisation (2b in Figure 4-21). It can be seen oxygen is mainly present in the bulk of the carbon particle rather than the edges. In the EELS mapping of sample 2 (Figure 4-23.c and d) it can be seen that there is a good distribution of Al over the carbon particle, and more specifically the edges of the particles. It can be assumed then that $LiAlH_4$ would be found predominantly at the edges of the carbon particle, potentially blocking the pores. The EELS mapping distribution of the elements is in good accordance with that of $LiBH_4$ confined in activated carbon nanofibers as reported in the literature.[43]

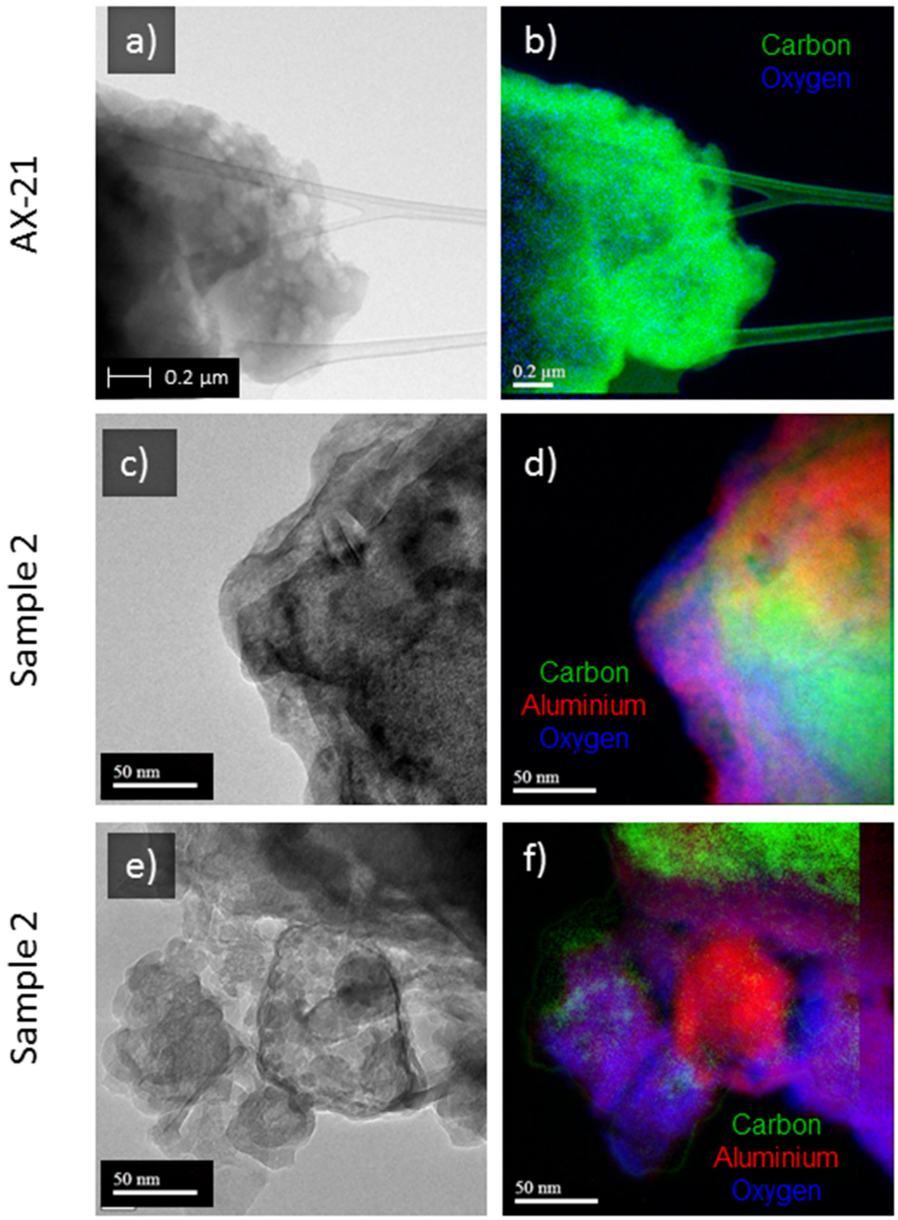

Figure 4-23. Bright field TEM images (a,c,e) and their respective colour false EELS mapping images from: (b) AX-21 and (d,f) sample 2. Further supplementary data available.[41]

Figure 4-24 shows a comparison of Raman spectra obtained for different samples. Two different spectra are presented for sample 1 (c and d). They originate from different regions of the same sample. Figure 4-24c shows only presence of D and G bands characteristic from the carbon host. Figure 4-24d however, shows only bands characteristic of $LiAlH_4$ vibrations (as observed in Figure 4-8). This indicates a heterogeneous mixture of these 2 materials in the sample. However, in sample 2 only D and G bands characteristic from the carbon host were observed, indicating a much better dispersion of the alanate within the porous host. Previous results on melt infiltration of $NaAlH_4$ in a nanoporous carbon material also did not show any characteristic $NaAlH_4$ vibrations on the confined material.[44]

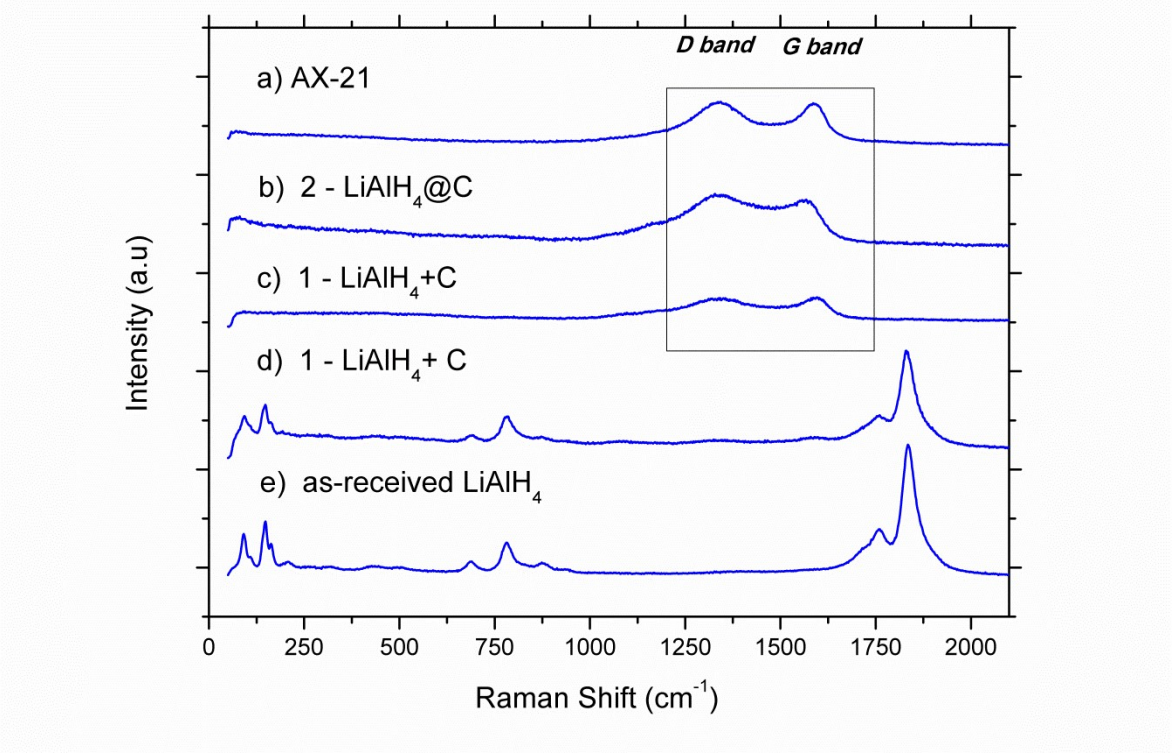

Figure 4-24. Comparison of Raman spectra obtained from samples: a) AX-21, b) sample 2, c,d) different regions of sample 1, and e) as-received $LiAlH_4$.

Figure 4-25 shows a comparison of XRD patterns obtained from as-received $LiAlH_4$, sample 1 and 2. Sample 1 shows a noticeable decrease of the intensity of the reflections in comparison with the ones of the as-received $LiAlH_4$, but all of the expected alanate reflections remain present. This is expected from the introduction of an amorphous material such as AX-21. The XRD pattern obtained from sample 2, shows a much more amorphous behaviour, with a very distinctive broad band, centred at 15- 35 ° 2ϑ, characteristic of AX-21. Some characteristic reflections from $LiAlH_4$ can still be observed, although their intensities are low compared to the physically mixed sample. The difference between the relative intensities from the two samples suggests that the solution treatment, at the very least, drastically changes the dispersion of $LiAlH_4$ with carbon (which is also suggested by Raman spectroscopy in Figure 4-24) and indicates that $LiAlH_4$ has been impregnated in the porous hosts. This decrease of intensity in the characteristic reflections of the confined material has also been observed in the powder XRD of other confined alanates ($NaAlH_4$).[45]

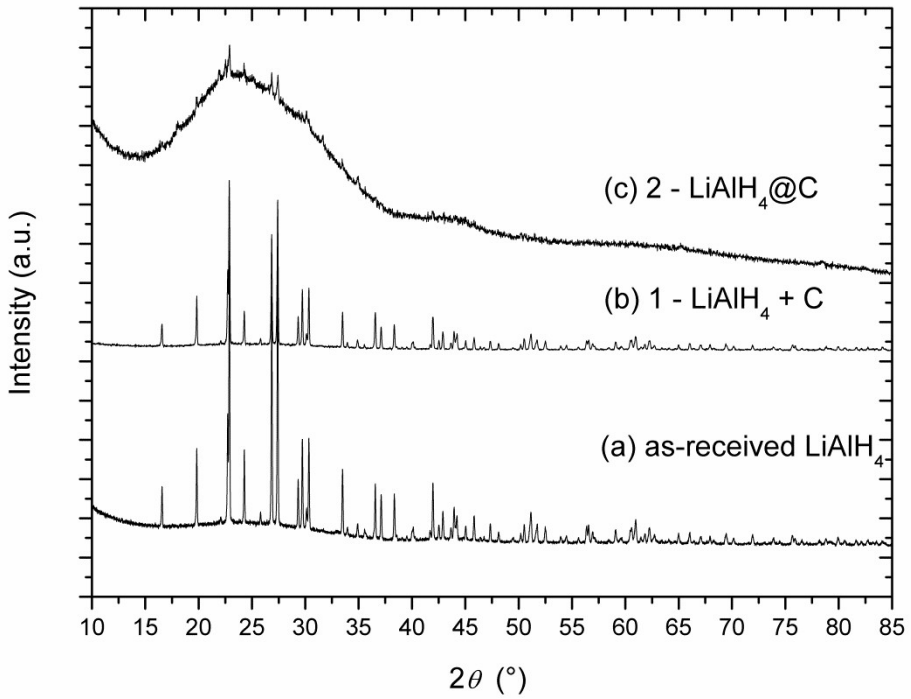

Figure 4-25. XRD patterns obtained for as-received a) $LiAlH_4$, b) sample 1 and c) sample 2.

4.3.3.2. Dehydrogenation studies

DTA profiles of different samples are shown in Figure 4-26 for comparison. The samples correspond to as-received $LiAlH_4$, sample 1 and 2. Table 4-8 collects the data from Figure 4-26 for each sample. The DTA profile of the sample 1 is very similar to that of the as-received sample; the major difference being in the apparent absence of the endothermic peak at 160.5 °C which contrasts with the sharp, intense peak from the as-received sample at 166.7 °C. The small intensity peak observed at 143.6 °C for the as-received $LiAlH_4$, and assigned by Dymova, et.al[3] to the reaction between traces of hydroxide impurities reacting with the hydride atoms from the alanate, is also observed in sample 1. However, in sample 1 the event is observed over a wider temperature range (from 135.6 - 146.5 °C). Introduction of hydroxide impurities by the carbon host, apart from the ones present in $LiAlH_4$, might be the cause of this. The temperatures of decomposition for $LiAlH_4$, Li_3AlH_6 and LiH happen at slightly lower temperatures than for the as-received product. Therefore, it seems that the porous carbon AX-21, in physical contact with $LiAlH_4$, can lower the hydrogen desorption temperatures from between 5 to 13 °C, probably due to electronic support effects. It has been observed that the presence of π-electron density close

to the carbon support might influence the ionic bonding strength between Na^+ and AlH_4^- units in $NaAlH_4$,[46] lowering the dehydrogenation temperatures. A similar effect might be expected for $LiAlH_4$.

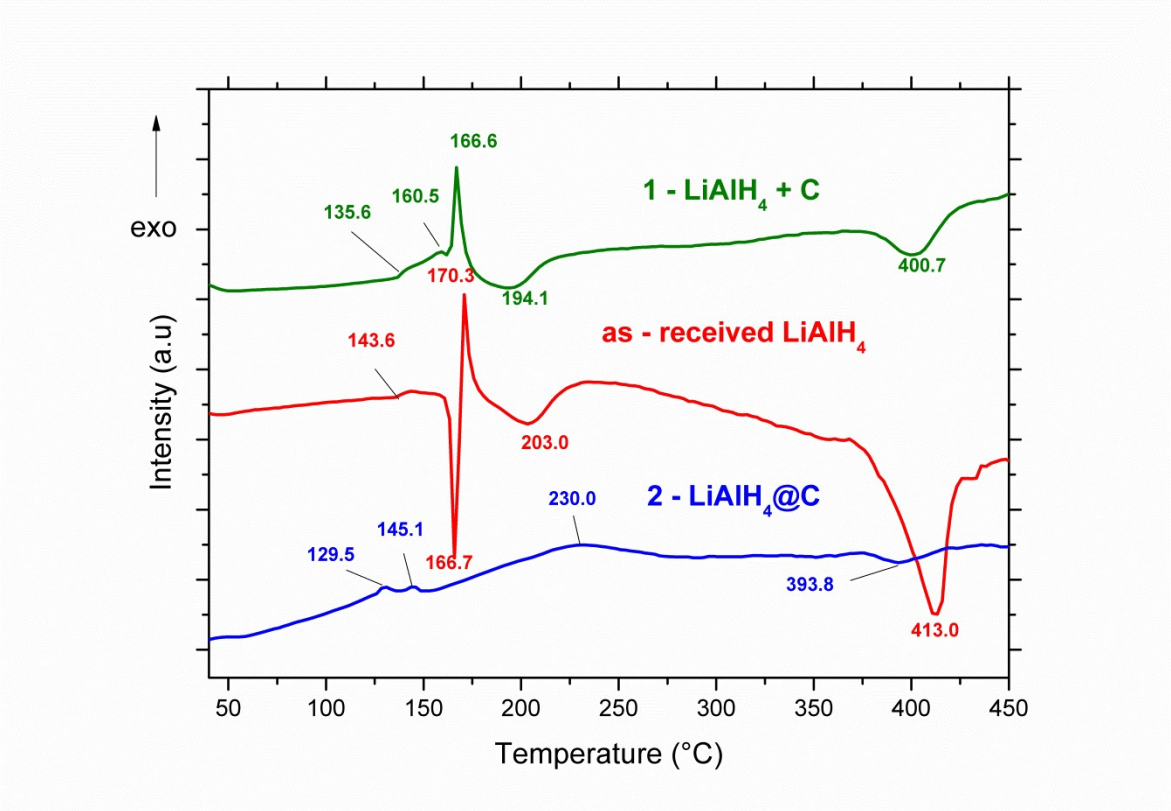

Figure 4-26. Comparison DTA profiles (simultaneously recorded with the TGA profile on Figure 4-28) of as-received $LiAlH_4$, sample 1 and 2, at 2 °C·min^{-1} until 450 °C.

The DTA profile of sample 2 is quite different to either of the two previous profiles. Two small exothermic peaks are observed at 129.5 °C and 145.1 °C, and there is no evident sign of any further event in Figure 4-26. However, a magnification of the DTA profile (Figure 4-27), along with the simultaneous corresponding TGA profile, shows other thermal events more clearly such as an exothermic peak with a maximum at 230 °C (not seen in the as-received $LiAlH_4$), and an endothermic event at 393.8 °C (in good agreement with LiH decomposition). The first two peaks coincide with the start of mass loss on the TG profile in Figure 4-27, but it is difficult to assign them to a characteristic $LiAlH_4$ thermal event or reaction (Table 4-8), because of the difference in shape and position of the peaks of the confined sample when compared to the as-received material.

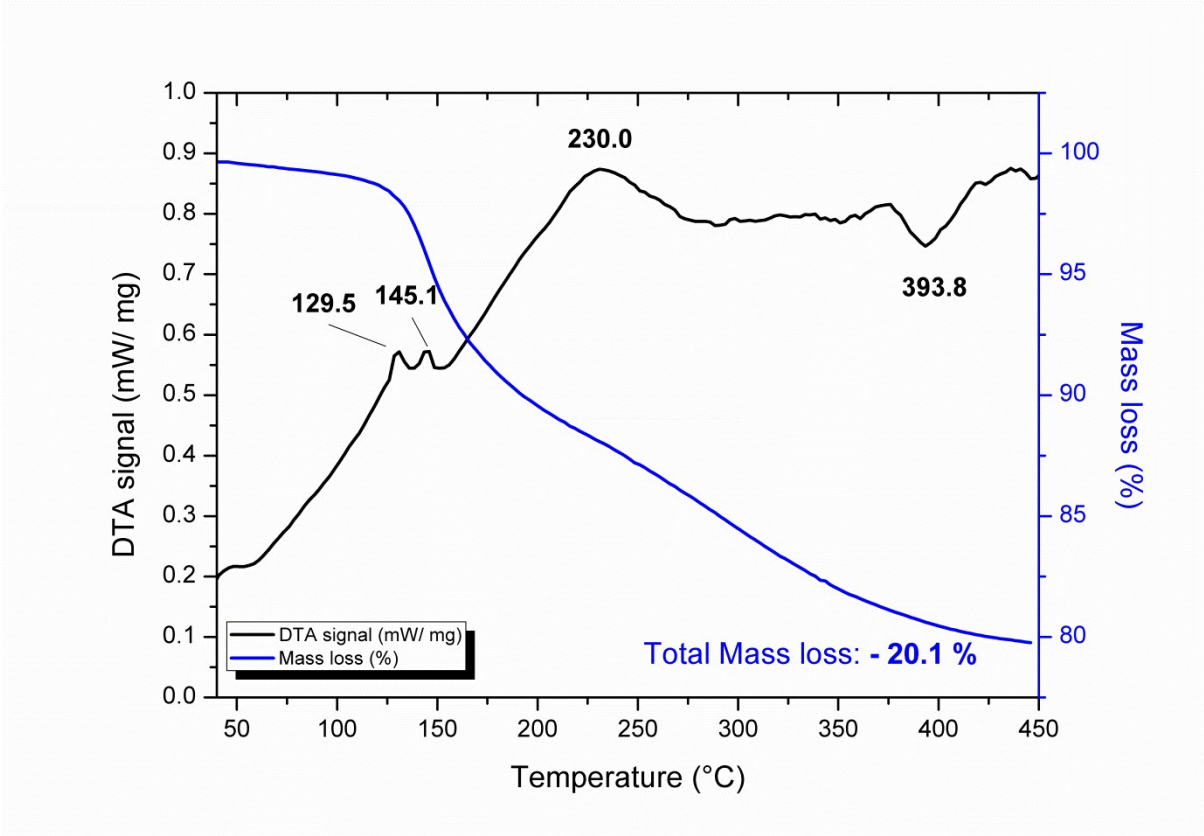

Figure 4-27. DTA and TG plots for sample 2, under a thermal treatment to 450 °C at 2°·min^{-1}.

Sample 2 has a very different behaviour from its analogue, sample 1. Therefore, it leads us to assume that the confinement approach has changed the nature of the samples, improving the hydrogen storage properties by decreasing the temperature that hydrogen is released with respect to that of the as-received $LiAlH_4$.

Table 4-8 summarizes the DTA shown in Figure 4-26, and assigns them to the respective thermal events.

Table 4-8. Summary of the events recorded on the DTA profile for each sample (from Figure 4-26) and their corresponding reaction assignment (when possible).

$LiAlH_4$	Sample 1	Reaction Assignment	Sample 2
143.6	135.6	-Al-OH + -Al-H→ -Al-O-Al- + H_2 [3]	129.5
166.7	160.5	Melting $LiAlH_4$	145.1
170.3	166.6	Decomposition $LiAlH_4$	
203	194.1	Decomposition Li_3AlH_6	230.0
413	400.7	Decomposition LiH	393.8

Figure 4-28 shows a comparison between the TG profiles of as-received $LiAlH_4$, sample 1 and 2. The theoretical content of hydrogen in $LiAlH_4$ is 10.5 wt.%, but experimentally from the TG results only 9.3 wt.% could be achieved as described in Section 4.3.1.2. This value will be considered as the maximum experimentally achievable for comparative purposes. Sample 1 showed a mass loss of 4.6 wt.%. which is in good agreement with the expected value, considering that the sample composition was $LiAlH_4$: AX-21 at a 50 : 50 weight ratio (9.3 / 2 = 4.65 % w.t.). The profile of the TG curve also has the same shape as that of the as-received material, with the distinctive 3 mass losses corresponding to the 3 dehydrogenation steps of the as-received $LiAlH_4$. However, the mass loss observed for sample 2 is 20.1 % w.t., much higher than expected. Considering that the sample composition of this sample was the same as sample 1, a similar mass loss might be expected. The TG profile of the confined sample is also quite different from that of the physical mixture and the as-received $LiAlH_4$. The mass loss starts earlier than in the other 2 samples, decreasing at a slow rate from 50 to 130 °C, but more obviously after 130 °C. Also, the 3 expected distinctive mass loss steps corresponding to the dehydrogenation steps are not obvious. Instead, it seems that there are 2 distinctive mass losses: one from 130 °C to around 200 °C, and another one from around 200 °C to 300 °C. The dehydrogenation of LiH (last dehydrogenation step) cannot be discerned as a discrete event.

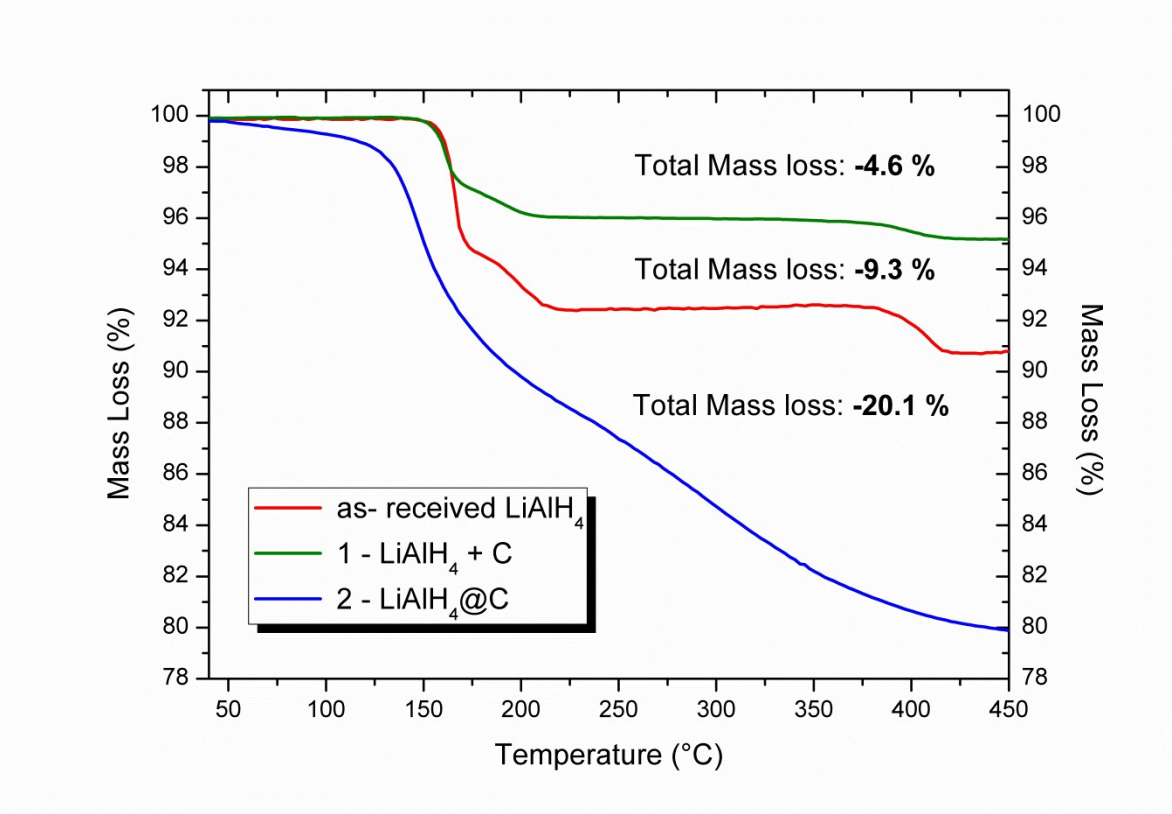

Figure 4-28. Comparison of the TGA profiles of as-received $LiAlH_4$, sample 1 and sample 2 under a thermal treatment to 450 °C at 2 °·min^{-1} under a flow of Argon gas.

The initial mass loss of sample 2 below 130 °C (ca. 1 wt. %) could originate from traces of solvent still present in the sample. The diethyl ether boiling point is fairly low (34.6 °C),[39] although sample 2 was pre-treated under vacuum at room temperature in the Schlenk line to facilitate solvent removal, and then dried under vacuum at 50 °C for 2 hours. However, the MS data recorded from the TGA/DTA experiment shows only hydrogen evolution with no evidence of diethyl ether or any other gas evolved from the sample (Figure 4-29). The only difference from sample 1 and sample 2, regarding the contents of the samples, is the introduction of solvent. Therefore, it is safe to assume that part of this unexpectedly high mass loss for sample 2 is caused by the solvent, although no fragments of diethyl ether were detected, probably due to a limitation issue of the mass spectrum detector.

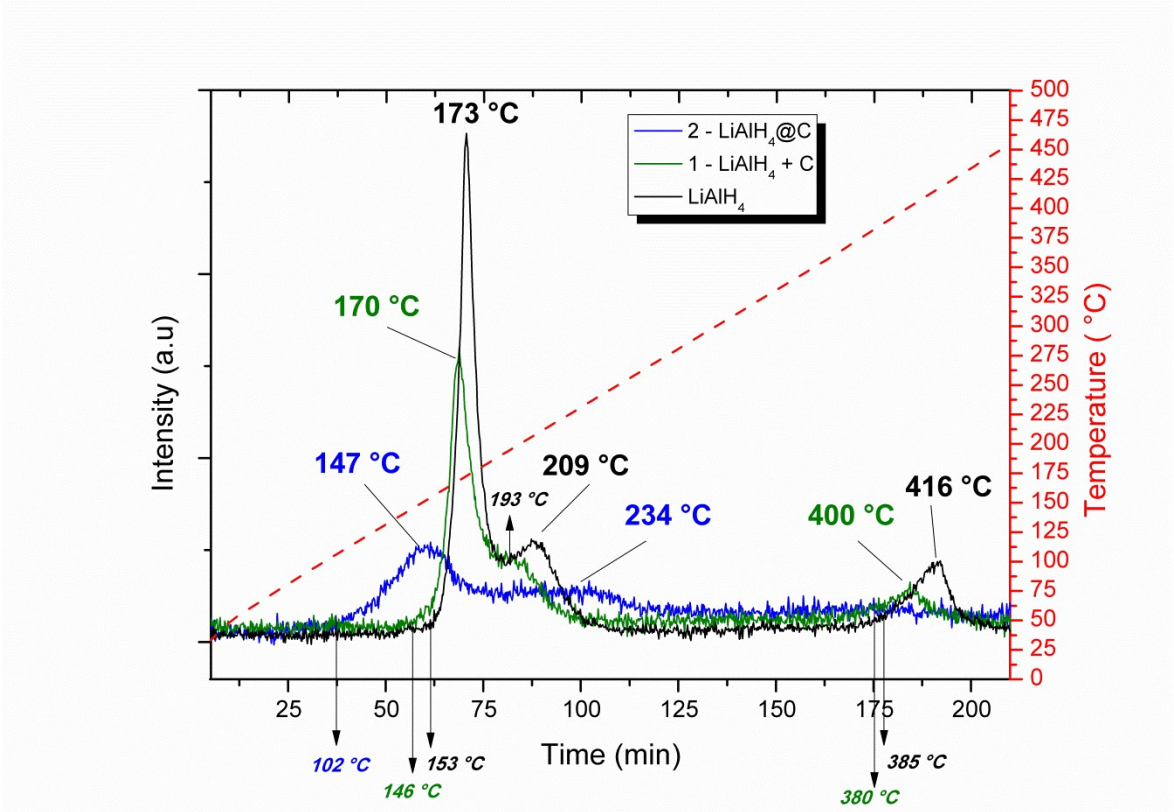

Figure 4-29. MS recording hydrogen release from the STA of as-received $LiAlH_4$, sample 1 and 2 under a thermal treatment to 450 °C at 2°·min^{-1}.

The hydrogen profile of the as-received sample showed the highest relative intensities, as expected due to the fact that more product was used than the other samples, where half the amount of the sample was the porous host and the other half the $LiAlH_4$. Sample 1 has a very similar behaviour to the as-received sample, with hydrogen evolving at a slightly lower temperature than the as-received sample, consistent with the DTA and TG profiles. Sample 2 shows an earlier hydrogen release when compared to the as-received material, a reduction of 26 °C at the maximum of the first (main) hydrogen release and a reduction of 51 °C in the onset temperature of this process. It also can be ruled out that this improvement is only due to the introduction of carbon in the sample: sample 2 starts releasing hydrogen 44 °C earlier than sample 1 and the peak dehydrogenation temperature is lowered by 23 °C. The difference in temperature between the start of hydrogen release and the maximum peak for sample 2 is higher (45 °C) than that of the other samples (20 °C and 24 °C, respectively), due to the fact that for the former the hydrogen release is much more gradual than for both sample 1 and the as-received alanate. Furthermore, no clear peak due to LiH decomposition is observed, although there is still hydrogen desorption above the expected temperature of Li_3AlH_6 decomposition (211 °C for bulk $LiAlH_4$ as observed in Figure 4-30). This means that LiH must at least be partially decomposed at

these temperatures. The fact that no clear hydrogen desorption step was observed for Li_3AlH_6 has been reported before for other similar systems, such as $NaAlH_4$ confined in carbon aerogels.[45,47] The authors speculated that the kinetics for the second decomposition step of Na_3AlH_6 to form NaH was enhanced by the presence of the carbon. Disappearance of a well-defined NaH decomposition step for the NaH was also observed. A possible explanation in the case of sample 2 is that the second decomposition step results in highly dispersed LiH that decomposes over a wide temperature range, reacting with the Al formed upon the decomposition of $LiAlH_4$ and Li_3AlH_6 to form LiAl and hydrogen, according to Eq. 4.3.

The unexpectedly high mass loss for sample 2, leads us to believe that some solvent or moisture are still present in the sample. Eckert, et al. studied the effect that THF had on the confined $LiAlH_4$ in mesoporous carbon CMK-3 by solution impregnation using THF as a solvent,[25] and tracing the most common fragments of THF on the mass spectrometer. A similar study was performed here, with the most common fragments of diethyl ether for sample 2, shown in Figure 4-30 . None of the fragments for diethyl ether or water was detected by the mass spectrometer. It is difficult to say with certainty if there were no solvent-gases evolved, or there were gases evolved but not detected by the mass spectrometer. Inability to detect some of the gases might come from a lack of sensitivity of the instrument or condensation of some gases in the transfer line (line coupling between STA and MS). When dried AX-21 was analysed on the STA a mass loss of 5.76 % was observed below 450 °C, without any detectable gas release in the mass spectrum (Figure 7-2 and Figure 7-3 in the Appendix Section 7.2). The possible explanation for this 5.76 % mass loss might be some impurities blocking the micropores of AX-21, like CO_2, formed by the synthetic process of AX-21, where KOH was used. The concentration of these impurities seemed to be too low to be able to be detected by the mass spectrometer. The mass loss observed for dried carbon therefore might be also contributing to the unexpectedly high mass loss in the confined sample when heated to 450 °C.

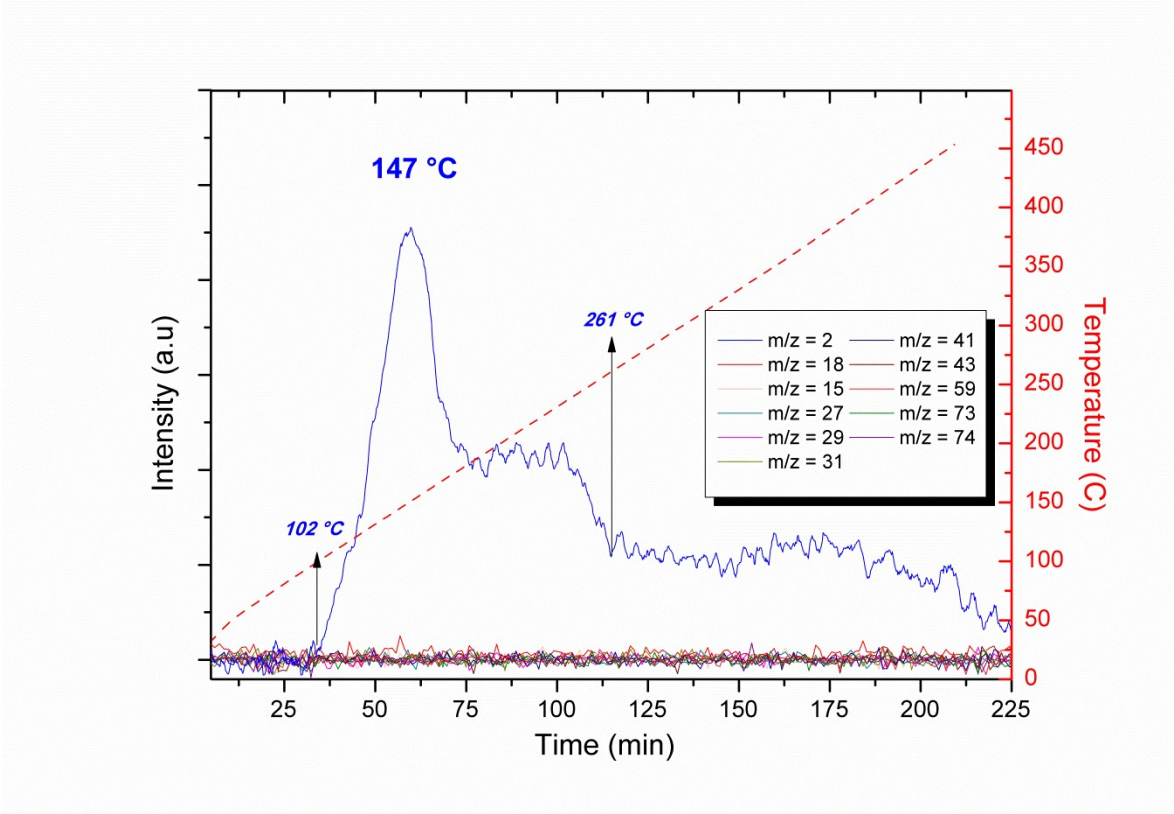

Figure 4-30. MS spectra recording the most common fragments of diethyl ether (m/z = 15, 27, 29, 31, 41, 43, 59, 73, 74), hydrogen and water at 450 °C at 2 °C·min^{-1}.

4.3.3.3. Post thermal treatment structural characterisation

Figure 4-31 shows a comparison between the XRD obtained after thermal treatment to 260 °C of as-received $LiAlH_4$, sample 1 and sample 2. It can clearly be observed that all the samples show the presence of reflections corresponding to LiH / Al phases. The only obvious difference between the patterns is the amorphous broad background in the confined sample ranging from 20 to 35. An interesting characteristic of the pattern obtained from sample 2 is the presence of sharp high intensity reflections when compared with the pattern obtained for the same sample before thermal treatment (Figure 4-25). This leads one to believe that the poor crystallinity of the sample before treatment was due to the fact that $LiAlH_4$ was confined in the pores of the carbon host. At least one of the decomposition products of the second step, Al, forms larger crystallites, which do not fit in the smallest pores, forcing Al migration out of the pores. This seems difficult to be quantified; it can be confirmed that some Al is located outside the pores but it is unclear if some Al remains in the pores. Dehydrogenation products migrating out of the pores is a common effect observed in alanates and borohydrides confined in porous hosts. De Jongh, et. al observed presence of Al, one of the decomposition products of $NaAlH_4$, when a confined sample in porous

carbon was heated after dehydrogenation.[17] Confined $LiBH_4$ after dehydrogenation also showed presence of LiH.[20,48] In both cases, the XRD pattern of the composite before dehydrogenation showed no reflections of the starting material.

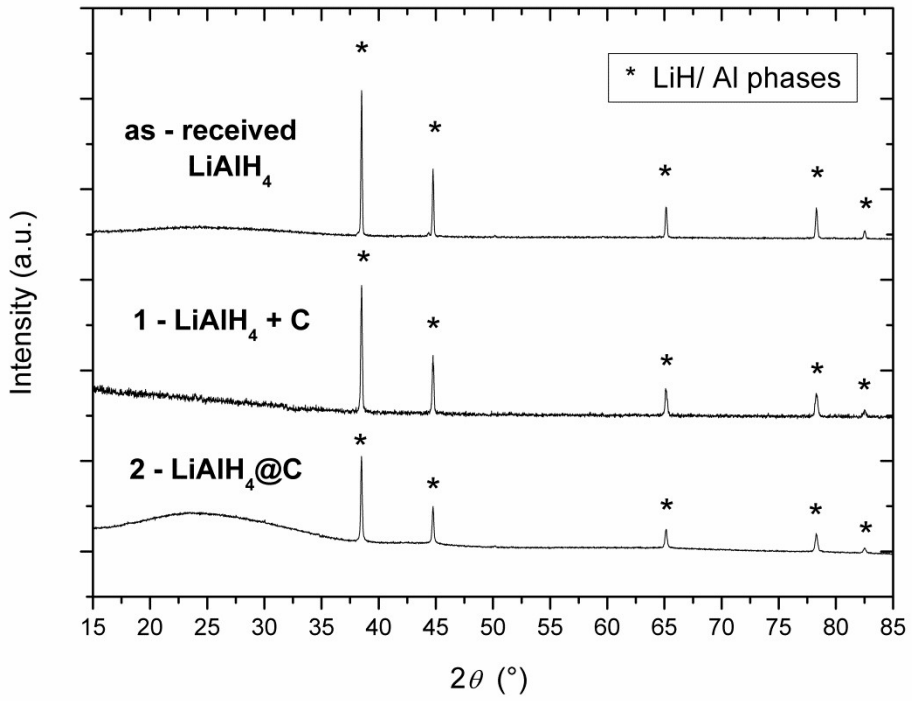

Figure 4-31. XRD patterns obtained for as-received $LiAlH_4$, sample 1 and 2 after being heated to 260 °C at 2 °C·min^{-1}.

Figure 4-32 shows a comparison between the XRD patterns obtained after thermal treatment to 450 °C of as-received $LiAlH_4$, sample 1 and sample 2. Most of the reflections for the as-received sample correspond to the fully dehydrogenated product in the Li-Al-H system (LiAl), with some low intensity peaks corresponding to remaining LiH/Al phases. However, for both sample 1 and 2 there is clear mixture of LiH/Al and LiAl, suggesting that the 3rd dehydrogenation step remains incomplete. The relative intensities of the LiAl reflections are higher in sample 1 than those for LiAl in sample 2. This evidence, suggests that the presence of carbon is altering the decomposition pathway of the $LiAlH_4$ system, significantly in the case of last dehydrogenation step. This can be also observed in the mass spectra shown in Figure 4-29, where the hydrogen desorption at higher temperatures for sample 1 show a weak release, and no well-defined peak for the dehydrogenation of LiH in sample 2. A possible explanation could be that the LiH/Al distribution within the carbon pores or on the carbon surface inhibits the reaction between the phases that

would normally lead to LiAl formation. The effect is more pronounced in sample 2, and would be consistent with one of the dehydrogenated phases, presumably some Al, migrating out of the pores. So assuming that Al and LiH are not in close contact with each other it could explain the difference in intensity of the LiAl reflections from the as-received sample and samples 1 and 2. The difference in relative intensity of the LiAl reflections between samples 1 and 2 could be explained by a longer distance between LiH and Al particles or from LiH and Al forming LiAl inside the pores, which could not be detected. Nevertheless, it seems clear that for sample 2 at least a certain degree of Al particles and LiAl remain outside of the pores, corroborating the findings of some Al particles migrating out of the pores observed in sample 2 treated at 260 °C.

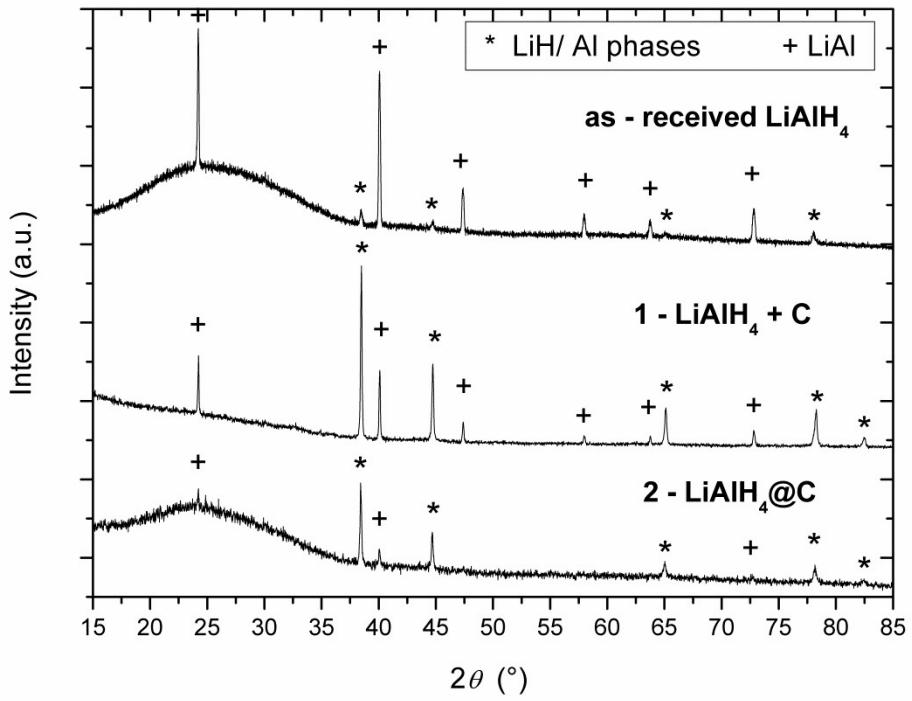

Figure 4-32. XRD patterns obtained for as-received $LiAlH_4$, sample 1 and 2 after being treated to 450 °C at a heating rate of 2°·min^{-1}.

4.3.4. $LiAlH_4$ confinement in FDU-15

The experimental methods for the confinement of $LiAlH_4$ in FDU-15 are the same as those used for confinement of $LiAlH_4$ in AX-21. The only difference is the amount of carbon with respect to $LiAlH_4$, given by the available pore volume of the porous carbon host used (see calculations in Appendix Section 7.2).

4.3.4.1. Structural characterization

SEM images in Figure 4-33a and Figure 4-34a show the particle morphology and particle size and the particle size distribution of samples 3 and 4 respectively. Sample 3 shows two different distinct particle sizes and shapes, presumably carbon particles and $LiAlH_4$, according to characteristic particle sizes and shapes of FDU-15 and $LiAlH_4$ particles reported in Chapter 3 and Figure 4-17 respectively. This heterogeneous mixture of both carbon and $LiAlH_4$ can be observed in the histogram in Figure 4-33b, where there is a region of smaller particles, ranging from 6 – 18 µm across and a another region at higher width values. Since the number of small particles is higher in number than that of bigger particles, the contribution of the latter is more important. It can be observed from Table 4-9 that the maximum frequencies and 80% population values for sample 3 are in good accordance with those of as-received $LiAlH_4$.

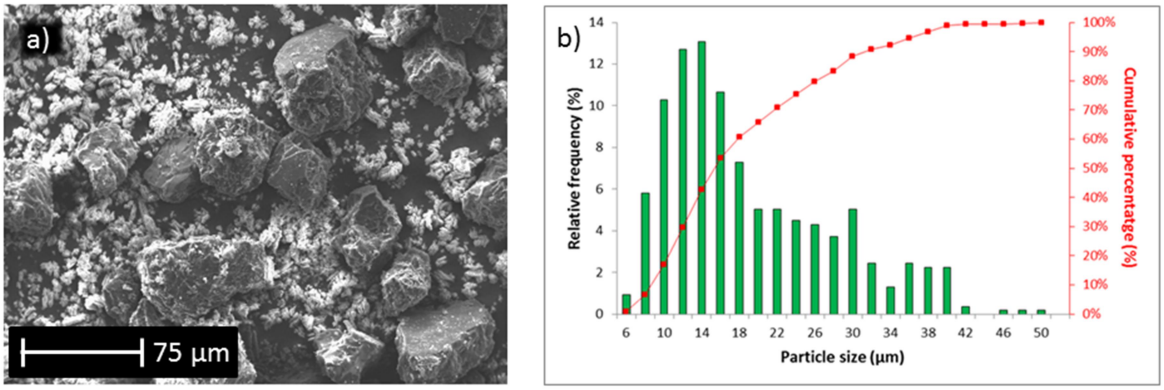

Figure 4-33. a) SEM images of sample 3 and b) Histogram of particle size distribution (µm) with relative frequency (%) and accumulative percentage

The sample 4 particle morphology and particle size is different from that of the sample 3. The main difference is that the particle morphology and sizes seem to be more similar to each other than sample 3. The particle size distribution is more homogenous, with 80 % of the particle sizes

ranging between 9 and 32 µm across, with the maximum relative frequencies between 28 – 30 µm across.

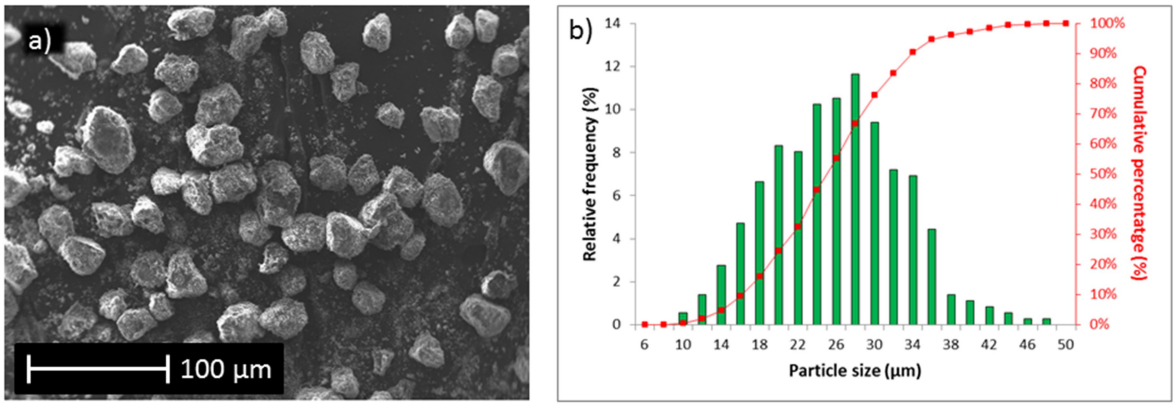

Figure 4-34. a) SEM images of sample 4 and b) Histogram of particle size distribution (µm) with relative frequency (%) and accumulative percentage.

Table 4-9 collects the data from figures Figure 4-33 and Figure 4-34. The particle size distribution of sample 3 resembles that of as- received $LiAlH_4$ (especially the maximum frequencies), whereas the maximum frequencies of sample 4 resembles those of FDU-15. As reported earlier, the confinement approach has a big impact on the dispersion of $LiAlH_4$ and carbon when compared to a physically mixed sample.

Table 4-9. Summary of the results obtained from figures Figure 4-33 and Figure 4-34.

	Particle size distribution / µm		
Sample	*100 % population*	*80 % population*	*Max. frequency (%)*
FDU – 15	10 – 70	10 – 55	30 – 35
$LiAlH_4$	6 – 62	6 – 26	10 – 12
3	5 - 50	6 - 28	12 - 14
4	9 – 47	9 - 32	28 – 30

Figure 4-35 shows the bright field TEM images of FDU-15 and sample 4. In this case, it is easier to identify the carbon particles than for AX-21, due to the presence of short range order features in the carbon. It can be easily observed from Figure 4-35b-c, the darker spots would correspond to a higher electron density material, in this case $LiAlH_4$, which seems to be supported in the ordered

carbon. It is difficult to tell from Figure 4-35b and Figure 4-35c, if the alanate is actually supported on the carbon, or confined inside the pores of the host. Different contrast in the images suggest that both cases might be possible. These images are very similar to those of Peru, et.al on confinement of $NaBH_4$ into highly-ordered mesoporous carbon.[49]

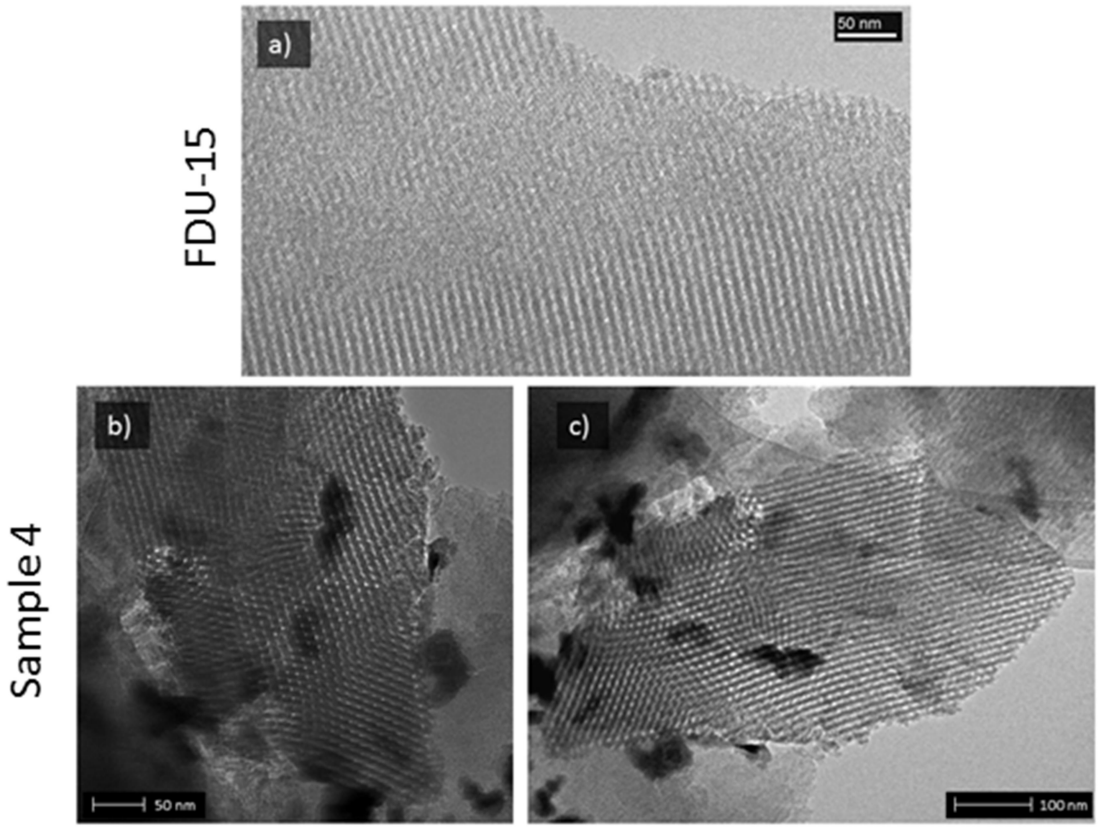

Figure 4-35. Bright field TEM images of FDU-15 (1a) and sample 4 (2a and 2b).

Figure 4-36 shows a comparison of the N_2 absorption isotherms at 77 K of dried FDU-15 and samples 3 and 4. Dried FDU-15 and sample 3 have the same isotherm type IV, characteristic from mesoporous adsorption.[40] Sample 4 exhibits a type II isotherm, from non-porous adsorbents (as observed for sample 2 in AX-21 – Figure 4-16), which indicates a blocking of the pores of the carbon host by the alanate using the confinement approach. Table 4-10 collects the specific surface areas and the total pore volumes of each sample.

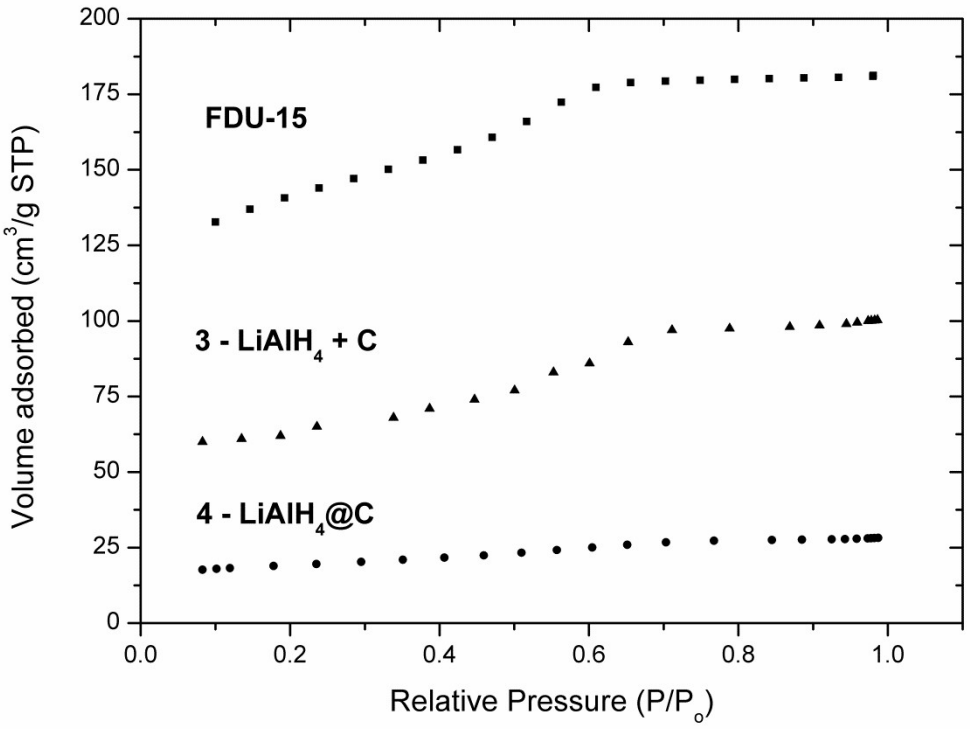

Figure 4-36. Comparison of N_2 absorption/desorption isotherms at 77 K of dried FDU-15, sample 3 and sample 4.

Table 4-10. Summary of the BJH model calculations results for specific BET surface area and total pore volume of each sample.

Sample	BET surface area / $m^2 \cdot g^{-1}$	Total pore Volume / $cm^3 \cdot g^{-1}$
FDU-15	500.7	0.32
3	272.3	0.18
4	19.7	0.07

Figure 4-37 illustrates a comparison of the PXRD patterns obtained from sample 3 and 4, as-received $LiAlH_4$ and FDU-15. As was shown in the case of AX-21 in sample 2 (Figure 4-25), sample

4 exhibits a considerable loss of intensity in the characteristic $LiAlH_4$ reflections, when the alanate is confined. It also shows the characteristic broad background characteristic from FDU-15. When the alanate is physically mixed with FDU-15, (sample 3) characteristic Bragg reflections of $LiAlH_4$ are more intense and resembles those from as-received $LiAlH_4$.

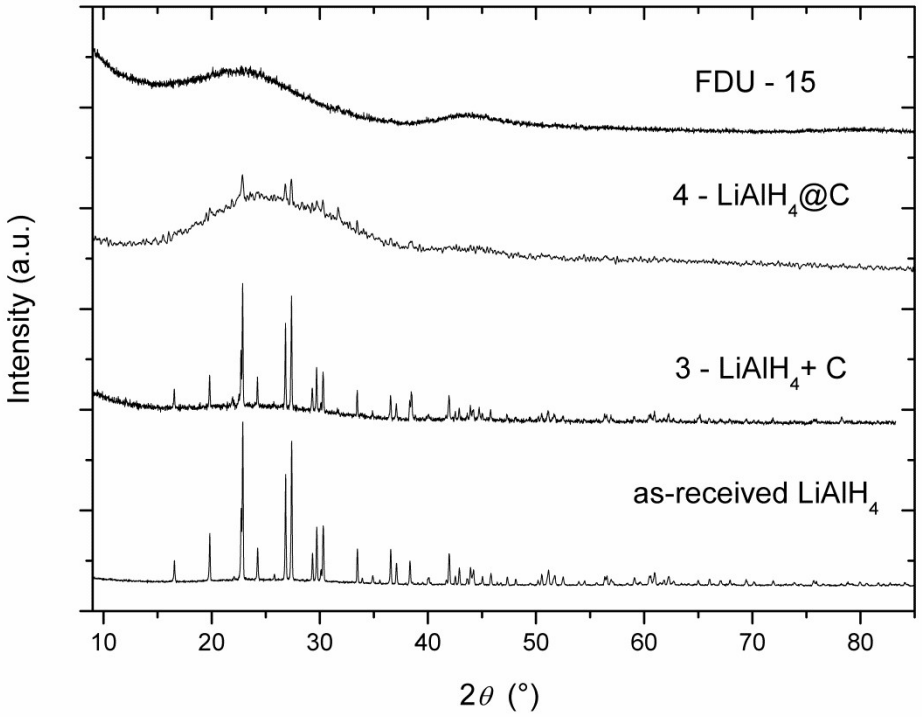

Figure 4-37. XRD patterns obtained for as-received $LiAlH_4$, FDU-15, sample 3 and 4.

4.3.4.2. Dehydrogenation studies

Figure 4-38 shows the comparison of the DTA profile for sample 3 and 4 and as-received $LiAlH_4$. As can also be seen for sample 1 in Figure 4-26, sample 3 has similar features to as-received $LiAlH_4$, such as the exothermic peak corresponding to the $LiAlH_4$ decomposition, the broad endothermic peak corresponding to Li_3AlH_6 decomposition and the endothermic peak at higher temperatures due to LiH decomposition. However, some differences are present because of the presence of carbon, such as a shift of the thermal events to slightly lower temperatures. This might be induced by the electronic effects of the carbon being in contact with $LiAlH_4$ particles, as was discussed above. As was also observed for sample 1, in sample 3 there is an absence of the sharp endothermic peak corresponding to $LiAlH_4$ melting. As observed in sample 2 in comparison with other AX-21 samples, the DTA profile of sample 4 looks quite different from those of sample 3 and as-received $LiAlH_4$, only showing two small-intensity exothermic peaks at 126 and 156 °C. The

endothermic peak corresponding to the decomposition of LiH at 388 °C is barely visible. As can be seen in Table 4-11, it is difficult to assign the peaks observed in sample 4 to a certain reaction or thermal event characteristic from the as-received $LiAlH_4$. This loss of characteristic DTA peaks seen in bulk hydrides has been reported when confining other alanates in porous carbons; thermal events can be difficult to distinguish in such cases.[17,24]

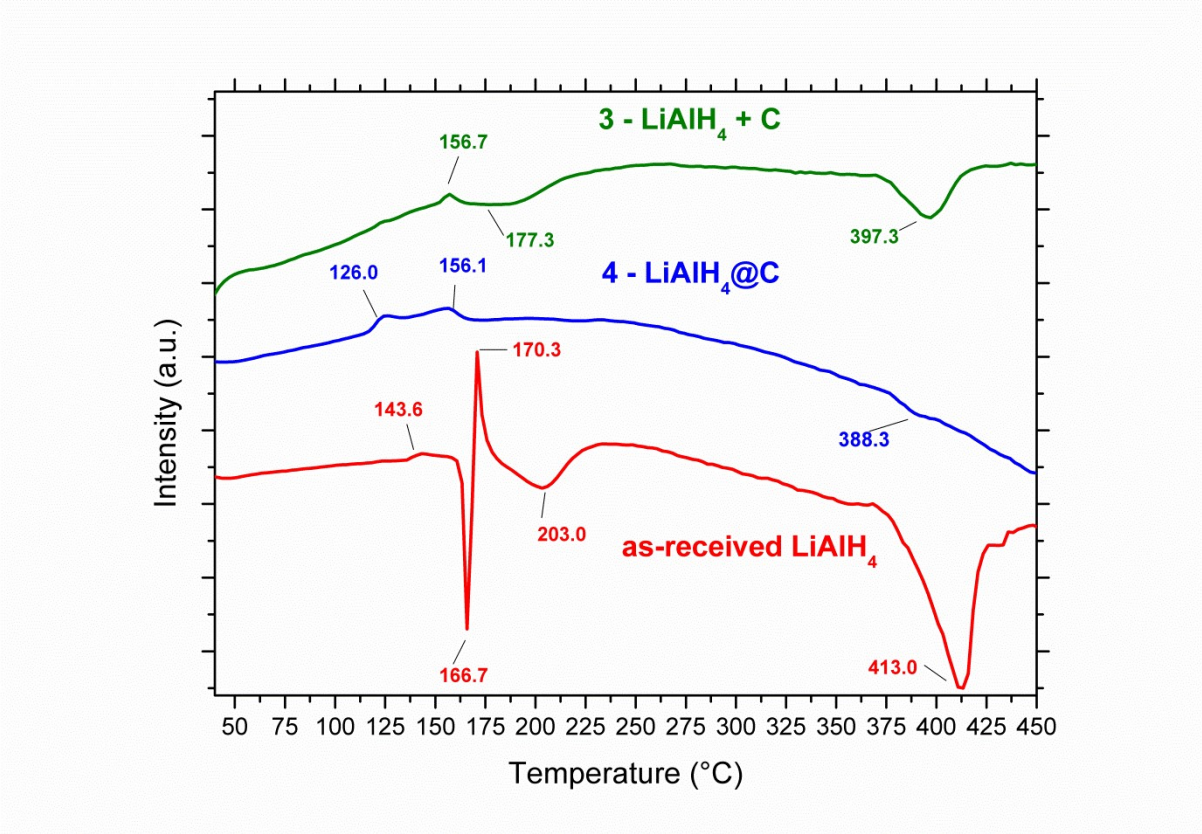

Figure 4-38. Comparative DTA profiles of as-received $LiAlH_4$, sample 3 and 4, at at 2 °C·min^{-1} to 450 °C.

Table 4-11. Summary of the events recorded from the DTA profiles for each sample (from Figure 4-26) and their corresponding assignments (where possible).

$LiAlH_4$	Sample 3	Reaction Assignment	Sample 4
143.6	-	-Al-OH + -Al-H→ -Al-O-Al- + H_2[3]	126.0
166.7	-	Melting $LiAlH_4$	
170.3	156.7	Decomposition $LiAlH_4$	156.1
203	194.1	Decomposition Li_3AlH_6	
413	397.3	Decomposition LiH	388.3

Figure 4-39 shows a comparison between the TG profiles of as-received $LiAlH_4$ and samples 3 and 4. The 3 decomposition steps of $LiAlH_4$ are clearly visible in sample 3, with the obvious difference that the total mass loss is lower due to the quantity of carbon ("dead weight") introduced in sample 3. The mass loss onset for sample 3 is slightly shifted to lower temperatures, possibly due to the electronic effects when introducing carbon to the sample. However, in sample 4 the mass loss is completely different from sample 3 and as-received $LiAlH_4$. The characteristic mass losses associated with each decomposition step in $LiAlH_4$ are not distinguishable and the sample starts losing weight at 60 °C, continuously until it stabilizes around 425 °C. The decline in mass from 100 °C to 175 °C seems to be irregular and it is impossible to distinguish and assign them. Above 175 °C the decline in mass seems smother and more regular. The total mass loss in sample 3 and 4 should have been the same, which indicates that retained solvent might be contributing to the unexpectedly high mass loss for sample 4. However, no trace of any of the most common fragments for diethyl ether was detected in the mass spectrometer, as reported for the confinement of $LiAlH_4$ in AX-21, sample 2 in Figure 4-30.

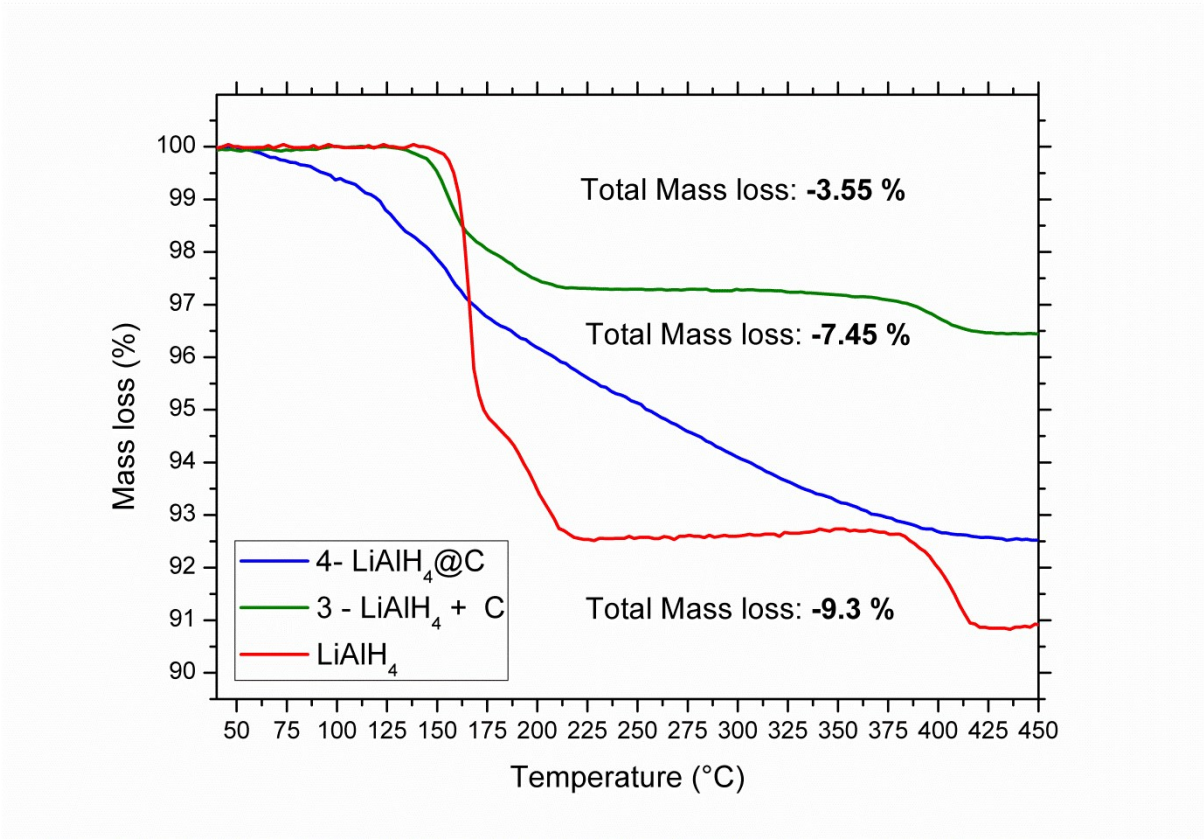

Figure 4-39. Comparative TGA profiles of as-received $LiAlH_4$, sample 3 and 4, at 2°C·min^{-1} to 450 °C.

The hydrogen release of samples 3 and 4 and as-received $LiAlH_4$ is shown with the variation of time and temperature in Figure 4-40. As observed in the DTA and TG profiles, sample 3 shows hydrogen releases that are shifted to slightly lower temperatures than the as-received material in the 1st and 3rd decomposition step. The 2nd decomposition step, corresponding to Li_3AlH_6 is not as obvious as in the bulk material, but it can be intuited. For sample 4, hydrogen release is detected at much lower temperatures than in as-received $LiAlH_4$, starting very smoothly at around 103 °C and reaching a maximum at 151 °C. After reaching the maximum intensity, the hydrogen desorption decreases considerably but remains present at temperatures over 200 °C. The distinctive hydrogen release associated with the LiH decomposition is not seen for sample 4, although the presence of LiAl in the PXRD pattern shows that this last step has taken place, as was also observed for sample 2 (Section 4.3.3.3).

Further comparison of the hydrogen release between samples 2 and 4 will be included at the end of the chapter.

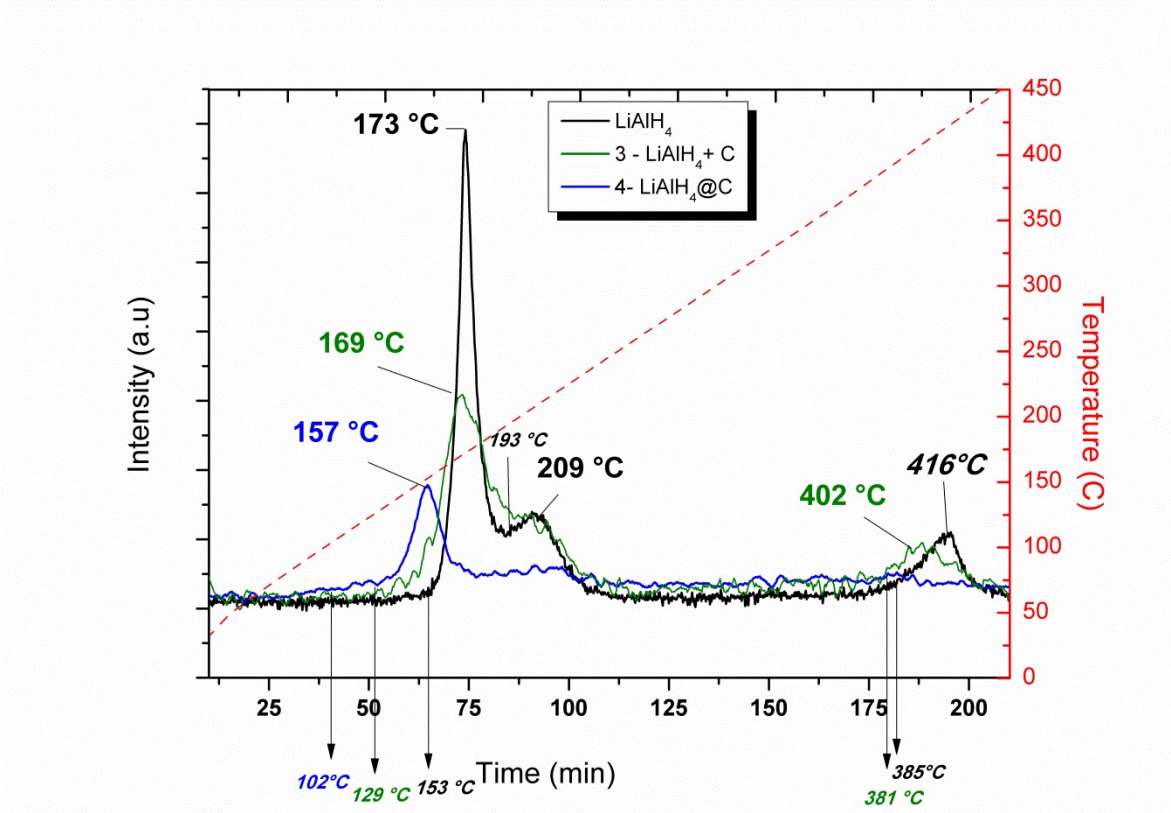

Figure 4-40. Mass Spectra for hydrogen release from the STA of as-received $LiAlH_4$, sample 3 and 4 under a thermal treatment to 450 °C at 2°·min^{-1}.

Table 4-12. Summary of the results obtained in Figure 4-40.

Sample	1st peak		2nd peak		3rd peak	
	Start T / °C	Max T / °C	Start T / °C	Max T / °C	Start T / °C	Max T / °C
as-received $LiAlH_4$	153	173	195	211	385	410
3	129	169	-	-	381	402
4	102	157	-	-	-	-

4.3.4.3. Post thermal treatment structural characterisation

Figure 4-41 shows a comparison between the XRD obtained after thermal treatment to 260 °C of samples 3 and 4 and as-received $LiAlH_4$ for comparison. The three patterns showed characteristic Bragg reflections of LiH and Al phases. Not much difference can be observed between the XRD patterns after thermal treatment after 260 °C for samples 1-2 and 3-4. LiH reflections are overlapped with Al ones at low angles and not present at higher angles, where Al reflections are still present. The only observable difference is the characteristic background from the carbon host FDU-15 in sample 4. Although this is not that obvious in sample 3, it is also present (intensity has been readjusted for comparative purposes). Sample 4 before treatment (Figure 4-37) lost definition of the characteristic $LiAlH_4$ reflections, but after treatment to 260 °C, Al and LiH crystalline reflections are noticeable, suggesting these phases have partially escaped the pores to a certain extent. This is in good agreement with our findings when using AX-21 as a carbon host and some similar work reported in the literature.[17,20,48]

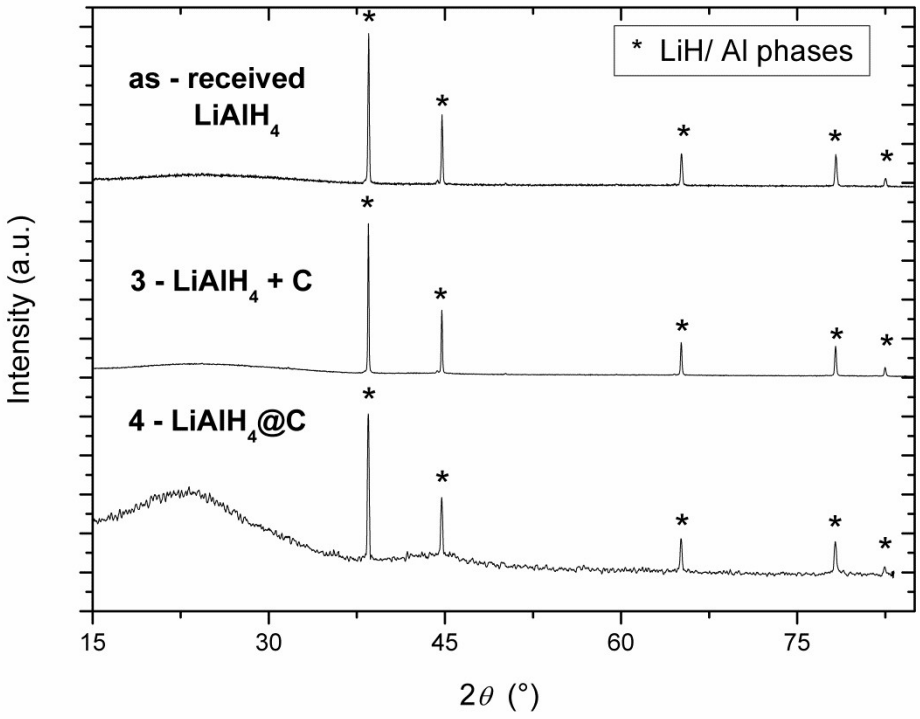

Figure 4-41. XRD patterns obtained for as-received $LiAlH_4$, sample 3 and 4 after being heated to 260 °C at 2 °C·min^{-1}.

Figure 4-42 shows a comparison between the XRD patterns obtained after heating samples 3 and 4 and as-received $LiAlH_4$ to 450 °C. Crystalline reflections from two different phases have been identified in the three samples; LiH/Al and LiAl. The ratio between these two phases varies notably in the three samples. For as-received $LiAlH_4$ the main phase present is LiAl suggesting almost complete dehydrogenation, whereas for sample 4 the main phase is Al and hence probably LiH as well. Sample 3 presents a mixed behaviour, with LiAl more predominant than Al/LiH. Sample 1 showed a similar XRD pattern but with LiH/Al being the predominant phase. Therefore, the 3rd dehydrogenation step is more hindered in sample 1 than in sample 3. This difference might be caused by the particle size of carbon used. An 80 % population of particle size is found at 10-55 µm for FDU-15, 2-16 µm for AX-21 and 6-26 µm for $LiAlH_4$. FDU-15 particles are much bigger than AX-21 and $LiAlH_4$. Due to closeness of particle size, a better and more homogenous dispersion of C and $LiAlH_4$ would be expected for sample 1, than for sample 3. This would make the contact between the decomposition products LiH and Al more difficult, hindering LiAl formation compared to sample 3.

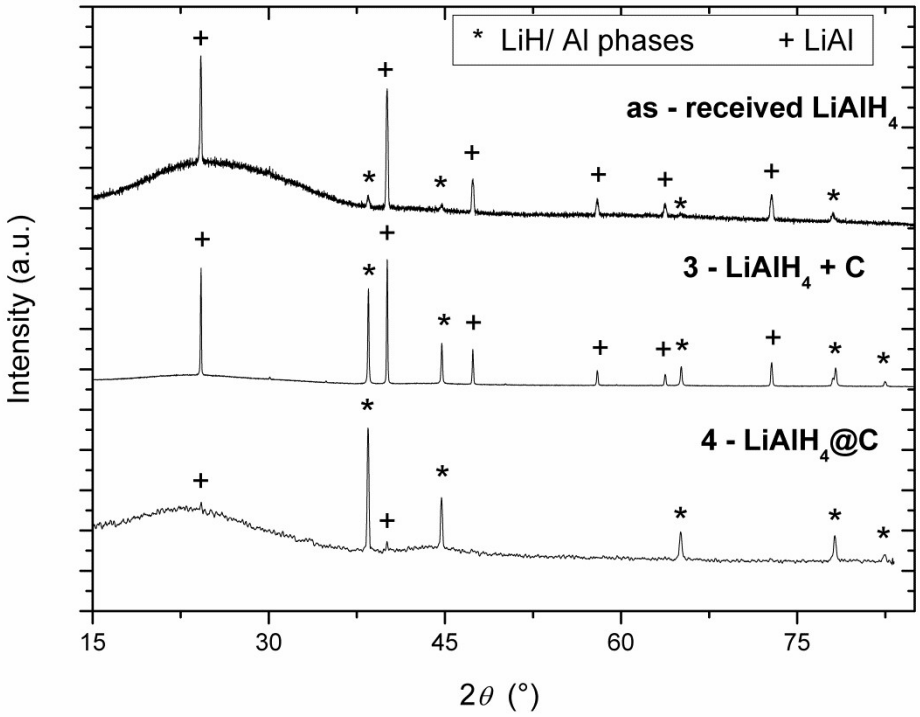

Figure 4-42. Powder XRD patterns obtained for as-received $LiAlH_4$, sample 3 and 4 after being treated to 450 °C at a heating rate of 2°·min^{-1}.

Sample 4 shows a poor intensity of LiAl reflections, implying that the 3rd dehydrogenation step was not completed. Sample 2 showed a similar XRD pattern, in which LiAl was the minority phase. This could be explained by the fact that one of the phases migrates out of the pores, presumably Al, therefore the contact between LiH particles and Al would be reduced. The only significant difference between sample 2 and sample 4 is the intensity of the LiAl reflections, which are slightly higher in the former. One of the possible explanations could be the differences in the porous carbon host used. Since the pores of FDU-15 are more uniform with no significant distribution of pores above 4 nm in diameter, one of the phases in sample 4, would have more difficulties to escape the pores, and preventing the completion of the last dehydrogenation step. Since AX-21 has a rather different pore-size distribution to FDU-15, with the major contribution from pores ranging between 4 and 10 nm but also a significant contribution from pores between 10 and 60 nm, the reaction between LiH and Al in sample 2 would be somehow hindered, but not as much as in sample 2. Confinement in porous hosts of different size have been widely reported[45,50,51] and the pore-size distribution of the porous host has been found to be crucial to tailor the properties of the final composite, although little effort has been put in to analysing the final composite structure and properties.

Comparison hydrogen release between confined samples (sample 2 and 4):

A comparison between the hydrogen evolution of samples 2 and 4 is shown in Figure 4-43. The hydrogen desorption profile for sample 4 looks quite similar to the one of sample 2, with the main difference being the hydrogen release at lower temperatures; both samples start releasing hydrogen around 102 °C, but hydrogen release of sample 4 increases slowly until around 134 °C, when the increase in hydrogen evolved is sharp until it reaches its maximum at 157 °C. In sample 2, the hydrogen release is more regular and continuous from the moment it starts until its maximum at 147 °C. A possible explanation for this can be related to the different pore sizes that the hosts contain. It has been well understood and reported how the size of the pores affects the dispersion of the composite and can lead to hydrogen release at earlier temperatures.[20,50] Since the pore size distribution of the two carbon hosts used is quite different, AX-21 containing a wide range of pores from micropores to macropores and FDU-15 contains mainly mesopores), a different hydrogen release would be expected. The narrower window of pores of FDU-15 gives a sharper hydrogen release, whereas when AX-21 is used there is contribution of different sizes of pores, leading to a more heterogeneous dispersion of $LiAlH_4$. The evolution of hydrogen gas after the first decomposition is present in both sample 2 and sample 4 but not as distinctive as that of as-received $LiAlH_4$.

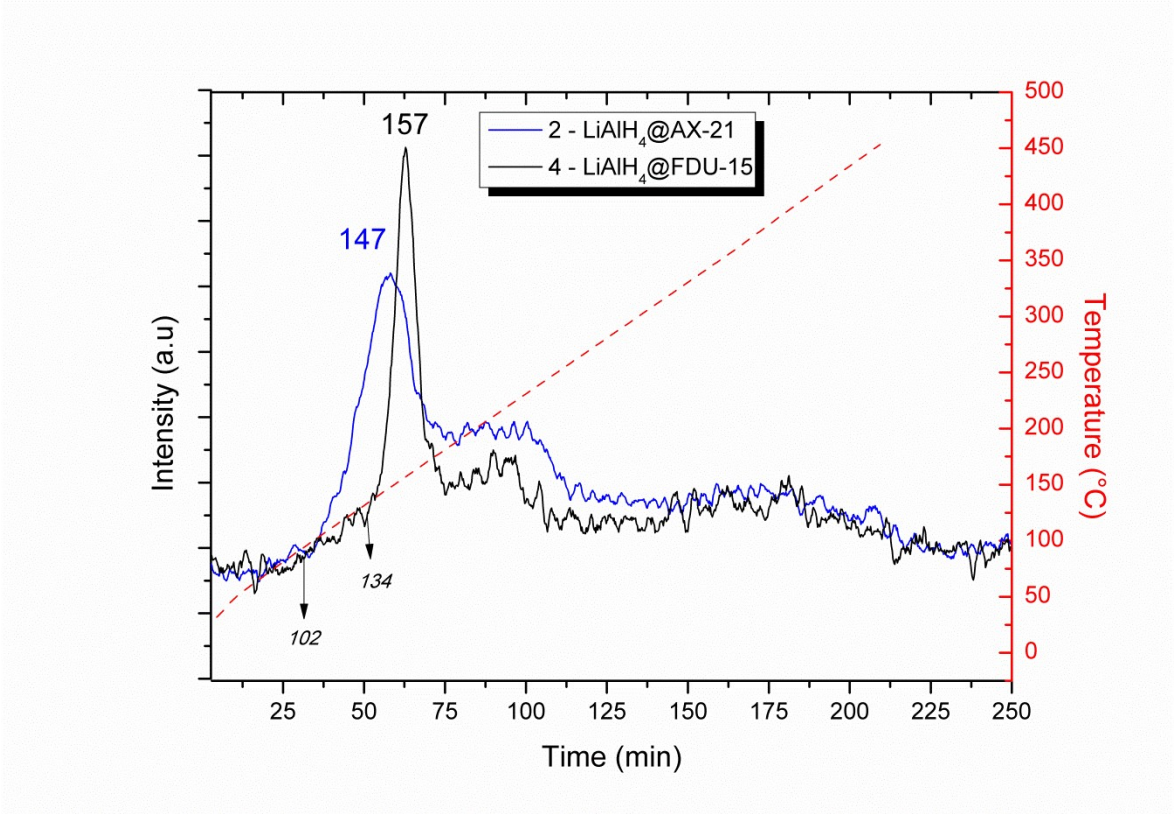

Figure 4-43. Comparative hydrogen release for sample 2 and 4. Further supplementary data available.[41]

From Figure 4-43 and all the previous work reported throughout this chapter it is safe to say that the effect of the pore size on the hydrogen release has been well studied and understood. How the hydrogen release would be affected by the porous host would be defined by the pore size distribution and the specific surface area. Narrow pore-size distributions would give sharp H_2 release, whereas broad pore-size distributions would give a more gradual and broad H_2 release. On the other hand the specific surface area will affect on the amount of product to be confined, and proportionally to the H_2 amount released (or Intensity on the mass detector). The higher the surface area is the higher the amount of product to be confined on the void pore volume, and consequently the higher amount of hydrogen released.

4.4. CONCLUSIONS

The confinement of $LiAlH_4$ in porous carbon has been attempted in order to improve the hydrogen release properties of the alanate, by lowering the temperature and time at which hydrogen is released, to make $LiAlH_4$ a more suitable candidate for hydrogen storage in mobile applications.

After initial characterisation of both host carbons (chapter 3) and the starting material (in this chapter), a wet impregnation approach was adopted by dissolving $LiAlH_4$ in diethyl ether. The solvent was carefully selected, in order to avoid reaction with $LiAlH_4$.

The results obtained for the confinement of $LiAlH_4$ in both carbons showed that the confinement reduced the specific surface area and available pore volume of the carbon host. This indicated a blocking of the pores to a much greater degree than in a physically mixed sample. EDX and EELS mapping results in AX-21 showed a better dispersion of the starting material when confined, although by SEM and TEM images it was difficult to confirm whether the alanate was actually confined inside the porous host or just supported on the outer surface of the carbon particles. Regardless of this, the onset of hydrogen release for the confined $LiAlH_4$ decreased significantly in temperature, being reduced by 51 °C in comparison with as-received $LiAlH_4$.

There is strong evidence that the pore size distribution of the porous host contributes significantly to the profile of the hydrogen release. When using a narrow pore-size distribution carbon like FDU-15 the hydrogen release was sharper, whereas when using a porous carbon with different pore sizes the hydrogen release was more gradual given the contribution of the different types of pore present.

Overall, this work has contributed to lower the dehydrogenation temperatures of $LiAlH_4$ which would be beneficial for hydrogen storage applications, making it a more suitable candidate. A novel confinement approach has been presented and thoroughly studied, proving to have a big impact on the dispersion of the material and its properties. The results of this chapter bring $LiAlH_4$ closer to the DOE requirements for hydrogen storage materials for mobile applications.

4.5. REFERENCES

1. A. E. Finholt, A. C. Bond and H. I. Schlesinger, *Journal of the American Chemical Society*, 1947, **69**, 1199-1203.
2. R. Ehrlich, A. R. Young, G. Rice, J. Dvorak, P. Shapiro and H. F. Smith, *Journal of the American Chemical Society*, 1966, **88**, 858-860.
3. T. N. Dymova, V. N. Konoplev, D. P. Aleksandrov, A. S. Sizareva and T. A. Silina, *Russ. J. Coord. Chem. (Transl. of Koord. Khim.)*, 1995, **21**, 165-172.
4. J. Block and A. P. Gray, *Inorganic Chemistry*, 1965, **4**, 304-305.
5. A. Andreasen, T. Vegge and A. S. Pedersen, *Journal of Solid State Chemistry*, 2005, **178**, 3672-3678.
6. S.-i. Orimo, Y. Nakamori, J. R. Eliseo, A. Züttel and C. M. Jensen, *Chemical Reviews*, 2007, **107**, 4111-4132.
7. R. A. Varin and L. Zbroniec, *Journal of Alloys and Compounds*, 2010, **504**, 89-101.
8. H. W. Brinks, B. C. Hauback, P. Norby and H. Fjellvåg, *Journal of Alloys and Compounds*, 2003, **351**, 222-227.
9. N. Sklar and B. Post, *Inorganic Chemistry*, 1967, **6**, 669-671.
10. B. C. Hauback, H. W. Brinks and H. Fjellvåg, *Journal of Alloys and Compounds*, 2002, **346**, 184-189.
11. V. P. Balema, J. W. Wiench, K. W. Dennis, M. Pruski and V. K. Pecharsky, *Journal of Alloys and Compounds*, 2001, **329**, 108-114.
12. J. Chen, N. Kuriyama, Q. Xu, H. T. Takeshita and T. Sakai, *The Journal of Physical Chemistry B*, 2001, **105**, 11214-11220.
13. X. Liu, G. S. McGrady, H. W. Langmi and C. M. Jensen, *Journal of the American Chemical Society*, 2009, **131**, 5032-5033.
14. H. W. Langmi, G. S. McGrady, X. Liu and C. M. Jensen, *The Journal of Physical Chemistry C*, 2010, **114**, 10666-10669.
15. P. E. de Jongh and P. Adelhelm, *ChemSusChem*, 2010, **3**, 1332-1348.
16. C. P. Baldé, B. P. C. Hereijgers, J. H. Bitter and K. P. de Jong, *Angewandte Chemie International Edition*, 2006, **45**, 3501-3503.
17. J. Gao, P. Adelhelm, M. H. W. Verkuijlen, C. Rongeat, M. Herrich, P. J. M. van Bentum, O. Gutfleisch, A. P. M. Kentgens, K. P. de Jong and P. E. de Jongh, *The Journal of Physical Chemistry C*, 2010, **114**, 4675-4682.

18. T. K. Nielsen, M. Polanski, D. Zasada, P. Javadian, F. Besenbacher, J. Bystrzycki, J. Skibsted and T. R. Jensen, *ACS Nano*, 2011, **5**, 4056-4064.
19. J. Kostka, W. Lohstroh, M. Fichtner and H. Hahn, *The Journal of Physical Chemistry C*, 2007, **111**, 14026-14029.
20. A. F. Gross, J. J. Vajo, S. L. Van Atta and G. L. Olson, *The Journal of Physical Chemistry C*, 2008, **112**, 5651-5657.
21. S. Cahen, J. B. Eymery, R. Janot and J. M. Tarascon, *Journal of Power Sources*, 2009, **189**, 902-908.
22. M. Konarova, A. Tanksale, J. Norberto Beltramini and G. Qing Lu, *Nano Energy*, 2013, **2**, 98-104.
23. C. Zlotea, C. Chevalier-Cesar, E. Leonel, E. Leroy, F. Cuevas, P. Dibandjo, C. Vix-Guterl, T. Martens and M. Latroche, *Faraday Discussions*, 2011, **151**, 117-131.
24. M. Christian and K.-F. Aguey-Zinsou, *Nanoscale*, 2010, **2**, 2587-2590.
25. M. Klose, I. Lindemann, C. B. Minella, K. Pinkert, M. Zier, L. Giebeler, P. Nolis, M. D. Baró, S. Oswald, O. Gutfleisch, H. Ehrenberg and J. Eckert, *Journal of Materials Research*, 2014, **29**, 55-63.
26. C. A. Schneider, W. S. Rasband and K. W. Eliceiri, *Nat Meth*, 2012, **9**, 671-675.
27. P. Vajeeston, P. Ravindran, R. Vidya, H. Fjellvag and A. Kjekshus, *Phys. Rev. B: Condens. Matter Mater. Phys.*, 2003, **68**, 212101/212101-212101/212104.
28. R. S. Chellappa, D. Chandra, S. A. Gramsch, R. J. Hemley, J.-F. Lin and Y. Song, *The Journal of Physical Chemistry B*, 2006, **110**, 11088-11097.
29. J.-C. Bureau, J.-P. Bastide, B. Bonnetot and H. Eddaoudi, *Materials Research Bulletin*, 1985, **20**, 93-98.
30. H. T. Takeshita, Y. Kamada, A. Taniguchi, T. Kiyobayashi, K. Ichii and T. Oishi, *Materials Transactions*, 2006, **47**, 405-408.
31. R. S. Calder, W. Cochran, D. Griffiths and R. D. Lowde, *Journal of Physics and Chemistry of Solids*, 1962, **23**, 621-632.
32. H. M. Otte, *Journal of Applied Physics*, 1961, **32**, 1536-1546.
33. T. Zhang, S. Isobe, Y. Wang, H. Oka, N. Hashimoto and S. Ohnuki, *Journal of Materials Chemistry A*, 2014, **2**, 4361-4365.
34. M. Ismail, Y. Zhao, X. B. Yu, I. P. Nevirkovets and S. X. Dou, *International Journal of Hydrogen Energy*, 2011, **36**, 8327-8334.
35. K. a. M. Kuriyama, N., *Acta Crystallographica Section B*, 1975, **31**, 1793.
36. G. C. Gerrans, P. Hartmann-Petersen and R. Hartmann-Petersen, *Sasol Encyclopaedia of Science and Technology*, New Africa Education, 2004.

37. V. I. Mikheeva and E. A. Troyanovskaya, *Russ Chem Bull*, 1971, **20**, 2497-2500.
38. T. D. Humphries, D. Birkmire, B. C. Hauback, G. S. McGrady and C. M. Jensen, *Journal of Materials Chemistry A*, 2013, **1**, 2974-2977.
39. Chemical Book - CAS DataBase List - Diethyl Ether, http://www.chemicalbook.com/ChemicalProductProperty_EN_CB6853949.htm, (accessed 17/04/2015).
40. K. S. W. Sing, D. H. Everett, R. A. W. Haul, L. Moscou, R. A. Pierotti, J. Rouquerol and T. Siemieniewska, in *Handbook of Heterogeneous Catalysis*, Wiley-VCH Verlag GmbH & Co. KGaA, 2008, DOI: 10.1002/9783527610044.hetcat0065.
41. M. Segales, Supplementary Deposited Data, 2015 http://dx.doi.org/10.5525/GLA.RESEARCHDATA.240
42. E. Roduner, *Chemical Society Reviews*, 2006, **35**, 583-592.
43. S. Thiangviriya and R. Utke, *International Journal of Hydrogen Energy*, 2015, **40**, 4167-4174.
44. D. Colognesi, A. Giannasi, L. Ulivi, M. Zoppi, A. J. Ramirez-Cuesta, A. Roth and M. Fichtner, *The Journal of Physical Chemistry A*, 2011, **115**, 7503-7510.
45. X. Fan, X. Xiao, J. Shao, L. Zhang, S. Li, H. Ge, Q. Wang and L. Chen, *Nano Energy*, 2013, **2**, 995-1003.
46. P. A. Berseth, A. G. Harter, R. Zidan, A. Blomqvist, C. M. Araújo, R. H. Scheicher, R. Ahuja and P. Jena, *Nano Letters*, 2009, **9**, 1501-1505.
47. R. D. Stephens, A. F. Gross, S. L. V. Atta, J. J. Vajo and F. E. Pinkerton, *Nanotechnology*, 2009, **20**, 204018.
48. P. Ngene, P. Adelhelm, A. M. Beale, K. P. de Jong and P. E. de Jongh, *The Journal of Physical Chemistry C*, 2010, **114**, 6163-6168.
49. F. Peru, S. Garroni, R. Campesi, C. Milanese, A. Marini, E. Pellicer, M. D. Baró and G. Mulas, *Journal of Alloys and Compounds*, 2013, **580,** Supplement 1, S309-S312.
50. X. Liu, D. Peaslee, C. Z. Jost, T. F. Baumann and E. H. Majzoub, *Chemistry of Materials*, 2011, **23**, 1331-1336.
51. S. Sepehri, B. Batalla Garcia and G. Cao, *MRS Online Proceedings Library*, 2008, **1098**

Chapter 5

5. NANOCONFINEMENT OF LITHIUM AMIDE IN FDU-15

5.1. INTRODUCTION

Light metal amides have several advantages over other hydrogen storage materials. Amides are interesting because they have high hydrogen content and the hydrogenation/dehydrogenation is partially reversible. The main drawback with amides is the conditions for desorption: usually the temperatures needed for desorption are too high and the hydrogen pressure too low. There is also quite frequently a loss of hydrogen capacity through ammonia loss, which poisons the fuel cell and should be avoided. Recent efforts have been focused on maximising the hydrogen release and minimising ammonia release.

One of the amide system that has been studied in depth as a promising hydrogen store is the Li–N–H system. Chen, et al.[1] originally described a promising hydrogen storage material based on $LiNH_2$ compounds and the Li-N-H system. They showed that lithium nitride (Li_3N) can uptake hydrogen in two steps, forming lithium imide and lithium hydride (Eq. 5-1) and lithium amide and more lithium hydride (Eq. 5-2) respectively. The total theoretical hydrogen capacity is 10.5 wt.% H_2. This made lithium amide, the lightest of amides, a promising hydrogen storage material when combined with lithium hydride, as when heated alone lithium amide decomposes to lithium imide with ammonia release (Eq. 5-3).

$$Li_3N + H_2 \leftrightarrow Li_2NH + LiH \qquad \Delta H = -148.07\ kJ \cdot mol^{-1}\ H_2 \qquad (5\text{-}1)$$

$$Li_2NH + H_2 \leftrightarrow LiNH_2 + LiH \qquad \Delta H = -44.63\ kJ \cdot mol^{-1}\ H_2 \qquad (5\text{-}2)$$

$$LiNH_2 \leftrightarrow Li_2NH + NH_3 \qquad \Delta H = 84.1\ kJ \cdot mol^{-1}\ NH_3 \qquad (5\text{-}3)$$

Unfortunately, the relatively extreme conditions required for the reverse reaction of Eq. 5-1 makes it impractical for hydrogen storage purposes. However, the lithium imide – lithium amide reaction (Eq. 5-2) releases 6.5 w.t % H_2 at 300 °C with favourable thermodynamics.[1] The $LiNH_2$ + LiH decomposition pathway remains unclear. Two possible mechanisms have been suggested. The

first involves a first step of ammonia release and lithium imide formation when lithium amide is heated (Eq. 5-3) (ΔH = +84 kJ·mol^{-1} NH_3).[2] Ammonia then reacts with lithium hydride to form lithium amide again, with the subsequent hydrogen release (Eq. 5-4) (ΔH = -42.1 kJ·mol^{-1}).[2] The 2 step process continues until the starting materials are consumed.[3]

$$LiH + NH_3 \rightarrow LiNH_2 + H_2 \qquad \Delta H = -42.1 \cdot mol^{-1}\, H_2 \qquad (5\text{-}4)$$

The second mechanism suggested involves direct reaction in the solid state between the hydride ($H^{\delta-}$) from lithium hydride and the proton ($H^{\delta+}$) of lithium amide. The formation of hydrogen is the driving force of this reaction (Eq. 5-5).[4,5]

$$H^{\delta+} + H^{\delta-} \rightarrow H_2 \qquad (5\text{-}5)$$

Lithium amide and imide unit cells are represented in Figure 5-1. Lithium amide crystallizes in the tetragonal space group $I\bar{4}$ with lattice parameters a = 5.003442(24) Å and c = 10.25558(52) Å.[6] Lithium atoms are found at the unit cell edge, at some of the faces and in the centre of the unit cell (Figure 5-1a). Hydrogen atoms are covalently bonded to nitrogen atoms found inside the unit cell. Nitrogen atoms form N_4 tetragonal clusters (highlighted in Figure 5-1a). Every lithium cation is tetrahedrally coordinated to $(NH_2)^-$ groups, forming a $Li(NH_2)_4$ unit. The loss of hydrogen induces a change of structure leading to the lithium imide crystal structure.[7,8] It crystallises in the cubic space group $F\bar{4}3m$ with lattice parameters a = 5.0769(1).[9] It has an anti-fluorite structure with nitrogen atoms in a face-centered cubic lattice.

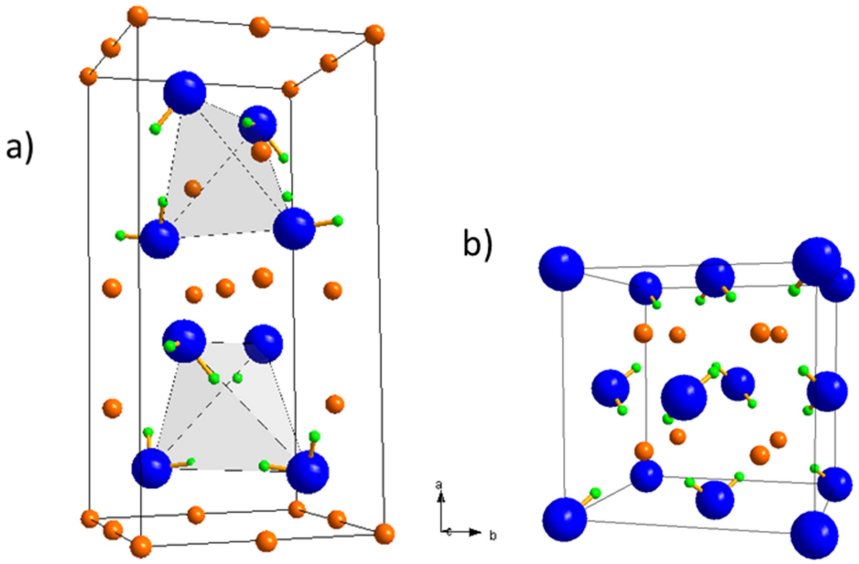

Figure 5-1. Crystal structure of: a) $LiNH_2$ and b) Li_2NH. Nitrogen, lithium and hydrogen atoms are shown in blue, orange and green respectively.

David et. a.l[10] highlighted the Li^+ mobility as a key factor in controlling the de/rehydrogenation conditions for Eq. 5-1 and Eq. 5-2. The structural relationship between lithium amide and lithium imide, as shown in Figure 5-1 allows de/rehydrogenation through non-stoichiometric processes, via a solid solution of the form $Li_{(1+x)}NH_{(2-x)}$ by either diffusing H^+ out of and Li^+ into the face centered cubic anion lattice (or vice versa).

Cation or anion doping is a known approach that has been used to improve properties in a wide range of materials. Doping lithium amide with halides can result in a reduction of the hydrogen desorption temperature via Eq. 5-6.[11]

$$Li_{1+m}(NH_2)X_m + LiH \rightarrow Li_{2+m}(NH)X_m + H_2 \qquad \text{where X= Cl, Br, I} \qquad (5\text{-}6)$$

The halide phases with higher ionic conductivity were also the quickest to release hydrogen on heating and to rehydrogenate. Other groups also confirmed the effect that inserting Cl^- has on the hydrogen release of lithium amide by lowering the decomposition temperature by about 110 °C.[12]

A decrease in the temperature of hydrogen release can also be achieved by replacing lithium amide by its magnesium counterpart.[13] Magnesium amide releases ammonia at a lower temperature than lithium amide, and the proposed subsequent reaction of the ammonia with lithium hydride results in the formation of lithium–magnesium imide phases. Similar phases may be formed through the reaction of lithium amide and magnesium hydride.[14] In general, the partial

introduction of magnesium in the lithium amide structure destabilizes the amide, facilitating lower temperature hydrogen release. The temperature that ammonia was released was also reduced, although ammonia suppression could not be achieved.[15]

Trapping the ammonia released by amides by adding magnesium halides has also been suggested as ammonia can coordinate to the magnesium to form stable ammoniate complexes.[16,17] Other additives have also been used for the Li – N – H system: by analogy to $NaAlH_4$, Ichikawa et. al. reported that the kinetics of hydrogen release was improved at 200 °C by adding $TiCl_3$ into mixtures of $LiNH_2$ and LiH powders.[18]

Mixing lithium amide with other promising hydrogen storage materials has also been reported as a way of destabilizing the products and obtaining lower hydrogen release temperatures, for instance with $LiBH_4$[19] ,which also lowered the amount of ammonia evolved upon heating. Choosing the appropriate ratios of starting materials in this reaction can lead to new borohydride amide materials, such as $Li_4BH_4(NH_2)_3$[20] and $Li_3BH_4(NH_2)_2$.[21,22]

As has been briefly demonstrated above, a large amount of work has been performed in order to improve the dehydrogenation properties of the Li – N – H system, by adopting a wide range of different approaches. However, there is a noticeable lack of work on applying confinement approaches to this system. The main reason for this lack of published work on confinement in the Li – N – H system is probably due to the high melting point of Li_3N (845 °C),[23] which makes a melt infiltration approach to nanoconfinement not cost-efficient. The negligible solubility of Li_3N in liquid solvents without decomposition makes a solution impregnation of porous hosts effectively impossible. However, Demir-Cakan et. al reported an original way to circumvent these problems of confining Li_3N, by wet impregnating mesoporous carbon with lithium azide (LiN_3), a precursor of lithium nitride.[24] Upon solvent removal, the azide composite was thermally decomposed to obtain lithium nitride confined in the porous carbon. The nanocomposite nitride showed faster hydrogen absorption/desorption kinetics at 200 °C than unconfined material (Figure 5-2).

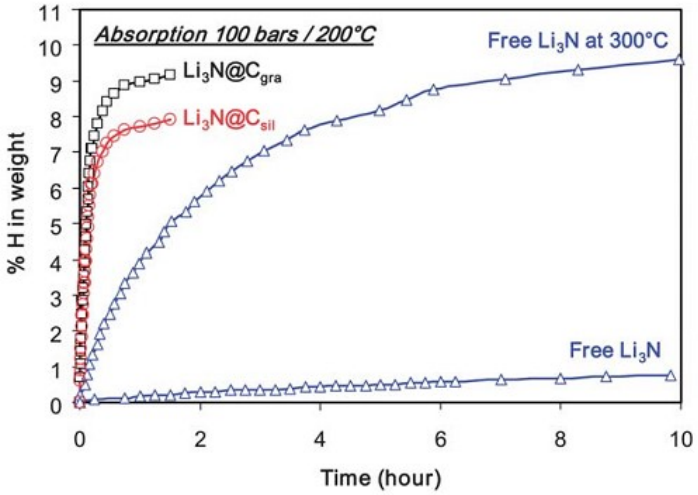

Figure 5-2. Absoprtion under 100 bars H_2. C_{gra} and C_{sil} corresponds to a graphitic carbon and a mesporous carbon prepared by hard-templating of SBA-15 silica, respectively. Reprinted with the permission of [24]. Copyright 2015 Royal Society of Chemistry.

A possible alternative synthesis of confined Li_3N in porous hosts would be infiltration of molten lithium followed by nitrogenation, which has been attempted by Liu et. al.[25] However, due to the high reactivity of liquid lithium in contact with porous carbons, lithium carbide (Li_2C_2) was formed, compromising the reversibility and H_2 desorption of the Li – N – H system.

Our attempt in this chapter have been to fill the gap in the knowledge of confinement of Li – N – H materials by rather than focusing on Li_3N, focusing on a novel approach to confine $LiNH_2$ for the first time. This is a challenging approach since technically speaking, to achieve reversibility in the Li – N – H system, $LiNH_2$ would have to be co-confined in a host with LiH. Our initial aim was to discover whether one could confine $LiNH_2$ alone (since it has never been reported before) and then, if successful, investigation of co-confinement could follow.

One of the problems encountered with $LiNH_2$ is that its melting point, 390 °C,[23] is higher than the temperature at which it begins to decompose and ammonia starts to be evolved (370 °C according to our findings, without the presence of LiH, an ammonia "getter"). This fact precluded a melt infiltration approach.

Exploration of a suitable and inert solvent that could dissolve $LiNH_2$ was needed. Lithium amide is insoluble in ether, benzene and toluene[26] but slightly soluble in liquid ammonia and alcohol.[27] Preliminary experiments performed using liquid ammonia showed a poor solubility of lithium amide in liquid ammonia, which was therefore not promising for nanoconfinement purposes.

However, it is well known that lithium metal can form lithium-ammonia solutions when ammonia molecules are solvated. Alkali metals dissolve in anhydrous ammonia, liquid or gas, leading to intensely coloured solutions (Figure 5-3), which have a characteristic fine blue colour for dilute solutions and a copper/bronze colour for concentrated solutions.[28]

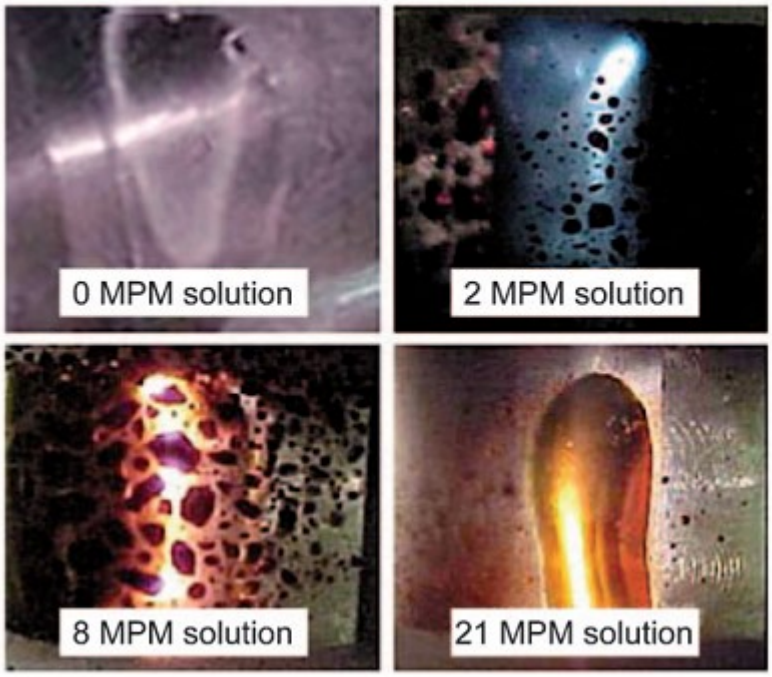

Figure 5-3. The colours of lithium–ammonia solutions, showing how they change with concentration from pure solvent to saturation. Reprinted with the permission of [28]. Copyright 2015 John Wiley and Sons.

The earliest observations of these spectacular colours can be traced to the work of Sir Humphry Davy.[29] The study of these solutions was advanced by W. Seeley who gave the first recognition of the "nonchemical" solvent action of ammonia: *" […] these metals (alkali) dissolve in ammonia as salt dissolves in water".*[30] Later Kraus and co-workers defined these types of solutions as being the constitutors of the direct link between electrolytes and metals.[31] He identified the negative charge carrier conductivity in metal – ammonia solutions as originating from the electron liberated from the metal via the dissolution process (Eq. 5-7), leading to "free" electrons or electrons associated with ammonia.

$$M \xrightarrow{NH_3} M_s^+ + e_s^- \qquad (5\text{-}7)$$

The dissolution process in these solutions results in the alkali metal valence s electron being spontaneously ionized into the solvent. At low metal concentrations, this leads to the formation

of solvated metal cations (in case of lithium: Li_s^+ or $Li(NH_3)_n^+$) as well as solvated electrons (e_s^- or $e^-@(NH_3)_n$.[28] Gibson *et.al* concluded and affirmed that the blue characteristic colour was due to solvated electrons.[32] If the metal concentration is increased in dilute solutions, conductance of the solution decreases, which shows evidence of the formation of ion pairs ($Li_s^+e_s^-$) due to the interactions between solvated electrons and solvated cations. With a further increase in the concentration up to 1 mol % metal (1MPM), the solvated electrons interact with each other and their spins become paired.[33] Werner, et al. characterized by eletrochemistry the spin-paired species as a trimer ion, a cluster of two single-electron solvated-electron species ($2e_s^{2-}$) combined with a solvated cation, forming " $e_s^- M_s^+ e_s^-$ ". Within this concentration range there are several species coexisting, due to the fact that there are several equilibria between electrons, metal ions, and solvent containing either paired (diamagnetic) and unpaired (diamagnetic) electrons.[28]

If the alkali metal concentration increases (1 to 8 MPM) the "transition to metallic state" occurs (abbreviated TMS),[34] leading to a bronze/gold-coloured liquid where the solvated electrons are delocalized, and the solutions truly metallic. A liquid-liquid phase separation occurs at about 4 MPM, if the solution is cooled, where the higher-concentration gold metallic phase sits on top of the more dilute blue one.[31]

Free electron behaviour is observed for solutions greater than 10 MPM. Near saturation (~21 MPM) the conductance of bronze solutions is higher than that of liquid mercury.[35]

Figure 5-4 shows a schematic figure showing the species present and the characteristics of the solution as a function of metal concentration.

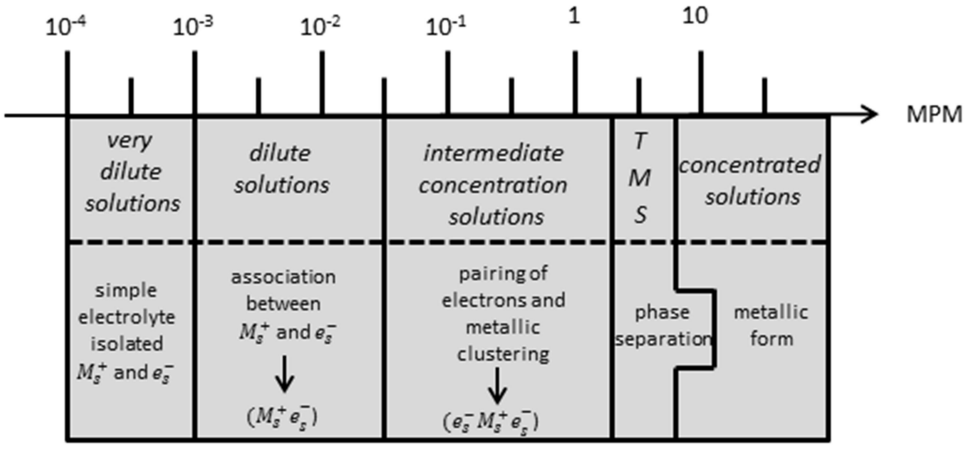

Figure 5-4. Schematic representation of the species present and characteristics of the solution as a function of lithium concentration in lithium – ammonia solutions. Modified from reference [28].

The synthesis of $LiNH_2$ can actually be performed in ammonia-solution by using lithium metal with liquid ammonia according to this reaction:[36,37]

$$Li_{(S)} + NH_{3\,(l)} \xrightarrow{-40\,^{\circ}C} LiNH_{2\,(s)} + H_{2\,(g)} \qquad (5\text{-}8)$$

The only problem with this reaction is that it takes 8 days to be completed. It can also be made at higher temperature (200 °C) in an ammonia gas stream with or without catalyst.[38,39] Lithium metal would be dissolved in ammonia gas forming the bronze/golden-coloured solution, and upon heating treatment or time, a white crystalline powder corresponding to lithium amide would be formed. The solution has to be continuously stirred to allow further lithium to react with ammonia. Ziurys et. al reported a similar synthetic route, but predominantly in the gas-phase, where lithium was heated to evaporation and its vapour reacted with a stream of ammonia.[40]

This chapter explores alternative synthesis routes for the confinement of $LiNH_2$. In an attempt to address the issue of finding a suitable solvent for the amide, and taking advantage of the existence of the lithium-ammonia solutions, lithium amide was prepared and confined in-situ, by flowing ammonia gas over lithium metal in contact with a porous host.

5.2. EXPERIMENTAL

All the samples prepared in this chapter have been manipulated in an argon filled recirculating glove box (< 0.5 ppm O_2 and H_2O) or using a Schlenk line under an argon gas flow or vacuum. The porous carbon host used for this work was FDU-15 prepared in the lab, as described in Section 3.2.1. Commercial $LiNH_2$ (powder, reagent grade, 95 %) was purchased from Sigma Aldrich.

Lithium amide (sample 1) was prepared in the lab following a similar synthesis route to that reported by Juza.[36] A typical mass of 0.1 g of lithium, purchased from Sigma Aldrich (ribbon shape, 1.5 mm x 100 mm, 99.9 % purity) was cut and transferred into a Schlenk tube properly sealed with a rubber septum. The Schlenk tube was punctured by a syringe connected to the ammonia line, and another syringe was attached from the Schlenk tube to the Schlenk line to facilitate removal of the excess ammonia. Ammonia was flushed into the Schlenk tube at a rate of 1 cm^3/min for 2 h at room temperature. The lithium rapidly started dissolving in the ammonia forming bronze/gold –coloured ammonia solutions (Figure 5-5). The sample was continuously stirred to ensure a homogenous contact between the lithium and ammonia in the sample. After 2 h, the ammonia flow was stopped and the Schlenk tube was sealed under an ammonia atmosphere and left for 3 days, until an off-white powder was obtained. The sample was heated to 50 °C and left under a dynamic vacuum (10^{-3} atm) for 4 h to ensure ammonia removal.

Sample 2 was obtained by mixing $LiNH_2$ prepared in the lab (sample 1) with FDU-15 using an agate mortar and pestle. Sample 3 was prepared following the same procedure as sample 1, but FDU-15 was added simultaneously with the lithium metal. The calculation of the amount of reagents needed to prepare sample 3 is described in the Appendix Section 7.3.

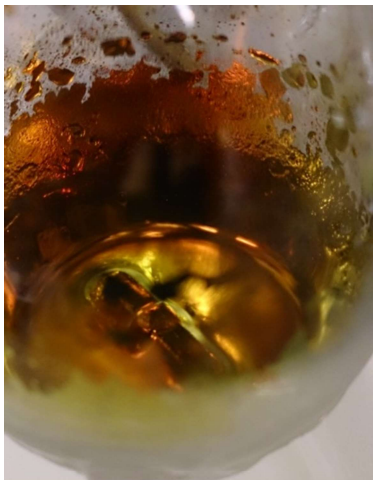

Figure 5-5. Bronze/gold-coloured lithium-ammonia solution from the preparation of sample 1.

Samples 4-8 were prepared from commercial $LiNH_2$ and FDU-15. Each starting material was weighed and ground using an agate mortar and pestle to ensure a good distribution of the amide within the carbon. The resulting mixture was a homogenous grey powder. Table 5-1 collects the list of samples presented in this chapter, including relevant information for each sample.

Table 5-1. Description of the samples analysed and discussed in this chapter. The numbers with * are calculated amounts, obtained assuming complete reaction of lithium to lithium amide. (See Appendix Section 7.3)

Samples	Identity	$LiNH_2$ type	Li / g	$LiNH_2$ / g	C / g	$LiNH_2$:C wt. ratio
1	Prepared $LiNH_2$	-	0.100	*0.191**	-	-
2	physically mixed ($LiNH_2$+ C)	sample 1	-	0.040	0.100	1 : 2.5
3	confined sample($LiNH_2$@C)	sample 1	0.018	*0.040**	0.100	1 : 2.5
4	physically mixed ($LiNH_2$+ C)	commercial	-	0.096	0.500	1 : 5.2
5	physically mixed ($LiNH_2$+ C)	commercial	-	0.096	0.200	1 : 2.1
6	physically mixed ($LiNH_2$+ C)	commercial	-	0.200	0.100	2 : 1
7	physically mixed ($LiNH_2$+ C)	commercial	-	0.200	0.050	4 : 1
8	physically mixed ($LiNH_2$+ C)	commercial	-	0.570	0.050	10 : 1

Nitrogen adsorption isotherms were measured at 77 K using a Micromeretics Gemini III 2375 surface area analyser. Before analysis, the samples were degassed under vacuum at different temperatures depending on the nature of the sample. The Brunauer-Emmet-Teller (BET) method was used to calculate the specific surface areas using adsorption data in a relative pressure range from 0.4 to 1 P/Po. The total pore volume was estimated from the adsorbed N_2 amount based on the Barret-Joyner-Hallenda (BJH) model.

The morphology of the samples was investigated using a Philips XL30 scanning electron microscope (SEM) as described in chapter 2. Particle size distribution histograms were obtained from the SEM images obtained of the products, measured and analysed by the image processing software ImageJ.[41] A population of over 300 particle measurements was taken to create the histograms at different magnifications, depending on the size of the particles studied.

Samples were analysed by powder X-ray diffraction (PXD). Sealed capillaries were prepared and analysed on the Bruker D8 diffractometer. Diffraction data were collected from 5 - 85 ° 2θ for 1 hour or 14 hours at a step size of 1.3 °/min and 0.09 °/min respectively, depending on the nature of the sample.

Thermal programmed desorption studies of the samples prepared were performed using a Netzsch STA 409 analyser, which was coupled to a Hiden HPR 20 Mass Spectrometer for evolved gas analysis. Hydrogen gas was the most relevant gas tracked on the Mass Sprectrometer, although other gases were also tracked (such as H_2O or O_2). Measurements were performed in an argon-filled recirculating glove box, with 30 mg of sample typically used.

Raman spectroscopy was performed using a Horiba LabRAM spectrometer HR confocal microscope system with a 532 nm green laser. A hole aperture of 50 µm, 600 grating/mm, 50x objective lens and a Synapse CCD detector were used at room temperature. Powdered air sensitive samples were placed in a glass capillary and sealed before running the analysis. Spectra were usually collected over a period of several minutes from an average of multiple scans, normally at a range of 3000 cm^{-1} to 3500 cm^{-1}.

5.3. RESULTS AND DISCUSSION

5.3.1. Commercial $LiNH_2$ characterzitation

5.3.1.1. Structural characterization

Figure 5-6a shows the powder X-ray diffraction pattern obtained for as-received $LiNH_2$. The powder pattern obtained is in good agreement with that from the structure of $LiNH_2$ (tetragonal space group $I\bar{4}$) suggested by Juza, et al.[42]

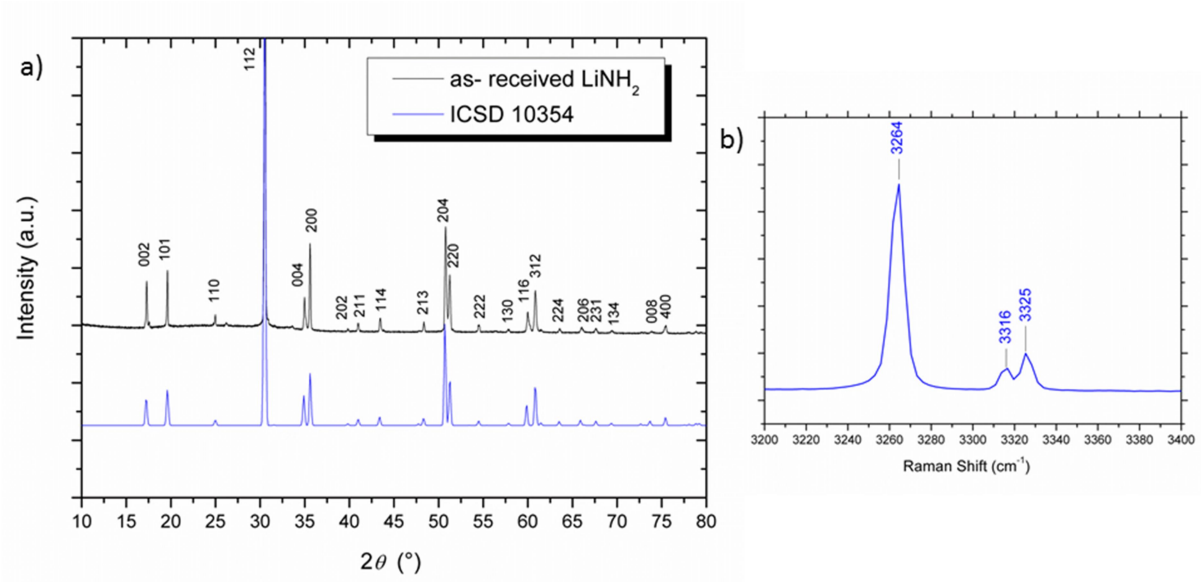

Figure 5-6. a) XRD powder pattern obtained of as-received $LiNH_2$ compared to the $LiNH_2$ pattern calculated using data obtained from the ICSD database (collection code 10354)[42] b) Raman spectrum obtained from as-received $LiNH_2$ between 3200 – 3400 cm^{-1}.

Figure 5-6b shows the Raman spectrum of as-received $LiNH_2$. Only the region of the spectrum where the stretching modes of NH_2 are located and shown (3200 -3400 cm^{-1}). These are the modes with the strongest intensity and the easiest ones to identify, although the Raman spectrum of lithium amide also contains other bands. The Li-N vibrations appear below 700 cm^{-1} and the bending modes of NH_2 appear at *ca.* 1500 cm^{-1},[43,44] but are not shown for simplistic reasons.

The three bands in Figure 5-6b correspond to the three Raman active N-H stretching modes. The first intense peak at 3264 cm^{-1} corresponds to the symmetric stretch whereas the two lower-intensity peaks at 3316 and 3325 cm^{-1} correspond to asymmetric stretches. These results are in good agreement with studies in the literature as reported in Table 5-2.

Table 5-2. Raman frequencies and stretching mode assignments for as-received $LiNH_2$ in this work, with results obtained from previous work for comparison.

Assignment	Raman Shift / cm^{-1}		
	This work	Bogher, et. al.[45]	Michigoe, et al.[43]
ν_{as} (N-H)	3325	3326	3321
ν_{as} (N-H)	3316	3313	3310
ν_{s} (N-H)	3264	3261	3260

The size and morphology of $LiNH_2$ particles can be observed from SEM images (Figure 5-7a) and the particle size distribution is shown in Figure 5-7b. It can be seen that the particles have a rather broad size distribution, ranging from 5 - 185 µm across.

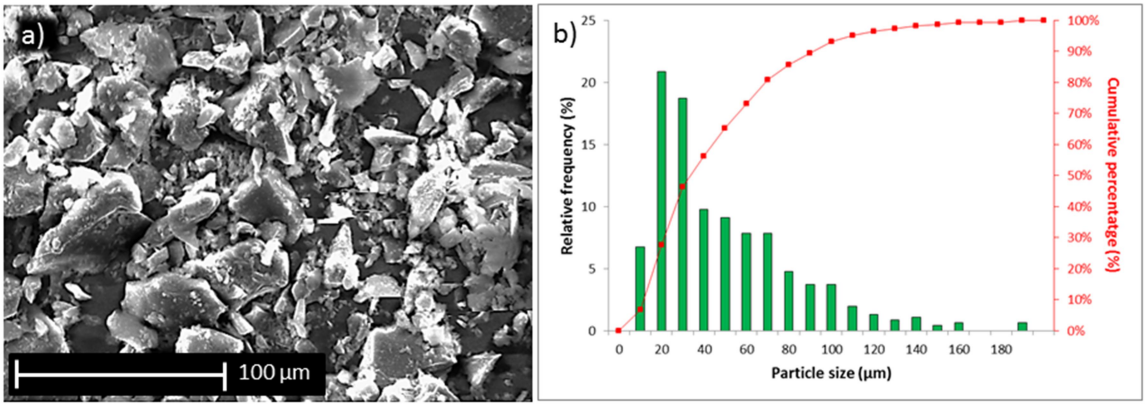

Figure 5-7. a) SEM images of as-received $LiNH_2$ and b) Histogram of particle size distribution (µm) with relative frequency (%) and accumulative percentage.

The maximum relative frequencies found in Figure 5-7b correspond to particles of 10 - 20 µm across, whereas 80 % of the population of the particles lie in a range from 5 - 70 µm across.

5.3.1.2. Dehydrogenation studies

Figure 5-8 shows the DTA profile along with the corresponding simultaneous TGA profile for as-received $LiNH_2$. The sample was heated at 5 °C·min^{-1} to 650 °C for 1 hour. No thermal events or mass losses are observed below 372 °C. The obvious sharp peak at 372 °C seen in the DTA profile corresponds to the melting point of lithium amide, which melts before decomposition.[46] No evolved gas was detected in the MS (Figure 5-9) before melting. There is a continous mass loss, until *ca.* 550 °C where the mass loss plateaus. The total mass loss at 600 °C totals 35.5 wt.%. This region contains a maximum in the DTA profile at 498 °C, which corresponds to the ammonia release from lithium amide.[47] The release of NH_3 can be clearly observed in the evolved gas mass spectrum (Figure 5-9), corresponding to Eq. 5-3. When the temperature was held at 650 °C a continuous mass loss of *c.a* 15 wt.% with a maximum DTA peak at 650 °C was observed. This peak seems to be disrupted by the change in the heating rate and correlates with hydrogen and nitrogen release, as observed in the evolved gas mass spectra (Figure 5-9). The nitrogen and hydrogen release can be considered as an extension the of ammonia release. At high temperatures (*ca.* > 400 °C) ammonia decomposes to nitrogen and hydrogen.[48] This decomposition (Eq. 5-9) becomes more evident as the temperature is increased, starting to be significant at *ca* 450 °C:

$$NH_{3(g)} \xrightarrow{400\,^{\circ}C} N_{2(g)} + H_{2(g)} \qquad (5\text{-}9)$$

The total mass loss of as-received $LiNH_2$ when heated to 600 °C is 35.5 %, increasing to 44.7 wt.% after holding at 650 °C for 1 hour. Assuming decomposition of $LiNH_2$ leads only to hydrogen and nitrogen (ammonia release) (Eq. 5-12) the sample should have a theoretical mass loss of 49.4 w.t. % NH_3 if the sample would have been totally dehydrogenated.

Amide to imide decomposition: $2LiNH_2 \leftrightarrow Li_2NH + NH_3$ 37.0 % w.t. NH_3 (5-10)

Imide to nitride decomposition: $3Li_2NH \rightarrow 2Li_3N + NH_3$ 12.4 % w.t. NH_3 (5-11)

Overall reaction: $3LiNH_2 \rightarrow Li_3N + 2NH_3$ 49.4 % w.t. NH_3 (5-12)

Although it is difficult to quantify the exact % of each gas released experimentally (ammonia, hydrogen and nitrogen), the findings in this work (35.5 wt. % mass loss at 600 °C) are in good agreement with the published literature,[47,49] and the theoretical content of NH_3 of Eq. 5-10.

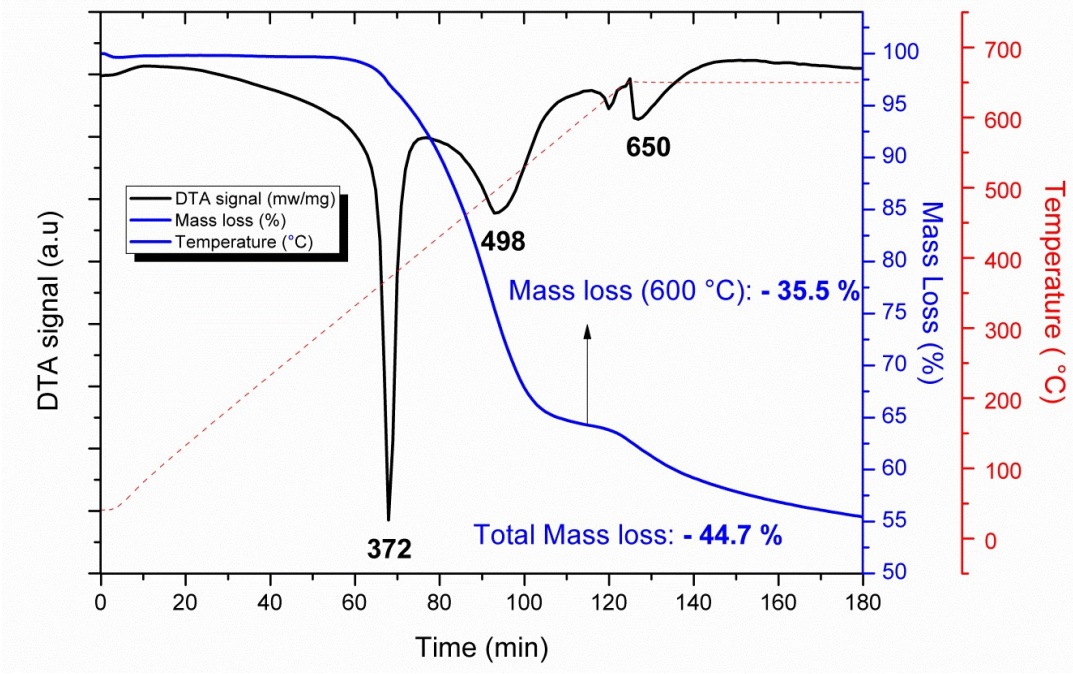

Figure 5-8. DTA and TG plots for as-received $LiNH_2$ sample, under a thermal treatment at 5°·min^{-1} to 650 °C holding for 1 hour. Further supplementary data available.[50] (For thermal treatment to 800 °C, see Figure 7-6 in Appendix Section 7.3).

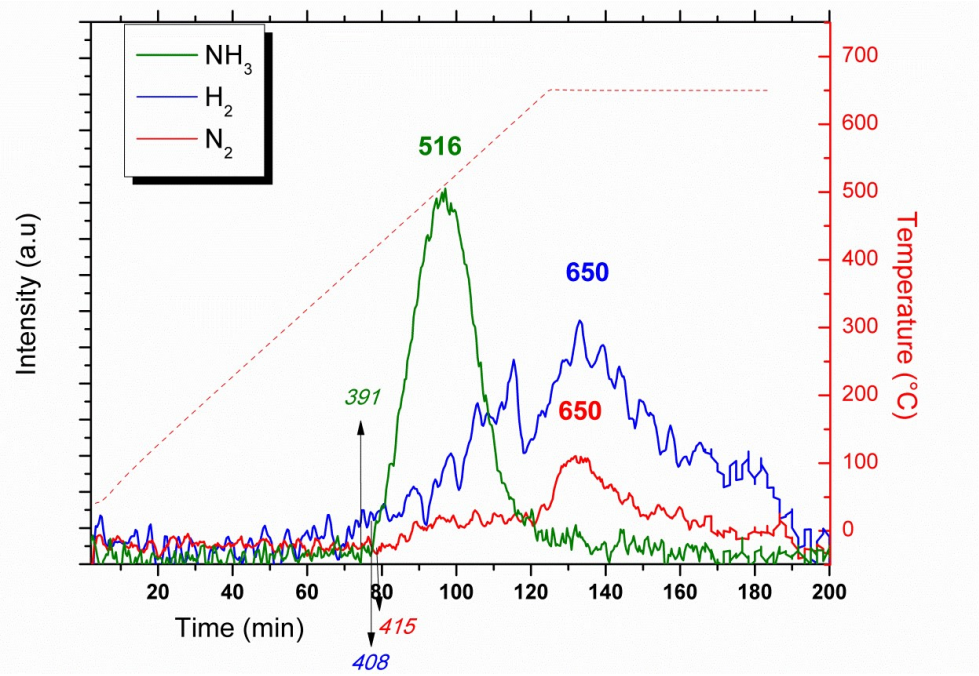

Figure 5-9. Mass spectrum of evolved gases during decomposition of as-received $LiNH_2$, recording NH_3, H_2 and N_2 evolution (m/z = 17, 2 and 14 respectively). The sample was heated under Argon atmosphere to 650 °C holding for 1 hour at 5°·min^{-1}. Further supplementary data available.[50] (For MS corresponding to thermal treatment to 800 °C, see Figure 7-6 in Appendix Section 7.3)

5.3.1.3. Post thermal treatment structural characterisation

Figure 5-10 shows a comparison of the XRD obtained for as-received $LiNH_2$ (Figure 5-10a) and the same material after heating at 5 °C·min^{-1} to 650 °C and then hold for 1 h (Figure 5-10b). In Figure 5-10a all of the observed reflections correspond to the $LiNH_2$ phase and no presence of any impurity is apparent. In Figure 5-10b, after thermal treatment, there is a significant reduction in the number of reflections present. The reflections are in good agreement with the dehydrogenated phase of $LiNH_2$, Li_2NH,[37] which is the expected phase after lithium amide has lost 35.5 wt.% (theoretically 37 wt.% - Eq. 5-10) at 600 °C. This phase shares a lot of the major reflections with the $LiNH_2$ phase, but lacks the minor intensity reflections characteristic of the $LiNH_2$ phase. Figure 5-10b also shows the presence of trace impurity (Li_2O).

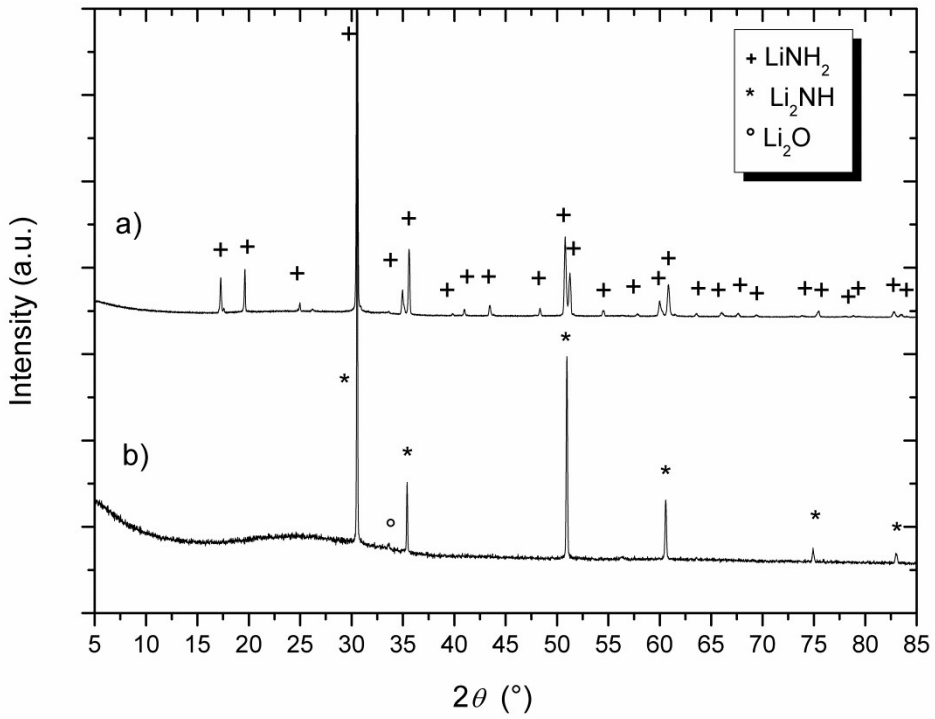

Figure 5-10. XRD patterns obtained for: (a) commercial $LiNH_2$ and (b) commercial $LiNH_2$ heated to 600 °C at 5 °C·min^{-1}. The following phases were used from the ICSD database to assign the Bragg's reflections present in the samples: *$LiNH_2$ (collection code 10354),*[42] *Li_2NH (collection code 28683)*[37] *and Li_2O (collection code 60431).*[51]

5.3.2. Sample 1 characterization ($LiNH_2$ prepared in the lab)

5.3.2.1. Structural characterisation

Figure 5-11 shows an SEM image and histogram of the particle sizes of sample 1 measured from the SEM images. The morphology of the particles appears to be quite regular, ranging from 5 - 75 µm across. The maximum frequencies were found to occur for particles 10 -15 µm across, which is very similar to as-received $LiNH_2$ (Figure 5-7). 80 % of the population of the particles range between 5 – 30 µm across. The histogram of as-received $LiNH_2$ shows the presence of a higher number of larger particles, especially those over 70 µm across. Hence, $LiNH_2$ prepared in the lab gives a narrower size range of $LiNH_2$ particles when compared to as-received $LiNH_2$.

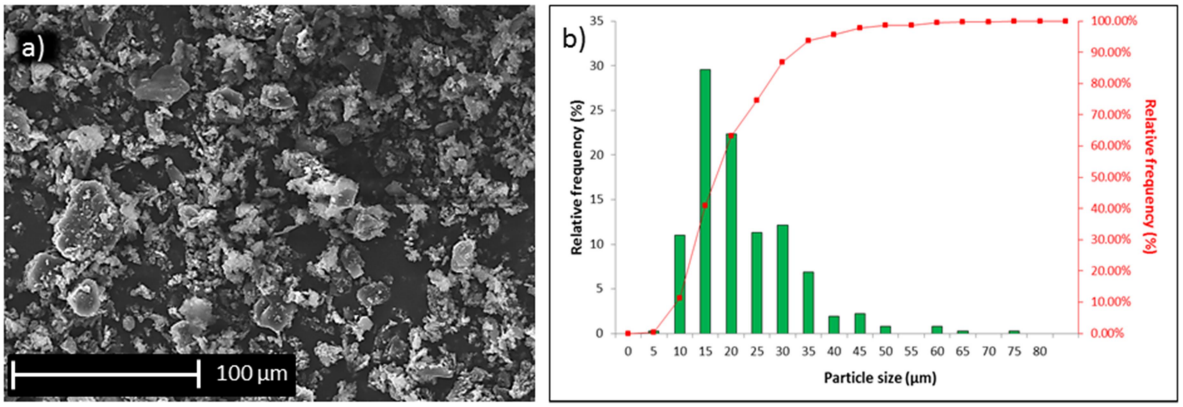

Figure 5-11. a) SEM images of sample 1 and b) Histogram of particle size distribution (µm) with relative frequency (%) and accumulative percentage.

Figure 5-12 shows the Raman spectrum of sample 1. The characersitic stretching modes of N-H were present in the spectrum. The symmetric mode peak appears at 3264 cm^{-1} and the asymmetric mode at 3316 and 3325 cm^{-1}, which are in good agreement with the positions of the corresponding bands in the Raman spectrum of as-received $LiNH_2$. It can be observed that an extra peak not observed in the as-received $LiNH_2$ is present at 3666 cm^{-1}. This peak corresponds to the stretching of O-H, with a frequency in perfect agreement with that of LiOH.[52] LiOH might be expected to form as an impurity if there was any trace of moisture or oxygen present during the preparation of $LiNH_2$ from Li metal.

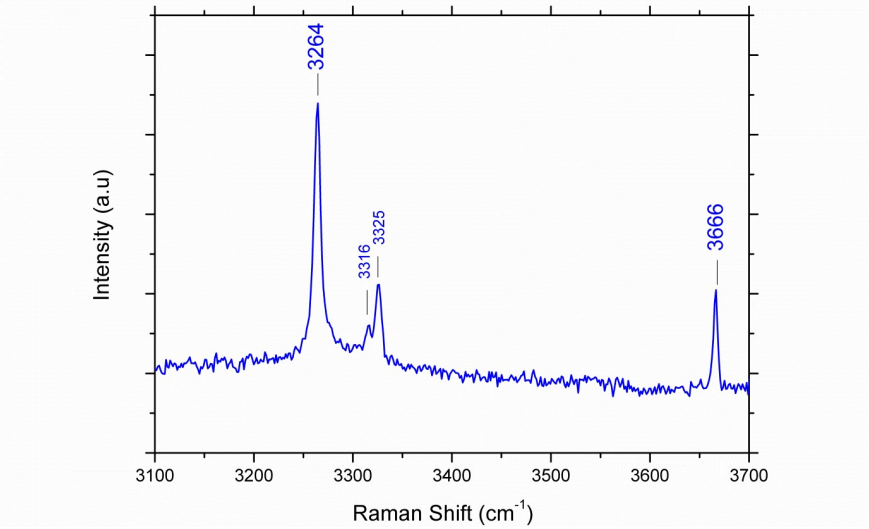

Figure 5-12. Raman frequencies obtained from sample 1 between 3200 – 3700 cm^{-1}

The powder X-Ray diffraction pattern of sample 1 is shown in Figure 5-13. The characteristic $LiNH_2$ reflections are present. However, there is also a presence of impurities, such as reflections corresponding to Li_2O and LiOH. The latter corroborates the O-H stretching modes observed in the Raman spectrum.

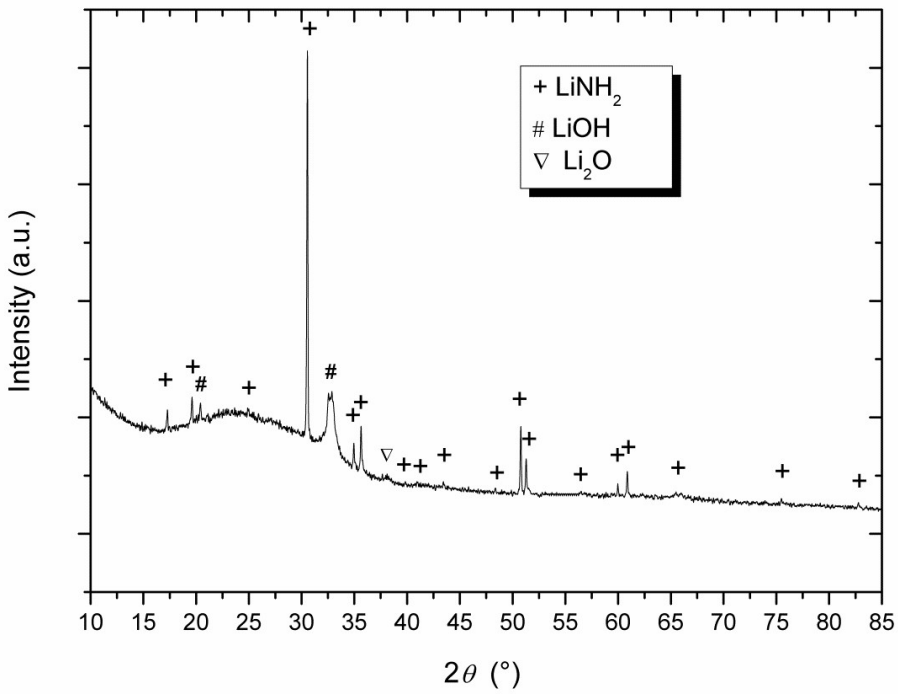

Figure 5-13. Powder XRD pattern obtained for sample 1. The following phases have been used from the ICSD database to assign the Bragg's reflections present in the samples: *$LiNH_2$ (collection code 1035),*[42] *LiOH (collection code 26892),*[53] *and Li_2O (collection code 60431)*[51].

5.3.2.2. Dehydrogenation studies

Figure 5-14 shows TGA and DTA results obtained from sample 1. Both the DTA peaks and the mass loss values are in good agreement with the ones obtained from as-received $LiNH_2$. The TGA profile shows a mass loss 32.8 wt.% by 600 °C and a total mass loss of 41.8 wt.%. The small difference in mass loss when compared to as-received $LiNH_2$ might be due to the formation of impurities, which cannot desorb ammonia, such as a LiOH and Li_2O. No observable signal for H_2O, possibly coming from LiOH, was detected in the mass spectrum. The onset of the mass loss however starts earlier (275 °C) than that for as-received $LiNH_2$. The melting of $LiNH_2$ is still clearly observable in the DTA signal at 369 °C. The endothermic events due to ammonia and nitrogen/ hydrogen release can also be seen in the DTA profile, at *ca.* 450 and 650 °C respectively. In the case of the ammonia release, the peak appears at slightly lower temperatures than that in as-received $LiNH_2$, but the hydrogen and nitrogen evolution temperatures remains unchanged.

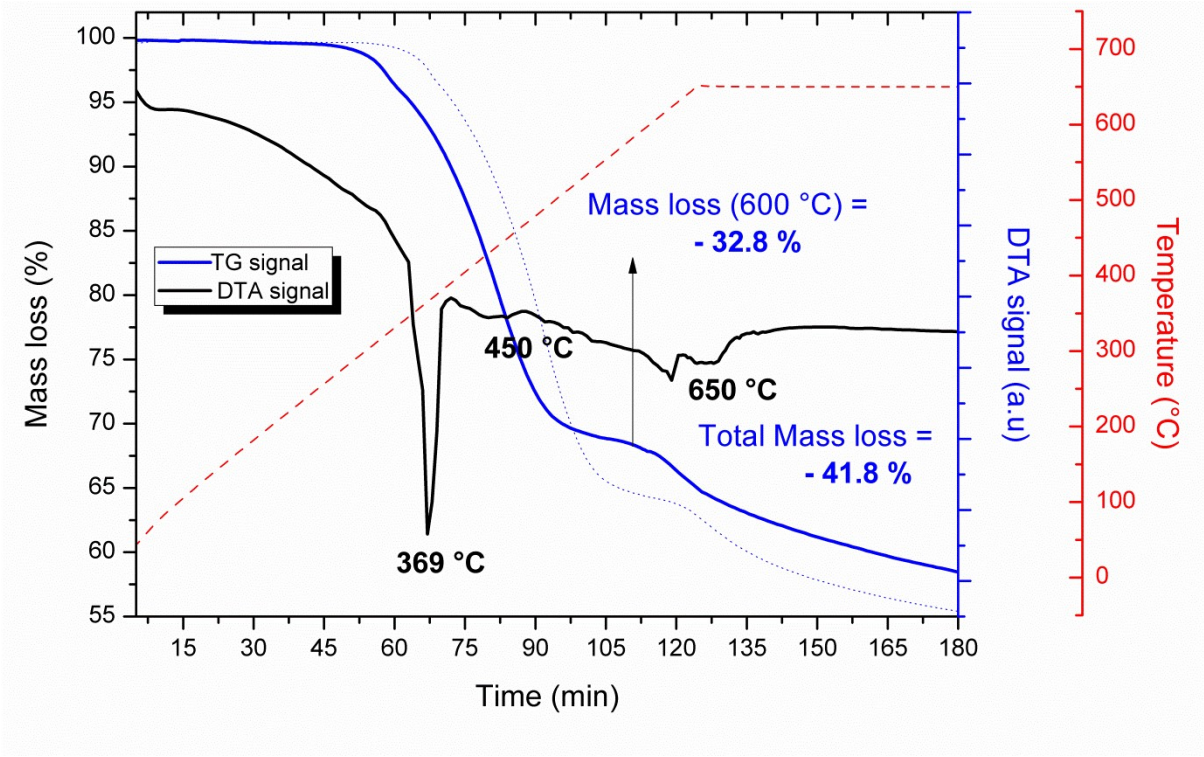

Figure 5-14. DTA and TG plots for sample 1 and as-received $LiNH_2$ sample (dotted line), on heating at 5°·min^{-1} to 600 °C.

Figure 5-15 shows the mass spectrum of the evolved gases after sample 1 was heated at 650 °C for 1 hour. There is no major difference between the hydrogen and nitrogen release of sample 1 in comparison with as-received $LiNH_2$. But the ammonia profile obtained is rather different: there is a weak ammonia release before the main release starting at around 350 °C and peaking at 470

°C. This correlates well with the earlier mass loss in the TG profile and earlier endothermic events in the DTA signal in Figure 5-14. This earlier ammonia release might be due to the reduction of the particle size of sample 1 in comparison with as-received $LiNH_2$, although from SEM characterization this is a subtle effect (Figure 5-11). Table 5-3 collects the results and compares them to those from as-received $LiNH_2$. The same earlier mass loss onset, hence earlier ammonia release, has been found on ball milling as-received $LiNH_2$ (average size *ca.* 2 μm).[47] This improvement could be due to a combination of a higher surface area that facilitates the gas-solid reaction and shorter diffusion lengths for ions to move in solid state. Although the mean particle size in sample 1 is not above 2 μm (which is the size of the ballmilled $LiNH_2$ discussed previously in the literature)[47] a lower temperature for mass loss and ammonia release is detected compared to the bulk material.

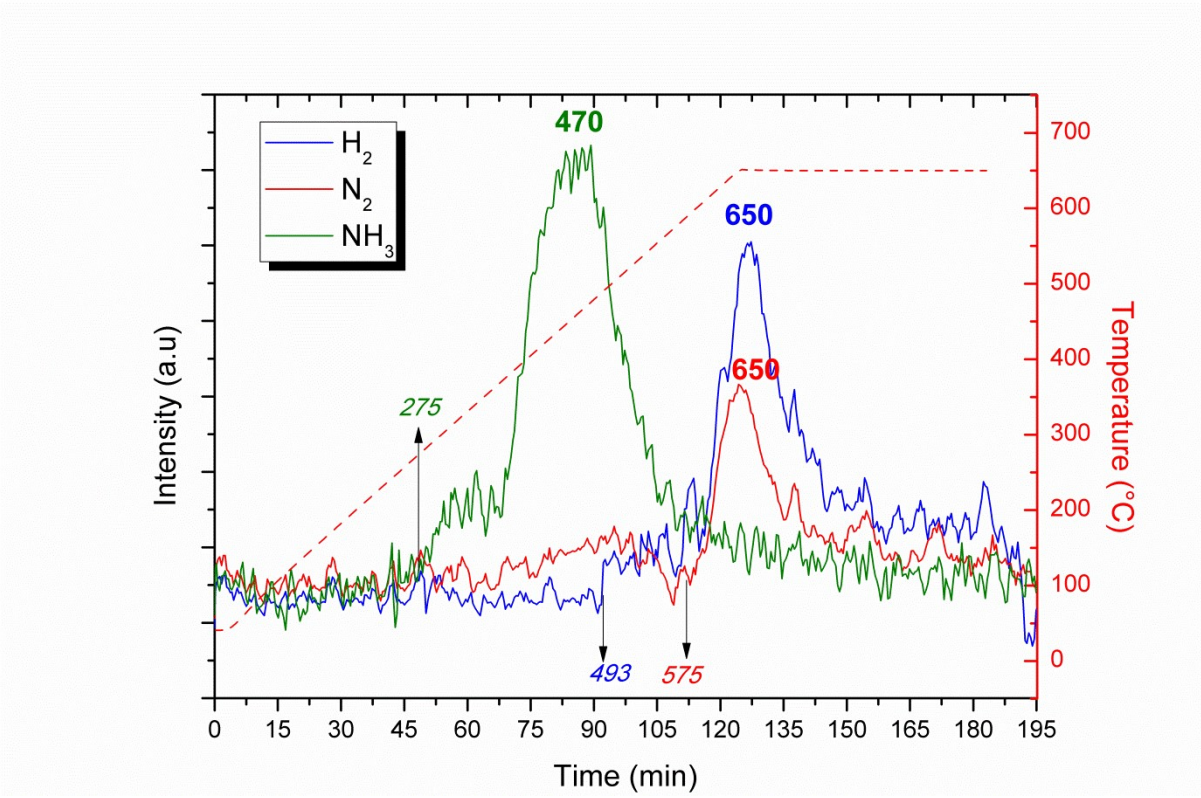

Figure 5-15. Mass spectra for NH_3, H_2 and N_2 evolution (m/z = 17, 2 and 28 respectively) from sample 1, on heating to 650 °C at 5°·min^{-1} and holding for 1 h.

Table 5-3. Summary of the ammonia release temperatures from mass spectrometry for sample 1 and as-received $LiNH_2$.

	Sample 1		As-received $LiNH_2$
NH_3	1st release *(weak)*	Main release	
Onset / °C	275	350	391
Tmax / °C	300	470	516

5.3.3. Confinement of $LiNH_2$ in FDU-15

5.3.3.1. Structural characterization

Figure 5-16 shows a comparison of the N_2 absorption/desoption isotherms at 77 K for sample 2 and 3 and for dried FDU-15. A summary of the specific surface area and the total pore volume of each sample is shown in Table 5-4. The isotherm of FDU-15 and sample 2, which are the ones that show a signifcant adsorbed volume, both exhibit type IV isotherms, whereas sample 3 exhibits a type II isotherm, characteristic of non-porous adsorbents. From the change in isotherm behaviour and the loss of surface area and porosity, the in-situ synthesis of $LiNH_2$ via lithium-ammonia appears to fill and/or block the pores of the carbon host.

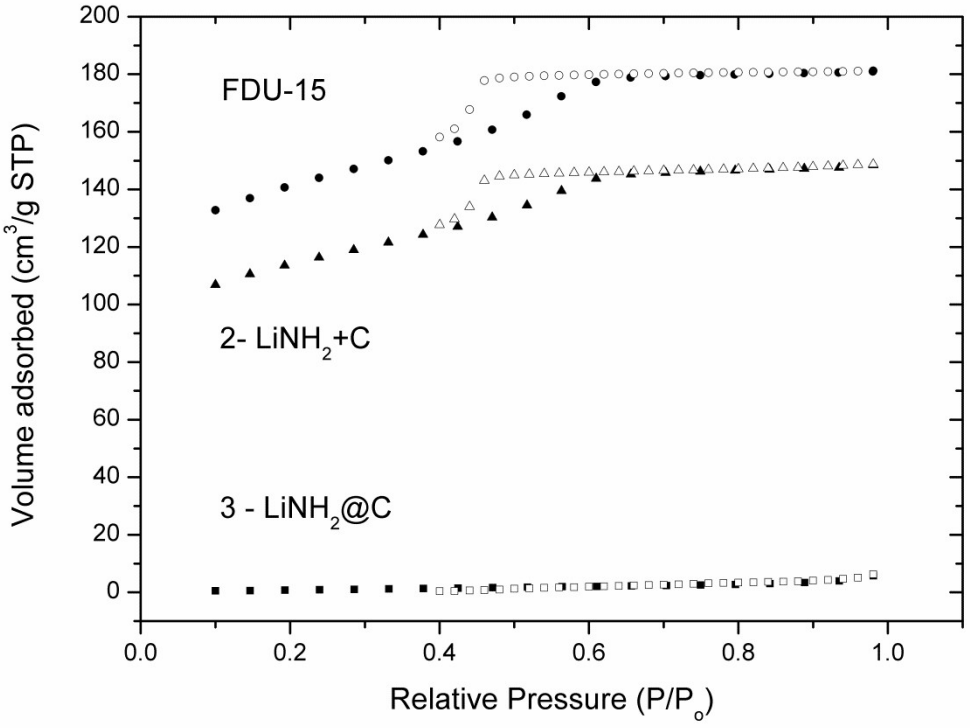

Figure 5-16. Comparison of N_2 absorption/desorption isotherms of dried FDU-15, sample 2 and sample 3 at 77 K.

Table 5-4. Summary of the results of specific BET surface area and total pore volume of each sample.

Sample	BET surface area / $m^2 \cdot g^{-1}$	Total pore Volume / $cm^3 \cdot g^{-1}$
FDU-15	500.7	0.32
2	340.2	0.25
3	9.3	0.03

SEM images (Figure 5-17 and Figure 5-18) show the morphology and particle size of sample 2 and 3 respectively, and the histograms of the particle sizes measured from several SEM images. Table 5-5 collects and summarises the data from these samples and from sample 1 and FDU-15 for comparison. Sample 2 (Figure 5-17) shows that the particle size ranges from 10 to 75 µm, with a maximum frequency of 25 – 30 µm and with 80 % of the population lying in a range of 10 – 50 µm. Sample 3 (Figure 5-18) contains similar size particles, ranging from 10 – 70 µm, with a maximum frequency of 25 – 30 µm and with 80 % of the population of the particles found in a range between 10 – 45 µm. The only subtle difference is the distribution of the cumulative percentage. Sample 2 has a longer tail in the distribution of the particle sizes, with a higher number of larger particles. In contrast, the distribution of the particle size for sample 3 is more even and gradual, indicating increased homogeneity in the composite. Although it is not strong evidence, the tendency observed in the results for sample 2 could be consistent with a mixture of two different phases.

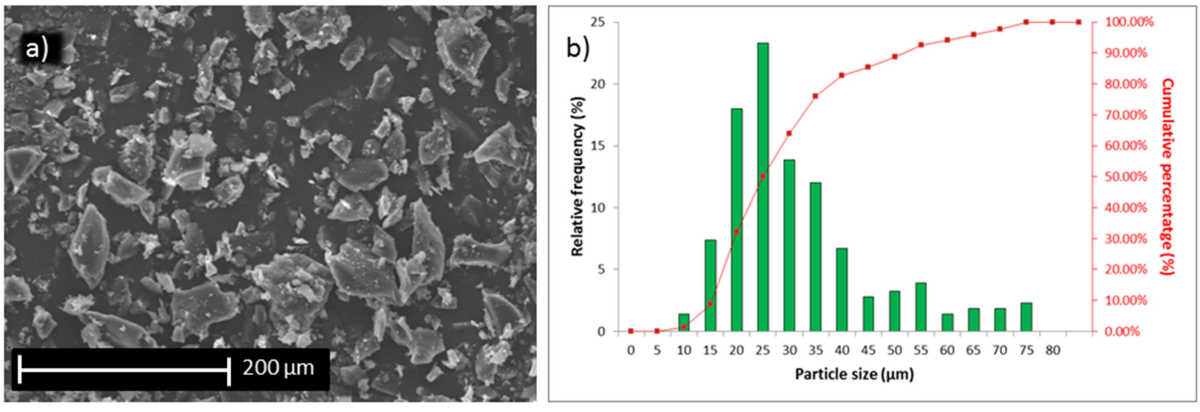

Figure 5-17. a) SEM image of sample 2 and b) Histogram of particle size distribution (µm) with relative frequency (%) and accumulative percentage.

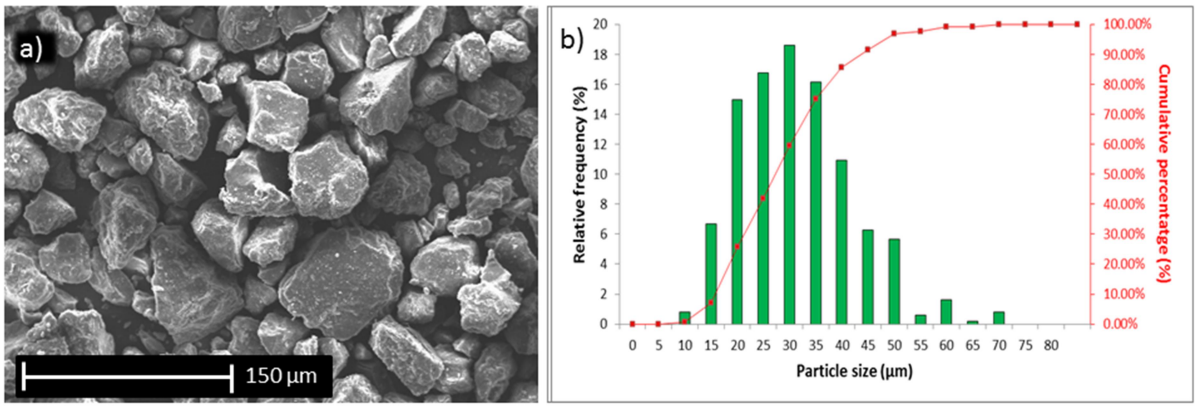

Figure 5-18. a) SEM image of sample 3 and b) Histogram of particle size distribution (µm) with relative frequency (%) and accumulative percentage.

The similarly of the results from sample 2 and sample 3 might be due to the fact that, unlike the case of $LiAlH_4$, discussed in the previous chapter, the $LiNH_2$ particles themselves (sample 1) are very similar in size to the particles of the carbon host used. It is thus difficult to see any obvious trend in the particle size histograms on moving from analysis of each of the starting materials as compared to the composites.

Table 5-5. Summary of the results obtained from the histograms of particle size for samples 1-3 and FDU-15.

	Particle size distribution (µm)		
Sample	*100 % population*	*80 % population*	*Max. frequency (%)*
FDU-15	10 - 70	10 - 55	30 - 35
1 – $LiNH_2$	5 - 75	5 - 30	10 - 15
2 - $LiNH_2$ + C	10 - 75	10 - 50	25 - 30
3 - $LiNH_2$@C	10 - 70	10 - 45	25 – 30

Figure 5-19 shows a comparison of the Raman spectra obtained for as-received $LiNH_2$ (sample 1) and samples 2 and 3. Both sample 1 and 2 show the bands for N-H stretching, charactersitic for $LiNH_2$ and the O – H stretching from the presence of LiOH impurity. However, in sample 3 no bands are observed in the region from 3100 – 3700 cm^{-1}, which might indicate a better dispersion of lithium amide induced by the inhomogenous nanometric enviroment of the porous host.[54] This

finding is in good agreement with our previous work on confinement of $LiAlH_4$, reported in the previous chapter and with previous work using melt infiltration for confinement of $NaAlH_4$ in porous carbon material. In these cases Raman spectra also did not show any charactersitic vibrations from the confined material in the high frequency region of the spectra.[54]

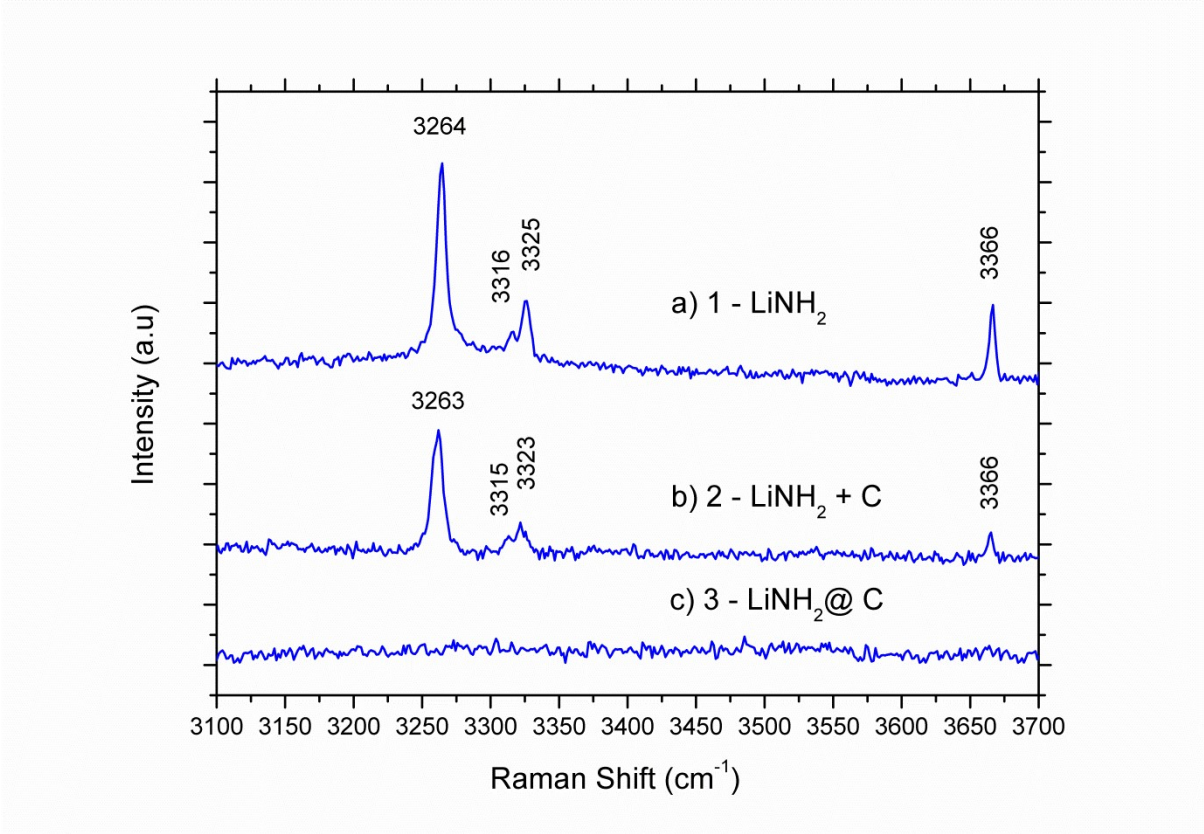

Figure 5-19. Comparison of Raman spectra obtained from samples a) sample 1, b) sample 2 and c) sample 3.

Figure 5-20 shows a comparison of the powder XRD patterns obtained from samples 1-3. Sample 2 shows all the characteristic reflections expected from the $LiNH_2$ structure, with the additional presence of low intensity reflections belonging to Li_2O. By contrast, sample 3 only shows the higher intensity reflections characteristic of $LiNH_2$. These are not well defined and have lost sharpness. The apparent loss of crystallinity in confined samples indicates that $LiNH_2$ has been dispersed in a manner that sample 2 has not. This evidence suggests that using lithium-ammonia solutions with carbon changes the dispersion of $LiNH_2$ within the carbon. The loss of crystallinity following confinement was also seen in the previous chapter and in other work reported in the literature.[55,56,57]

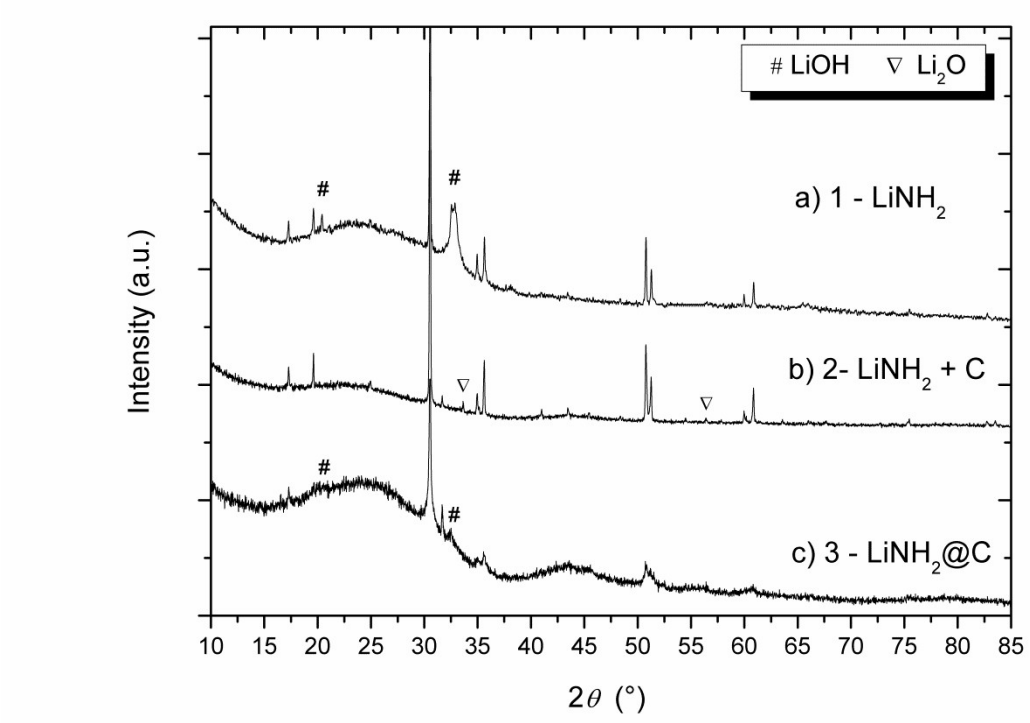

Figure 5-20. Comparison of powder XRD patterns for a) sample 1, b) sample 2 and c) sample 3. (not indexed peaks common to three samples correspond to $LiNH_2$ reflections)

5.3.3.2. Dehydrogenation studies

DTA profiles of as-received $LiNH_2$, sample 2 and sample 3 are shown in Figure 5-21 for comparison. Sample 2 shows the endothermic sharp peak at 368 °C corresponding to the melting of $LiNH_2$. However, no other thermal event can be observed after this, whereas the as-received $LiNH_2$ proceeds with a broad endothermic event at 498 °C corresponding to the large ammonia release that occurs on decomposition. Taking a look at the onset of sample 3, it can be seen that there is also a very small endothermic peak at 370 °C, which could also be caused by the melting of $LiNH_2$. No obvious thermal event is observed after this either.

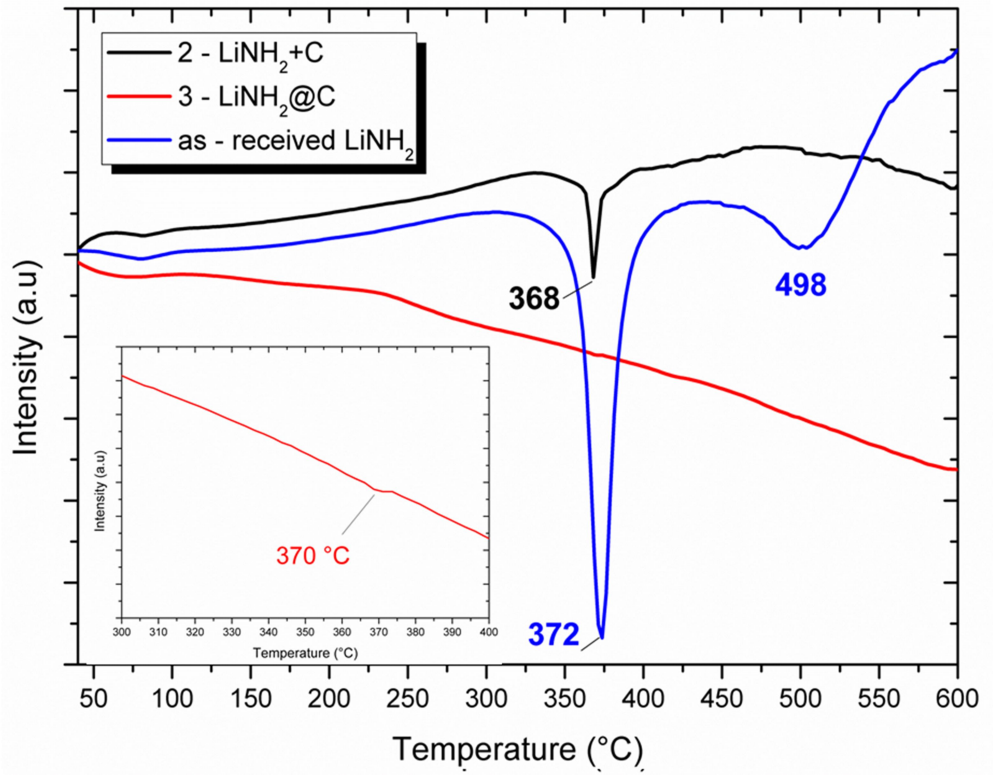

Figure 5-21. Comparison of the DTA profiles of as-received $LiNH_2$, sample 2 and sample 3 heated at 5 °C·min^{-1} to 600 °C.

Figure 5-22 shows a comparison of the TG profiles simultaneously recorded with the DTA profiles from Figure 5-21. Both sample 2 and sample 3 exhibit lower mass losses than expected; several times less than that for as-received $LiNH_2$. The mass losses are recorded as 3.6 and 8.1 wt.% for sample 3 and 2 respectively. Moreover, the onset of the mass loss for both these latter samples begins at earlier temperatures (ca. < 300 °C) than that of as-received $LiNH_2$.

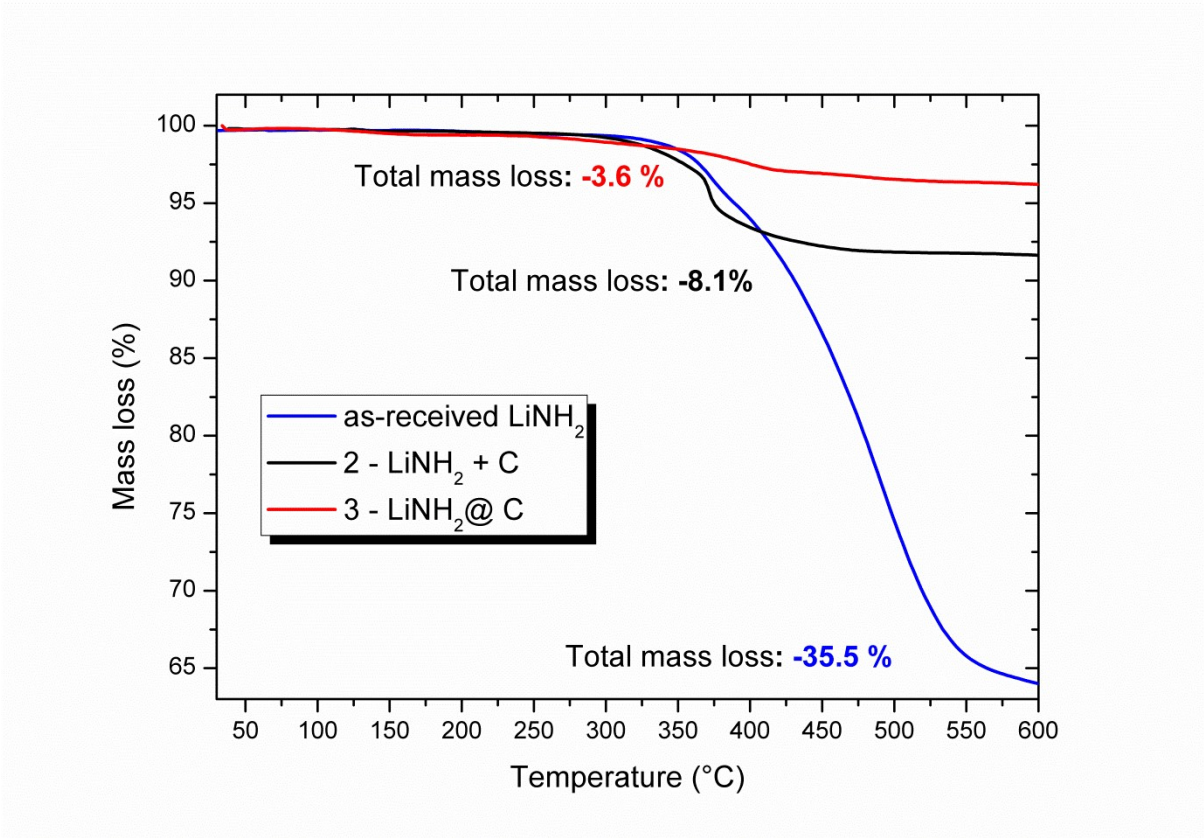

Figure 5-22. Comparison of the TGA profiles of as-received $LiNH_2$, sample 2 and sample 3 on heating to 600 °C at 5 °C·min^{-1}.

Figure 5-23 shows the H_2 desorption profile recorded simultaneous to the TG/DTA data by the mass spectrometer. The spectra from the total decomposition of as-received $LiNH_2$ have also been plotted for comparison (these latter data were collected to 800 °C at 5 °C·min^{-1}). Both samples 2 and 3 demonstrate hydrogen release at much lower temperature than the as-received $LiNH_2$. Sample 2 shows a hydrogen desorption starting at 356 °C and peaking at 428 °C, which is similar in profile shape and temperature to the NH_3 release from the as-received $LiNH_2$ in Figure 5-9. Sample 3 shows an even earlier hydrogen release than sample 2, starting to release hydrogen at 134 °C and reaching a maximum at 411 °C, 17 °C earlier than sample 2. It also can be observed that sample 3 starts releasing hydrogen at a temperature considerably below the $LiNH_2$ melting point (*ca.* 240 °C earlier), whereas sample 2 evolves hydrogen just 20 °C below the amide melting point. Despite some notable differences between sample 2 and sample 3, it is also evident that they share features in their thermal behaviour that are distinct from pure $LiNH_2$. This is most apparent when comparing the maxima of H_2 release which occur at temperatures *ca*. 400 °C below that of as-received $LiNH_2$ (dotted line).

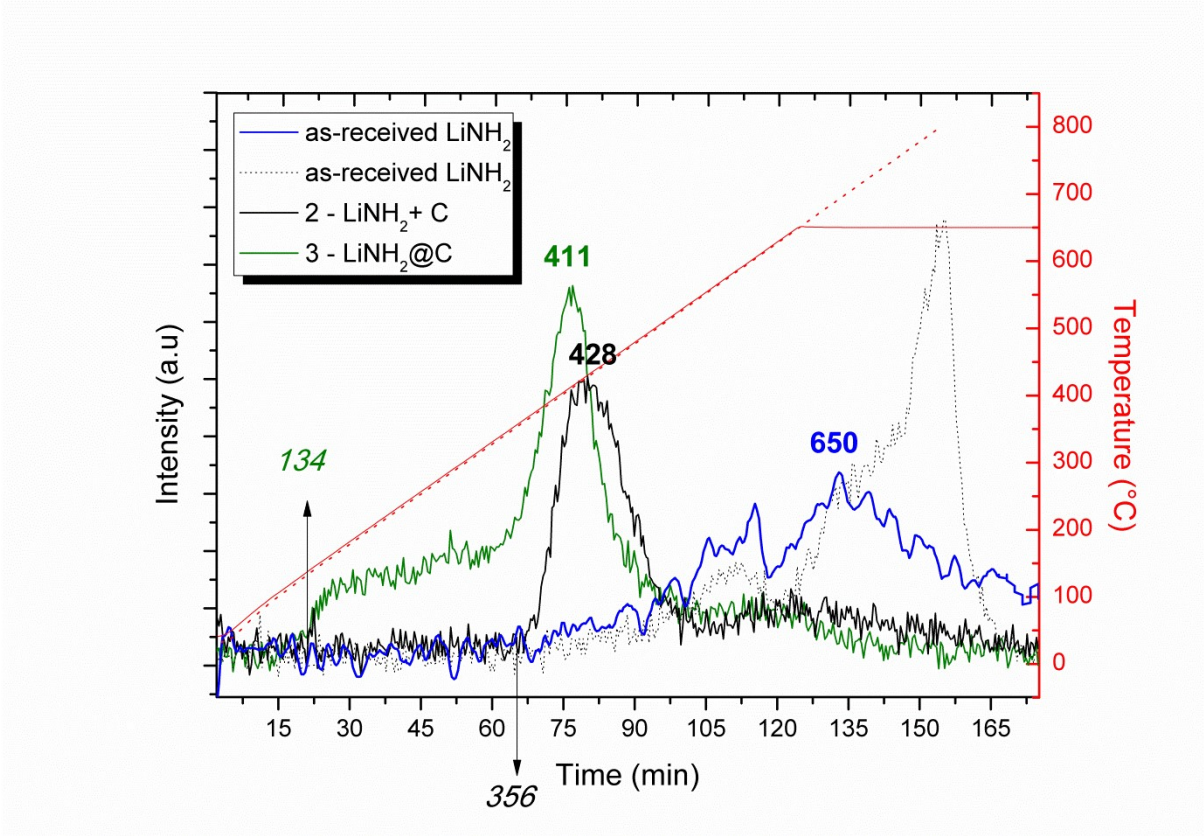

Figure 5-23. Mass Spectra of hydrogen release from as-received $LiNH_2$, sample 2 and sample 3 on heating to 650 °C for 1 h at 5 °C·min^{-1}. The dotted line represents full $LiNH_2$ decomposition on heating at 5 °C·min^{-1} to 800 °C.

Figure 5-24 shows a comparison of the mass spectra for evolved NH_3 from as-received $LiNH_2$, sample 2 and sample 3 on heating under the same conditions as above. Sample 2 shows a lesser amount of ammonia released than that of as-received $LiNH_2$, which correlates with the high mass loss of as-received $LiNH_2$ compared to sample 2. The ammonia release for sample 2 is small and peaks at 393 °C, over 100 °C lower than as-received $LiNH_2$. However, both samples start to release ammonia at the same temperature (364 °C). Sample 3 shows negligible ammonia release and one can conclude that the mass loss of 3.6 wt.% observed in the TG profile (Figure 5-22) mainly corresponds to hydrogen release, because evolution of any other gas was not observed.

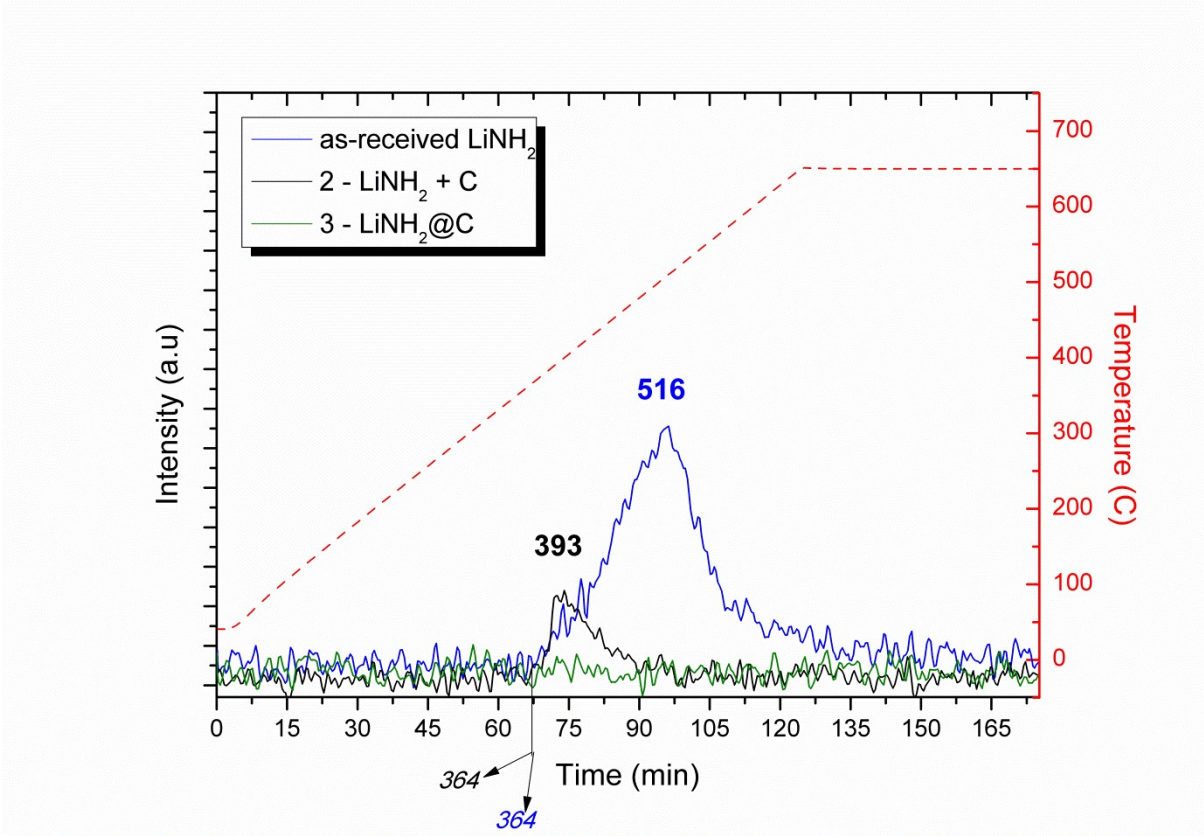

Figure 5-24. Mass spectra for ammonia release from as-received $LiNH_2$, sample 2 and sample 3 on heating to 650 °C for 1h at 5 °C·min^{-1}.

5.3.3.3. Post thermal treatment structural characterisation

Figure 5-25 shows the powder XRD patterns obtained from as-received $LiNH_2$, sample 2 and sample 3 after being heated to 600 °C. The patterns obtained for both sample 2 and 3 are very different from that of as-received $LiNH_2$, suggesting that $LiNH_2$ decomposition has followed a completely different pathway. Both patterns show an almost amorphous background and a very broad peak which seems to be a reflection characteristic from a previously phase unobserved, corresponding to lithium cyanamide (Li_2CN_2).

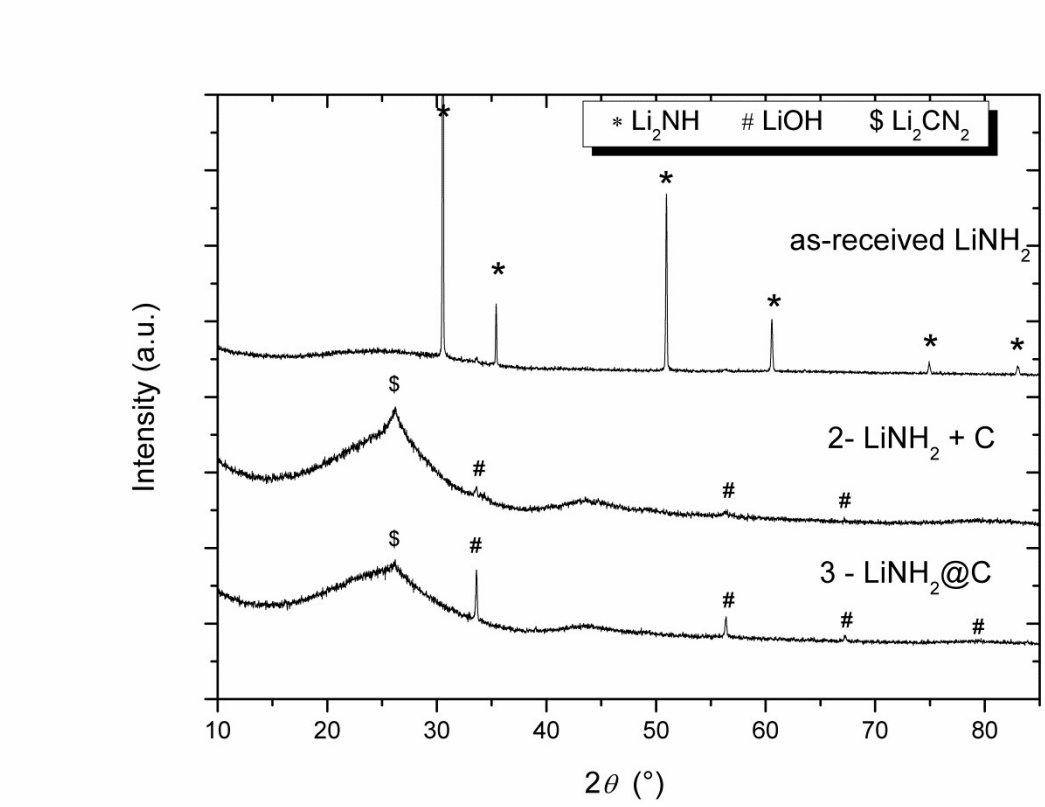

Figure 5-25. Powder XRD patterns obtained from as-received $LiNH_2$, sample 2 and sample 3 after heating to 600 °C at 5 °C·min^{-1}.

The presence of Li_2CN_2 phase in sample 2 and 3 was confirmed by Raman Spectroscopy, as seen in Figure 5-26. The samples present a low intensity bands at 1273 and 1274 cm^{-1} respectively, which can be assigned to the symmetric stretching mode of N=C=N.[58,59]

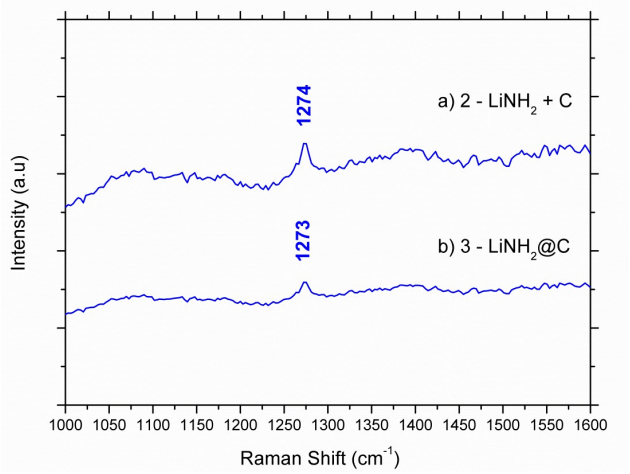

Figure 5-26. Raman spectra obtained between 1000 – 1600 cm^{-1} from a) sample 2 and b) sample 3.

Although the XRD patterns of samples 2 and 3 after thermal treatment both contain a broad peak corresponding to Li_2CN_2 (confirmed by Raman spectroscopy in Figure 5-26), the evolved gas mass spectra for the samples are quite different. Sample 3 starts releasing hydrogen at a temperature much lower than the $LiNH_2$ melting point, which is not the case for sample 2. Sample 2 starts to release hydrogen almost at the moment $LiNH_2$ melts, and this is initially accompanied by the release of ammonia. Presumably once $LiNH_2$ melts, it rapidly reacts with the carbon, which explains why the low-intensity ammonia peak in the mass spectrum seems to be suddenly inhibited for sample 2 in Figure 5-24. These observations might indicate that the dispersion of $LiNH_2$ with the carbon is clearly different for samples 2 and 3, leading to different gas desorption profiles, although Li_2CN_2 is present in both final products upon further heating.

It seems that more than one effect might be affecting the decomposition of these samples at the same time. Both samples must follow a decomposition pathway that is different from that of $LiNH_2$ itself since no lithium imide phase is present in the final product after heating treatment at 600 °C (Figure 5-10b), and lithium cyanamide is present. This must be induced by the introduction of carbon in the samples, which might lead to Li_2CN_2 formation by Eq. 5-13.[60]

$$2LiNH_2 + C \rightarrow Li_2CN_2 + 2H_2 \qquad (5\text{-}13)$$

A set of experiments to study the processes that occur in the presence of carbon were performed and will be presented and discussed in the following section. After knowing how the introduction of carbon in the samples affects the decomposition pathway, the obvious differences between sample 2 and 3 could be analysed and discussed in more detail. It would be expected that these differences would be induced by the dispersion of lithium amide within the carbon, introduced by the nanoconfinement synthetic approach.

5.3.4. Physically mixed samples of $LiNH_2$ and C

In order to study the formation of Li_2CN_2 further, a set of physically mixed samples containing different amount of $LiNH_2$ and C were prepared (Table 5-6). Sample 7 is the one whose wt. ratio corresponds to the molar ratio of the stoichiometric reaction ($LiNH_2$: C = 2 : 1) assuming Eq. 5-13 occurs. As-received $LiNH_2$ was used as a starting material to reduce the possibility of the presence of any impurity affecting the results of this work.

Table 5-6. List of samples presented in this section.

Samples	Identity	$LiNH_2$ type	$LiNH_2$ (g)	C (g)	$LiNH_2$: C wt. ratio
4	physically mixed ($LiNH_2$+ C)	commercial	0.096	0.500	1 : 5.2
5	physically mixed ($LiNH_2$+ C)	commercial	0.096	0.200	1 : 2.1
6	physically mixed ($LiNH_2$+ C)	commercial	0.200	0.100	2 : 1
7	physically mixed ($LiNH_2$+ C)	commercial	0.200	0.050	4 : 1
8	physically mixed ($LiNH_2$+ C)	commercial	0.570	0.050	11.4 : 1

5.3.4.1. Dehydrogenation studies

Figure 5-27a shows the TG profile of as-received $LiNH_2$ and samples 4-8. It can be observed that each sample has a different mass loss at 500 °C. The temperature heating programme was stopped at 500 °C, because the thermal events of interest occur below that temperature (*ie.* Li_2NH and possible Li_2CN_2 formation). The value of the mass loss observed is directly dependent on the amount of $LiNH_2$ used in the sample. The higher the quantity of $LiNH_2$ used, the higher the total mass loss, with as-received $LiNH_2$ the sample that has the greatest mass loss (25.18 %). In contrast, sample 4 (the sample with the lowest $LiNH_2$: C ratio), is the sample with the lowest mass loss value (6.50 %). The DTA profiles (Figure 5-27b) recorded from the same samples each exhibit an endothermic peak at *ca.* 370 °C, which seems to correspond to the melting of $LiNH_2$. This

endothermic peak is shifted to slightly lower temperature if $LiNH_2$ is mixed with carbon. The peak temperature of this event for the as-received $LiNH_2$ is at 372 °C, whereas the lowest temperature peak is observed at 366 °C for sample 4. The DTA profile shows some unidentified thermal events in some of the samples between 450 and 500 °C, with no subsequent gas release indicated in the MS spectra.

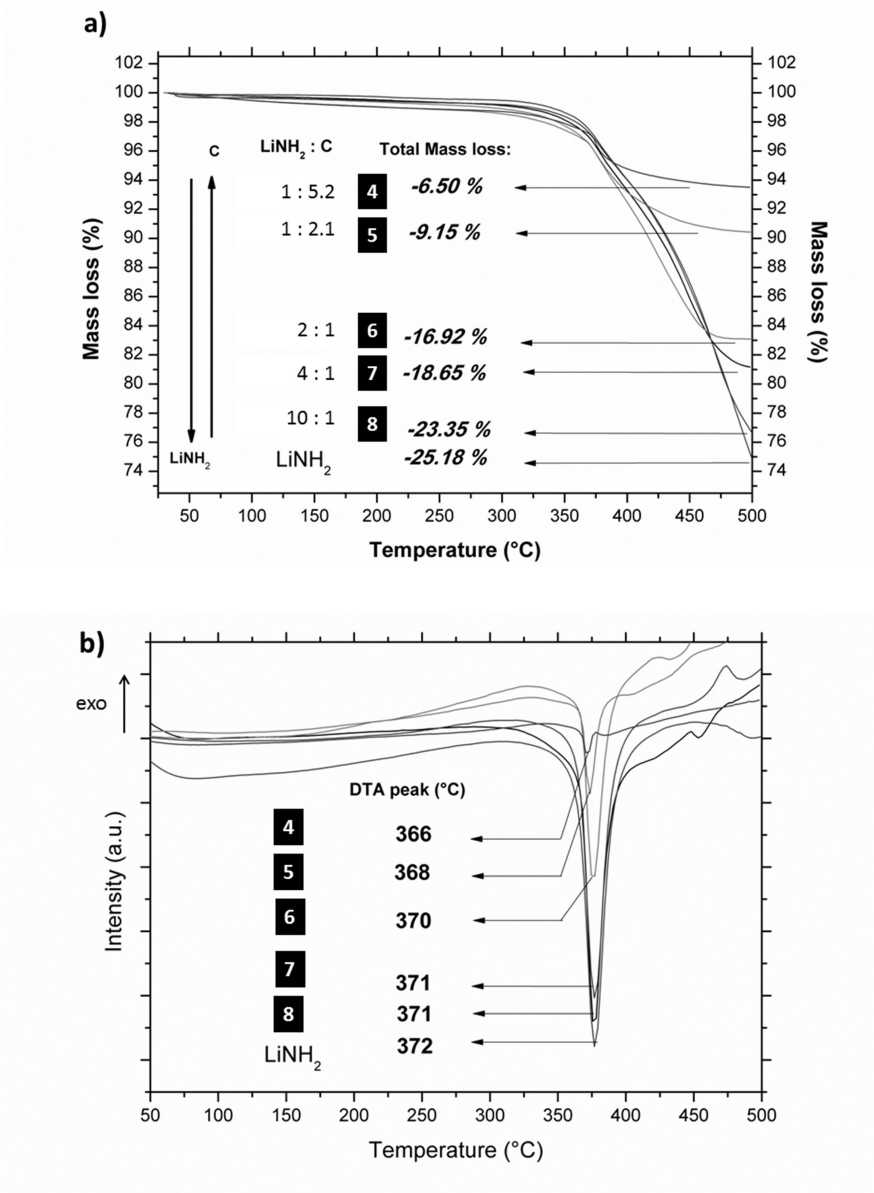

Figure 5-27. Comparison profiles obtained of as-received $LiNH_2$ and samples 4 – 8, at 5 °C·min-1 to 500 °C: a) TGA b) DTA.

Figure 5-28 shows the mass spectra for evolved H_2 from as-received $LiNH_2$ and samples 4-8. All the samples, with the exception of as-received $LiNH_2$, release hydrogen with a main peak centred between the temperatures 441 – 474 °C. The temperature at which the hydrogen release peak is

centred depends on the amount of carbon mixed with $LiNH_2$. The sample with the highest amount of $LiNH_2$ is sample 8, which has the peak at 474 °C, whereas the sample with the lowest amount of $LiNH_2$ is sample 4, where the hydrogen release peaks at 441 °C. The temperatures of H_2 release for samples 4-8 follows the same trend as the STA endotherms and TG mass loss temperatures for the same samples (Figure 5-27).

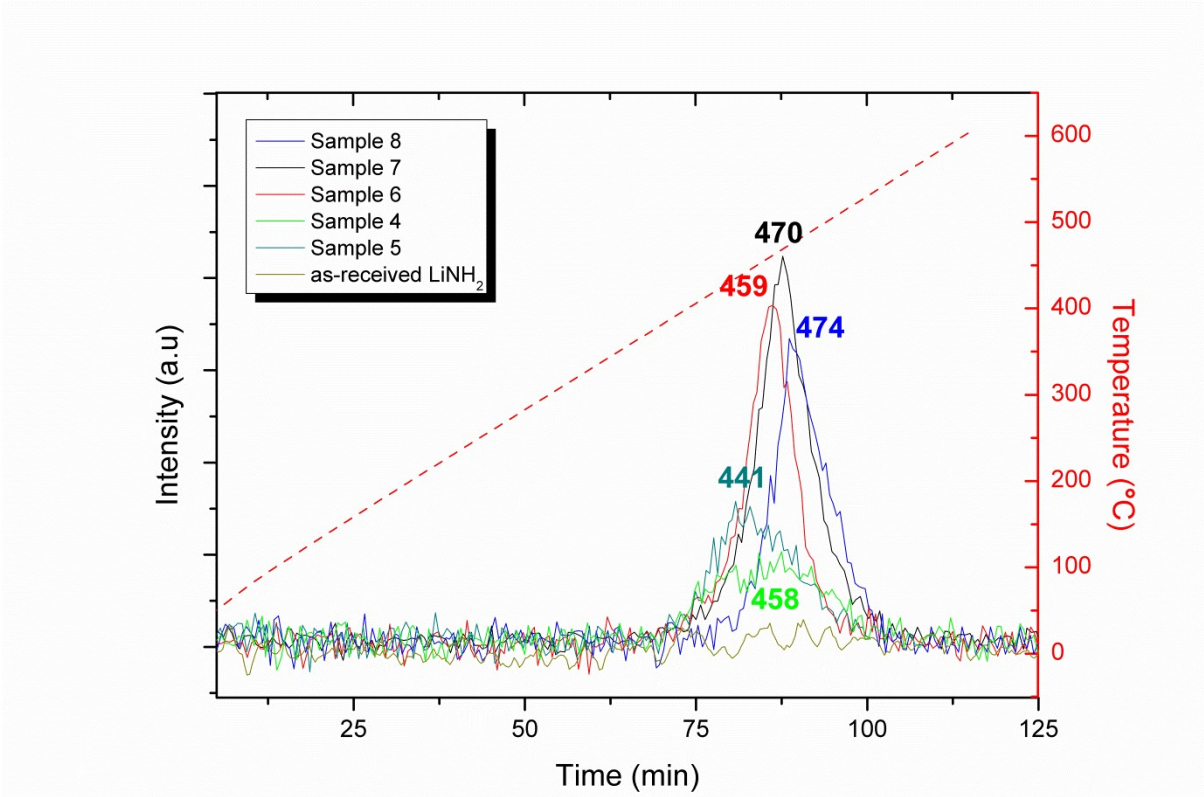

Figure 5-28. Hydrogen mass spectra for as-received $LiNH_2$ and samples 4-8 on heating to 500 °C at 5 °C·min^{-1}.

Figure 5-29 shows the evolved NH_3 mass spectra from as-received $LiNH_2$ and samples 4-8. The peak temperature of ammonia release varies from sample to sample, between 516 °C (for as-received $LiNH_2$) and 396 °C (for sample 7). The temperature of ammonia release apparently has no direct correlation to the molar ratio $LiNH_2$: C. It can be observed though, that samples 4 – 8 have a significantly lower relative intensity of evolved ammonia when compared to as-received $LiNH_2$, which will be discussed at the end of the section. No other gas was recorded by the mass spectrometer (*e.g* CH_4, HCN, CN_2). Sample 5 has the closest $LiNH_2$: C wt. ratio to sample 3 and also shows a negligible release of ammonia, as can be seen by comparison with Figure 5-24.

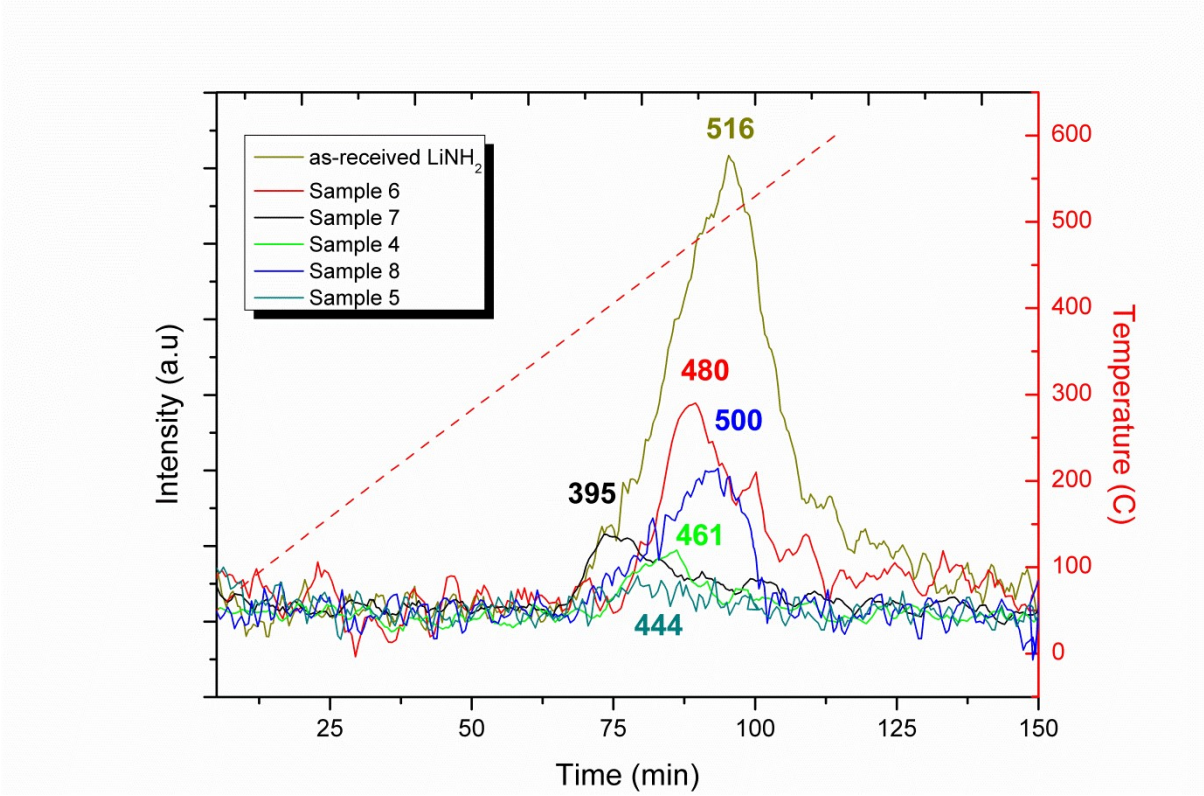

Figure 5-29. Evolved ammonia mass spectra from as-received $LiNH_2$ and samples 4-8 on heating to 500 °C at 5 °C·min^{-1}.

5.3.4.2. Post thermal treatment structural characterisation

Figure 5-30 shows the powder XRD patterns obtained from samples 4 - 8 after heating to 500 °C. It can be observed that two phases predominates across most of the samples. (And some low intensity reflections from lithium oxide are also present in some cases). These 2 phases are Li_2NH, from the expected decomposition of $LiNH_2$ and Li_2CN_2, from the reaction between $LiNH_2$ and C. The relative intensity of the reflections from Li_2NH and Li_2CN_2 vary across samples, increasing in favour of the Li_2NH reflections for the samples that contain the highest amount of $LiNH_2$ in the starting mixture. The only sample that does not show the presence of Li_2NH is 4, which represents the sample with the lowest initial $LiNH_2$: C ratio.

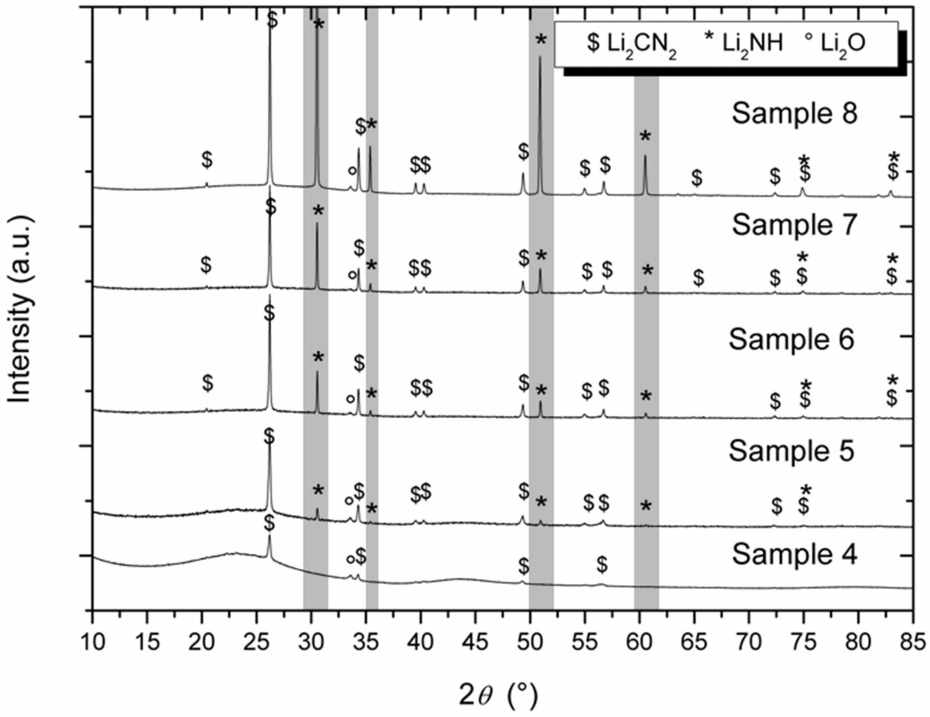

Figure 5-30. Powder XRD patterns obtained from sample 4 - 8 after heating to 500°C at 5 °C·min^{-1}.

Hence, the presence of these two phases provides evidence that these 2 reactions happen in parallel: Eq. 5-15 which will lead to Li_2NH and Eq. 5-14 which will lead to Li_2CN_2. Clearly, in the absence of carbon (i.e as-received $LiNH_2$) only the decomposition of amide to imide occurs.

$$2LiNH_2 + C \rightarrow Li_2CN_2 + 2H_2 \quad (5\text{-}14)$$

$$LiNH_2 \leftrightarrow Li_2NH + NH_3 \quad (5\text{-}15)$$

Formation of Li_2CN_2 as an undesired by-product is not an isolated event of this work. Several cases have been reported in the literature, when lithium compounds have been treated at high temperatures in presence of carbon. For example, Li_2CN_2 was observed in the dehydrogenation product of lithium borohydride – melamine complex ($LiBH_4 \cdot C_6N_6H_6$) at 340 °C, but was not present at 210 °C.[61]

Lithium cyanide presence in the Li-Mg-N-H system was also observed. ($2LiNH_2 + MgH_2$) transforms to $Li_2Mg(NH)_2$ in the first hydrogen desorption process (Eq. 5-16). Subsequently $Li_2Mg(NH)_2$ reacts with H_2 to yield $Mg(NH_2)_2$ and LiH reversibly (Eq. 5-17).[62] Formation of Li_2CN_2 (and MgO) was observed when H_2 (1% CO), as opposed to pure hydrogen, was used for rehydrogenation of $Li_2Mg(NH)_2$ (Eq. 5-18).[63] The sample desorption capacity decreased from the first to the sixth cycle, whereas it was stable in pure hydrogen. Therefore, in presence of CO, the bond between C and O breaks and the carbon reacts with the Li^+ and N^{3-}, whereas the O reacts with the Mg^{2+}.

$$LiNH_2 + MgH_2 \rightarrow Li_2Mg(NH_2)_2 + H_2 \qquad (5\text{-}16)$$

$$Li_2Mg(NH_2)_2 + 2H_2 \leftrightarrow Mg(NH)_2 + 2LiH \qquad (5\text{-}17)$$

$$Li_2Mg(NH_2)_2 + 2H_2(1\%\, CO) \leftrightarrow Mg(NH)_2 + 2LiH + Li_2CN_2 + MgO \qquad (5\text{-}18)$$

The reaction between lithium nitride and carbon dioxide has also led to lithium cyanamide formation by the following equation:[64]

$$CO_{2\,(g)} + 2Li_3N \rightarrow Li_2CN_{2(s)} + 2Li_2O_{(s)} \qquad \Delta H° = -759.9\ kJ{\cdot}mol^{-1} \qquad (5\text{-}19)$$

This enthalpically favoured reaction has also been of interest to control CO_2 emissions while producing lithium cynamide, which is an important organic reagent[65] and a unique precursor of fertilizers.[66]

Taking a look at the thermodynamics, it can be observed that lithium amide decomposition is most favoured when in presence of LiH, as part of the Li – N – H system (Eq. 5-20).[18] Alapi et. al calculated by first-principle calculations the reaction enthalpy of the interaction between lithium amide and carbon (Eq. 5-21),[60] which was lower in value than the enthalpy for lithium amide decomposition leading to lithium imide and ammonia release (Eq. 5-22).[2] Therefore, amide reaction with carbon requires less heating than amide decomposition or amide reaction with LiH.

$$LiNH_2 + LiH \leftrightarrow Li_2NH + H_2 \qquad \Delta H = 44.5\ kJ \cdot mol^{-1}\, H_2 \qquad (5\text{-}20)$$

$$2LiNH_2 + C \rightarrow Li_2CN_2 + 2H_2 \qquad \Delta U_O^* = 31.4\ kJ \cdot mol^{-1}\, H_2 \qquad (5\text{-}21)$$

**ΔUo corresponds to reaction enthalphy computed by total energy calculations, which can be compared to standard reaction enthalpies for comparison.*

$$LiNH_2 \rightarrow Li_2NH + NH_3 \qquad \Delta H = 84.1\ kJ \cdot mol^{-1}\, NH_3 \qquad (5\text{-}22)$$

The lower enthalpy reaction from the lithium amide with carbon compared to the decomposition of lithium amide alone, would explain that the former reaction is favoured, although the latter is still happening in a certain degree (Figure 5-30).

5.3.4.3. Comparison of confined samples with physically mixed samples

After establishing the formation of Li_2CN_2 in the presence of carbon, one might propose sample 2 and 3 have different decomposition pathways from as-received $LiNH_2$ (Figure 5-31).

Sample 2 starts evolving hydrogen at 356 °C, reaching a maximum release at 428 °C. A peak was also observed for samples 4 – 8, with different shape and intensity, found between 441 – 474 °C. This hydrogen release can be assigned to the formation of Li_2CN_2, by reaction of $LiNH_2$ and C (since it was only observed in the presence of carbon and not for as-received $LiNH_2$ as observed in Figure 5-31). The difference in hydrogen release temperature from sample 2 to samples 4 – 8, might be influenced by the nature of the lithium amide used. Lab-synthesised $LiNH_2$ (sample 1) was used, as opposed to commercial $LiNH_2$, in the preparation of samples 2 and 3. And sample 1 had demonstrated hydrogen release at lower temperature than commercial $LiNH_2$, due to its particle size. XRD characterization shows that the final products after dehydrogenation for samples 5 – 8 (Figure 5-30), consist of a mixture of Li_2CN_2 and Li_2NH phases whereas sample 4, where a lower amount of $LiNH_2$ starting material was used contains no imide. Similarly sample 2 did not show the presence of Li_2NH after dehydrogenation and the ratio $LiNH_2$: C in the starting mixture lies in between sample 4 and sample 5, which shows only very low intensity peaks of the

Li_2NH phase in the partly-dehydrogenated product. Ammonia release nevertheless occurs in sample 2 (Figure 5-24), although its intensity is considerably diminished in comparison with that of as-received $LiNH_2$, leading one to believe that the formation of Li_2CN_2 depletes the evolution of ammonia and favours hydrogen evolution. However, the presence of Li_2NH in the dehydrogenated amorphous sample (sample 2) has not been confirmed.

Sample 3 has some similarities in the hydrogen release profile with sample 2 at higher temperatures (> 300 °C), but a distinct unique hydrogen release profile at lower temperatures (< 300 °C). It is safe to assume that the hydrogen release at 411 °C would also correspond to the reaction of lithium amide in the presence of carbon leading to Li_2CN_2 formation and this is corroborated by Raman spectroscopy. The difference between the lower temperature of hydrogen release in comparison with sample 2, can be due to the closer contact of lithium amide with the carbon, which would facilitate Li_2CN_2 formation, leading to this earlier hydrogen evolution. No presence of Li_2NH was observed in the dehydrogenated product in Figure 5-25, presumably due to the small amount of $LiNH_2$ used in the starting mixture. At lower temperatures (under 300 °C), a hydrogen release event occurs in sample 3 that does not occur in any of the other samples. This starts at 134 °C, and can be assigned to confinement effects (Figure 5-31), or at least to a better dispersion of the product within the carbon, because it is the only condition that is different from all of the other physically mixed samples. Since no ammonia release was observed for sample 3 (Figure 5-24), it is safe to assume that the dehydrogenation of sample 3 has followed the Li_2CN_2 formation pathway uniquely, being facilitated at earlier temperatures due to confinement effects. All the available lithium amide is consumed before it could be decomposed to Li_2NH formation and ammonia. The Li_2CN_2 formation has thus probably been facilitated by the intimate contact that lithium amide has in occupying the pores of the carbon host. To confirm this hypothesis, structural characterization over the 100 – 300 °C range would need to be performed to provide evidence of lithium cyanamide formation prior to the main hydrogen release at 411 °C.

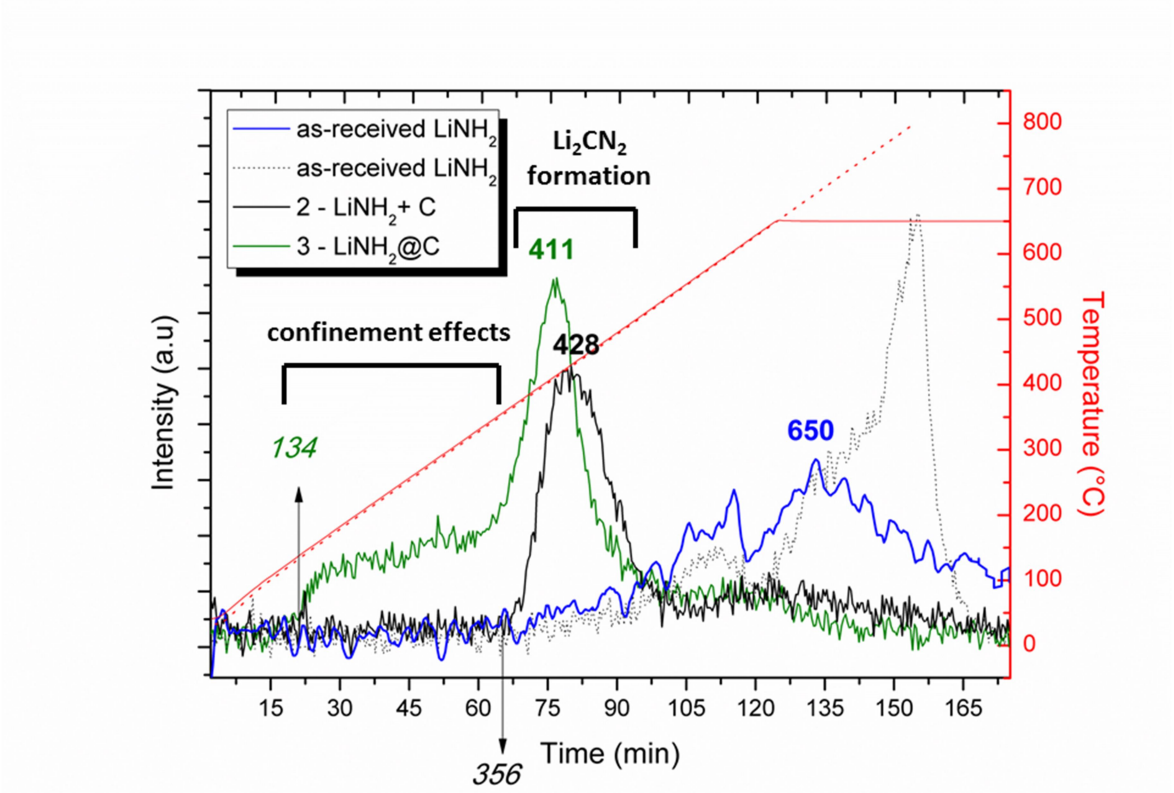

Figure 5-31. MS recording hydrogen release from the as-received $LiNH_2$, sample 2 and sample 3 (which has been split in 2 parts) on heating to 650 °C at 5 °C·min^{-1} followed by 1 h holding the temperature at 650 °C. The dotted line represents full $LiNH_2$ decomposition on heating at 5 °C·min^{-1} to 800 °C.

These experiments are clear examples of why in any confinement synthesis it is very important to choose a porous host that not only is of appropriate porosity and surface area but is also inert to the material to be confined. Kanoh et. al[25] attempted the confinement of Li_3N in carbon aerogels by melt infiltration. The resulting composite was a mixture of Li_3N/Li_2C_2 originating from the reaction of the nitride with the porous host. Nevertheless, the final composite delivered an enhanced hydrogen absorption capacity and reduced temperatures of hydrogenation and dehydrogenation. The authors claimed that lithium carbide confined/segregated within lithium nitride and/or the hydrogenated products (lithium amide and lithium hydride) was responsible for the improved properties. However, formation of Li_2C_2 led to the loss of reversibility. This example also broke "the first rule of confinement", where the porous host used (carbon aerogel, pore average diameter 15.5 nm) reacted with the active material to be confined.

In order to see what changes the nanoconfinement approach would have had on the decomposition of $LiNH_2$, without changing the decomposition pathway, two alternatives could be attempted: ammonia release without hydrogen evolution or Li_2CN_2 formation could be studied if

a partial hydrogen gas pressure was applied on heating. It has been reported that flushing hydrogen gas over lithium amide inhibits the Li_2CN_2 formation.[67] Alternatively, confinement of $LiNH_2$ in a different inert porous host, such as zeolites, MOF's or SiO_2 could also be attempted (*ie*. carbon – free host) and results obtained could be compared with the ones obtained in this work. Ammonia release from the formation of Li_2NH, and subsequent H_2 release temperatures could be improved by nanoconfinement if the host did not interact with the sample to be confined. For instance, Wu et. al, confined $Li_3BN_2H_8$ in a carbon aerogel (average pore diameter 13 nm), with no Li_2CN_2 formation, and increased ammonia release.[68] The authors suspected that the dehydrogenation pathway changed because of the reduced particle size due to the confinement, but did not suggested what this pathway could be.

Some other research groups have supressed some of the expected unwanted gases evolved by preparing nanoconfined composites, but have not given an insight into the nature of any possible new dehydrogenation pathways. This is the case for confinement of $LiBH_4$ in porous carbon of different average pore diameter sizes (15 nm, 9 nm, 4 nm and 2 nm), where toxic B_2H_6 release was decreased, and even eliminated for the smallest pore diameter host (2 nm).[57] $Li_4BN_3H_{10}$ releases ammonia before hydrogen in bulk form, but when confined in nanoporous carbon (average pore diameter of 4.4 nm) ammonia release was supressed and B_2H_6 evolution was eliminated.[69] Again this suggests that the decomposition pathway was altered by nanoconfinement, although not further information about it was given.

In this work ammonia is supressed and hydrogen released via Li_2CN_2 formation. Therefore, it could be said that mixing $LiNH_2$ with carbon significantly improves the hydrogen release properties of $LiNH_2$, giving birth to the Li – C – N – H system. First, given that $LiNH_2$ otherwise requires LiH to produce H_2 over NH_3, mixing $LiNH_2$ with C provides an alternative pathway to H_2 release. Second, the material releases hydrogen at much lower temperatures than as-received $LiNH_2$ (even for non-confined composites). Physical mixtures of $LiNH_2$ and C start to release hydrogen between 400 – 450 °C, a range of temperatures at which as-received $LiNH_2$ did not show any hydrogen evolution (Figure 5-28).

At the same time, the beneficial effects of hydride confinement on hydrogen release temperatures have also been demonstrated. Confined $LiNH_2$ releases hydrogen *ca.* 220 °C earlier than the physically mixed sample. Importantly, however, the formation of the stable Li_2CN_2 phase destroys any reversibility in the system, since Li_2CN_2 cannot be rehydrogenated, at least not at practical hydrogen gas pressure and temperatures.[70] Nevertheless the $LiNH_2$ + C system could still

be used as an irreversible ("one-shot") hydrogen release system.[71] Such systems can be sustainably and inexpensively regenerated *ex-situ*, for instance, by reaction with hydrogen gas or water. An example of these systems would be the LiOH – LiH system.[72] This would appear not to be the case of the Li – N – H – C system due to the thermodynamically favourable formation of Li_2CN_2. Nonetheless, the system could be used for hydrogen generation in stationary applications while being of use to chemical or fertilizer industry, where there is a potential demand of Li_2CN_2 (as a chemical reagent[65] or as a precursor of fertilizers[66]).

5.4. CONCLUSIONS

The confinement of $LiNH_2$ in porous carbon via a novel synthesis, consisting of "in-situ" confinement using lithium-ammonia solutions has been attempted. The aim was to improve the hydrogen release properties of the amide, by lowering the temperature at which hydrogen is released.

Lithium amide was prepared in the laboratory and fully studied using different characterization techniques. DTA, TG, MS profiles showed that the lithium amide synthetized was similar in behaviour to the as-received $LiNH_2$, and could be used as such. The main difference is the shift of ammonia release to lower temperatures, presumably due to a reduction of the amide particle size from the synthesis.

The results obtained for the confinement of $LiNH_2$ in porous carbon FDU-15 showed that confinement by the "in-situ" novel synthesis led to a reduced specific surface area and a decrease in the available pore volume of the carbon host. This indicated a filling or blocking of the pores to a much greater degree than in an equivalent physically mixed sample. It was difficult to confirm whether the amide was supported on the outer surface of the carbon particles or confined within the pores of the carbon particles. Evolved gas mass spectrometry showed that hydrogen release originated not from the dehydrogenation of $LiNH_2$ in itself, but from a reaction of lithium amide with carbon at higher temperatures. This in itself is interesting, given normally $LiNH_2$ would thermally decompose to Li_2NH with ammonia release. The reaction with carbon led to irreversible Li_2CN_2 formation. A set of experiments to establish the formation of Li_2CN_2 with physically mixed samples were performed. The physically mixed samples showed hydrogen release between 400 - 450 °C, whereas as-received $LiNH_2$ did not, producing a mixture of Li_2NH and Li_2CN_2, suggesting both decomposition pathways were followed (with supressed NH_3 release in comparison with as-received $LiNH_2$). In contrast, confined $LiNH_2$ released hydrogen *ca.* 220 °C lower than the physically mixed sample, with no detectable trace of ammonia release, suggesting the only decomposition pathway followed was via Li_2CN_2 formation, presumably facilitated by intimate contact of $LiNH_2$ particles with the porous host. These findings make the Li – N – H – C system a valid one for hydrogen storage applications, releasing hydrogen at lower temperatures than the Li – N – H system. This improvement, though, comes with a price, that is the loss of reversibility, due to the formation of the stable Li_2CN_2 phase, but could still be considered as an irreversible "one-shot" primary hydrogen storage material.

5.5. REFERENCES

1. P. Chen, Z. Xiong, J. Luo, J. Lin and K. L. Tan, *Nature*, 2002, **420**, 302-304.
2. T. Ichikawa, N. Hanada, S. Isobe, H. Y. Leng and H. Fujii, *Journal of Alloys and Compounds*, 2005, **404–406**, 435-438.
3. T. Ichikawa, N. Hanada, S. Isobe, H. Leng and H. Fujii, *The Journal of Physical Chemistry B*, 2004, **108**, 7887-7892.
4. P. Chen, Z. Xiong, J. Luo, J. Lin and K. L. Tan, *The Journal of Physical Chemistry B*, 2003, **107**, 10967-10970.
5. K.-F. Aguey-Zinsou, J. Yao and Z. X. Guo, *The Journal of Physical Chemistry B*, 2007, **111**, 12531-12536.
6. J. Yang, Q. Cai, W. Wang, W. B. Yelon and W. J. James, *Materials Research Soc. Symposia Proceedings* 2005, 1 - 6
7. D. H. Gregory, *Journal of Materials Chemistry*, 2008, **18**, 2321-2330.
8. T. K. Mandal and D. H. Gregory, *Annual Reports Section "A" (Inorganic Chemistry)*, 2009, **105**, 21-54.
9. K. Ohoyama, Y. Nakamori, S.-i. Orimo and K. Yamada, *Journal of the Physical Society of Japan*, 2005, **74**, 483-487.
10. W. I. F. David, M. O. Jones, D. H. Gregory, C. M. Jewell, S. R. Johnson, A. Walton and P. P. Edwards, *Journal of the American Chemical Society*, 2007, **129**, 1594-1601.
11. P. A. Anderson, P. A. Chater, D. R. Hewett and P. R. Slater, *Faraday Discussions*, 2011, **151**, 271-284.
12. J. Zhang and Y. H. Hu, *Industrial & Engineering Chemistry Research*, 2011, **50**, 8058-8064.
13. H. Y. Leng, T. Ichikawa, S. Hino, N. Hanada, S. Isobe and H. Fujii, *The Journal of Physical Chemistry B*, 2004, **108**, 8763-8765.
14. W. Luo, *Journal of Alloys and Compounds*, 2004, **381**, 284-287.
15. D. Pottmaier, F. Dolci, M. Orlova, G. Vaughan, M. Fichtner, W. Lohstroh and M. Baricco, *Journal of Alloys and Compounds*, 2011, **509, Supplement 2**, S719-S723.
16. C. H. Christensen, R. Z. Sorensen, T. Johannessen, U. J. Quaade, K. Honkala, T. D. Elmoe, R. Kohler and J. K. Norskov, *Journal of Materials Chemistry*, 2005, **15**, 4106-4108.
17. A. Leineweber, M. W. Friedriszik and H. Jacobs, *Journal of Solid State Chemistry*, 1999, **147**, 229-234.
18. T. Ichikawa, S. Isobe, N. Hanada and H. Fujii, *Journal of Alloys and Compounds*, 2004, **365**, 271-276.

19. M. Aoki, K. Miwa, T. Noritake, G. Kitahara, Y. Nakamori, S. Orimo and S. Towata, *Appl. Phys. A*, 2005, **80**, 1409-1412.
20. P. A. Chater, W. I. F. David, S. R. Johnson, P. P. Edwards and P. A. Anderson, *Chemical Communications*, 2006, DOI: 10.1039/B518243C, 2439-2441.
21. M. E. Straumanis, *Journal of Applied Physics*, 1959, **30**, 1965-1969.
22. F. E. Pinkerton, G. P. Meisner, M. S. Meyer, M. P. Balogh and M. D. Kundrat, *The Journal of Physical Chemistry B*, 2005, **109**, 6-8.
23. D. L. Perry and S. L. Phillips, *Handbook of Inorganic Compounds*, Taylor & Francis, 1995.
24. R. Demir-Cakan, W. S. Tang, A. Darwiche and R. Janot, *Energy & Environmental Science*, 2011, **4**, 3625-3631.
25. Y.-J. Liu, Y. Cheng, T. Ohba, K. Kaneko and H. Kanoh, *International Journal of Hydrogen Energy*, 2011, **36**, 12902-12908.
26. M. J. O'Neil, *The Merck Index - An Encyclopedia of Chemicals, Drugs, and Biologicals. 13th Edition, Whitehouse Station, NJ: Merck and Co., Inc.*, 2001, 990.
27. R. C. West, *Handbook of Chemistry and Physics 60th ed. Boca Raton, Florida: CRC Press Inc*, 1979, B-91.
28. E. Zurek, P. P. Edwards and R. Hoffmann, *Angewandte Chemie International Edition*, 2009, **48**, 8198-8232.
29. S. J. M. Thomas, P. P. Edwards and V. L. Kuznetsov, *ChemPhysChem*, 2008, **9**, 59-66.
30. C. A. Seely, *J. Franklin Inst.* , 1871, **61**, 110-114.
31. C. A. Kraus, G. Lepoutre and M. J. Sienko, *Solutions métal-ammoniac, propriétés physicochimiques: Colloque Weyl, Lille, juin 1963*, Benjamin, 1964.
32. G. E. Gibson and W. L. Argo, *Journal of the American Chemical Society*, 1918, **40**, 1327-1361.
33. N. W. Taylor and G. N. Lewis, *Proceedings of the National Academy of Sciences of the United States of America*, 1925, **11**, 456-457.
34. N. F. Mott, *Philosophical Magazine*, 1961, **6**, 287-309.
35. C. A. Kraus, *Journal of Chemical Education*, 1953, **30**, 83.
36. R. Juza, *Angewandte Chemie International Edition in English*, 1964, **3**, 471-481.
37. R. Juza and K. Opp, *Zeitschrift für anorganische und allgemeine Chemie*, 1951, **266**, 313-324.
38. C. W. Kamienski, D. P. McDonald, M. W. Stark and J. R. Papcun, in *Kirk-Othmer Encyclopedia of Chemical Technology*, John Wiley & Sons, Inc., 2000, DOI: 10.1002/0471238961.1209200811011309.a01.pub2.

39. *Ullmann's Encyclopedia of Industrial Chemistry. 6th ed. Federal Republic of Germany: Wiley-VCH Verlag GmbH & Co. 2003 to Present*, 2003, **1**, p. V20 47
40. D. B. Grotjahn, P. M. Sheridan, I. Al Jihad and L. M. Ziurys, *Journal of the American Chemical Society*, 2001, **123**, 5489-5494.
41. C. A. Schneider, W. S. Rasband and K. W. Eliceiri, *Nat Meth*, 2012, **9**, 671-675.
42. H. Jacobs and R. Juza, *Zeitschrift für anorganische und allgemeine Chemie*, 1972, **391**, 271-279.
43. A. Michigoe, T. Hasegawa, N. Ogita, T. Ichikawa, Y. Kojima, S. Isobe and M. Udagawa, *Journal of the Physical Society of Japan*, 2012, **81**, 094603.
44. A. Michigoe, T. Hasegawa, N. Ogita, M. Udagawa, M. Tsubota, T. Ichikawa, Y. Kojima and S. Isobe, *Chinese Journal of Physics*, 2011, **49**, 294.
45. J. P. O. Bohger, R. R. Eßmann and H. Jacobs, *Journal of Molecular Structure*, 1995, **348**, 325-328.
46. L. H. Jepsen, D. B. Ravnsbaek, C. Grundlach, F. Besenbacher, J. Skibsted and T. R. Jensen, *Dalton Transactions*, 2014, **43**, 3095-3103.
47. F. E. Pinkerton, *Journal of Alloys and Compounds*, 2005, **400**, 76-82.
48. A. H. White and W. Melville, *Journal of the American Chemical Society*, 1905, **27**, 373-386.
49. T. Markmaitree, R. Ren and L. L. Shaw, *The Journal of Physical Chemistry B*, 2006, **110**, 20710-20718.
50. M. Segales, Supplementary Deposited Data, 2015 http://dx.doi.org/10.5525/GLA.RESEARCHDATA.240
51. E. Zintl, A. Harder and B. Dauth, *Zeitschrift fuer Elektrochemie*, 1934, **40**, 588-593.
52. G. E. Walrafen and R. T. W. Douglas, *The Journal of Chemical Physics*, 2006, **124**, 114504.
53. T. Ernst, *Zeitschrift fuer Physikalische Chemie*, 1933, **20**, 65-88.
54. D. Colognesi, A. Giannasi, L. Ulivi, M. Zoppi, A. J. Ramirez-Cuesta, A. Roth and M. Fichtner, *The Journal of Physical Chemistry A*, 2011, **115**, 7503-7510.
55. X. Fan, X. Xiao, J. Shao, L. Zhang, S. Li, H. Ge, Q. Wang and L. Chen, *Nano Energy*, 2013, **2**, 995-1003.
56. X. Liu, D. Peaslee, C. Z. Jost and E. H. Majzoub, *The Journal of Physical Chemistry C*, 2010, **114**, 14036-14041.
57. X. Liu, D. Peaslee, C. Z. Jost, T. F. Baumann and E. H. Majzoub, *Chemistry of Materials*, 2011, **23**, 1331-1336.
58. M. G. Down, M. J. Haley, P. Hubberstey, R. J. Pulham and A. E. Thunder, *Journal of the Chemical Society, Dalton Transactions*, 1978, DOI: 10.1039/DT9780001407, 1407-1411.
59. O. Reckeweg and A. Simon, *Journal*, 2003, **58**, 1097.

60. S. V. Alapati, J. K. Johnson and D. S. Sholl, *The Journal of Physical Chemistry C*, 2008, **112**, 5258-5262.
61. L. Liu, D. Hu, T. He, Y. Zhang, G. Wu, H. Chu, P. Wang, Z. Xiong and P. Chen, *Journal of Alloys and Compounds*, 2013, **552**, 98-101.
62. W. Luo and E. Rönnebro, *Journal of Alloys and Compounds*, 2005, **404–406**, 392-395.
63. F. Sun, M.-y. Yan, J.-h. Ye, X.-p. Liu and L.-j. Jiang, *Journal of Alloys and Compounds*, 2014, **616**, 47-50.
64. Y. H. Hu and Y. Huo, *The Journal of Physical Chemistry A*, 2011, **115**, 11678-11681.
65. M. W. Powner, B. Gerland and J. D. Sutherland, *Nature*, 2009, **459**, 239-242.
66. K. Gibson, M. Ströbele, B. Blaschkowski, J. Glaser, M. Weisser, R. Srinivasan, H.-J. Kolb and H.-J. Meyer, *Zeitschrift für anorganische und allgemeine Chemie*, 2003, **629**, 1863-1870.
67. A. Yoshida, H. Yoshimura, T. Terada, Y. Nakayama, H. Kuno, T. Miyao and S. Naito, *International Journal of Hydrogen Energy*, 2011, **36**, 6751-6755.
68. H. Wu, W. Zhou, K. Wang, T. J. Udovic, J. J. Rush, T. Yildirim, L. A. Bendersky, A. F. Gross, S. L. Van Atta, J. J. Vajo, F. E. Pinkerton and M. S. Meyer, *Nanotechnology*, 2009, **20**, 204002.
69. X. Liu, D. Peaslee and E. H. Majzoub, *Journal of Materials Chemistry A*, 2013, **1**, 3926-3931.
70. K. C. Kim, M. D. Allendorf, V. Stavila and D. S. Sholl, *Physical Chemistry Chemical Physics*, 2010, **12**, 9918-9926.
71. D. A. J. Rand, R. Dell and R. S. o. Chemistry, *Hydrogen Energy: Challenges and Prospects*, Royal Society of Chemistry, 2008.
72. G. Balducci, Ph.D in Chemsitry, University of Glasgow, 2015.

Chapter 6

“It’s not the destination, but the journey, that matters”

Konstantinos P. Kavafis

6. CONCLUSIONS

The main aim of this work was to synthesise new nanocomposites as hydrogen storage materials. Specifically, the nanoconfinement synthetic approach has been used because it offers a recently developed strategy to improve the kinetics for hydrogen absorption and desorption in complex hydrides, stemming from the reduction of the hydride particle size to the range of nanometres. Nanoconfinement leads to the enhancement of the specific surface area and the diffusion distances are reduced compared to bulk materials, allowing faster dehydrogenation of the complex hydrides.

An inert porous host with a desired pore size in the range of the nanonometers is needed, in order to facilitate the introduction of the selected hydride in the porous host, which will in turn adopt the size of the pores. Two different type of porous carbon with different properties were selected for this work. As discussed in **Chapter 3**, the two carbons used were commercially available AX-21, with a very large specific area (*ca* 2000 m^2/g), and a wide distribution of pores sizes, ranging from < 4 nm to 100 nm (micropores, mesopores and macropores) and FDU-15, a highly ordered mesoporous carbon, prepared in the laboratory, via an evaporation induced self-assembly mechanism (EISA), which had a very narrow pore size distribution centred at 4 nm. Using two carbons with notably different characteristics allowed the study at how the pore size would affect the dehydrogenation properties of selected hydrides.

As detailed in **Chapter 4,** nanoconfinement of $LiAlH_4$ was achieved by wet impregnation, selecting diethyl ether as a solvent. The selected solvent proved an effective medium for the dissolution of the alanate without reaction. The results obtained with both carbons showed that the confinement approach reduced the specific surface area and available pore volume of the carbon host following treatment as would be expected for successful impregnation. This indicated a blocking of the pores to a much greater degree than in an equivalent physically mixed sample. The onset of hydrogen release for confined $LiAlH_4$ decreased significantly in temperature, being reduced by 51 °C (in both AX-21 and FDU-15) in comparison with as-received $LiAlH_4$. The temperature at which the hydrogen release was maximised was also lowered (by 16 °C in FDU-15 and by 26 °C in AX-21) in comparison with as-received $LiAlH_4$. From the findings of these results, it could be concluded that the pore size distribution of the porous host contributes significantly to the hydrogen release. It is suspected that the earlier and more gradual dehydrogenation of $LiAlH_4$@AX-21 is related to the wide dispersity of pore sizes in AX-21, which contrasts with the sharp dehydrogenation of $LiAlH_4$@FDU-15, where the pore-size distribution centred at 4 nm is well defined.

The aim of **Chapter 5** was to expand the applicability and versatility of the nanonconfinement approach, by addressing the challenges associated with performing wet impregnation in the Li-N-H system. With no known suitable solvent to impregnate the hydrogenated material, $LiNH_2$, a novel route was designed and adopted exploiting lithium-ammonia solutions. Lithium metal was mixed with porous carbon FDU-15 and flushed with a stream of ammonia gas, leading to in-situ formation of nanoconfined lithium amide. The confined amide showed a much earlier release of hydrogen in comparison with as-received $LiNH_2$. Normally $LiNH_2$ would thermally decompose to Li_2NH with ammonia evolution, but ammonia release was eliminated for the confined sample. Reaction with carbon led to irreversible Li_2CN_2 formation and hydrogen evolution. A set of experiments to establish the formation of Li_2CN_2 with physically mixed samples were performed. The physically mixed samples showed hydrogen release between 400 - 450 °C, producing a mixture of Li_2NH and Li_2CN_2, suggesting two decomposition pathways were followed. In contrast, confined $LiNH_2$ released hydrogen *ca.* 220 °C lower than the physically mixed sample, with no detectable trace of ammonia release, suggesting the only decomposition pathway followed was via Li_2CN_2 formation, presumably facilitated by intimate contact of $LiNH_2$ particles with the porous host. These findings make the Li – N – H – C system a valid one to consider for hydrogen storage applications, releasing hydrogen at lower temperatures than the Li – N – H ($LiNH_2$/LiH) system.

In summary, this thesis has discussed some novel methods to prepare nanosized complex hydrides on carbon supports. An improved understanding of the effects and influence of the carbon support on complex hydrides, potentially interesting for hydrogen storage applications, was addressed. The nanoconfinement approach has once more been proved a viable method to lower the dehydrogenation temperatures of complex hydrides. Although the focus of this work was restricted to hydrogen storage, the application of nanoconfined hydride composites is not limited this field. The findings reported in this thesis regarding the state-of-art of nanocomposites, can be utilised in many other fields, like rechargeable batteries, catalysis, among others where reduction of the particle size to improve bulk material properties is needed. Since the first time that it was reported how nanoconfinement could improve hydrogen storage properties in 2005,[1] it has attracted a lot of attention and a lot of improvement in this field has been done. Despite this increasing interest in nanoconfinement, we are still far from tailoring the composite properties at will, from predicting the results and of a total understanding of the observed effects. Given the rapid knowledge progression in the field it would be very interesting to see what awaits us in the near future.

1. A. Gutowska, L. Li, Y. Shin, C. M. Wang, X. S. Li, J. C. Linehan, R. S. Smith, B. D. Kay, B. Schmid, W. Shaw, M. Gutowski and T. Autrey, *Angewandte Chemie International Edition*, 2005, **44**, 3578-3582.

Chapter 7

7. APPENDICES

The appendices and supplementary information can be found at:
http://dx.doi.org/10.5525/GLA.RESEARCHDATA.240

7.1. APPENDIX A – Chapter 3

Table 7-1 and Table 7-2 present some of the values obtained for the particles size of AX-21 from the SEM images. These values have been used to plot the particle size distribution (from a population of 250 values - only 120 values shown for space economy purposes).

Table 7-1. Number of measurement and the particle size of SEM images for AX-21.

Nº measurement	Particle size / µm	Nº measurement	Particle size / µm	Nº measurement	Particle size / µm
1	3.718	41	12.146	81	12.614
2	5.884	42	9.481	82	19.294
3	3.711	43	5.649	83	6.365
4	7.159	44	8.05	84	6.938
5	4.242	45	15.385	85	24.467
6	3.193	46	4.325	86	15.857
7	4.696	47	9.51	87	12.753
8	5.276	48	7.958	88	19.223
9	1.93	49	12.641	89	4.138
10	2.798	50	9.671	90	5.729
11	11.987	51	11.942	91	5.046
12	3.929	52	6.198	92	7.037
13	6.914	53	3.674	93	4.216
14	7.766	54	7.866	94	9.226
15	11.657	55	5.7	95	7.734
16	3.377	56	7.564	96	5.641
17	2.566	57	5.333	97	6.732
18	2.67	58	6.6	98	11.009
19	2.934	59	11.619	99	9.249
20	2.042	60	19.482	100	8.33
21	3.448	61	9.384	101	13.704
22	2.669	62	19.276	102	16.305
23	2.695	63	10.464	103	18.535
24	12.526	64	7.648	104	20.416
25	15.099	65	2.81	105	9.232
26	2.05	66	3.095	106	19.229
27	1.251	67	10.241	107	33.617
28	1.454	68	14.672	108	15.312
29	1.401	69	8.956	109	18.85
30	18.435	70	10.271	110	14.464
31	2.268	71	6.144	111	15.765
32	1.956	72	12.227	112	17.735
33	1.811	73	5.316	113	16.116
34	4.018	74	10.446	114	14.464
35	3.912	75	8.304	115	22.544
36	15.543	76	11.848	116	22.996
37	21.307	77	7.803	117	32.726
38	5.027	78	7.127	118	24.322
39	6.203	79	3.898	119	28.016
40	6.399	80	3.668	120	13.172

Table 7-2. Number of measurement and the respective particle size of SEM images for FDU-15.

Nº measurement	Particle size / µm	Nº measurement	Particle size / µm	Nº measurement	Particle size / µm
1	38.906	41	56.412	81	56.763
2	25.364	42	66.123	82	83.654
3	11.483	43	74.194	83	26.923
4	23.083	44	110.221	84	38.473
5	27.336	45	50.166	85	52.884
6	14.878	46	38.485	86	50.009
7	30.108	47	74.038	87	50
8	52.237	48	100.004	88	77.89
9	25.245	49	25.979	89	42.242
10	17.99	50	32.749	90	42.056
11	37.733	51	22.136	91	40.396
12	18.455	52	30.904	92	38.461
13	38.564	53	22.136	93	44.491
14	39.429	54	35.577	94	32.692
15	49.343	55	59.615	95	60.584
16	29.627	56	53.88	96	53.024
17	29.627	57	63.469	97	22.855
18	20.335	58	31.745	98	28.862
19	35.103	59	34.629	99	40.258
20	10.518	60	27.885	100	60.546
21	26.845	61	42.308	101	44.491
22	19.649	62	38.461	102	28.296
23	36.864	63	37.512	103	70.297
24	38.843	64	57.724	104	91.427
25	44.986	65	25.018	105	35.355
26	31.026	66	23.077	106	64.681
27	27.945	67	33.654	107	24.514
28	19.276	68	24.115	108	29.823
29	22.362	69	60.813	109	35.59
30	39.355	70	36.195	110	19.231
31	17.666	71	48.622	111	31.963
32	14.431	72	65.962	112	33.763
33	21.017	73	24.477	113	19.446
34	25.994	74	61.568	114	19.47
35	12.47	75	50.083	115	21.241
36	27.177	76	56.763	116	26.94
37	11.517	77	53.855	117	34.961
38	11.517	78	70.985	118	25.074
39	23.644	79	25.961	119	28.28
40	16.119	80	34.629	120	17.886

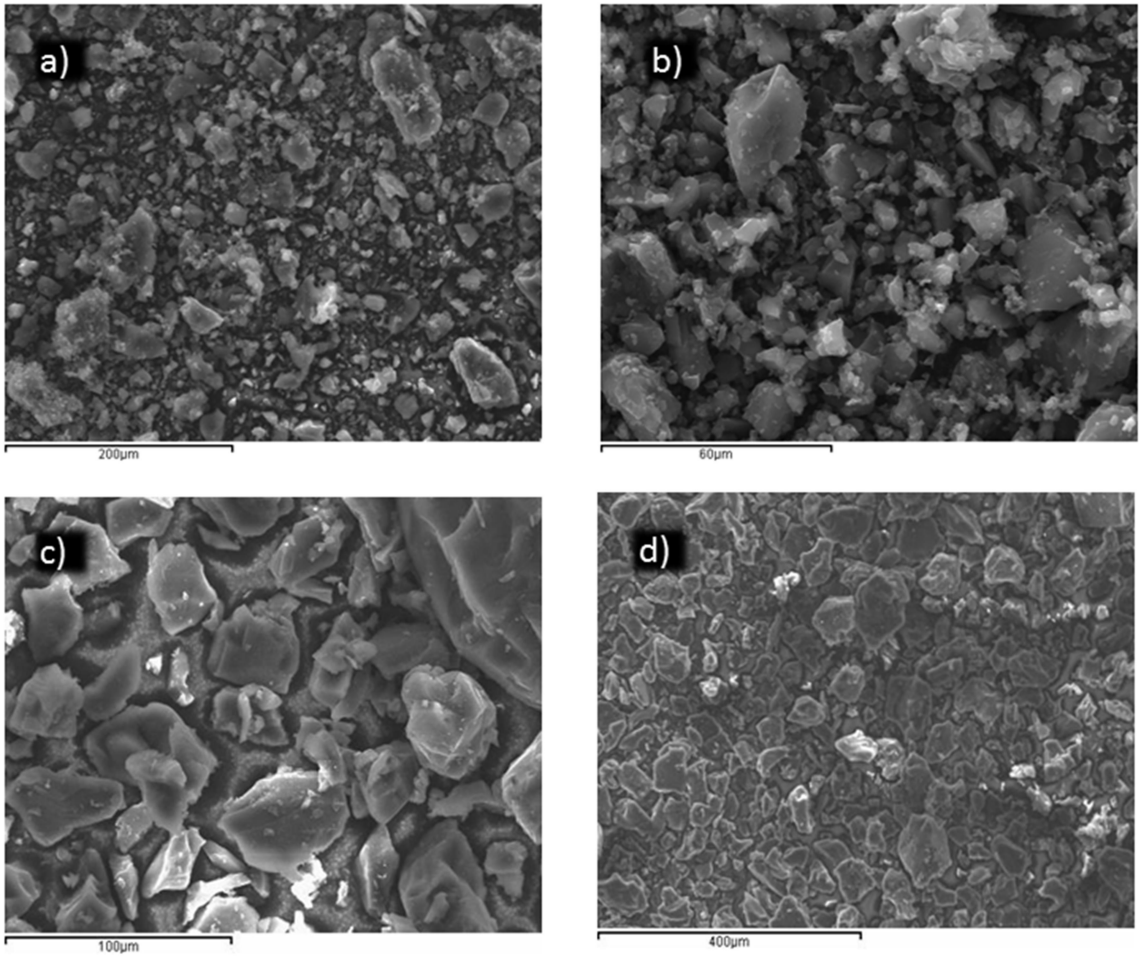

Figure 7-1. SEM images used for measuring particle size of: a - b) AX-21, c-d) FDU-15

7.2. APPENDIX B – Chapter 4

Section 1: Calculations

Theoretical hydrogen capacity in $LiAlH_4$

Overall:

$LiAlH_4$ MR = 37.95 g mol-1

H = 1 g mol-1

$$\frac{4\ g\ H}{37.95\ g\ LiAlH_4} \cdot 100\ =\ 10.54\ wt.\%\ H$$

In 1 mol of $LiAlH_4$, there is 4 g of H available (in 37.95 grams of $LiAlH_4$)

First step:

$$3LiAlH_4 \xrightarrow{150\text{–}175\ ^\circ C} Li_3AlH_6 + 2Al + 3H_2$$

$LiAlH_4$: MR = 37.95 g·mol^{-1}

H: MR = 1 g·mol^{-1}

$$1\ g\ LiAl_4 \cdot \frac{1\ mol\ LiAlH_4}{37.95\ g\ LiAlH_4} \cdot \frac{3\ mol\ H_2}{3\ mol\ LiAlH_4} \cdot \frac{2\ g\ H_2}{1\ mol\ H_2} = 0.0527\ g\ H_2$$

$$\frac{0.0527\ g\ H_2}{1\ g\ LiAlH_4} \cdot 100 = \mathbf{5.27\ wt.\%}$$

Second step:

$$3LiAlH_4 \xrightarrow{150\text{–}175\ ^\circ C} Li_3AlH_6 + 2Al + 3H_2$$

$$Li_3AlH_6 \xrightarrow{180\text{–}220\ ^\circ C} LiH + Al + \frac{3}{2}H_2$$

$LiAlH_4$: MR = 37.95 g mol-1

Li_3AlH_6: MR = 53.85 g·mol^{-1}

H: MR = 1 g·mol^{-1}

$$1\ g\ LiAlH_4 \cdot \frac{1\ mol\ LiAl_4}{37.95\ g\ LiA_4} \cdot \frac{3/2\ mol\ H_2}{3\ mol\ LiAlH_4} \cdot \frac{2\ g\ H_2}{1\ mol\ H_2} = 0.0264\ g\ H_2$$

$$\frac{0.0264\ g\ H_2}{1\ g\ LiAl_4} \cdot 100 = \mathbf{2.64\ wt.\%}$$

Third step:

$$3LiAlH_4 \xrightarrow{150\text{–}175\ ^\circ C} Li_3AlH_6 + 2Al + 3H_2$$

$$Li_3AlH_6 \xrightarrow{180-220\ ^\circ C} LiH + Al + \frac{3}{2}H_2$$

$$LiH + 3Al \xrightarrow{400\ ^\circ C} 3LiAl + \frac{3}{2}H_2$$

$LiAlH_4$: MR = 37.95 g·mol^{-1}

H: MR= 1 g·mol^{-1}

$$1\ g\ LiA_4 \cdot \frac{1\ mol\ LiAl_4}{37.95\ g\ LiAlH_4} \cdot \frac{3/2\ mol\ H_2}{3\ mol\ LiAlH_4} \cdot \frac{2\ g\ H_2}{1\ mol\ H_2} = 0.0264\ g\ H_2$$

$$\frac{0.0264\ g\ H_2}{1\ g\ LiAl_4} \cdot 100 = \mathbf{2.64\ wt.\%}$$

Combination of (1) + (2) + (3) = **10.55 wt. % H**

Calculations % confinement: or how many material it can be theoretically "confined" in the porous hosts.

1. **IN AX-21 (Sample 2):**

Total Pore Volume AX-21: 1.18 $cm^3 \cdot g^{-1}$

$LiAlH_4$ solid density: 0.917 $g \cdot cm^{-3}$

First of all, for a given amount (of our choice – in this case, 0.2 g) of AX-21, it has to be calculated what is the "free" volume available (V) for confinement, using the specific carbon mass (m) and the total pore volume carbon (V_p):

$$V_p = \frac{V}{m} = \left[\frac{cm^3}{g}\right]$$

$$\mathrm{V} = \mathrm{m} \cdot V_p = \ [cm^3]$$

$$0.236\ cm^3 = \ 0.2\ g\ \cdot\ 1.18 \frac{cm^3}{g}$$

Therefore, in 0.2 grams of AX-21, there is a volume available for hosting a material of 0.236 cm^3. Now, using the solid density of the material (ρ) to be confined ($LiAlH_4$), the mass of this material (m) in order to fill the volume in AX-21 (V) can be calculated:

$$\rho = \frac{m}{V} = \left[\frac{g}{cm^3}\right]$$

$$m = V \cdot \rho = [g]$$

$$0.216\ g\ LiAl\ _4 = 0.236\ cm^3 \cdot\ 0.917 \frac{g}{cm^3}$$

Therefore, in a sample of 0.2 grams of AX-21, there is space available for 0.216 grams of $LiAlH_4$ (which will correspond to a confinement of 100% of the available space). In order to ensure, that

all the $LiAlH_4$ present will be confined in the pores a lower confinement than 100 % was set. (92.6 %, which will correspond to 0.2 grams of $LiAlH_4$ in 0.2 grams of AX-21.)

Calculation expected mass loss in confined sample:

0.2 grams AX-21 + 0.2 grams $LiAlH_4$

*Considering that $LiAlH_4$ experimentally only desorbs 9.3 % w.t. H_2

0.2 grams $LiAlH_4$, after desorbing 9.3 % w.t., will remain 0.4814 g decomposed product

*Assuming nothing is desorb from the porous host (previously dried)

After desorption in the sample holder will remain, 0.2 grams carbon + 0.1814 g decomposed product = 0.3814 g total sample decomposed

$$\frac{0.3814\ grams\ decomposed\ product}{0.4\ grams\ initial\ product} \cdot 100 = 95.35\ \%\ remainder\ product$$

$$100\ \% - 95.35\ \% = 4.65\ \%\ mass\ loss\ H_2$$

2. **IN FDU-15 (sample 3):**

Total Pore Volume FDU-15: 0.32 $cm^3 \cdot g^{-1}$

$LiAlH_4$ solid density: 0.917 $g \cdot cm^{-3}$

The same calculations as above have been done to calculate the amount of $LiAlH_4$ that can be confined in the void space of FDU-15 carbon (V_p) (selected amount of porous host in this case was again 0.2 grams (m)):

$$V_p = \frac{V}{m} = \left[\frac{cm^3}{g}\right]$$

$$\mathrm{V} = \mathrm{m} \cdot V_p = \ [cm^3]$$

$$0.064\ cm^3 = 0.2\ g \cdot \frac{0.32\ cm^3}{1\ g}$$

Therefore, in 0.2 grams of FDU-15, there is a volume available for hosting a material of 0.064 cm^3.

$$\rho = \frac{m}{V} = \left[\frac{g}{cm^3}\right]$$

$$m = V \cdot \rho = [g]$$

$$0.0587\ g\ LiAlH_4 = 0.064\ cm^3 \cdot\ 0.917 \frac{g\ LiAlH_4}{cm^3}$$

Therefore, in a sample of 0.2 grams of FDU-15, there is space available for 0.0587 grams of $LiAlH_4$ (which will correspond to a confinement of 100% of the available space).

The selected value for confinement was set at 95 %, which corresponds to 0.055 grams of $LiAlH_4$ in 0.2 grams of FDU-15.

Calculation expected mass loss in confined sample:

0.2 grams FDU-15 + 0.055 grams $LiAlH_4$

*Considering that $LiAlH_4$ experimentally only desorbs 9.3 % w.t. H_2

0.055 grams LiAlH4, after desorbing 9.3 % w.t., will remain 0.0498 g decomposed product

*Assuming nothing is desorb from the porous host (previously dried)

After desorption in the sample holder will remain, 0.2 grams carbon + 0.0498 g decomposed product = 0.2498 g total sample decomposed

$$\frac{0.2498\ grams\ decomposed\ product}{0.255\ grams\ initial\ product} \cdot 100 = 97.96\ \%\ remainder\ product$$

$$100\ \% - 97.96\ \% = 2.04\ \%\ mass\ loss\ H_2$$

<u>Section 2:</u> Comparison of dried carbon with as-received carbon.

AX-21

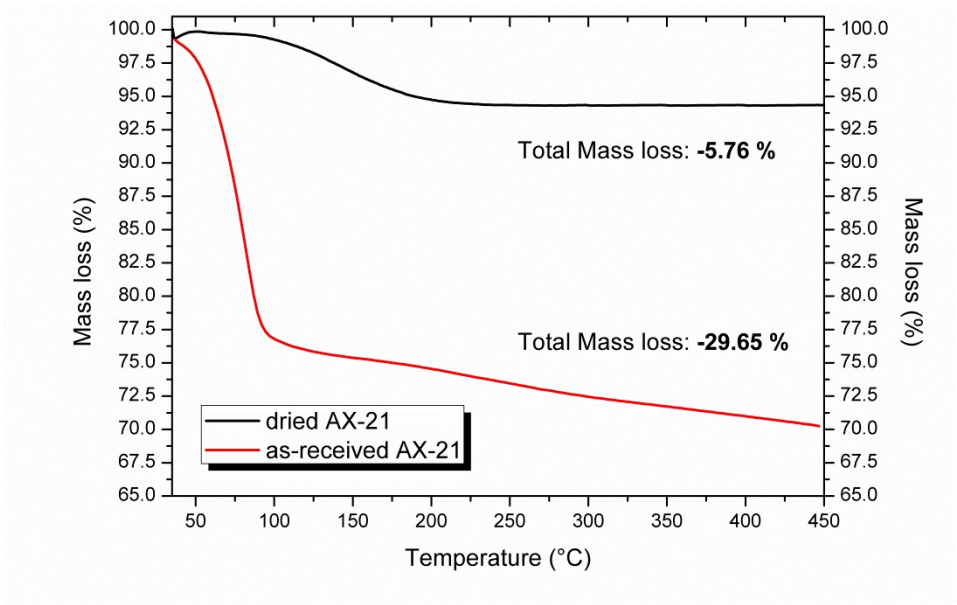

Figure 7-2. Mass loss observed for AX-21 dried and undried.

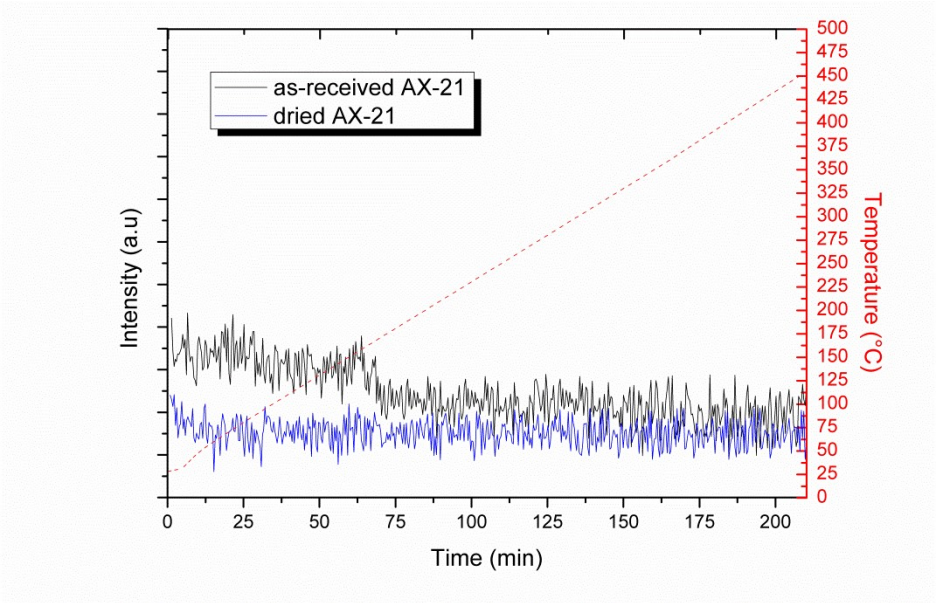

Figure 7-3. H_2O (moisture) release obtained by MS for dried and undried AX-21. This was the only gas detected on the analyser.

FDU-15

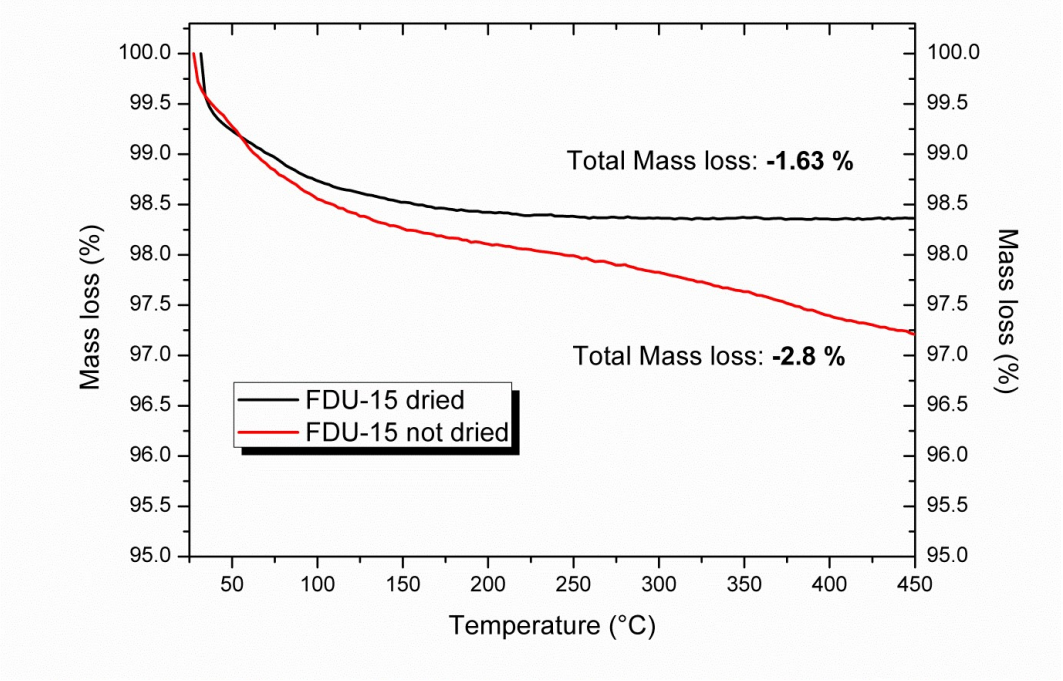

Figure 7-4. Mass loss observed for dried and undried FDU-15.

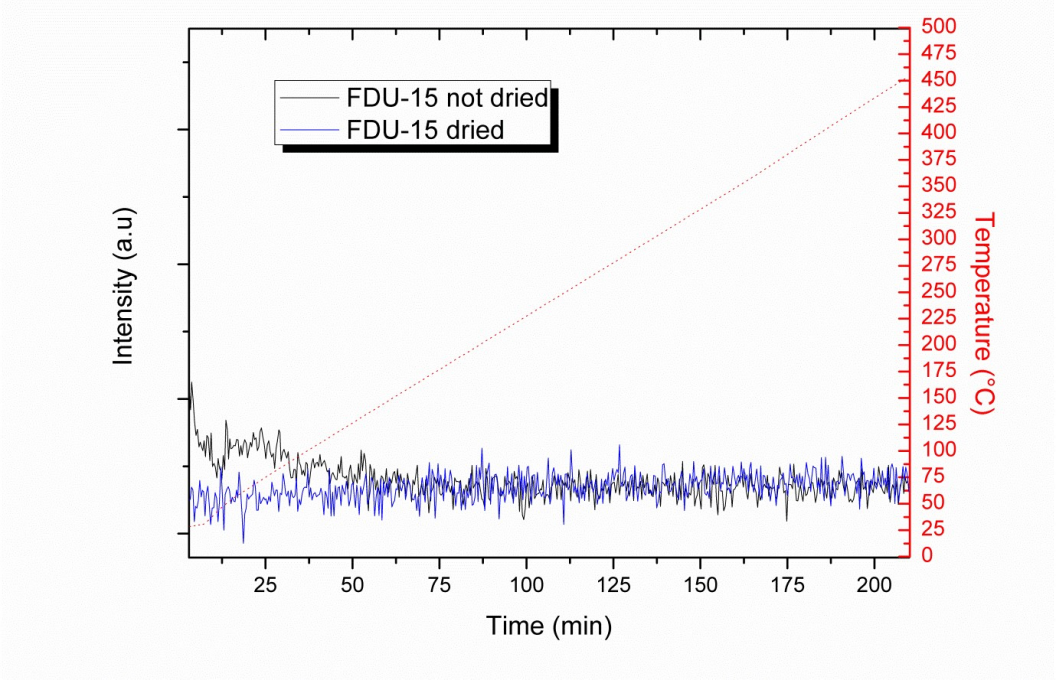

Figure 7-5. H_2O (moisture) release obtained from the Mass Spectra analyser for dried and not dried FDU-15. This was the only gas detected on the analyser.

7.3. APPENDIX C – Chapter 5

Calculations of the % confinement of $LiNH_2$ in FDU-15.

Total Pore Volume FDU-15: 0.32 $cm^3 \cdot g^{-1}$

$LiNH_2$ solid density[23]: 1.18 $g \cdot cm^{-3}$

For a given amount of porous carbon (0.1 grams), the "free" volume available for confinement (V) can be calculated from using the specific carbon mass (m), and the total pore volume of the carbon (V_p):

$$V_p = \frac{V}{m} = \left[\frac{cm^3}{g}\right]$$

$$\mathrm{V} = \mathrm{m} \cdot V_p = \ [cm^3]$$

$$0\ 0.032\ cm^3 = 0.1\ g \cdot\ 0.32 \frac{cm^3}{g}$$

Therefore, in 0.1 grams of FDU-15, the volume available for hosting a material is 0.032 cm^3.

Now, using the solid density (ρ) of the material to be confined ($LiNH_2$), the mass of this material required (m)to fill the volume in FDU-15 is given by:

$$\rho = \frac{m}{V} = \ \left[\frac{g}{cm^3}\right]$$

$$m = V \cdot \rho = [g]$$

$$0.03776\ g\ LiNH_2 = 0.032\ cm^3 \cdot\ 1.18 \frac{g}{cm^3}$$

Therefore, in a sample of 0.1 grams of FDU-15, theoretically there is space available for 0.03776 grams of $LiNH_2$ (which will correspond to 100 % confinement).

The selected value for confinement was set at 95 %, which corresponds to 0.036 grams of $LiNH_2$ in 0.1 grams of FDU-15.

Calculation of the expected amount of $LiNH_2$, from the preparation of Li and ammonia:

Sample 1 has been prepared by flushing ammonia gas over lithium metal. Given a certain amount of lithium metal, it has been calculated that the expected amount of lithium amide (considering a stoichiometric reaction) is given by:

Molar mass (Li)[23] = 12.01 g · mol^{-1}

Molar mass ($LiNH_2$)[23] = 22.96 g · mol^{-1}

$$Li + NH_3 \rightarrow LiNH_2 + \frac{1}{2} H_2$$

$$0.1\ g\ Li \cdot \frac{1\ mol\ Li}{12.01\ g\ Li} \cdot \frac{1\ mol\ LiNH_2}{1\ mol\ Li} \cdot \frac{22.96\ g\ LiNH_2}{1\ mol\ LiNH_2} = 0.19117\ g\ LiNH_2$$

Explanation: Grams of starting material, lithium, have been converted to moles of Li. Using the stoichiometric ratio of $LiNH_2$: Li (1:1), moles of lithium have been converted to moles of $LiNH_2$. And finally, using the molar mass of $LiNH_2$, moles of $LiNH_2$ have been converted to grams of $LiNH_2$.

Calculation of the expected $LiNH_2$ formed during "in-situ" confinement (sample 3):

To prepare sample 3, $LiNH_2$ from the synthesis of Li and ammonia gas is prepared in-situ in the presence of the porous carbon. Using the theoretical value of $LiNH_2$ needed to fill 95 % of the pores (calculated above), the amount of corresponding lithium needed can be calculated from:

Confinement (95 %) = 0.036 grams of $LiNH_2$ in 0.1 grams of FDU-15.

How many grams of lithium are needed to achieve 95 % confined $LiNH_2$@C?

$$0.036g\ LiNH_2 \cdot \frac{1\ mol\ LiNH_2}{22.96\ g\ LiNH_2} \cdot \frac{1\ mol\ Li}{1\ mol\ LiNH_2} \cdot \frac{12.01\ g\ Li}{1\ mol\ Li} = 0.0188\ g\ Li$$

Explanation: the mass of $LiNH_2$ to achieve a confinement of 95 % in FDU-15 (calculated above) has been converted to moles of $LiNH_2$. Using the stoichiometric ratio of $LiNH_2$: Li (1:1), moles of $LiNH_2$ have been converted to moles of lithium, which finally have been converted to grams of lithium needed using the lithium molar mass.

DTA/MS characterization of as-recevied $LiALH_4$ to 800 °C at 5 °C·min^{-1}

Figure 7-6 shows the DTA profile along with the simultaneos correspondent TGA profile for the as-received $LiNH_2$. No thermal events or mass loss is observed below 372 °C. There is a continuos mass loss until over 500 °C, of 35 % mass loss which contains another DTA maximum peak at 503 °C. Then around 650 °C it can be observed another continuous mass loss of 19 % until 800 °C, with different DTA maximum peaks, the most significant at 662 and 775 °C. The total mass loss of as-received $LiNH_2$ heated at 800 °C is 51.02 wt.%.

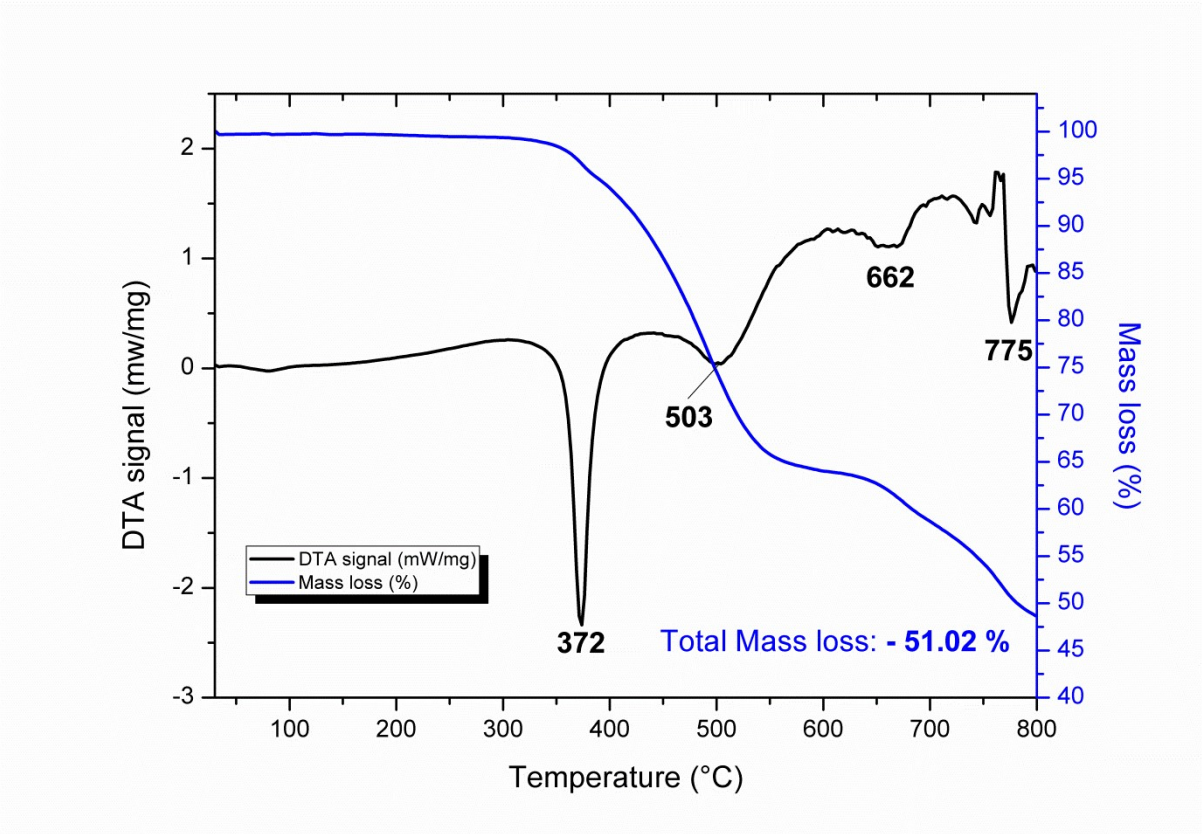

Figure 7-6. DTA and TG plots for as-received $LiNH_2$ sample, under a thermal treatment to 800 °C at 5°·min^{-1}.

If Figure 7-6 is complemented with the mass spectrum profile shown in Figure 7-7, an assignement of the mass losses observed and DTA maximum peaks to the gasses evolved can be performerd. Figure 7-7 shows the detection of 3 different evolved gasses; NH_3, H_2 and N_2. Ammonia gas release is the first gas observed at lower temperatures, starting at 380 °C and peaking at 514 °C. Nitrogen gas release is the last gas observed, at higher temperatures, starting at 636 °C and peaking at 800 °C. Whereas, hydrogen gas seems to have a two-step release happening simultaneously with both NH_3 and N_2 gas release, slowly starting at 435 °C and having a small maximum peak at 581 °C and then a more sharp release starting at 636 °C and peaking at 800 °C. These results obtained are in good accordance with the ones obtained from the DTA and

TG profile, where the first higher mass loss obtained of 35 % would correspond to NH_3 and H_2 gas release (lower contribution of the latter), and the second lower mass loss obtained of 19 % would correspond to H_2 and N_2 gas release (again lower contribution of the latter).

These findings are in very good accordance with the reaction pathway of $LiNH_2$ published in the literature, where NH_3 and H_2 gas released are observed on the decomposition of $LiNH_2$ to form Li_2NH and where the H_2 and N_2 gas released observed would correspond to the total decomposition of ammonia released by Li_2NH to give Li metallic. No solid product could be recollected from the STA pan after thermal treatment at 800 °C, probably due to the total composition of the studied material (with the consequently lack of XRD structural characterisation of the final prodcut at 800 °C). Although Li metallic was expected to remain in the STA pan, the fact that the alumina pan appeared darker after thermal treatment suggest that the Lithium metalic diffused through the pan.

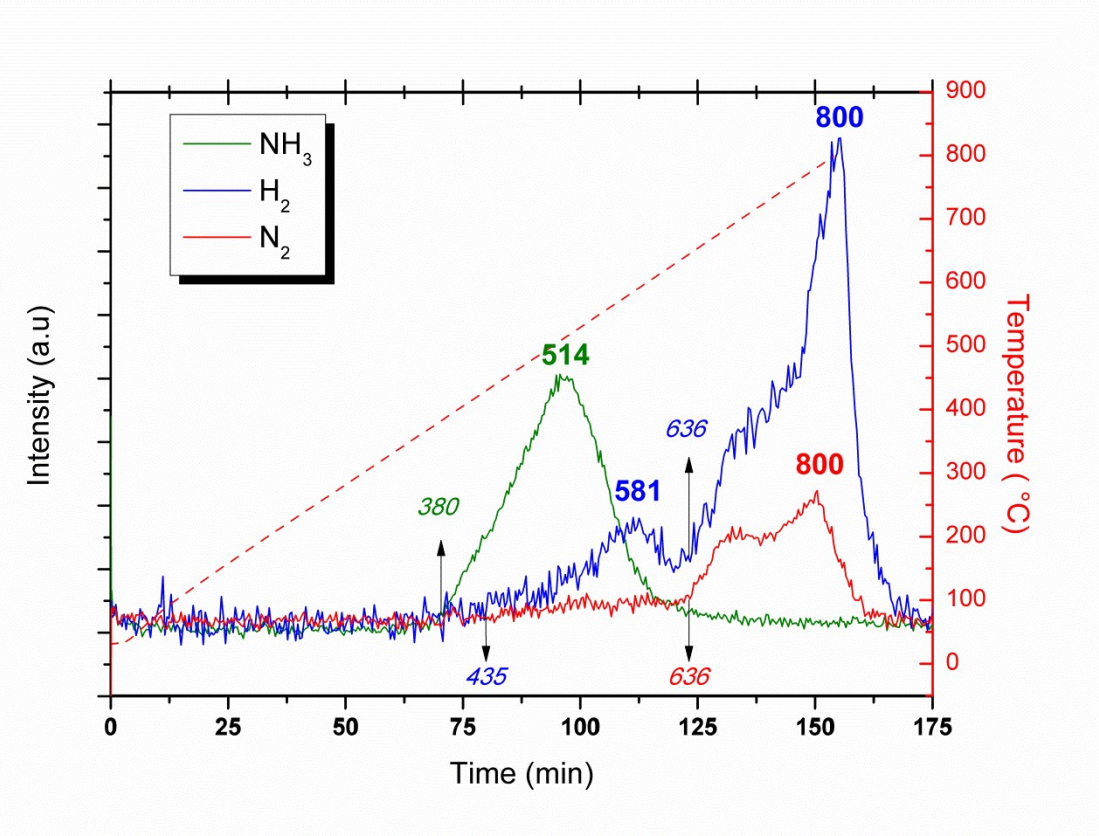

Figure 7-7. MS profile recording H_2, N_2 and NH_3 evolution (m/z = 2, 14 and 17 respectively) for as-received $LiNH_2$, under a thermal treatment to 800°C at 5°·min^{-1}.